

DISSERTATION

submitted to the

Combined Faculties for the Natural Sciences and for Mathematics

of the Ruperto-Carola University of Heidelberg, Germany

for the degree of

Doctor of Natural Sciences

Put forward by

Dennis Kleimaier, M.Sc.

born in Mindelheim, Germany

Oral examination: February 3rd 2021

Exploring Protein Interactions with
 ^{23}Na Triple-quantum MRS and
 ^1H Chemical Exchange Saturation Transfer MRI

Referees: Prof. Dr. Lothar Schad
Prof. Dr. Peter Bachert

Erforschung von Proteinwechselwirkungen mittels ^{23}Na Tripelquanten MRS und ^1H Chemical Exchange Saturation Transfer MRI

Die Kernspinresonanz (NMR) ermöglicht die nichtinvasive Untersuchung von Proteinen mit Hilfe der ^{23}Na Tripelquanten (TQ) und ^1H Chemical Exchange Saturation Transfer (CEST) Signale. Wechselwirkungen von Natriumionen mit Makromolekülen erzeugen ein intrazellulär-empfindliches TQ-Signal. Ein TQ-Signalanstieg kann mit einem Verlust der Zellvitalität einhergehen. Ein tieferes Verständnis des TQ-Signals auf zellulärer Ebene ist jedoch notwendig, um einen potenziellen Biomarker für die Zellvitalität zu erhalten. CEST ermöglicht die indirekte Messung von niedrig konzentrierten organischen Verbindungen durch ihren Magnetisierungsaustausch mit Wasser. CEST-Signale von Proteinen *in vitro* hängen dabei vom Proteinfaltungszustand ab, weswegen diese Signale ein großes Potenzial als ein nichtinvasives diagnostisches Werkzeug für Erkrankungen, wie Krebs und neurodegenerative Erkrankungen, haben. Nichtsdestotrotz muss die Nachweisbarkeit von Denaturierungsprozessen in lebenden Zellen erst noch experimentell gezeigt werden. In dieser Arbeit wurde zuerst eine Abhängigkeit des TQ-Signals vom pH-Wert und dem Proteinfaltungszustand in Proteinlösungen gezeigt. Die Zunahme der Verfügbarkeit von negativ geladenen Gruppen in Proteinen führte zu einem TQ-Signalanstieg während der pH-Variation ($224,5 \pm 25,1\%$) oder der Proteinfaltung ($40,7 \pm 2,3\%$). Zweitens wurde die zelluläre Antwort auf eine Na/K-ATPase-Blockade mittels verbesserter TQ Signaldetektion beobachtet. Die Perfusion mit 1 mM Ouabain Medium verursachte einen TQ-Signalanstieg um $38,9 \pm 4,1\%$, während die Perfusion mit 0 mM K^+ Medium zu einem TQ-Signalanstieg um $83,4 \pm 8,9\%$ führte. Beide TQ-Signalanstiege stimmen mit einem Einstrom von Natriumionen während der Na/K-ATPase-Blockade überein. Schließlich wurde die zelluläre Hitzeschockantwort mittels CEST-Signalen von Proteinen untersucht. Die Anwendung eines Hitzeschocks führte zu einer Signalabnahme von $8,0 \pm 0,4\%$ gefolgt von einem kontinuierlichem Signalanstieg, der mit einer Rückfaltung von denaturierten Proteinen durch Chaperone übereinstimmt. Die vorgestellten NMR-Techniken kombiniert mit dem Bioreaktorsystem sind erfolgversprechende Forschungsinstrumente zur nichtinvasiven Untersuchung von zellulären Prozessen mittels NMR.

Exploring Protein Interactions with ^{23}Na Triple-quantum MRS and ^1H Chemical Exchange Saturation Transfer MRI

Nuclear magnetic resonance (NMR) allows the non-invasive investigation of proteins using ^{23}Na triple-quantum (TQ) and ^1H chemical exchange saturation transfer (CEST) signals. Interactions of sodium ions with macromolecules yield an intracellular sensitive TQ signal. A TQ signal increase has been shown to correlate with the loss of cell viability. However, a deeper understanding of the TQ signal on a cellular level is necessary to determine its capability to serve as a potential biomarker for cell viability. CEST indirectly detects low concentrated organic compounds by their magnetization transfer with water. Protein-based CEST signals have been demonstrated *in vitro* to be closely connected to the protein folding state and have great potential as a non-invasive diagnostic tool for diseases, like cancer and neurodegenerative diseases. Nonetheless, the detectability of denaturation processes in living cells by CEST NMR remains to be verified experimentally. In the first part of this thesis, a dependence of the TQ signal on the pH and protein folding state was demonstrated using protein solutions. An increase in the availability of negatively charged groups in proteins caused an increase in the TQ signal during pH variation ($224.5 \pm 25.1\%$) or protein unfolding ($40.7 \pm 2.3\%$). Second, the cellular response to a Na/K-ATPase inhibition was monitored using improved TQ signal detection. The TQ signal increased by $38.9 \pm 4.1\%$ and $83.4 \pm 8.9\%$ during perfusion with 1 mM ouabain and 0 mM K^+ medium, respectively, which agreed with an influx of sodium ions during the Na/K-ATPase inhibition. Finally, the cellular heat shock response was investigated using protein-based CEST signals. Heat shock application resulted in a substantial signal decrease by $8.0 \pm 0.4\%$ followed by a continuous signal recovery, which agreed with chaperone-induced refolding of misfolded proteins. The proposed NMR techniques combined with the bioreactor system are promising research tools to non-invasively investigate cellular processes by NMR.

Acknowledgement

All men dream: but not equally. Those who dream by night in the dusty recesses of their minds wake up in the day to find it was vanity, but the dreamers of the day are dangerous men, for they may act their dreams with open eyes, to make it possible.

–T. E. Lawrence, Seven Pillars of Wisdom

A PhD is a journey, which involves the help, support and guidance of many people.

First and foremost, I would like to thank Prof. Dr. Lothar Schad for the opportunity to continue my academic journey within your research group. The continuous support and trust in all my crazy ideas allowed me to explore my own projects under your scientific guidance. I especially appreciate your trust in my skills to work on the extremely complex and interdisciplinary MR-compatible bioreactor system. Moreover, I am grateful for the ability to attend all these enlightening conferences in beautiful locations and that you introduced me to Dr. Victor Schepkin.

Furthermore, I would like to thank Prof. Dr. Peter Bachert for his willingness to act as the second referee for this thesis and for his medical physics lecture, which introduced me to the exciting field of NMR.

I am deeply indebted for the cooperation with Prof. Dr. Eric Gottwald and Cordula Nies of the Karlsruher Institute of Technology. Most of the research in this thesis would not have been possible without their endless help and support, even on weekends. They provided the cleanest bioreactor and the best cells in the whole world.

Likewise, I want to express my gratitude to Dr. Victor Schepkin from the National Magnetic Field Laboratory who shared with me his insights into the exciting world of the sodium triple-quantum. Your guidance during your stay at our department finally helped me to finish my first publication. In addition, your patience and your careful error analysis changed my way of thinking forever. Let us finally achieve the transition to 21 T!

I am also grateful to Dr. Steffen Goerke from the German Cancer Research Center for taking me on the journey of the fascinating heat shock experiments. Thank you for showing me how to improve scientific writing by starting with the most difficult parts. Our journey did not end here, as there is still more to see!

Additionally, I gratefully acknowledge the support of Felix Hoerner and Dr. Thorsten Lau from the Central Institute of Mental Health. Thank you, Felix, for being present during the many crashes of the MR scanner, especially when the room temperature was so high that every device produced an error. Moreover, thank you, Thorsten, for the access to the cell culture laboratory and all the other equipment.

Many thanks go to Michaela and Ruomin for these endless bioreactor nights at the ZI and the joint effort to take the bioreactor system to the next level. Furthermore, thank you, Michaela, for these endless discussions and especially for the many sports activities, e.g. skiing, cross country skiing, mountain biking, ... Likewise, thanks go to Ruomin for your 5 minutes, for these many gaming events and for your commitment to improve my writing skills in your exploding comments. I guess the word count of these comments is equal to the word count in my original draft. I also enjoyed all these snacks and whatsoever I had to eat because of you. Finally, special thanks go to you for proofreading this thesis despite your busy postdoc life.

Special thanks go to Simon (2) for all these crazy discussions beginning with the sodium triple-quantum and ending with quantum computing, sports, proteins, ... I am grateful that you took time out of your busy schedule reading thousand of papers to proofread this thesis. Your journey just started!

Additionally, thanks go to all my colleagues at the CKM which were a part of this fascinating PhD journey. I deeply enjoyed the social events, the conferences and the excellent working atmosphere. I am especially thankful to all the X-nuclei group members. Special thanks go to my office roommate Efe. It was a pleasant time with you through my PhD journey and the office feels empty in this new age. I am also deeply sorry for breaking the window and damaging your plant.

Kristina, thank you for being with me throughout my academic journey. The bioreactor experiments would have been much more exhausting without your delicious food and support, even though you rarely saw me during these days. Thank you for Luna, who distracted me throughout the home office days.

Last but not least, I would like to thank my parents and my brother for their trust in my abilities to achieve all these goals. Your endless support during the difficult times combined with the distraction during all these times has made all this possible. Special thanks for caring for Lucie during my academic journey. This dissertation is dedicated to you.

Contents

1	Introduction	1
2	Theoretical Background	7
2.1	Nuclear Magnetic Resonance	7
2.1.1	Nuclear Spin and Nuclear Zeeman Effect	7
2.1.2	Macroscopic Magnetization	9
2.1.3	Bloch Equations and Relaxation	10
2.1.4	Sensitivity	13
2.1.5	Nuclear Magnetic Resonance Spectrum	14
2.2	Quadrupole Nuclei	16
2.2.1	Density Operator	17
2.2.2	Irreducible Tensor Formalism	18
2.2.3	Nuclear Spin Hamiltonian	19
2.2.4	Electric Spin Hamiltonian	20
2.2.5	Effects of Hard RF Pulses	27
2.2.6	Relaxation in Isotropic Environment	28
2.2.7	Multi-quantum Pulse Sequence	32
2.3	Magnetization Transfer and Chemical Exchange Saturation Transfer	35
2.3.1	Magnetization Transfer Processes	35
2.3.2	Chemical Exchange Saturation Transfer	40
2.4	Proteins and Sodium in Biology	48
2.4.1	Proteins	48
2.4.2	Physiological Role of Sodium	55
3	Materials and Methods	59
3.1	Experimental Setup	59
3.1.1	Preclinical NMR Scanner	59
3.1.2	RF Coils	59
3.1.3	Model Systems	62
3.1.4	MR-compatible Microcavity Array-based Bioreactor System	65
3.2	MR Methods and Pulse Sequences	72
3.2.1	B_0 Shim Setup	72
3.2.2	Flip Angle Calibration	72
3.2.3	T_1 Measurement	73
3.2.4	Triple-quantum Spectroscopy	74
3.2.5	CEST Imaging	80
3.3	Fluorescence Measurements	84

3.4	Quantitative Analysis	85
3.4.1	Quantification of Protein Conformational Changes	85
3.4.2	Quantification of Heat Shock Recovery	85
4	Results	87
4.1	Influence of B_0 Inhomogeneity on TQ Signal	87
4.2	Sodium TQ Signal of Amino Acids	89
4.3	Bovine Serum Albumin	90
4.3.1	Competitive Binding of Sodium Ions with Potassium Ions	90
4.3.2	Variation of the pH Value	91
4.3.3	Urea-induced Unfolding of BSA	92
4.4	Comparison of the Standard and the Fixed TQTPPI Pulse Sequences	95
4.5	Sodium TQ Spectroscopy of the MR-compatible Bioreactor System	98
4.5.1	Contributions to the Sodium TQ Signal	98
4.5.2	Inhibition of the Na/K-ATPase	99
4.6	CEST Spectroscopic Imaging of the MR-compatible Bioreactor System	103
4.6.1	Contributions to the Z-spectrum from the Bioreactor	103
4.6.2	Control Experiments	105
4.6.3	Heat Shock Experiments	108
5	Discussion	110
5.1	Sodium TQ Spectroscopy of Model Solutions	111
5.2	Sodium TQ Spectroscopy of the MR-compatible Bioreactor System	117
5.3	CEST Spectroscopic Imaging of the MR-compatible Bioreactor System	121
6	Conclusion	124
A	Appendix	126
A.1	B_1^+ Maps	126
A.2	Alternative rNOE CEST Evaluation Metrics	128
	Bibliography	129
	List of Figures	150
	List of Tables	152

List of Abbreviations

AREX	apparent exchange-dependent relaxation
BSA	bovine serum albumin
CE	chemical exchange
CEST	chemical exchange saturation transfer
cw	continuous wave
DAM	double flip angle method
DQ	double-quantum
DQC	double-quantum coherence
DS	direct water saturation
EFG	electric field gradient
FID	free induction decay
FoV	field of view
FT	Fourier transform
FWHM	full width at half maximum
LS	large shift limit
MCA	microcavity array
MQ	multi-quantum
MQC	multi-quantum coherence
MR	magnetic resonance
MRI	magnetic resonance imaging
MRS	magnetic resonance spectroscopy
MT	magnetization transfer
MTR	magnetization transfer rate

NMR	nuclear magnetic resonance
NOE	nuclear Overhauser effect
PCC	Pearson correlation coefficient
PTR	proton transfer ratio
RARE	rapid acquisition with relaxation enhancement
RF	radiofrequency
rNOE	exchange-relayed nuclear Overhauser effect
ROI	region of interest
SAR	specific absorption rate
SNR	signal-to-noise ratio
SQ	single-quantum
SQC	single-quantum coherence
ssMT	semi-solid Magnetization Transfer
TPPI	time proportional phase increment
TQ	triple-quantum
TQC	triple-quantum coherence
TQTPPI	triple-quantum time proportional phase increment
ZQ	zero-quantum
ZQC	zero-quantum coherence

1 Introduction

Nuclear magnetic resonance (NMR) is a powerful non-invasive diagnostic tool for the investigation of biological systems without the use of ionizing radiation or radioactive nuclei. The NMR technique enables the detection of nuclei with a non-zero nuclear spin, such as ^{23}Na and ^1H , via radiofrequency (RF) excitation. Sodium nuclei are involved in vital cellular functions, while proton nuclei are found in organic compounds and the abundant water molecules. Magnetic resonance spectroscopy (MRS) exploits the spectroscopic information of nuclei in different molecular environments to study changes in the composition and environment of organic compounds, such as proteins [Wilson et al. (2019), Ladd et al. (2018) and Hu et al. (2020)]. Consequently, the non-invasive capability combined with the possibility to detect physiological changes prior to a manifestation on a macroscopic scale makes NMR one of the most important diagnostic techniques for the assessment of cell viability.

Proteins are responsible for a variety of biological functions and a dysfunction of proteins results in a loss of cell viability. Proteins are the main constituents of cells, as they occupy up to 35% of the cell volume [Brown (1991)]. The biological function of proteins covers a wide range, e.g. transport processes, structural stability and catalysing metabolic reactions [Alberts et al. (2017)]. The integrity of the three-dimensional structure of proteins is crucial for their biological function. Chemical substances and changes in temperature or of the solvents can yield a loss of the biological function of proteins and thus impact the normal cell function. Hence, the non-invasive investigation of proteins is a powerful diagnostic tool for early detection of physiological changes on a cellular level. Therefore, the aim of this thesis was to non-invasively explore protein interactions using the sodium triple-quantum (TQ) and the chemical exchange saturation transfer (CEST) magnetic resonance (MR) signals.

The ATP-driven Na/K-ATPase membrane protein establishes a sodium concentration gradient across the cell membrane, which is crucial for a normal functioning of the cell. The continuous pump activity of the Na/K-ATPase maintains a low intracellular sodium concentration of $c_{\text{Na},\text{in}} = 5\text{--}15\text{ mM}$ in cells against a large extracellular sodium concentration of $c_{\text{Na},\text{ex}} = 135\text{--}145\text{ mM}$. This active transport process consumes up to two-thirds of the available cellular energy [Clausen et al. (2017) and Alberts et al. (2017)]. Coupled transporters transport solutes across the cell membrane by using the stored energy in the electrochemical gradient of sodium ions. The sodium concentration gradient is also crucial for the electrical signaling between neurons and for the excitability of muscle cells [Madelin et al. (2013) and Thulborn (2018)]. Both irreversible damages and a breakdown of the energy supply cause a failure of the Na/K-ATPase, which in turn leads to an influx of

sodium ions into the cell. This is followed by an influx of water into the cell, which results in cell swelling. Hence, the cell viability is closely connected to the sodium concentration gradient and changes thereof indicate the early onset of pathophysiological alterations.

Apart from the biological properties, the physical properties of the sodium nucleus are also attractive for a variety of biomedical MR applications. The sodium nucleus has a physical NMR sensitivity of 9.2% relative to ^1H and possess the second strongest *in vivo* NMR signal. The low natural abundance of sodium ions results in a sodium signal-to-noise ratio (SNR), which is approximately 20 000 times lower relative to the SNR of protons in water molecules [Madelin et al. (2013)]. In the clinical routine, magnetic resonance imaging (MRI) exploits the signal of water protons to obtain very detailed anatomical images. Additionally, these images contain information about pathological changes on a macroscopic scale. In contrast to the water proton signal, the sodium NMR signal provides information about cell viability and physiology. The sodium nucleus has a spin of $\frac{3}{2}$ and therefore allows the excitation of multi-quantum coherences (MQCs), which include the single-quantum coherence (SQC), the double-quantum coherence (DQC) and the triple-quantum coherence (TQC). The sodium single-quantum (SQ) MR signal, that is the transition between two neighboring Zeeman energy levels, represents a weighted average of the intra- and extracellular sodium concentration. This average tissue sodium concentration has been shown to provide valuable information about cell viability in multiple conditions, e.g. stroke [Neumaier-Probst et al. (2015) and Thulborn et al. (2005)], tumor [Jacobs et al. (2011), Schepkin et al. (2005) and Zaric et al. (2016)] and multiple sclerosis [Inglese et al. (2010), Zaaraoui et al. (2012), Petracca et al. (2016a) and Petracca et al. (2016b)]. The cell viability is closely linked to the sodium concentration gradient and consequently a low intracellular sodium content. However, an increase in the average tissue sodium concentration may be caused by an increase in the intracellular sodium concentration, an increase in the extracellular space, or a combination of both. Therefore, the sodium SQ signal cannot distinguish between these causes [Rooney et al. (2015)]. On the other hand, the sodium TQ signal represents an intracellular sensitive parameter and thus may be a valuable biomarker for cell viability. Hence, the sodium TQ signal was of special interest in this thesis. A sodium TQ signal is created when positively charged sodium ions interact with surrounding electrical field gradients created by negatively charged groups of macromolecules, for example proteins. This intrinsic selectivity of the sodium TQ signal results in the intracellular sensitivity. In the extracellular space, there is a high concentration of sodium ions but a low protein content. In contrast, the sodium concentration in the intracellular space is low, while there is a large abundance of proteins. Consequently, the intracellular sodium has a large contribution of 30–70% to the total sodium TQ signal [Dizon et al. (1996), Eykyn et al. (2015), Schepkin et al. (1996) and Schepkin et al. (1998)]. The intrinsic selectivity of the sodium TQ signal comes at a cost of a lower signal of approximately 10% of the sodium SQ signal [Schepkin et al. (2017) and Hancu et al. (1999)]. In summary, the intrinsic selectivity of the sodium TQ signal to sodium interactions with proteins yields an intracellular sensitive parameter, which may be a valuable biomarker for cell viability.

The intrinsic selectivity of the sodium TQ signal resulted in a great effort to investigate a correlation of the sodium TQ signal with the intracellular sodium concentration and the cell viability. In the perfused rat heart system, Schepkin et al. (1998) demonstrated a linear correlation of the sodium TQ signal with the intracellular sodium concentration determined by destructive methods during a variety of Na/K-ATPase inhibitions. In similar experiments using a perfused mouse heart system, Eykyn et al. (2015) also observed a linear correlation of the ratio of the TQ and the double-quantum (DQ) signals to the intracellular sodium concentration determined by chemical shift reagent during a variety of Na/K-ATPase inhibitions. Further experiments with a perfused rat heart system [Dizon et al. (1996), Choy et al. (1997) and Schepkin et al. (1999)], brain ischemia [LaVerde et al. (2007)] and tumors [Babsky et al. (2007) and Winter et al. (2001b)] revealed a correlation of sodium TQ signal increase and the loss of cell viability. For instance, Schepkin et al. (1999) showed that multi-dose cardioplegia better preserved the viability of myocytes, which also conserved the sodium TQ signal and the heart rate pressure product. Recent studies by Neubauer et al. (2017) and Hoesl et al. (2019a) demonstrated a reduction in the sodium TQ signal of living cells during a Na/K-ATPase inhibition with simultaneous stop of perfusion and during ischemia using an MR-compatible bioreactor system, respectively. These results are in contradiction with an influx of sodium ions and a subsequent increase in the sodium TQ signal [Tauskela et al. (1997), Schepkin et al. (1998) and Eykyn et al. (2015)]. Consequently, the first objective of this thesis was to obtain a deeper understanding of the sodium TQ signal on a cellular level and its capability to serve as a potential biomarker for cell viability.

The second MR method utilized in this thesis was used to non-invasively explore the change in the protein folding state. The three-dimensional native conformation of proteins, which is only marginally stable, is closely linked to their biological function. A protein conformational change, for example unfolding or aggregation of proteins, results in the loss of the native protein conformation and can be associated with stress, disease and age. Cells combat the toxic effects of misfolded proteins by transcription of molecular chaperones [Richter et al. (2010)]. Under normal conditions, these proteins assist partly folded proteins to obtain their native structure. Furthermore, during stressful conditions molecular chaperones keep unfolded proteins soluble, actively refold them or dissolve protein aggregate deposits to allow their refolding [Balchin et al. (2016)]. These quality control mechanisms degrade with age, which occasionally permits the formation of misfolded proteins. Initiation of protein aggregation can be triggered by either a broad aggregation of several proteins during stressful conditions in healthy cells or an aggregation of a single protein species in compromised cells [Mogk et al. (2018)]. The most prominent diseases associated with changes in the protein expression are neurodegenerative diseases and cancer. Hence, the non-invasive visualization of the protein folding state would represent a valuable diagnostic tool.

CEST is a powerful MR technique for the study of proteins, as it combines the spectroscopic information of low concentrated organic compounds with a high-resolution imaging comparable to conventional MRI. CEST indirectly detects organic compounds

by utilizing magnetization transfer (MT) processes, such as chemical exchange (CE) and exchange-relayed nuclear Overhauser effect (rNOE), between protons in organic compounds and free water protons [Wolff et al. (1989) and Wolff et al. (1990)]. CE refers to a physical exchange of protons, while rNOE describes the exchange of spin states via through-space dipolar cross-relaxation followed by CE. In CEST, a saturation RF pulse saturates protons in organic compounds and MT processes transfer this saturation to the abundant water protons. This saturation transfer occurs several times during the saturation RF pulse, which results in a substantial reduction of the water signal and hence an amplification of signals from organic compounds. Thus, CEST indirectly detects signals from proteins with an improved SNR using the change in the water signal. Consequently, protein-based CEST signals may be a valuable non-invasive diagnostic tool for the visualization of changes in the protein expression.

Both CE and rNOE signals of proteins have been demonstrated to provide valuable diagnostic information for diseases associated with pathological changes in the protein expression, like cancer and neurodegenerative diseases [Yan et al. (2015), Jones et al. (2013), Zaiss et al. (2015), Paech et al. (2019) and Meissner et al. (2019)]. The rNOE CEST signal, which is mainly associated with mobile proteins and peptides [Y. Zhou et al. (2020)], depends on the protein concentration [Jin et al. (2013) and Goerke et al. (2018)] and the protein conformational state [Zaiss et al. (2017), Goerke et al. (2015) and Goerke et al. (2017)], while it is insensitive to pH [Jin et al. (2013) and Zaiss et al. (2017)]. Selective protein unfolding of *in vitro* model solutions yielded a reduction in the rNOE signal, which was in agreement with the protein folding state [Zaiss et al. (2017) and Goerke et al. (2015)]. Protein aggregation of protein solutions and cell lysates also decreased the rNOE CEST signal [Goerke et al. (2017)]. In an initial investigation of Alzheimer's disease using a mice model, Chen et al. (2019) attributed the decrease in the rNOE signal to aggregated proteins. However, the dependence on the protein folding state has only been demonstrated *in vitro* in proteins in a severely denatured condition. Thus, the second objective of this thesis was the experimental verification of the detectability of denaturation processes on a physiologically relevant scale in living cells.

To investigate the sodium TQ and the rNOE CEST signals on a cellular level, an MR-compatible bioreactor system is necessary to establish a biological active environment, which maintains the cell viability inside an MR scanner. Gottwald et al. (2013) recently proposed an MR-compatible bioreactor system containing a densely packed organotypic 3D cell culture on a microcavity array (MCA) within a finely tunable environment, such as pH and temperature. In this bioreactor system, an external perfusion pump continuously provides the cells with fresh medium, which contains nutrients and oxygen. In addition, the bioreactor design features excellent filling and washout characteristics during the administration of a bolus [Gottwald et al. (2013)]. Thus, the proposed MR-compatible bioreactor system allows the non-invasive monitoring of the cellular response to pharmaceutical treatments by NMR. The MR-compatible bioreactor system from Gottwald et al. (2013) was employed in this thesis to correlate changes in the sodium TQ and rNOE CEST signals to cellular processes caused by a loss of the biological function of proteins.

The two main objectives of this thesis were (i) to obtain a deeper understanding of the sodium TQ signal on a cellular level using model solutions and an MR-compatible bioreactor system, and (ii) to experimentally verify the detectability of denaturation processes in living cells using the rNOE CEST signal. These two objectives were achieved in three steps:

In the first step, the dependence of the sodium TQ signal on pH and the protein folding state was investigated using protein bovine serum albumin (BSA). BSA was selected as a suitable model system due to the strong sodium TQ signal [Torres et al. (2005), Rooney et al. (1991b) and Chung et al. (1990)]. Cancer or stop-flow ischemia can induce a change in pH *in vivo* [White et al. (2017) and Nedergaard et al. (1991)], while cancer or neurodegenerative diseases are associated with changes in the protein folding state. The pH value and the protein folding state can influence the availability of negatively charged groups of proteins and thus affect the sodium TQ signal. Therefore, these experiments aim to determine the influence of the availability of negatively charged groups of proteins on the sodium TQ signal. At low pH values, the availability of negatively charged groups is minimal, while it increases with rising pH. This change in the availability of negatively charged groups affects the affinity of proteins for cations [Carr (1956), Pfister et al. (1964) and Saroff (1957)]. In agreement with these studies, Hutchison et al. (1990) revealed a dependence of the sodium DQ signal on pH. Hence, a dependence of the sodium TQ signal on pH is also expected. To study the dependence of the sodium TQ signal on the protein folding state, BSA unfolding was induced by urea. Protein unfolding disrupts the tertiary and secondary protein structure and causes an exposure of the protein backbone to the aqueous phase [Das et al. (2009) and Matouschek et al. (1989)]. The disruption of ion pairs and the exposure of the hydrophobic protein core to the aqueous phase can increase the availability of negatively charged groups. These investigations were published in Kleimaier et al. (2020c).

In the second step, the feasibility of monitoring intracellular sodium changes by the sodium TQ signal was verified by an inhibition of the Na/K-ATPase of HepG2 cells by either 1 mM ouabain or 0 mM K⁺-free medium for 60 min using the MR-compatible bioreactor system. A previous study by our group [Neubauer et al. (2017)] revealed a reduction of the sodium TQ signal during the Na/K-ATPase inhibition by ouabain with simultaneous stop of perfusion. This result is in contradiction with an influx of sodium ions into the cells during the Na/K-ATPase inhibition and a subsequent increase in the sodium TQ signal [Tauskela et al. (1997), Schepkin et al. (1998) and Eykyn et al. (2015)]. In contrast to the previous study [Neubauer et al. (2017)], no perfusion stop was used, as the decrease in the sodium TQ signal during a perfusion stop observed by Hoesl et al. (2019a) potentially interferes with the increase in the sodium TQ signal during the Na/K-ATPase inhibition. For these experiments, a fixed triple-quantum time proportional phase increment (TQTPPI) pulse sequence, which yielded several times gain in TQ SNR, was developed. To verify the capability of monitoring intracellular sodium changes using the sodium TQ signal, the first step was to determine the origin of the sodium TQ signal from the bioreactor. In a second step, the cellular response to 1 mM ouabain ($n = 3$) or 0 mM K⁺-free medium

($n = 3$) in six independent 3D cell cultures was dynamically monitored using the sodium TQ signal. These experiments were published in Kleimaier et al. (2020f).

In the final step, the detectability of protein denaturation processes by the rNOE CEST signal was verified by application of a mild, non-lethal heat shock of 42°C for 20 min to HepG2 cells using the MR-compatible bioreactor system. The aim was to dynamically monitor the cellular heat shock response using the rNOE CEST signal. The native protein conformation is crucial for the biological function of proteins. However, certain proteins are highly susceptible to aggregation and loss of function. Thus, they denature already at a slightly increased temperature above the optimal growth temperature of cells [Baldwin et al. (2011), Ciryam et al. (2015) and Kundra et al. (2017)]. Cells transiently overexpress molecular chaperones to combat the toxic effects of misfolded proteins caused by a heat shock [Mogk et al. (2018) and Sottile et al. (2018)]. Molecular chaperones prevent protein aggregation during heat shock. In addition, they dissolve and refold misfolded proteins upon return to native temperatures [Mogk et al. (2018) and Sottile et al. (2018)]. Based on the results of protein unfolding and aggregation of *in vitro* model solutions [Zaiss et al. (2017), Goerke et al. (2015) and Goerke et al. (2017)], a mild, non-lethal heat shock followed by chaperone-induced refolding of misfolded proteins should affect the rNOE CEST signal. In a first step, the origin of the CEST signals from the bioreactor was determined, and a reliable and fast high-resolution CEST imaging pulse sequence was implemented. In a second step, the cellular heat shock response of two independent 3D cell cultures was dynamically monitored by the rNOE CEST signal. These results were published in Kleimaier et al. (2020e).

2 Theoretical Background

This chapter covers the basic concepts of NMR, the physics of spin $\frac{3}{2}$ systems, the concepts of MT experiments, and the biological background of cells and proteins. This chapter is intended to provide a brief overview to support the understanding of the subsequent work.

2.1 Nuclear Magnetic Resonance

In 1922, Otto Stern and Walther Gerlach performed the revolutionary Stern-Gerlach experiment by sending silver atoms through a spatially varying magnetic field [Gerlach et al. (1924)]. They observed a quantized deflection of the silver atoms owed to the 5s electron with the intrinsic spin. By extending the Stern-Gerlach experiment, Isidor Isaac Rabi was able to measure the nuclear spin in a molecular beam [Rabi et al. (1938)]. Otto Stern and Isidor Isaac Rabi were awarded the Nobel Prize in Physics in 1943 and 1944, respectively. Nearly at the same time, the groups of Purcell et al. (1946) and Bloch (1946) detected radiofrequency signals from paraffin wax and water. Edward Mills Purcell and Felix Bloch received the Nobel Prize in Physics in 1952 for their nuclear magnetic precision measurements, which resulted in the field of NMR spectroscopy. Further technical advances paved the road for recording the first NMR images [Lauterbur (1973), Mansfield et al. (1973) and Damadian (1971)]. Paul Christian Lauterbur and Peter Mansfield received the Nobel Prize in Physiology or Medicine in 2003. In NMR imaging, linear magnetic field gradients result in a specific Larmor frequency for each voxel, which allows the non-invasive image acquisition of living subjects.

This section provides a brief description of the fundamental NMR concepts, e.g. the Nuclear Zeeman splitting, macroscopic magnetization and relaxation effects. These concepts are based on the books by Graaf (2019), Levitt (2008) and Haacke et al. (1999).

2.1.1 Nuclear Spin and Nuclear Zeeman Effect

Atomic nuclei consist of nucleons, i.e. protons and neutrons, which are fermions with a spin quantum number $s = \frac{1}{2}$. Nucleons also possess an orbital angular momentum l , which means that the total angular momentum of a nucleon is $j = |l \pm \frac{1}{2}|$. In some cases, the total angular momentum of a nucleus, the so-called nuclear spin \hat{I} , can be calculated by the nuclear shell model. A general rule is that all nuclei with an odd number of protons and/or neutrons possess a nuclear spin. The commutator identities of the angular momentum operator \hat{I} are

$$[\hat{I}_i, \hat{I}_j] = i\hbar\epsilon_{ijk}\hat{I}_k \quad \text{and} \quad [\hat{I}_i, \hat{I}^2] = 0. \quad (2.1)$$

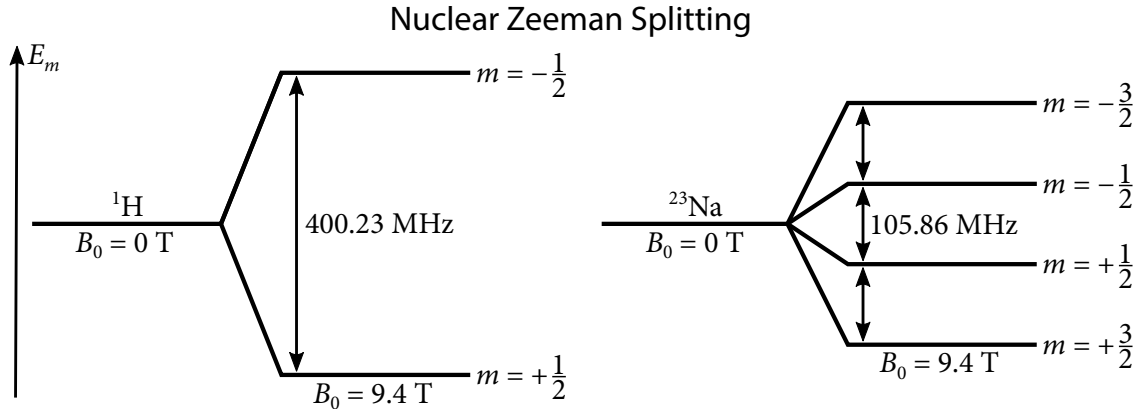


Figure 2.1: The nuclear Zeeman splitting at $B_0 = 9.4$ T depicted for the nuclei ^1H and ^{23}Na . The energy difference between neighboring levels is identical.

\hat{I}_i is one component of the angular momentum operator and the reduced Planck constant is defined as $\hbar = \frac{h}{2\pi} = 1.0545 \cdot 10^{-34}$ Js. If the quantization axis is chosen to be the z-axis, then the eigenvalue equations of the magnitude and the z-component are

$$\hat{I}^2 |I, m\rangle = \hbar^2 I(I+1) |I, m\rangle \quad \text{and} \quad \hat{I}_z |I, m\rangle = \hbar m |I, m\rangle. \quad (2.2)$$

I and $m = -I, -I+1, \dots, I-1, I$ are the nuclear spin quantum number and the magnetic quantum number, respectively. Without an external magnetic field, the energy level is independent of m and therefore $(2I+1)$ -fold degenerated. Alongside a nuclear spin $I > 0$, nuclei are associated with a magnetic moment $\hat{\mu}_I$

$$\hat{\mu}_I = \frac{g\mu_N}{\hbar} \hat{I} = \gamma \hat{I} \quad (2.3)$$

with the nucleus-specific Landé g-factor, the nuclear magneton $\mu_N = 5.05 \cdot 10^{-27} \frac{\text{J}}{\text{T}}$ and the nucleus-specific gyromagnetic ratio γ . The nuclear magnetic moment $\hat{\mu}_I$ interacts with surrounding magnetic fields from the sample or from external sources. In the presence of an external magnetic field, the $(2I+1)$ -fold degeneracy of the energy levels is lifted, which is described by the so-called Zeeman effect (Figure 2.1). In NMR, it is common to refer to the magnetic flux density \vec{B} as the magnetic field. If a static magnetic field \vec{B}_0 is applied along the z-axis, the Hamiltonian $\hat{\mathcal{H}}$ of the nuclear Zeeman interaction is

$$\hat{\mathcal{H}} = -\hat{\mu} \vec{B}_0 = -\gamma B_0 \hat{I}_z. \quad (2.4)$$

According to this equation, the energy is minimal when the magnetic moment is parallel to the applied magnetic field. The nuclear Zeeman Hamiltonian is time-independent and therefore solving the stationary Schrödinger equation

$$\hat{\mathcal{H}} |I, m\rangle = E_m |I, m\rangle \quad (2.5)$$

yields the following energy eigenvalues E_m

$$E_m = -\hbar m \gamma B_0. \quad (2.6)$$

The Zeeman interaction results in an equidistant energy splitting with an energy difference between two neighboring energy levels of

$$\Delta E = \hbar\gamma B_0 = \hbar\omega_0. \quad (2.7)$$

The nucleus-specific Larmor frequency is

$$\omega_0 = \gamma B_0. \quad (2.8)$$

A photon with the Larmor frequency ω_0 can induce transitions between two states either by absorption or emission. In NMR, the application of a second, time-dependent magnetic field $\vec{B}_1(t)$ with the Larmor frequency ω_0 perpendicular to \vec{B}_0 induces transitions between the energy levels. Consequently, such a $\vec{B}_1(t)$ field can create observable transverse magnetization.

2.1.2 Macroscopic Magnetization

Without an external magnetic field, thermal motions lead to a random distribution of the magnetic moments of all nuclei. Therefore, all magnetic moments cancel each other out resulting in no net macroscopic magnetization. When an external magnetic field is switched on, a single magnetic moment with a transverse component, i.e. x-y-plane, starts to precess on a cone around the magnetic field direction. In classical physics, the torque on a magnetic moment $\vec{\mu}$ in an external magnetic field \vec{B}_0 is described by

$$\frac{d\vec{\mu}}{dt} = \vec{\mu} \times \gamma\vec{B}_0. \quad (2.9)$$

The precession frequency around the main magnetic field axis equals the Larmor frequency ω_0 . After the spin ensemble has reached thermal equilibrium, there is only a slight tendency of the spins to point along the main magnetic field direction, as the thermal energy is larger than the energy of the spin states $E_m \ll k_B T$. Nevertheless, this slight tendency is already sufficient to create a net macroscopic magnetization.

NMR utilizes the manipulation of the net effect of all nuclei. Consider an imaging volume of 1 mm^3 , the number of protons is approximately $6.68 \cdot 10^{19}$. This calculation considers a water hydrogen molarity of 111 M with the Avogadro constant $N_A = 6.02 \cdot 10^{23} \text{ mol}^{-1}$. The huge number of protons in a volume of 1 mm^3 justifies the consideration of the net effect of all nuclei. The macroscopic magnetization is the sum of all expectation values of the individual magnetic moments from N spins within a unit volume V

$$\vec{M}_0 = \sum_{i=1}^N \frac{\langle \hat{\mu}_{iI} \rangle}{V}. \quad (2.10)$$

At thermal equilibrium with temperature T , the normalized Boltzmann distribution describes the occupation probability p_m of a Zeeman energy level with spin quantum number m

$$p_m = \frac{1}{Z} e^{-\frac{E_m}{k_b T}}. \quad (2.11)$$

$k_B = 1.38 \cdot 10^{-23} \frac{\text{J}}{\text{K}}$ is the Boltzmann constant. The occupation probability is normalized to the partition function Z

$$Z = \sum_{m=-I}^I e^{-\frac{E_m}{k_B T}}. \quad (2.12)$$

The use of the occupation probabilities and a magnetic field along z-direction allows to simplify Equation 2.10 to

$$\vec{M}_0 = \frac{N}{V} \gamma \hbar \sum_{m=-I}^I p_m m \hat{z}. \quad (2.13)$$

In the case of protons, the population ratio between the population distribution of the two possible spin states $m = \pm \frac{1}{2}$ is given by:

$$\left(\frac{N_{m=+\frac{1}{2}}}{N_{m=-\frac{1}{2}}} \right) = e^{\frac{\Delta E}{k_B T}} = e^{\frac{\hbar \gamma B_0}{k_B T}} \approx 1 + \frac{\hbar \gamma B_0}{k_B T}, \quad (2.14)$$

where $N_{m=\pm \frac{1}{2}}$ is the number of spins in the $m = \pm \frac{1}{2}$ state. In the last step of Equation 2.14, the high temperature approximation $E_m \ll k_B T$ is used to truncate the Taylor series. At a main magnetic field strength of $B_0 = 9.4 \text{ T}$ and a temperature of $T = 310 \text{ K}$, approximately 31 protons per million will contribute to the macroscopic magnetization M_0 . Therefore, NMR is a rather insensitive technique. The huge number of protons per 1 mm^3 only partially compensates this small contribution. The use of the high temperature approximation further simplifies Equation 2.13 for the macroscopic magnetization

$$\vec{M}_0 \approx \frac{N}{V} \frac{\gamma^2 \hbar^2 I(I+1)}{3k_B T} B_0 \hat{z}. \quad (2.15)$$

This implies that nuclei with a high spin density $\frac{N}{V}$ and a high gyromagnetic ratio result in a strong NMR signal. Both parameters are among the many obstacles for X-nuclei, which will be further discussed in Subsection 2.1.4.

2.1.3 Bloch Equations and Relaxation

According to Equation 2.9, a single magnetic moment $\vec{\mu}$ will precess around the static magnetic field direction, i.e. z-axis, when $\vec{\mu}$ has a transverse component, i.e. x-y-plane. Thus, the net magnetization \vec{M} will also precess around the static magnetic field direction, as it is the sum over all magnetic moments (Equation 2.10). At thermal equilibrium, there is only a slight tendency of the magnetic moments to point along \vec{B}_0 creating a static macroscopic magnetization M_z . In the x-y-plane, the magnetic moments are randomly distributed and therefore the transverse magnetization equals $M_x = M_y = 0$. To measure the magnetization M_z via Faraday induction, a second, time-dependent magnetic field $\vec{B}_1(t)$ in the x-y-plane is necessary to rotate the magnetization M_z into the x-y-plane.

This second, time-dependent magnetic field is commonly referred to as the RF field. An efficient RF field is e.g. a left-circularly polarized RF field defined as

$$\vec{B}_1 = B_1 \begin{pmatrix} \cos(\omega t) \\ -\sin(\omega t) \\ 0 \end{pmatrix}, \quad (2.16)$$

whereby ω is the frequency of the RF field. This RF field causes a precession of the magnetization around the effective magnetic field $\vec{B}_{eff} = \vec{B}_0 + \vec{B}_1$. To simplify the motion of the magnetization, a transformation to a rotating frame with frequency $\vec{\Omega}$ can be performed according to

$$\frac{d\vec{F}}{dt} = \left(\frac{d\vec{F}}{dt} \right)' + \vec{\Omega} \times \vec{F}. \quad (2.17)$$

The prime indicates the rotating frame and \vec{F} is a general vector function. Thus, a transformation to a rotating frame with frequency $\vec{\Omega} = -\vec{\omega}_0$ removes the precession around the static magnetic field direction. To obtain the Bloch equations, Equation 2.9 is transformed to a rotating frame with frequency $\vec{\Omega} = -\omega\hat{z}$ and $\vec{\mu}$ is replaced by \vec{M} . By considering also the application of a left-circular polarized RF pulse, Equation 2.9 then reads

$$\frac{d\vec{M}}{dt} = \vec{M} \times \gamma \left(\left(B_0 - \frac{\omega}{\gamma} \right) \hat{z}' + B_1 \hat{x}' \right). \quad (2.18)$$

When the RF pulse is applied on-resonance $\omega = \omega_0$, the precession around the static magnetic field vanishes and the magnetization rotates around \hat{x}' . The rotation angle α of the magnetization around \hat{x}' depends on the duration τ and the amplitude B_1 of the RF pulse:

$$\alpha = \int_0^\tau \gamma B_1(t') dt' = \gamma B_1 \tau. \quad (2.19)$$

The last step of Equation 2.19 is only valid for a rectangular RF pulse of length τ .

After application of an RF pulse, the transverse magnetization component decays with the relaxation rate $\frac{1}{T_2}$, while the longitudinal magnetization component recovers with the relaxation rate $\frac{1}{T_1}$. Several relaxation mechanism contribute to the relaxation process. The dominant relaxation mechanism depends on the nucleus and its environment (Subsection 2.2.6 and Subsection 2.3.1). The Bloch equations combine the relaxation process with Equation 2.18.

T_1 Relaxation

The application of an RF pulse, which can rotate the magnetization into the x-y-plane, transfers energy into the spin ensemble. Emission of this transferred energy to the surrounding environment reestablishes the equilibrium magnetization M_0 along the z-axis.

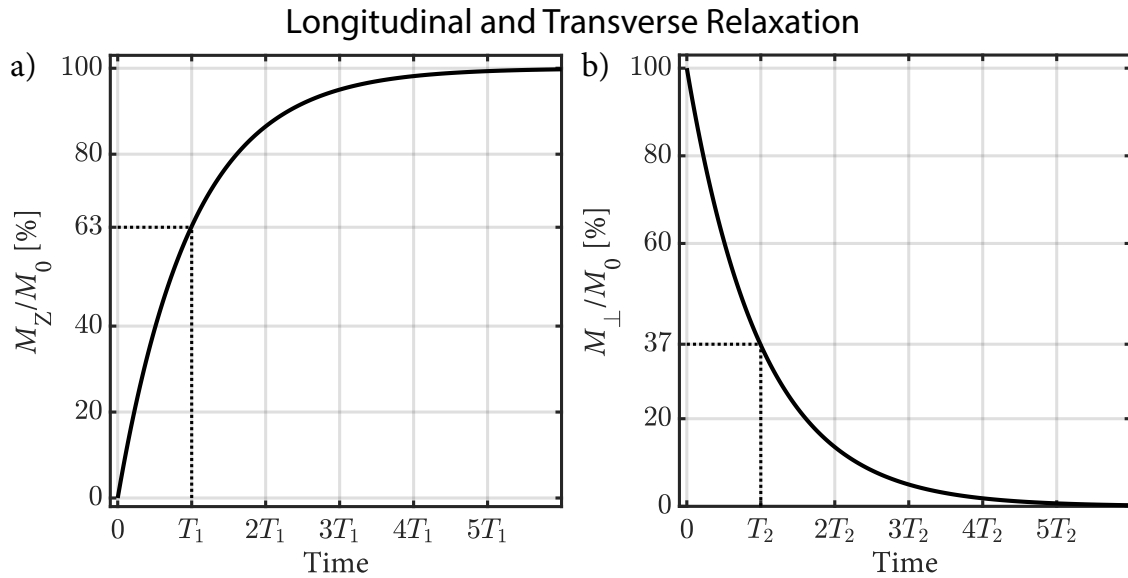


Figure 2.2: a) Exponential regrowth of the longitudinal magnetization M_z after a 90° RF pulse. After the time $5T_1$, the longitudinal magnetization approximately reaches thermal equilibrium. b) Exponential decay of the transverse magnetization M_{\perp} after a 90° RF pulse. After the time T_2 , only 37% of the transverse magnetization is left.

In NMR, this process of energy emission is achieved by stimulated emission and not by spontaneous emission. The latter process depends on ω^3 and thus is not efficient in the RF range. Regrowth of the longitudinal magnetization is given by

$$\frac{dM_z}{dt} = \frac{M_0 - M_z}{T_1}. \quad (2.20)$$

The solution of this differential equation is

$$M_z(t) = M_0 - (M_0 - M_z(0))e^{-\frac{t}{T_1}}. \quad (2.21)$$

Hence, the longitudinal magnetization recovers exponentially back to the equilibrium magnetization M_0 (Figure 2.2a). After an initial 90° RF pulse, the longitudinal magnetization approximately reaches thermal equilibrium after the time $5T_1$. The energy transport to the surrounding environment is most effective if the fluctuating fields fluctuate close to the Larmor frequency ω_0 . Consequently, the longitudinal relaxation time depends on the magnetic field strength.

T_2 Relaxation

The magnetization $\vec{M}_{\perp} = \vec{M}_x\hat{x} + \vec{M}_y\hat{y}$, which the RF pulse rotated to the transverse plane, decays exponentially with relaxation time T_2 . This coherence loss is also called dephasing, which increases the entropy of the system opposed to the energy transfer for T_1 relaxation.

Surrounding atoms and molecules produce small local magnetic fields $B_{loc}(t)$, which lead to small changes in the Larmor frequency $\omega(t) = \gamma(B_0 + B_{loc}(t))$. Brownian motion causes fluctuations in these local magnetic fields, which results in an accumulation of phase differences between different spins and subsequently the loss of coherence. This coherence loss is an irreversible process. The differential equation in the rotating frame is

$$\frac{d\vec{M}'_{\perp}}{dt} = -\frac{1}{T_2}\vec{M}'_{\perp}. \quad (2.22)$$

The solution of this equation is given by

$$\vec{M}'_{\perp}(t) = \vec{M}'_{\perp}(0)e^{-\frac{t}{T_2}}. \quad (2.23)$$

Figure 2.2b shows an exemplary transverse magnetization decay. In contrast to the effectiveness of high frequency components of the fluctuating fields for T_1 relaxation, quasi-static frequency components are most efficient for T_2 relaxation. The former components are averaged over time to zero. Both relaxation processes are independent of each other, as they originate from different physical processes. However, T_1 relaxation also contributes to the dephasing of the transverse magnetization and therefore T_1 sets an upper limit for T_2 :

$$T_2 \leq T_1. \quad (2.24)$$

T_2^* Relaxation

The observed decay of the transverse magnetization after a 90° RF pulse is in general faster than the T_2 relaxation time. This results from the fact that also the external magnetic field inhomogeneity contributes to the dephasing of \vec{M}_{\perp} . The relaxation time T_2' describes the inhomogeneity of the static magnetic field as well as object-specific, susceptibility-induced field distortions. Therefore, the decay of the transverse magnetization is described by

$$\frac{1}{T_2^*} = \frac{1}{T_2} + \frac{1}{T_2'}. \quad (2.25)$$

The dephasing of the magnetization caused by an external magnetic field inhomogeneity and object-specific field distortions can be refocused by application of a 180° RF pulse.

2.1.4 Sensitivity

Suppose an 90° RF pulse rotates the magnetization to the x-y-plane. The precession around the z-direction creates a rotating magnetic flux Φ , which induces a voltage U_{ind} in the RF coil. This phenomena is Faraday's law of induction

$$U_{ind}(t) = -\frac{d\Phi(t)}{dt} = -\frac{d}{dt} \int_V d^3r \vec{M}_{\perp}(\vec{r}, t) \vec{B}_1^-(\vec{r}). \quad (2.26)$$

Table 2.1: Properties of some commonly used NMR nuclei.

Isotope	Spin I	$\frac{\gamma}{2\pi} \left[\frac{\text{MHz}}{\text{T}} \right]$	c [%]	Relative sensitivity
^1H	$\frac{1}{2}$	42.58	99.99	1.0
^{19}F	$\frac{1}{2}$	40.08	100	$8.3 \cdot 10^{-1}$
^{23}Na	$\frac{3}{2}$	11.27	100	$9.3 \cdot 10^{-2}$
^{31}P	$\frac{1}{2}$	17.25	100	$6.7 \cdot 10^{-2}$
^{39}K	$\frac{3}{2}$	1.99	93.26	$4.8 \cdot 10^{-4}$

The relative sensitivity is relative to ^1H and does not take into account the biological abundance (Equation 2.27). The values are from Harris et al. (2002).

\vec{B}_1^- is the receive field of the RF coil. In the case of a perfectly homogeneous static magnetic field, an uniform 90° rotation of the equilibrium magnetization to the x-y-plane, neglect of relaxation effects, and receiver amplification factors, Equation 2.26 can be simplified to

$$U_{\text{ind}} \propto \gamma^3 I(I+1) c c_{\text{bio}}. \quad (2.27)$$

c and c_{bio} are the isotope and the biological abundance, respectively. Table 2.1 lists the properties of some commonly used nuclei. From this table and Equation 2.27 it is obvious why ^1H is the only investigated nucleus in clinical NMR. The high gyromagnetic ratio, isotope and biological abundance result in a strong NMR signal even at low magnetic field. The ^{23}Na nucleus has the second strongest biological NMR signal. However, the SNR is already approximately 20 000 times lower compared to ^1H , due to the low gyromagnetic ratio and biological abundance [Madelin et al. (2014)].

2.1.5 Nuclear Magnetic Resonance Spectrum

Detection of a global signal from a sample is the simplest NMR experiment. Consider the application of an uniform 90° RF pulse, Equation 2.23 describes the transverse magnetization with $\vec{M}_\perp(0) = \vec{M}_0$. As discussed in Subsection 2.1.3, in a real NMR experiment the transverse magnetization decays with the relaxation time T_2^* . In the laboratory frame, the received signal $S(t)$ in the RF coil, which is proportional to the induced voltage U_{ind} , is

$$S(t) \propto \omega_0 e^{-\frac{t}{T_2^*}} e^{-i\omega_0 t} \int_V d^3r \vec{B}_1^-(\vec{r}) \vec{M}_0(\vec{r}, 0). \quad (2.28)$$

Transformation of Equation 2.23 to the laboratory frame and inserting into Equation 2.26 yields Equation 2.28. This received signal is also referred to as the free induction decay (FID), shown in Figure 2.3. A Fourier transform (FT) of the time-domain signal $S(t)$ results in the NMR spectrum (Figure 2.3), which in case of a mono-exponential decay is a

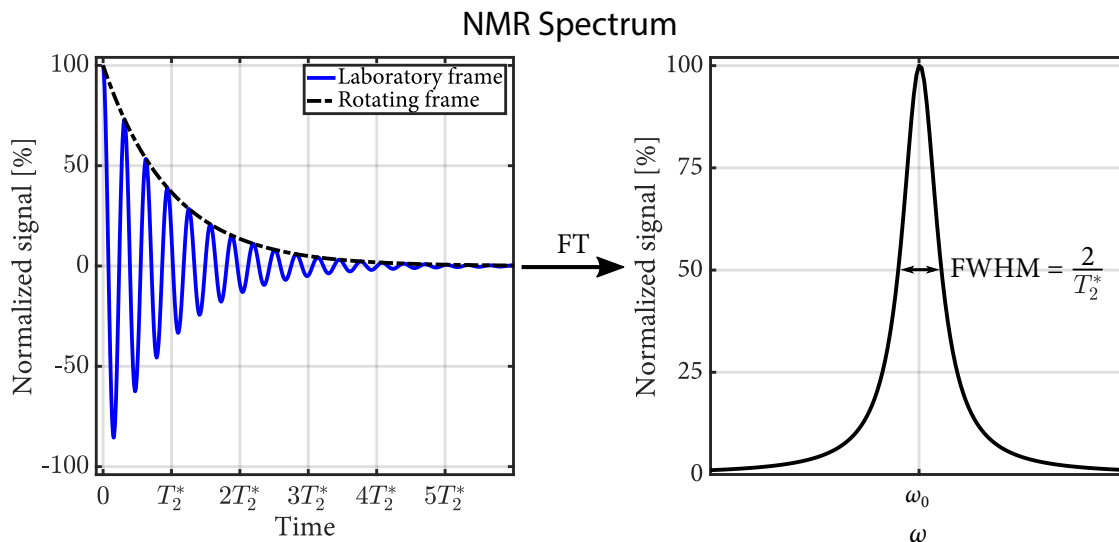


Figure 2.3: The left and right side show the FID and the corresponding spectrum, respectively. A FT of the FID yields the NMR spectrum.

single Lorentzian that is centered at frequency ω_0 and has a full width at half maximum (FWHM) of $\frac{2}{T_2^*}$. In Equation 2.28, all nuclei from the same isotope resonate at the same frequency. This is not necessarily the case, as the electron cloud surrounding a nucleus shields it from the main magnetic field. This electron shielding effect leads to a slightly different local field $B_{loc} = B_0 + \delta B$ at the location of the nucleus. ^1H nuclei in different molecular environments experience different degrees of electron shielding and thus have slightly different local fields. An alteration of the local field results in a change of the Larmor frequency by $\delta\omega = \gamma\delta B$, which is also referred to as chemical shift. In this case, the NMR spectrum consists of several spectral peaks at different resonance frequencies originating from different chemical groups. The chemical shift can be expressed independent of the main magnetic field with

$$\delta[\text{ppm}] = \frac{\omega - \omega_{\text{ref}}}{\omega_{\text{ref}}} \cdot 10^6 \quad (2.29)$$

by referencing to a reference frequency ω_{ref} , e.g. tetramethylsilane for ^1H NMR spectroscopy. The representation of the chemical shift frequency axis is from higher frequency to lower frequency. In CEST experiments, a saturation RF pulse saturates protons in organic compounds and magnetization transfer processes transfer this saturation to protons in water molecules. As the signal of protons in organic compounds is detected by the reduction in the water signal, the water proton resonance frequency is set as the reference frequency in CEST experiments, see Section 2.3.

2.2 Quadrupole Nuclei

Up to this point, only magnetic interactions of the nucleus with its environment were considered. However, for quadrupole nuclei, which are nuclei with a spin $I > \frac{1}{2}$, the nuclear electric charge distribution interacts with electric field gradients, affecting the energy required to reorient the nucleus. This results from an asymmetric charge distribution for quadrupole nuclei (Figure 2.4). In the case of $I = \frac{1}{2}$, the charge distribution is spherical and a rotation of the nucleus does not alter the electrostatic energy. But for an asymmetric charge distribution the electric energy changes as the nucleus rotates, for example the charge distribution in Figure 2.4c corresponds to a lower energy configuration compared to Figure 2.4b. Quadrupole nuclei possess an electric-quadrupole moment which interacts with electrical field gradients from the surrounding, e.g. negatively charged groups of proteins. This interaction is the dominant relaxation mechanism for quadrupole nuclei and is much stronger than the magnetic dipole-dipole interaction [Hubbard (1970) and Berendsen et al. (1973)].

This section introduces the basic concept of the electric-quadrupole interaction and the respective influence on the NMR spectrum and the relaxation times. At first, the density operator and the irreducible tensor formalism are discussed to describe the electric-quadrupole Hamiltonian and the coherence evolution during multi-quantum (MQ) pulse sequences. The following subsections illustrate the influence of the electric-quadrupole interaction on the NMR spectrum and the relaxation times. The final subsection describes the general concept of a MQ pulse sequence. This section is based on the work by Levitt (2008), Slichter (1990), Maarel (2003a), Maarel (2003b) and Jaccard et al. (1986).

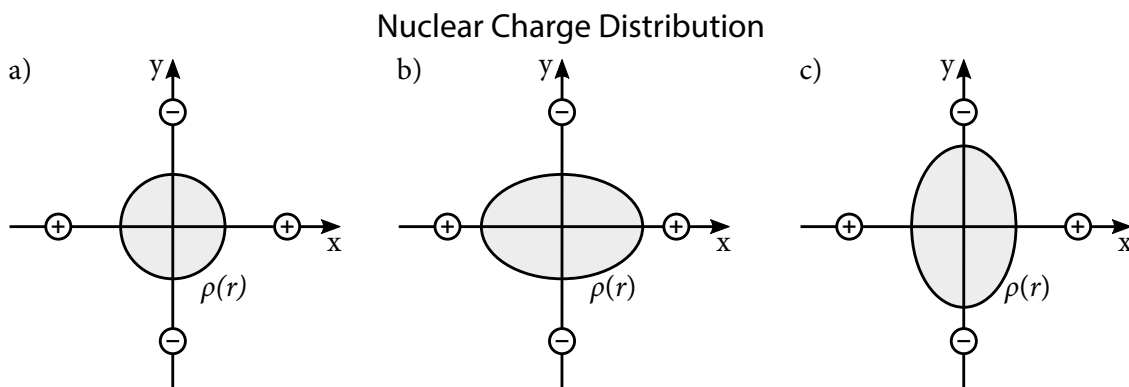


Figure 2.4: a) Spherical electrical charge distribution $\rho(r)$ of a nucleus in the field of two positive charges on the x-axis and two negative charges on the y-axis. Nuclei with a spin of $I = \frac{1}{2}$ have a spherical charge distribution. b) and c) show an asymmetric nuclear electrical charge distribution $\rho(r)$ in the field of two positive and two negative charges on the x-axis and y-axis, respectively. Configuration c) is energetically more favorable, as it minimizes the distance between the positively charged nucleus and the negative charges on the y-axis.

2.2.1 Density Operator

The wave function of a single spin $\frac{3}{2}$ nucleus i in the angular momentum basis $|n\rangle$ is

$$|\psi_i\rangle = \sum_n c_n^i |n\rangle = c_{\frac{3}{2}}^i |\frac{3}{2}\rangle + c_{\frac{1}{2}}^i |\frac{1}{2}\rangle + c_{-\frac{1}{2}}^i |-\frac{1}{2}\rangle + c_{-\frac{3}{2}}^i |-\frac{3}{2}\rangle. \quad (2.30)$$

The coefficients c_n^i are complex time-dependent amplitudes of the state $|n\rangle$. This notation abbreviates the eigenstates $|I, m\rangle$ by $|m\rangle$ and neglects any additional quantum numbers, which describe the system. In NMR, an ensemble of nuclei yields the macroscopic magnetization, which consists of independent and identical systems. The wave function of this spin ensemble can be in a pure or mixed state. In a pure state, the wave function of a single nucleus is the same for all nuclei in the ensemble, while in the mixed state the c_n^i differ for some or all nuclei of the ensemble. The mixed state reflects on the situation encountered in NMR, which is best described by the density operator $\hat{\sigma}$:

$$\hat{\sigma} = \sum_i p_i |\psi_i\rangle \langle \psi_i|. \quad (2.31)$$

$p_i = \frac{N_i}{N}$ is the probability to find an individual system of N_i spins of the ensemble with N spins in the pure state $|\psi_i\rangle$. The spin density operator $\hat{\sigma}$ represents the quantum state of the entire ensemble and the macroscopic observable of the operator \hat{Q} can then be calculated in an elegant way by

$$\langle \hat{Q} \rangle = \text{Tr}\{\hat{\sigma} \hat{Q}\}. \quad (2.32)$$

Consequently, it is important to have a closer look at the density matrix, especially at its matrix elements. A single element of the density matrix is the average of the eigenstate coefficients

$$\sigma_{\alpha\beta} = \langle \alpha | \hat{\sigma} | \beta \rangle = \sum_i p_i \langle \alpha | \psi_i \rangle \langle \psi_i | \beta \rangle = \overline{c_\alpha c_\beta^*}. \quad (2.33)$$

Considering that the respective eigenstate coefficients are normalized, the trace of the density operator equals 1. The real diagonal elements $\sigma_{\alpha\alpha} \geq 0$ represent the occupation probability of the angular momentum basis states, which are also referred to as populations. The complex off-diagonal elements describe the coherences between two states. The coherence order $m = \alpha - \beta$ is the difference of the magnetic quantum numbers of the two states $|\alpha\rangle$ and $|\beta\rangle$. Hence, the populations are zero-quantum coherences (ZQCs). In thermal equilibrium, the Boltzmann distribution yields the occupation probability of each state and the off-diagonal elements vanish. The density matrix for an ensemble of spin $I = \frac{3}{2}$ nuclei consists of 16 elements (Figure 2.5). The complex off-diagonal elements represent the three different coherences, i.e. SQCs, DQCs, and TQCs. This spin system allows the creation of intra-atomic MQCs. This is in contrast to a spin $I = \frac{1}{2}$ system, where only inter-atomic MQCs are possible (Subsection 2.3.1). Of particular interest in this work is the TQC, which is the superposition of the quantum states $|\pm\frac{3}{2}\rangle$ $\langle \mp\frac{3}{2}|$. For the excitation of the TQC, which has the threefold resonance frequency of the SQC, a multi-pulse sequence is necessary (Subsection 2.2.7).

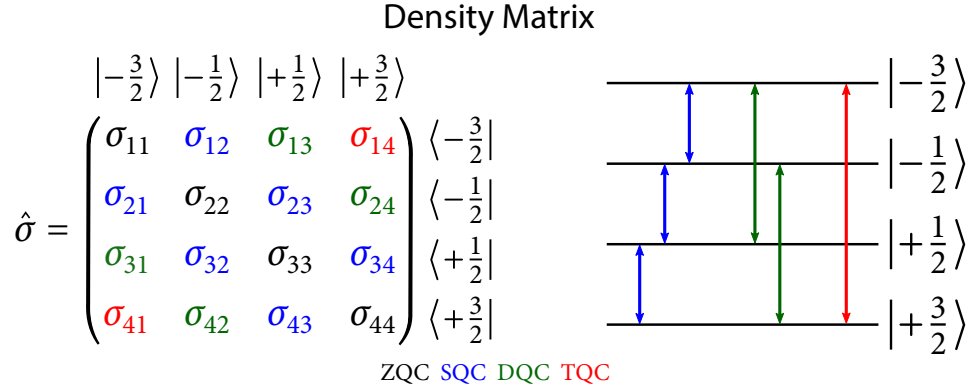


Figure 2.5: The left side shows the density operator in matrix representation for an ensemble of spin $I = \frac{3}{2}$ nuclei. On the right side are the corresponding Zeeman energy levels with the different coherences indicated by arrows.

2.2.2 Irreducible Tensor Formalism

For spin $I = \frac{3}{2}$ systems, the density operator is regularly expressed in terms of irreducible spherical tensor operators \hat{T}_{lm} according to

$$\hat{\sigma} = \sum_{l,m} c_{lm} \hat{T}_{lm}, \quad (2.34)$$

where c_{lm} are complex coefficients. For this spin system, the irreducible spherical tensor operators \hat{T}_{lm} are a set of 16 operators with rank $l = 0, 1, 2, 3$ and coherence order $m = -l, -l + 1, \dots, l - 1, l$. The cap hat indicates that the tensor operator is normalized. A detailed explanation of the irreducible spherical tensor operators can be found in Rose (1957), Bowden et al. (1986a) and Bowden et al. (1986b). In contrast to the irreducible spherical tensor operators, Cartesian tensor operators, commonly used for spin $I = \frac{1}{2}$ systems, are reducible, i.e. they can be expanded into a set of Cartesian tensors which transform differently under rotation. Thus, the use of the irreducible spherical tensor operators allows the utilization of their rotational properties under the influence of RF pulses and relaxation. To define the irreducible spherical tensor operators, the raising and lowering operators $\hat{I}_{\pm} = \hat{I}_x \pm i\hat{I}_y$ are needed. The 16 tensor operators are listed in Table 2.2. In the following, these operators are used to express the Hamiltonian and to describe the coherence evolution during MQ pulse sequences. To reflect the Hermitian nature of the density operator, symmetric and antisymmetric tensor combinations can be defined

$$\hat{T}_{lm}(s) = \frac{1}{\sqrt{2}} (\hat{T}_{l-m} + \hat{T}_{lm}), \quad (2.35)$$

$$\hat{T}_{lm}(a) = \frac{1}{\sqrt{2}} (\hat{T}_{l-m} - \hat{T}_{lm}). \quad (2.36)$$

RF pulses and relaxation effects transform the rank and coherence order of the tensor operators according to:

- Hard RF pulses change only the coherence order m (Subsection 2.2.5). Hard RF pulses are short, nonselective RF pulses, where relaxation effects can be neglected.
- Relaxation effects alter the rank l (Subsection 2.2.6).

 Table 2.2: Irreducible spherical tensor operators for spin $I = \frac{3}{2}$.

T_{lm}	Cartesian decomposition	Definition
T_{00}	$\mathbf{1}$	Identity
T_{10}	\hat{I}_z	Longitudinal magnetization
$T_{1\pm 1}$	$\mp \frac{1}{\sqrt{2}} \hat{I}_{\pm}$	Rank one SQC
T_{20}	$\frac{1}{\sqrt{6}} (3\hat{I}_z^2 - I(I+1))$	Quadrupole magnetization
$T_{2\pm 1}$	$\mp \frac{1}{2} [\hat{I}_z, \hat{I}_{\pm}]_+$	Rank two SQC
$T_{2\pm 2}$	$\frac{1}{2} \hat{I}_{\pm}^2$	Rank two DQC
T_{30}	$\frac{1}{\sqrt{10}} (5\hat{I}_z^3 - (3I(I+1) - 1)\hat{I}_z)$	Octupole magnetization
$T_{3\pm 1}$	$\mp \frac{1}{4} \sqrt{\frac{3}{10}} [5\hat{I}_z^3 - I(I+1) - \frac{1}{2}, \hat{I}_{\pm}]_+$	Rank three SQC
$T_{3\pm 2}$	$\frac{1}{2} \sqrt{\frac{3}{4}} [\hat{I}_z, \hat{I}_{\pm}^2]$	Rank three DQC
$T_{3\pm 3}$	$\mp \frac{1}{2\sqrt{2}} \hat{I}_{\pm}^3$	Rank three TQC

$[\hat{A}, \hat{B}]_+ = \hat{A}\hat{B} + \hat{B}\hat{A}$ defines the anticommutator for arbitrary operators \hat{A} and \hat{B} . The unit tensors can be calculated according to $\hat{T}_{00} = \frac{1}{2}T_{00}$, $\hat{T}_{1m} = \frac{1}{\sqrt{5}}T_{1m}$, $\hat{T}_{2m} = \frac{1}{\sqrt{6}}T_{2m}$ and $\hat{T}_{3m} = \frac{1}{3\sqrt{2}}T_{3m}$. The tensor definitions are from Bowden et al. (1986a) and Bowden et al. (1986b).

2.2.3 Nuclear Spin Hamiltonian

The full wave function $|\psi_{full}(t)\rangle$ and Hamiltonian $\hat{\mathcal{H}}_{full}$, which contain the information and interaction of all electrons and nuclei within the sample, describe the dynamics of nuclear spins by solving the time-dependent Schrödinger equation

$$\frac{d}{dt} |\psi_{full}(t)\rangle = -i\hat{\mathcal{H}}_{full} |\psi_{full}(t)\rangle. \quad (2.37)$$

The spin Hamiltonian hypothesis assumes that the nuclear and electronic motions are on a different timescale, such that the nuclear spins sense only a time average of the magnetic and electrical influences of the electrons. In addition, the small nuclear spin energies do not affect the motion of electrons and molecules. This simplification is not completely valid. Longitudinal relaxation results in a nuclear spin ensemble with an asymmetric equilibrium state. Thus, the nuclear spin states slightly alter the motion of molecules. Still this

hypothesis is a valid concept for most systems and it reduces Equation 2.37 to

$$\frac{d}{dt} |\psi_{spin}(t)\rangle \cong -i\hat{\mathcal{H}}_{spin} |\psi_{spin}(t)\rangle. \quad (2.38)$$

The spin Hamiltonian is further characterized by interactions of (i) the nuclear electric charges with electrical fields $\hat{\mathcal{H}}_{spin}^{elec}$ and (ii) the nuclear magnetic moment with magnetic fields $\hat{\mathcal{H}}_{spin}^{mag}$. In NMR, the rotational motion of the nucleus alters the energy of the nucleus, as it affects the orientation of the electric charges and magnetic moment with respect to the surrounding fields.

Magnetic Spin Hamiltonian

In general, the magnetic interactions originate from internal or external spin interactions, while electric interactions are purely internal spin interactions. Internal interactions are between the nucleus and the electric and magnetic fields created by atoms and molecules within the sample. Internal magnetic interactions include chemical shift and dipole-dipole coupling. External interactions are between the nucleus and an external apparatus, which manipulates the nuclear spins. There are three kinds of externally applied magnetic fields: (i) The static magnetic field (Subsection 2.1.1); (ii) the RF pulse (Subsection 2.1.3) and (iii) the gradient fields.

The Zeeman Hamiltonian rewritten in terms of the tensor operators is

$$\hat{\mathcal{H}}_Z = \omega_0 \sqrt{5} \hat{T}_{10}. \quad (2.39)$$

This Hamiltonian vanishes under the transformation into the Larmor frequency rotating frame. An on-resonant RF pulse along the x-axis with respect to the tensor operators has the form

$$\hat{\mathcal{H}}_1' = \sqrt{5} \omega_1 \hat{T}_{11}(a). \quad (2.40)$$

2.2.4 Electric Spin Hamiltonian

A decomposition of the classical charge density $\rho(\vec{r})$ into electric multipoles yields

$$\rho(\vec{r}) = \rho^{(0)}(\vec{r}) + \rho^{(1)}(\vec{r}) + \rho^{(2)}(\vec{r}) + \dots \quad (2.41)$$

The multipoles of the charge density are the spherical electrical charge distribution $\rho^{(0)}(\vec{r})$, the electric-dipole charge distribution $\rho^{(1)}(\vec{r})$, the electric-quadrupole charge distribution $\rho^{(2)}(\vec{r})$, and so on. The nuclear spin I restricts the highest multipole order to $\rho^{(n)}(\vec{r}) = 0$ for $n > 2I$. Hence, the dipole is the highest for spin $I = \frac{1}{2}$, while the octupole is the highest for spin $I = \frac{3}{2}$.

The surrounding environment creates an electric potential field $V(\vec{r})$ for the nucleus, which can be expanded into a Taylor series about the center of the nucleus:

$$V(\vec{r}) = V^{(0)}(\vec{r}) + V^{(1)}(\vec{r}) + V^{(2)}(\vec{r}) + \dots, \quad (2.42)$$

where $V^{(0)}(\vec{r})$ is the electric potential, $V^{(1)}(\vec{r})$ is the gradient of the electric potential, i.e. the electric field, and $V^{(2)}(\vec{r})$ is the electric field gradient (EFG). The interaction energy E_{elec} of a nuclear charge distribution with an electric potential is

$$E_{elec} = \int \rho(\vec{r}) V(\vec{r}) d^3r. \quad (2.43)$$

The combination of Equation 2.41 and Equation 2.42 with Equation 2.43 yields

$$E_{elec} = E_{elec}^{(0)} + E_{elec}^{(1)} + E_{elec}^{(2)} + \dots \quad (2.44)$$

with

$$E_{elec}^{(0)} = V^{(0)}(0)Ze, \quad (2.45)$$

$$E_{elec}^{(1)} = \sum_{i=1}^3 \left. \frac{\partial V}{\partial x_i} \right|_{\vec{r}=0} \int x_i \rho^{(1)}(\vec{r}) d^3r, \quad (2.46)$$

$$E_{elec}^{(2)} = \frac{1}{2} \sum_{i,j=1}^3 \left. \frac{\partial^2 V}{\partial x_i \partial x_j} \right|_{\vec{r}=0} \int x_i x_j \rho^{(2)}(\vec{r}) d^3r. \quad (2.47)$$

The center of the nucleus is set to $\vec{r} = 0$.

The first term $E_{elec}^{(0)}$ is the electrostatic energy of the nucleus approximated as a point charge, i.e. Coulomb energy. It is of importance for atomic and molecular structures but has no direct effect for NMR.

The second term $E_{elec}^{(1)}$ describes the interaction of the electric-dipole moment with electric fields. This term vanishes as the center of mass and the center of charge coincide, i.e. nuclear states have definite parity. Thus, all odd terms in Equation 2.44 vanish and for spin $I = \frac{1}{2}$ nuclei there is no electric interaction Hamiltonian $\hat{\mathcal{H}}_{spin}^{elec} = 0$. The latter implies that for spin $I = \frac{1}{2}$ nuclei the electric interaction energy depends neither on the external electric potential nor on the orientation or structure of the nucleus (Figure 2.4).

The third term $E_{elec}^{(2)}$ corresponds to the interaction of the nuclear electric-quadrupole moment with EFGs. Thus, all quadrupole nuclei have an asymmetric electrical charge distribution, which senses EFGs of the surrounding environment. The definition of the EFG tensor V_{ij} equals

$$V_{ij} = \left. \frac{\partial^2 V}{\partial x_i \partial x_j} \right|_{\vec{r}=0}. \quad (2.48)$$

The off-diagonal elements disappear by finding the principal axes of the electric potential. In addition, the electric potential satisfies the Laplace equation $\Delta V = 0$ and consequently the trace of the EFG tensor vanishes $\sum_{\alpha=1}^3 V_{\alpha\alpha} = 0$. Similar to the EFG tensor, the electric-quadrupole tensor Q_{ij} can be defined according to

$$Q_{ij} = \int (3x_i x_j - \delta_{ij} r^2) \rho^{(2)}(\vec{r}) d^3r. \quad (2.49)$$

This simplifies the interaction energy (Equation 2.47) to

$$E_{elec}^{(2)} = \frac{1}{6} \sum_{i,j=1}^3 \left(V_{ij} Q_{ij} + V_{ij} \delta_{ij} \int r^2 \rho^{(2)}(\vec{r}) d^3 r \right) = \frac{1}{6} \sum_{i,j=1}^3 V_{ij} Q_{ij}. \quad (2.50)$$

The quantum mechanical description for the electric-quadrupole coupling is obtained by replacing the classical charge distribution by its quantum mechanical operator. The expressions for the electric-quadrupole tensor and Hamiltonian then read

$$\hat{Q}_{ij} = e \sum_{k=1}^Z (3x_{ik}x_{jk} - \delta_{ij}r_k^2), \quad (2.51)$$

$$\hat{\mathcal{H}} = \frac{1}{6} \sum_{i,j=1}^3 V_{ij} \hat{Q}_{ij}. \quad (2.52)$$

In the principal axis system of the electric potential, the EFG tensor is completely described by two variables called the field gradient q and the asymmetry parameter η :

$$eq = V_{zz}, \quad (2.53)$$

$$\eta = \frac{V_{xx} - V_{yy}}{V_{zz}}. \quad (2.54)$$

Furthermore, the nuclear quadrupole moment eQ entirely represents the quadrupole tensor, as the nucleus is in a state of definite angular momentum. The latter implies that the reorientation energy depends only on the difference between the electric charge distribution parallel and perpendicular to the z -axis, when z is the symmetry axis. In addition, the use of the angular momentum operators further simplify the electric-quadrupole Hamiltonian to

$$\hat{\mathcal{H}}_Q = \frac{e^2 q Q}{4I(2I-1)} \left[3\hat{I}_z^2 - I(I+1) + \frac{\eta}{2}(\hat{I}_+^2 + \hat{I}_-^2) \right]. \quad (2.55)$$

Consequently, the electric-quadrupole interaction depends on a nuclear property, the quadrupole moment, and on a molecular property, the EFGs at the site of the nucleus. The quadrupole moment is a constant for each nucleus. The value for ^{23}Na is 10.4 fm^2 , which is relatively large compared to 2.0 fm^2 for ^{14}N and 5.9 fm^2 for ^{39}K [Levitt (2008)]. However, the quadrupole interaction can still be weak when the nucleus finds itself in an isotropic environment with small EFGs. This is the case for biological environments, where sodium ions encounter small molecules and macromolecules. Therefore, in biological environments the quadrupole interaction is weak compared to the Zeeman interaction and can be treated by perturbation theory. Assuming an axial symmetry of the EFG, i.e. $V_{xx} = V_{yy}$, the first-order electric-quadrupole Hamiltonian simplifies to

$$\hat{\mathcal{H}}_Q = \hbar \omega_Q^{(1)} \left(\frac{3 \cos^2 \theta - 1}{2} \right) \frac{[3\hat{I}_z^2 - I(I+1)]}{6} = \hbar \omega_Q \hat{T}_{20}, \quad (2.56)$$

where

$$\omega_Q^{(1)} = \frac{3e^2qQ}{2I(2I-1)\hbar} \quad \text{and} \quad \omega_Q = \omega_Q^{(1)} \left(\frac{3\cos^2\theta - 1}{2} \right). \quad (2.57)$$

$\omega_Q^{(1)}$ is the maximum first-order electric-quadrupole coupling and ω_Q considers the transformation of the principal axes system into the local system. Hereby, represents θ the angle between the z-axis of the EFG principal axis system and the direction of \vec{B}_0 . The field gradient q as well as the angle θ show temporal fluctuations due to Brownian motion and therefore a time-averaged value of ω_Q needs to be considered

$$\bar{\omega}_Q = \frac{3e^2Q}{4I(2I-1)\hbar} \overline{q(3\cos^2\theta - 1)}. \quad (2.58)$$

The first-order quadrupole energy now reads

$$E_Q = \hbar \frac{\bar{\omega}_Q}{2} \frac{[3m^2 - I(I+1)]}{3}. \quad (2.59)$$

Consequently, energy levels with the same absolute magnetic quantum number $|m|$ are shifted by the identical energy value (Figure 2.6). Hence, in the presence of no static magnetic field, only the degeneracy in $\pm m$ is left. The electric-quadrupole energy shift vanishes at the magic angle $\theta = 54.7^\circ$, whereas it is maximal for $\theta = 0^\circ$.

To discuss the influence of the electric-quadrupole interaction on the energy levels and relaxation times, a static and a fluctuating component of the electric-quadrupole interaction need to be considered. According to Rooney et al. (1991a), the quadrupole interaction results in four different types of NMR spectra for isolated spin $\frac{3}{2}$ nuclei immersed in different molecular environments (Figure 2.6). The individual types of spectra depend on the time-averaged quadrupole interaction $\bar{\omega}_Q$ and on the motional regime $\omega_0\tau_c$, where τ_c is the rotational correlation time. This rotational correlation time is defined as the time an atom or molecule takes to rotate by 1 rad about an arbitrary axis, which depends on the respective size of the atom or molecule and its surrounding environment, for example viscosity.

Static Nuclear Quadrupole Hamiltonian

A macroscopic anisotropy results in a residual quadrupole interaction $\bar{\omega}_Q \neq 0$. This causes a shift of the energy levels $|\pm\frac{1}{2}\rangle$ and $|\pm\frac{3}{2}\rangle$ by $-\frac{\bar{\omega}_Q}{2}$ and $\frac{\bar{\omega}_Q}{2}$, respectively. Hence, the central transition $|\frac{1}{2}\rangle \leftrightarrow |-\frac{1}{2}\rangle$ is unaffected by the residual quadrupole interaction, while the two satellite transitions $|\frac{3}{2}\rangle \leftrightarrow |\frac{1}{2}\rangle$ and $|-\frac{1}{2}\rangle \leftrightarrow |-\frac{3}{2}\rangle$ are shifted by $-\bar{\omega}_Q$ and $+\bar{\omega}_Q$ (Figure 2.6), respectively. In samples with a macroscopic anisotropy, the tensors \hat{T}_{2m} are no longer decoupled and therefore $\hat{T}_{\pm 2}$ DQCs can be excited [Maarel (2003a)]. Consequently, the magic angle DQ signal, which suppresses the $\hat{T}_{\pm 2}$ DQ signal, is a probe for the anisotropy of a sample [Kemp-Harper et al. (1997)]. On the other hand, the $\hat{T}_{\pm 2}$ DQ signal probes bi-exponential relaxation similarly to the TQ signal, which is not exclusive to anisotropic

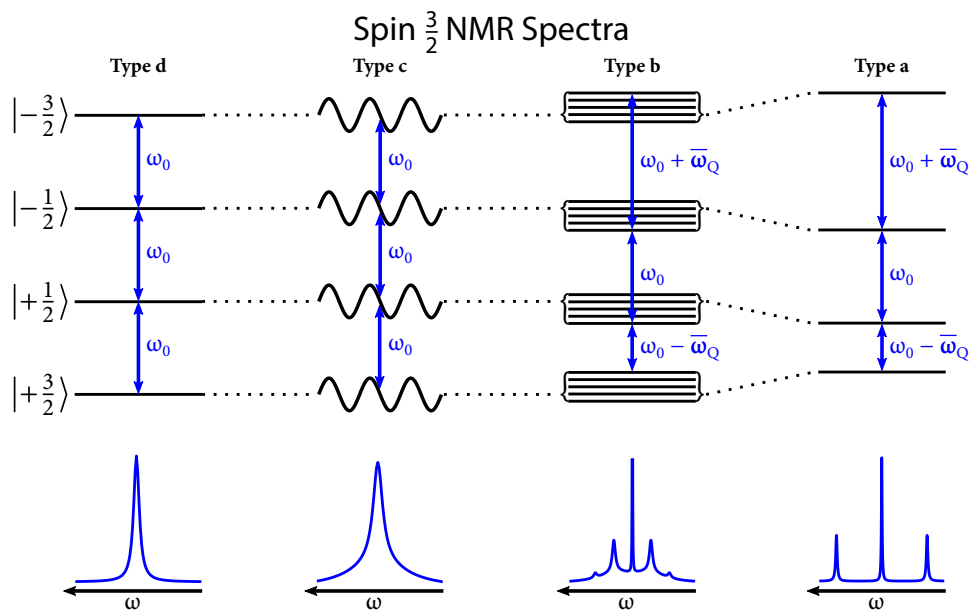


Figure 2.6: Energy levels and corresponding NMR spectra of spin $\frac{3}{2}$ nuclei in different molecular environments according to Rooney et al. (1991a). The type d and c spectra reflect an isotropic molecular environment with $\bar{\omega}_Q = 0$. In a type d spectrum, the correlation time τ_c is in the ps range, i.e. $\omega_0\tau_c \ll 1$, and the fast fluctuating quadrupole interaction is averaged to zero, such as in aqueous solution of NaCl. For a type c spectrum, e.g. sodium ions are exposed to negatively charged groups of macromolecules. This interaction results in a slower modulation of the quadrupole interaction (Figure 2.7). The correlation time increases to a few ns, i.e. $\omega_0\tau_c \approx 1$, resulting in bi-exponential relaxation (Equation 2.74). For the type b and a spectra, the sample has a macroscopic anisotropy $\bar{\omega}_Q \neq 0$ and $\omega_0\tau_c > 1$. Nuclei in domains with a distribution of $\bar{\omega}_Q \neq 0$ yield a type b spectrum, which is the superposition of a homogeneous central transition and two inhomogeneous satellite transitions. Type a is a crystal spectrum, where the satellite transitions are shifted by $\bar{\omega}_Q$ and thus three distinct SQ resonances are visible. Adapted from Rooney et al. (1991a).

environments. The macroscopic anisotropy can either be homogeneous or inhomogeneous across the sample. This results in two different types of NMR spectra, type b and a (Figure 2.6). In both cases, nuclei are in a slow motion regime $\omega_0\tau_c > 1$. The NMR spectra for an isotropic environment, type d and c, are described in the following paragraphs after the explanation of the type b and a NMR spectra.

- **Type b spectrum** originates from an inhomogeneous sample, which lacks global uniformity. Therefore, the sample consists of little domains with an individual residual quadrupole coupling $\bar{\omega}_Q$ and corresponding triplet spectrum [Maarel (2003a)]. The global response of all domains is called a powder-like spectrum. The spectrum consists of two inhomogeneous satellite transitions and one homogeneous central transition.

- **Type a spectrum** is a crystal-like spectrum. The sample has a global uniformity and consequently the entire sample assumes one residual quadrupole interaction $\bar{\omega}_Q$. The SQ spectrum has three distinct peaks with an intensity ratio of 3 : 4 : 3, where each of the two satellite transitions contributes 30% to the total SQ signal [Berendsen et al. (1973)]. This spectrum is typical for crystals, where $\bar{\omega}_Q$ can take values up to several MHz. This makes it necessary to consider also the second-order perturbation term in solid-state NMR.

Residual quadrupole interactions in the biological environment are usually very small (< 200 Hz), which result in a superposition of the central transition and the satellite transitions [Schepkin et al. (2017)]. Nevertheless, for sodium ions there is some evidence of a residual quadrupole interaction in human brain [Tsang et al. (2015) and Stobbe et al. (2016)] and muscle [Gast et al. (2018)] tissue, whereas Eliav et al. (2003) observed a triplet spectrum in bovine cartilage. Roesler et al. (2016) also recorded a triplet spectrum in human muscle tissue for ^{39}K .

Fluctuating Nuclear Quadrupole Hamiltonian

In the biological environment, nuclei encounter a variety of different atoms and molecules among which water molecules are the most common. For ions like sodium, normal vibration modes of the ion hydration shell create local EFGs resulting in a fast fluctuating electric-quadrupole interaction. The presence of larger molecules imposes a slower modulation onto the fast quadrupole interaction from the hydration shell. These interactions with atoms and molecules yield either a type d or a type c NMR spectrum depending on the motional regime (Figure 2.6). In both types of spectra, the time-averaged quadrupole interaction $\bar{\omega}_Q$ equals zero on a timescale of the inverse Larmor frequency $\frac{2\pi}{\omega_0}$. At 9.4 T this time corresponds to approximately 9.4 ns.

- **Type d spectrum** is the extreme narrow spectrum. The nucleus is within the extreme narrowing motional regime $\omega_0\tau_c \ll 1$. In this case, the fluctuations of the EFGs are so rapid such that the time-averaged quadrupole interaction $\bar{\omega}_Q = 0$ (Figure 2.7c). This corresponds to interactions with EFGs created by the hydration shell, atoms and small molecules [Rooney et al. (1991a) and Schepkin et al. (2017)]. The correlation time τ_c is on the order of ps resulting in spectral densities approximately independent on the frequency ω , i.e. $J_0(\omega_0) \approx J_1(\omega_0) \approx J_2(\omega_0)$ (Figure 2.7e). The spectral density $J_m(\omega)$ describes at which frequency ω and correlation time τ_c the electric-quadrupole interaction is most effective (Subsection 2.2.6). In a type d spectrum, the SQ spectrum consists of a single resonance at frequency ω_0 and the SQCs decay with the same relaxation time in longitudinal and transverse relaxation (Subsection 2.2.6).
- **Type c spectrum** is the bi-exponential spectrum. In the biological environment, nuclei also come across larger molecules and macromolecules, which increase the correlation time τ_c to the order of ns, i.e. intermediate motional regime $\omega_0\tau_c \approx 1$

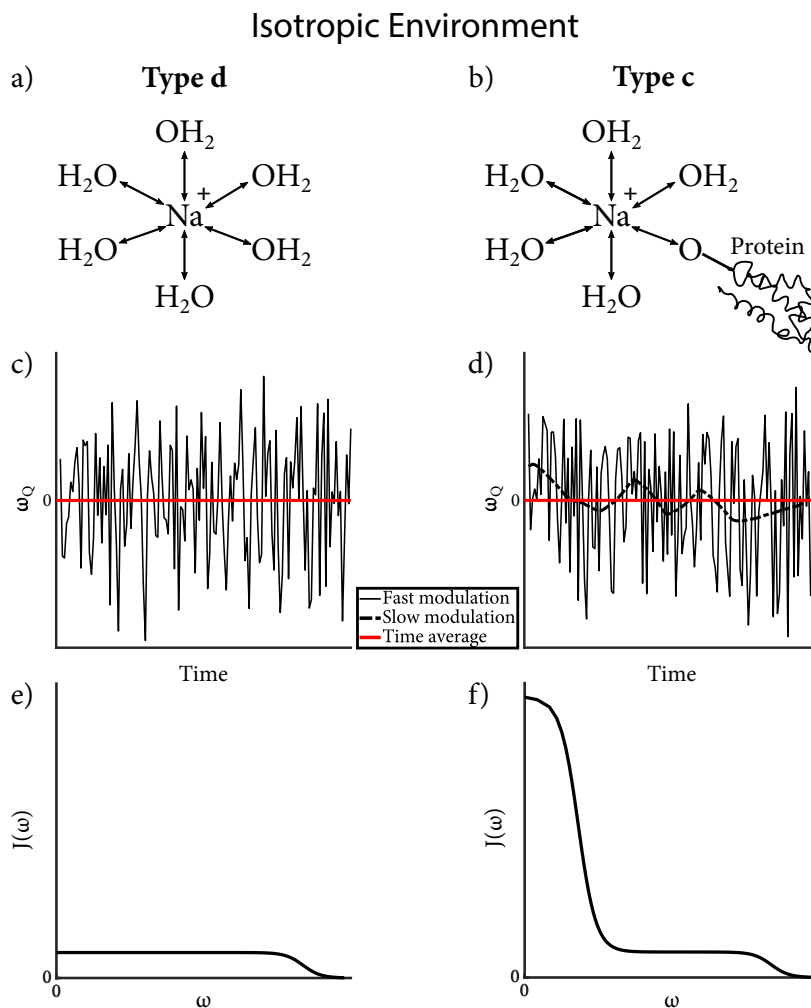


Figure 2.7: a), b) Sodium electric-quadrupole interactions in an isotropic environment corresponding to the two types of NMR spectra (Figure 2.6) with the respective time course of the quadrupole interaction, shown in c) and d), and associated spectral density $J(\omega)$, shown in e) and f). a) In a fluidic environment, a hydration shell surrounds the sodium ion. c) Normal vibration modes of this hydration shell result in a fast fluctuating quadrupole interaction (black line), which is averaged to zero on the timescale $\frac{2\pi}{\omega_0}$ (red line). This yields a type d spectrum with mono-exponential relaxation times as the spectral densities, shown in e), are $J_0(\omega_0) \approx J_1(\omega_0) \approx J_2(\omega_0)$. b) In a biological environment, sodium ions also encounter negatively charged groups of larger molecules, e.g. macromolecules. d) Electric-quadrupole interactions with these negatively charged groups result in a slower modulation (dashed black line). f) If the molecule is sufficiently large such that $\tau_c \approx \text{ns}$, the spectral density $J_0(\omega_0)$ is different from $J_1(\omega_0)$ and $J_2(\omega_0)$. This creates a type c spectrum with bi-exponential relaxation, whereas the quadrupole interaction is still averaged to zero.

[Graaf (2019)]. For cations, the very transient interactions of the quadrupole moment with EFGs created by negatively charged groups of macromolecules impose a slow modulation onto the fast fluctuating quadrupole interaction from the hydration shell [Berendsen et al. (1973)] (Figure 2.7d). These negatively charged groups are carboxyl groups (COO^-), phosphate groups (PO_4^{3-}) and hydroxyl groups (CO^-) from proteins, DNA, RNA and carbohydrates [Schepkin et al. (2017) and Torres et al. (2005)]. Proteins occupy up to 35% of the cell volume *in vivo* [Brown (1991)] and provide the majority of negatively charged groups. This slower quadrupole modulation causes $J_0(\omega_0)$ to be substantially different from $J_1(\omega_0)$ and $J_2(\omega_0)$ (Figure 2.7f). Consequently, 60% of the SQ signal, i.e. satellite transitions, decay with a fast transverse relaxation time T_{2F} , while the central transition decays with a slow transverse relaxation time T_{2S} (Subsection 2.2.6). The time-averaged quadrupole interaction $\bar{\omega}_Q$ still equals zero which results in the superposition of a broad SQ resonance onto a narrow SQ resonance (Figure 2.6).

The biological environment is mainly compromised of type d and c spectra, while type b and a spectra are rarely found [Rooney et al. (1991a)]. Consequently, in an isotropic environment only electric-quadrupole interactions which result in a type c spectrum can lead to MQCs. Hence, the TQ signal reflects on interactions of ions with macromolecules. In contrast to the selectivity of the TQ signal, the SQ signal yields information about the total sodium concentration. This selectivity of the TQ signal results in a higher specificity to the intracellular compartment compared to the SQ signal [Schepkin et al. (1998), Knubovets et al. (1998), Eykyn et al. (2015), Dizon et al. (1996), Jelicks et al. (1993), Seshan et al. (1997), Winter et al. (2001a) and Schepkin et al. (1996)]. Thus, the TQ signal may be a valuable biomarker for cell viability (Section 2.4).

2.2.5 Effects of Hard RF Pulses

The effects of RF pulses depend on the properties of the RF pulse, e.g. pulse length and flip angle, and on the electric-quadrupole interaction. Hard RF pulses are short, non-selective pulses, where the effect of a static and fluctuating quadrupole interaction can be neglected during the RF pulse. In the case of long RF pulses and/or a large quadrupole interaction, relaxation effects during the RF pulse need to be considered. The use of a preclinical NMR system without limitations of specific absorption rate (SAR) combined with a biological environment satisfies the validity of hard RF pulses.

Consider an on-resonant RF pulse along the x-axis, Equation 2.40 represents the static Hamiltonian in the rotating frame. In the case of a static Hamiltonian, the Liouville equation describes the temporal evolution of the density operator

$$\frac{d\sigma'}{dt} = -i [\hat{\mathcal{H}}'_1, \sigma'] = -i\sqrt{5}\omega_1 [\hat{T}_{11}(a), \sigma'] \quad (2.60)$$

with the solution $\sigma'(t) = e^{-i\hat{\mathcal{H}}'_1 t} \sigma'(0) e^{i\hat{\mathcal{H}}'_1 t}$. The use of the commutation relations [Bowden et al. (1986b)] results in a set of five coupled differential equations, where irreducible

tensors with a different rank are decoupled [Maarel (2003a)]. Therefore, an hard RF pulse can change the coherence order, while it conserves the rank of the tensor operators (Figure 2.8). The Wigner matrix elements [Mueller et al. (1987)] are the corresponding weighting factors for the transitions between different coherence orders. During a multi-pulse sequence, the flip angle dependence of a certain coherence can be calculated by multiplication of the respective Wigner matrix elements. A special case is represented by a 180° RF pulse, which negates the coherence order, i.e. $\pm m$ to $\mp m$. This is particularly useful for the refocusing of B_0 inhomogeneity. In addition to the flip angle, an RF pulse is also associated with a phase ϕ . To align the RF pulse with phase ϕ along the x-axis, the reference coordinate system is rotated around the z-axis by an angle ϕ . In this new reference coordinate system, the effects of the RF pulse can be evaluated with Equation 2.60. An inverse rotation around the z-axis by an angle $-\phi$ rotates the new reference frame back to the initial reference frame.

2.2.6 Relaxation in Isotropic Environment

In the absence of a residual quadrupole interaction $\bar{\omega}_Q = 0$, the spectral shifts of the satellite transitions vanish (Figure 2.6). However, the electric-quadrupole interaction is still the dominant relaxation mechanism, which yields short relaxation times and therefore broad lineshapes [Berendsen et al. (1973)]. To consider the effect of the fluctuating electric-quadrupole interaction on the relaxation characteristics, the fluctuating quadrupole interaction Hamiltonian $\mathcal{H}'_{QF}(t)$ can be expressed as:

$$\mathcal{H}'_{QF}(t) = C_Q \sum_{m=-2}^2 (-1)^m \hat{T}_{2m} e^{im\omega_0 t} F_{2-m}(t), \quad (2.61)$$

where $C_Q = \frac{eQ}{\hbar}$ is a constant and F_{2-m} are combinations of the time-dependent EFG tensor elements. In an isotropic environment and in the absence of an RF pulse, all static Hamiltonians are zero. Consequently, the time-evolution of the density operator describes only the fluctuating quadrupole Hamiltonian according to

$$\frac{d\sigma'}{dt} = - \int_0^\infty \langle [\mathcal{H}'_{QF}(t), [\mathcal{H}'_{QF}(t-\tau), \sigma'(t)]] \rangle d\tau. \quad (2.62)$$

Inserting Equation 2.61 yields the time-evolution of the density operator

$$\frac{d\sigma'}{dt} = - \sum_{m=-2}^2 [\hat{T}_{2m}, [\hat{T}_{2m}^\dagger, \sigma']] (J_m(\omega_0) + iK_m(\omega_0)). \quad (2.63)$$

The Hermitian conjugate of the tensor operator equals $\hat{T}_{lm}^\dagger = (-1)^m \hat{T}_{l-m}$. The spectral densities $J_m(\omega_0)$ and $K_m(\omega_0)$ correspond to the real and imaginary parts of the Fourier transformed EFG time correlation function, respectively. The imaginary part $K_m(\omega_0)$ causes a small dynamic shift of the energy levels, which differs for the central and satellite transitions. However, this dynamic shift is in general too small for an experimental observation and consequently neglected in most applications [Maarel (2003a)]. In the case

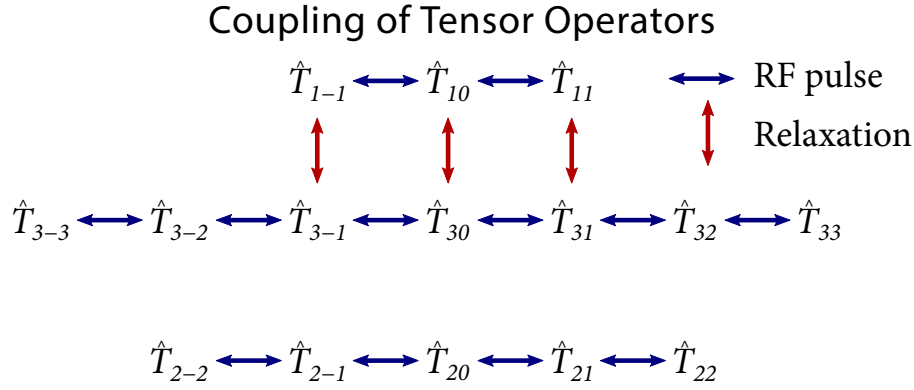


Figure 2.8: Coupling of the irreducible tensor operators under the influence of an hard RF pulse and relaxation in an isotropic environment. Relaxation only changes the tensor rank, while an hard RF pulse alters the coherence order. In an anisotropic environment rank two tensor are no longer decoupled, which results in the unique possibility to probe the anisotropy of the sample by rank two DQC.

of an exponential EFG time correlation function with correlation time τ_c , a Lorentzian function represents the spectral densities

$$J_m(\omega) = \frac{(\omega_Q^{(1)})^2}{5} \left(\frac{\tau_c}{1 + (m\omega\tau_c)^2} \right), \quad (2.64)$$

$$K_m(\omega) = \omega\tau_c J_m(\omega). \quad (2.65)$$

The real part of the spectral density shows at which frequency ω and correlation time τ_c the electric-quadrupole interaction is most effective (Figure 2.7e,f). In the biological environment, a single correlation time τ_c does not accurately represent the EFG time correlation function, as several independent processes on different timescales cause the loss of correlation. In such a case, the EFG time correlation function is a multi-exponential function [Maarel (2003a)]. Consequently, the spectral density is a sum of Lorentzians with different correlation times and quadrupole coupling constants (Figure 2.7f).

The symmetry properties of the double commutator in Equation 2.63 results in two decoupling effects. (i) The various coherence orders as well as (ii) odd and even rank tensors are decoupled (Figure 2.8). In contrast to an hard RF pulse, relaxation only affects the rank of the tensor operators, while it conserves the coherence order. Furthermore, the decoupling of even and odd rank tensors yields the unique possibility to probe the anisotropy of the sample by rank two DQCs [Kemp-Harper et al. (1997)]. In the following, only the relaxation of the odd rank tensors is considered.

Zero-quantum Coherence

The relaxation of the ZQCs (spin polarizations) \hat{T}_{10} and \hat{T}_{30} corresponds to the eigenstate populations. Under relaxation both tensor operators transform according to

$$\hat{T}_{10} \xrightarrow{R^{(0)}} \hat{T}_{10} f_{11}^{(0)}(t) + \hat{T}_{30} f_{31}^{(0)}(t), \quad (2.66)$$

$$\hat{T}_{30} \xrightarrow{R^{(0)}} \hat{T}_{30} f_{33}^{(0)}(t) + \hat{T}_{10} f_{13}^{(0)}(t). \quad (2.67)$$

The superscript (0) indicates the relaxation of coherence order $|m|$, in this case longitudinal relaxation. The transfer function $f_{l_2 l_1}^{(m)}$ describes the transformation of tensor operator $\hat{T}_{l_1 m}$ to $\hat{T}_{l_2 m}$. The bi-exponential transfer functions are

$$f_{11}^{(0)}(t) = \frac{1}{5} \left(e^{-R_1^{(0)} t} + 4e^{-R_2^{(0)} t} \right), \quad (2.68)$$

$$f_{13}^{(0)}(t) = f_{31}^{(0)}(t) = \frac{2}{5} \left(e^{-R_1^{(0)} t} - e^{-R_2^{(0)} t} \right), \quad (2.69)$$

$$f_{33}^{(0)}(t) = \frac{1}{5} \left(4e^{-R_1^{(0)} t} + e^{-R_2^{(0)} t} \right) \quad (2.70)$$

with the relaxation rates $R_1^{(0)} = 2J_1(\omega_0)$ and $R_2^{(0)} = 2J_2(\omega_0)$. In general, the longitudinal relaxation is bi-exponential with a fast component $T_{1F} = \frac{1}{R_1^{(0)}}$ and a slow component $T_{1S} = \frac{1}{R_2^{(0)}}$. The fast and slow component contribute 20% and 80% to the signal, respectively. There are only a few studies [Andrasko (1974) and Monoi (1985)] which were able to detect a bi-exponential longitudinal relaxation for sodium ions. This indicates that the two relaxation times are close in value and therefore difficult to separate even outside the extreme narrowing limit $\omega_0 \tau_c \ll 1$ [Rooney et al. (1991a)]. Consequently, a mono-exponential longitudinal relaxation in the biological environment is a reasonable assumption. In the extreme narrowing limit, the spectral densities are approximately independent of the frequency, i.e. $J_1(\omega_0) \approx J_2(\omega_0)$, (Figure 2.7e) and hence the relaxation time is given by

$$T_1 \equiv T_{1S} = T_{1F} = \frac{5}{2 \left(\omega_Q^{(1)} \right)^2 \tau_c}. \quad (2.71)$$

In case of a mono-exponential longitudinal relaxation, relaxation time measurements at a minimum of two Larmor frequencies are required to determine the correlation time and the quadrupole coupling constant [Woessner (2001)].

Single-quantum Coherence

The SQCs $\hat{T}_{1\pm 1}$ and $\hat{T}_{3\pm 1}$ transform under the effects of relaxation according to

$$\hat{T}_{1\pm 1} \xrightarrow{R^{(1)}} \hat{T}_{1\pm 1} f_{11}^{(1)}(t) + \hat{T}_{3\pm 1} f_{31}^{(1)}(t), \quad (2.72)$$

$$\hat{T}_{3\pm 1} \xrightarrow{R^{(1)}} \hat{T}_{1\pm 1} f_{13}^{(1)}(t) + \hat{T}_{3\pm 1} f_{33}^{(1)}(t). \quad (2.73)$$

The transfer functions are also bi-exponential and read

$$f_{11}^{(1)}(t) = \frac{1}{5} \left(3e^{-R_1^{(1)}t} + 2e^{-R_2^{(1)}t} \right), \quad (2.74)$$

$$f_{13}^{(1)}(t) = f_{31}^{(1)}(t) = \frac{\sqrt{6}}{5} \left(e^{-R_1^{(1)}t} - e^{-R_2^{(1)}t} \right), \quad (2.75)$$

$$f_{33}^{(1)}(t) = \frac{1}{5} \left(2e^{-R_1^{(1)}t} + 3e^{-R_2^{(1)}t} \right) \quad (2.76)$$

with the transverse relaxation rates $R_1^{(1)} = J_0(\omega_0) + J_1(\omega_0)$ and $R_2^{(1)} = J_1(\omega_0) + J_2(\omega_0)$. These relaxation rates also contain a dynamic shift, which is difficult to detect and usually neglected [Maarel (2003a)]. The fast component $T_{2F} = \frac{1}{R_1^{(1)}}$, which contributes 60% to the signal, is sensitive to slow molecular motion at zero frequency. In contrast, the slow component $T_{2S} = \frac{1}{R_2^{(1)}}$, which contributes 40% to the signal, is only sensitive to molecular motion at high frequency similarly to the longitudinal relaxation rates. Consequently, a slight increase in the correlation time τ_c is sufficient to result in bi-exponential transverse relaxation contrary to longitudinal relaxation [Andrasko (1974)]. Hence, the biological environment yields bi-exponential transverse relaxation and only a single pool of nuclei results in the theoretical amplitudes of 40% and 60% for the slow and fast component, respectively [Burstein et al. (2019)]. In the extreme narrowing limit $\omega_0\tau_c \ll 1$, the spectral densities are approximately independent on the frequency (Figure 2.7e), which yields a mono-exponential transverse relaxation with the relaxation time

$$T_2 \equiv T_{2S} = T_{2F} = \frac{5}{2 \left(\omega_Q^{(1)} \right)^2 \tau_c}. \quad (2.77)$$

In this case, the transverse and longitudinal relaxation times are equal (cf. Equation 2.71 and Equation 2.77). In addition, the transfer function $f_{3\pm 1}^{(1)}$ vanishes and consequently relaxation does not create rank three tensors. The latter implies that only in the presence of bi-exponential relaxation, which requires macromolecules, MQCs are possible.

Consider a single pool of nuclei, i.e. one-compartment model, with bi-exponential transverse relaxation, the measurement of both relaxation times allows calculating the electric-quadrupole coupling constant and correlation time [Jaccard et al. (1986) and Rooney et al. (1991a)]. The ratio of the transverse relaxation rates yields

$$\alpha = \frac{R_1^{(1)}}{R_2^{(1)}} = \frac{J_0(\omega_0) + J_1(\omega_0)}{J_1(\omega_0) + J_2(\omega_0)} = \frac{4x^2 + 9x + 2}{2 + 5x} \quad (2.78)$$

with $x = (\omega_0\tau_c)^2$. The solution of Equation 2.78 with respect to x results in following equation for the correlation time

$$\omega_0\tau_c = \sqrt{\frac{5\alpha - 9 + \sqrt{25\alpha^2 - 58\alpha + 49}}{8}}. \quad (2.79)$$

The difference between both relaxation rates results in

$$\beta = R_1^{(1)} - R_2^{(1)} = J_0(\omega_0) - J_2(\omega_0) = \left(\omega_Q^{(1)}\right)^2 \frac{4x\tau_c}{5(1+4x)}. \quad (2.80)$$

Consequently, the equation for the quadrupole coupling constant is

$$\omega_Q^{(1)} = \sqrt{\frac{5\beta(1+4x)}{4x\tau_c}}. \quad (2.81)$$

These equations are only valid for a single pool of nuclei, where a single correlation time describes the EFG time correlation function. When both relaxation times are equal, only a measurement at a minimum of two Larmor frequencies allows extracting the quadrupole coupling constant and the correlation time [Woessner (2001)].

Multi-quantum Coherence

The excitation of MQCs is only possible for bi-exponential relaxation. The DQCs and TQCs relax independently according to

$$\hat{T}_{3\pm 2} \xrightarrow{R^{(2)}} \hat{T}_{3\pm 2} f_{33}^{(2)}(t), \quad (2.82)$$

$$\hat{T}_{3\pm 3} \xrightarrow{R^{(3)}} \hat{T}_{3\pm 3} f_{33}^{(3)}(t) \quad (2.83)$$

with the transfer functions

$$f_{33}^{(2)}(t) = e^{-R_1^{(2)}t}, \quad (2.84)$$

$$f_{33}^{(3)}(t) = e^{-R_1^{(3)}t}. \quad (2.85)$$

The relaxation rates are $R_1^{(2)} = J_0(\omega_0) + J_2(\omega_0)$ and $R_1^{(3)} = J_1(\omega_0) + J_2(\omega_0)$. In a TQ pulse sequence, the time during the presence of TQCs is set to a minimum in order to reduce the signal loss due to relaxation.

2.2.7 Multi-quantum Pulse Sequence

As outlined in the previous subsections, hard RF pulses change only the coherence order of the tensor operators, while relaxation effects alter the rank. Consequently, in the absence of bi-exponential relaxation (Equation 2.73 and Equation 2.75) MQCs cannot be created. The presence of negatively charged groups of macromolecules, proteins, is already sufficient for the creation of MQCs. Hence, a pulse sequence needs to be designed which exploits the effects of relaxation and RF pulses to excite MQCs and convert them back to SQCs. The last step is necessary as RF coils are only capable of detecting dipole radiation, i.e. SQCs. Figure 2.9 shows a general transversal MQ pulse sequence. Similarly, a longitudinal MQ pulse sequence can be designed [Jaccard et al. (1986) and Maarel (2003a)]. Both pulse sequences differ only in their sensitivity to the range of correlation

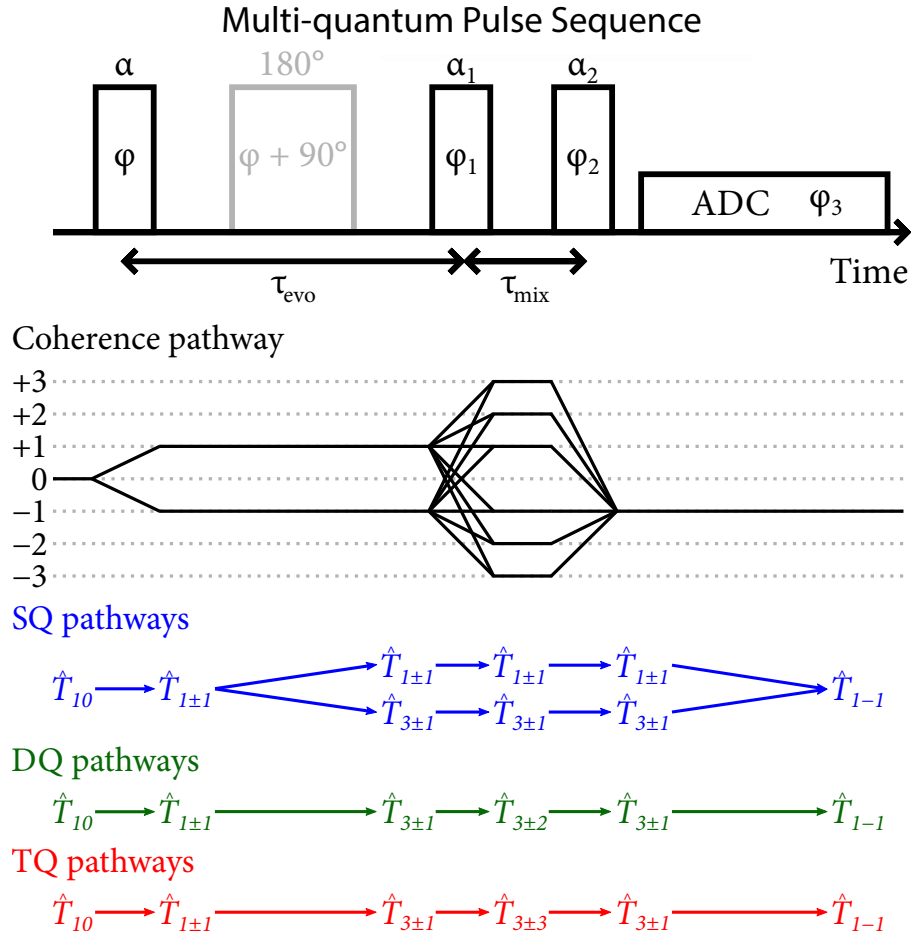


Figure 2.9: Transversal MQ pulse sequence with optional refocusing RF pulse during the evolution time. The changes in the coherence orders and tensor operators are shown below the sequence diagram. These coherence pathways do not consider the optional refocusing RF pulse and are only valid for an isotropic environment.

times [Maarel (2003a)]. The longitudinal MQ pulse sequence is sensitive to the motional regime $\omega_0 \tau_c \approx 1$, while the transversal MQ pulse sequence is sensitive to $\omega_0 \tau_c \geq 1$. Consequently, the transversal MQ pulse sequence detects nuclei in slow molecular motion, i.e. low-frequency dispersion in the spectral densities (Figure 2.7f).

In the arrow notation [O. W. Sørensen et al. (1984)], the evolution of the tensor operators during an RF pulse with flip angle α and phase ϕ is given by:

$$\hat{T}_{lm} \xrightarrow{\alpha(\hat{I}_y \cos \phi - \hat{I}_x \sin \phi)} \sum_{m'=-l}^l \hat{T}_{lm'} d_{m'm}^l(\alpha) e^{-i\Delta m \phi} \quad (2.86)$$

with the new coherence order m' and the change in the coherence order $\Delta m = m' - m$. The Wigner matrix elements $d_{m'm}^l(\alpha)$ are listed in Mueller et al. (1987). The MQ pulse

sequence consists of at least three RF pulses (Figure 2.9). The first RF pulse converts the equilibrium magnetization \hat{T}_{10} to rank one SQCs $\hat{T}_{1\pm 1}$. According to Equation 2.72, these SQCs evolve during the evolution time τ_{evo} to rank one and three SQCs $\hat{T}_{1\pm 1}$ and $\hat{T}_{3\pm 1}$, respectively. The next RF pulse excites MQCs in the presence of rank three SQCs. MQCs exist only during the mixing time τ_{mix} and undergo relaxation during this time period. Therefore, the mixing time is set to the minimal value. To detect these MQCs, the last RF pulse transforms these coherences into rank three SQCs. These rank three SQCs evolve into detectable rank one SQCs during the acquisition period. By convention [Bain (1984)], the receiver only detects \hat{T}_{1-1} SQCs. The $m = +1$ and $m = -1$ SQCs represent clockwise and counter-clockwise rotating transverse magnetization and therefore are equivalent.

The current RF pulse sequence detects all possible coherences. To select the desired coherence, phase cycling is required. A phase cycle is the repetition of the pulse sequence where only the phase of the RF pulses are changed, while all other parameters are the same. This alters the signal phase of each coherence pathway differently (Equation 2.86). There are two different phase cycling schemes: Filtration [Jaccard et al. (1986)] and separation of coherence orders in frequency using time proportional phase increment (TPPI) [Marion et al. (1983)]. The filtration technique varies the phases of the RF pulses such that the summation of all signals from the phase cycle leads to constructive interference for the desired coherence, while all other coherences cancel out. Filtration has the disadvantage that all coherences are detected at the same frequency and consequently an imperfect cancellation will interfere with the desired coherence. The TPPI method increments the phases of the RF pulses and a FT along the RF pulse phase dimension results in the separation of different coherence orders, see Subsection 3.2.4. Therefore, a simultaneous acquisition of different coherence orders can be achieved [Schepkin et al. (2017)].

The use of a minimum of three RF pulses and an evolution time in the range of a few ms results in a higher sensitivity of MQCs to B_1^+ and B_0 inhomogeneity compared to SQCs, respectively [Hancu et al. (1999), Matthies et al. (2010) and Fleyscher et al. (2010)]. To obtain a quantitative signal, removal of signal biases caused by B_1^+ and B_0 inhomogeneities is necessary. The multiplication of the Wigner matrix elements during the MQ pulse sequence allows the calculation of the flip angle dependence of each coherence. In the case of the three RF pulse sequence, the flip angle dependence of the TQ signal is $\sin \alpha \sin^2 \alpha_1 \sin^2 \alpha_2$. Hence, the acquisition of a B_1^+ map provides a straightforward correction of B_1^+ inhomogeneity. In contrast, the three RF pulse sequence with a 180° refocusing RF pulse results in a TQ signal flip angle dependence, which also depends on τ_{evo} and the relaxation times [Hancu et al. (1999)]. Consequently, a good B_1^+ homogeneity is a prerequisite for the three RF pulse sequence with a 180° refocusing RF pulse. Two different methods exist to compensate for B_0 inhomogeneity: An extension of the phase cycle or the use of a 180° refocusing RF pulse during the evolution time. The first method also requires an acquisition of a B_0 map. The second method requires a good B_1^+ homogeneity as an imperfect refocusing pulse will already create MQCs during the evolution time [Reddy et al. (1994) and Hancu et al. (1999)]. For a non-localized MQ pulse sequence, which was used in this thesis, a volume coil minimizes B_1^+ inhomogeneity and a 180° refocusing RF pulse compensates for signal loss due to B_0 inhomogeneity.

2.3 Magnetization Transfer and Chemical Exchange Saturation Transfer

The second method to investigate non-invasively proteins by NMR and consequently obtain physiological parameters by NMR utilizes magnetization transfer processes between protons from low concentrated organic compounds ($c \sim \text{mM}$) and water protons. Chemical exchange saturation transfer (CEST) indirectly detects protons from organic compounds by frequency-selective saturation and subsequent acquisition of the reduced water signal.

The first part of this section introduces the relevant magnetization transfer processes, e.g. chemical exchange and dipolar coupling, which can transfer the saturation between solute and water protons. The second part of this section explains the basic principles of CEST. This section is based on the work of P. C. M. van Zijl et al. (2011), Zaiss et al. (2013a), P. C. M. van Zijl et al. (2018), Liu et al. (2013) and Neuhaus et al. (2000).

2.3.1 Magnetization Transfer Processes

In a biological sample, protons exist in different magnetic environments. Protons within the same magnetic environment can be grouped into one pool i with the same physical properties, e.g. the same resonance frequency ω_i , the same relaxation times T_{1i} and T_{2i} , and the same exchange rates k_{ij} with other pools j (Figure 2.10). The exchange rates describe the magnetization transfer between different pools. In CEST, the magnetization transfer from protons in solutes (pool s), which refer to low concentrated organic compounds, to protons in the large water pool (pool w) is of importance. In aqueous solutions, magnetization transfer between different pools can occur by three different mechanisms:

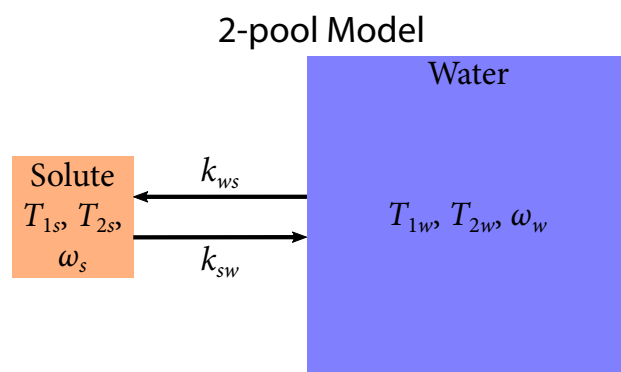


Figure 2.10: Schematic sketch of a 2-pool model using the large water pool and a less abundant solute pool. Each pool of protons $i = s, w$ has its characteristic resonance frequency ω_i and relaxation times T_{1i} and T_{2i} . The exchange rates k_{ij} , $i, j = s, w$ for $i \neq j$, describe the magnetization transfer between both pools.

- **Chemical exchange** is the physical exchange of protons between different pools induced by chemical reactions. This exchange of protons does not affect the quantum mechanical properties of the nuclear spin. Consequently, chemical exchange transfers magnetization between different pools [Otting et al. (2002) and J. Zhou et al. (2006)].
- **Dipolar interaction** occurs between nuclear spins in close proximity and results in coupled spin systems. These coupled spin systems yield new cross-relaxation pathways, which can either cause a signal enhancement or signal reduction of the coupled partner nucleus. This transfer of magnetization is also known as the nuclear Overhauser effect (NOE) [Solomon (1955) and Neuhaus et al. (2000)].
- **Molecular exchange** is defined by the transition between the bound and the free state of motion of a molecule caused by diffusion. This transition between both states alters the NMR properties of protons within the molecule, e.g. chemical shift and relaxation times [Stanisz et al. (2005)]. Thus, molecular exchange yields a magnetization transfer [Henkelman et al. (2001)].

The following paragraphs describe these magnetization transfer processes in more detail.

Chemical Exchange

Organic compounds, e.g. sugars and amino acids, contain exchangeable groups of protons, for example amide (NH) and hydroxyl (OH) protons. These exchangeable protons (pool *s*) can exchange with free water protons (pool *w*) and therefore transfer magnetization to the water pool. This exchange of protons is an acid-base catalyzed chemical reaction and the exchange rate k_{sw} characterizes this chemical reaction [Otting et al. (2002) and J. Zhou et al. (2006)]:

$$k_{sw}(\text{pH}, T) = k_{acid}(T) \cdot 10^{-\text{pH}} + k_{base}(T) \cdot 10^{\text{pH} - pK_W(T)} + k_0 \quad (2.87)$$

with k_{acid} and k_{base} being the acid catalyzed exchange and the base catalyzed exchange, respectively. k_0 contains all other possible contributions, such as the buffer concentration and type. pK_W is the autodissociation constant of water, i.e. negative base 10 logarithm of Equation 2.116. According to Equation 2.87, the exchange rate k_{sw} decreases or increases with increasing pH depending on whether the exchange of the functional group is acid or base catalyzed, respectively. The Arrhenius Law describes the exponential temperature dependence of the exchange rates [Bai et al. (1993)]. For rising temperature, the exchange rates increase.

Dipolar Coupling

In NMR spectroscopy, heteronuclear NOE, e.g. $^1\text{H} - ^{13}\text{C}$ and $^1\text{H} - ^{31}\text{P}$, is a powerful tool to achieve a signal enhancement for the respective X-nucleus. However, for CEST only the transfer of magnetization between protons in different pools is of importance for the transfer of saturation to the water pool. Dipolar couplings can result in an exchange of spin

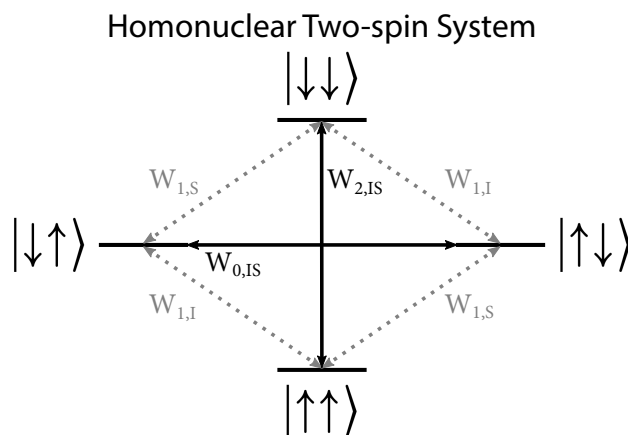


Figure 2.11: Energy levels of a dipolar coupled two-spin system $|IS\rangle$ ($I, S = \downarrow, \uparrow$) in an external magnetic field with the corresponding transition probabilities $W_{j,n}$ ($j = 0, 1, 2$ and $n = I, S, IS$). The cross-relaxation pathways $W_{0,IS}$ and $W_{2,IS}$ act on both spin states and consequently can transfer magnetization.

states, which is indistinguishable from chemical exchange, between two protons. The following discussion of the magnetization transfer via dipolar coupling, i.e. NOE, is based on a homonuclear two-spin systems of different proton pools.

Two dipolar coupled spins from proton pool I and S couple to a spin system with four spin states in an external magnetic field (Figure 2.11): $|IS\rangle = |\uparrow\uparrow\rangle, |\uparrow\downarrow\rangle, |\downarrow\uparrow\rangle$ and $|\downarrow\downarrow\rangle$. The corresponding transition probabilities are $W_{j,n}$ with $j = 0, 1, 2$ and $n = I, S, IS$. This dipolar coupled spin system is not restricted to the water and solute pools but can be arbitrary proton pools. The coupled spin system results in new cross-relaxation pathways $W_{0,IS}$ and $W_{2,IS}$, which act on both spin states of pool I and S and are of central importance for NOE (Figure 2.11). In contrast, $W_{1,I}$ and $W_{1,S}$ are only independent T_1 relaxation pathways of each individual spin system I and S, respectively. The $W_{0,IS}$ transition is called the flip-flop or the zero-quantum (ZQ) transition, while the $W_{2,IS}$ transition is called the flip-flip or the DQ transition (Figure 2.11). The evolution of the magnetization for the dipolar coupled spin system by introduction of the dipole-dipole Hamiltonian in the context of perturbation theory is described by the Solomon equations [Solomon (1955)]. The Solomon equations introduce a cross-relaxation rate $\sigma_{IS} = W_{2,IS} - W_{0,IS}$, similar to the case of magnetization transfer by chemical exchange, whose exchange rate is defined as $k_{IS} = W_{0,IS} - W_{2,IS} = -\sigma_{IS}$. With the use of spectral densities, similar to Subsection 2.2.6, an expression for the $W_{0,IS}$ and the $W_{2,IS}$ transition probabilities can be obtained:

$$W_{0,IS} = \frac{\omega_{DD}^2}{10} \frac{\tau_c}{1 + (\omega_I - \omega_S)^2 \tau_c^2}, \quad (2.88)$$

$$W_{2,IS} = \frac{3\omega_{DD}^2}{5} \frac{\tau_c}{1 + (\omega_I + \omega_S)^2 \tau_c^2}, \quad (2.89)$$

where $\omega_{DD} = \frac{\mu_0 \hbar \gamma^2}{4\pi r^3}$ is the dipole-dipole coupling constant and τ_c is the rotational correlation time, i.e. the time a molecule takes to rotate 1 radian about an arbitrary axis. In the case of a homonuclear coupled two-spin system of protons, the frequencies of the two pools are $\omega_I \approx \omega_S \approx \omega_0$. Hence, the frequency difference $\omega_I - \omega_S$ equals the chemical shift difference, which is in the range of a few Hz up to a few kHz. Under the assumption of a negligible frequency difference, the cross-relaxation rate simplifies to:

$$\sigma = \frac{\omega_{DD}^2 \tau_c}{10} \left[\frac{6}{1 + (2\omega_0 \tau_c)^2} - 1 \right]. \quad (2.90)$$

The cross-relaxation rate has a zero crossing at $\omega_0 \tau_c = 1.12$, which separates the cross-relaxation rate into two regimes. Depending on the correlation time, either the $W_{0,IS}$ or the $W_{2,IS}$ is the dominant cross-relaxation pathway:

- $\omega_0 \tau_c \ll 1.12$ ($\sigma > 0$): In the extreme narrowing limit, the $W_{2,IS}$ transition is the dominant cross-relaxation pathway (Figure 2.11). This motional regime corresponds to small molecules in aqueous solutions.
- $\omega_0 \tau_c \gg 1.12$ ($\sigma < 0$): In the spin diffusion limit, the $W_{0,IS}$ transition is the dominant cross-relaxation pathway (Figure 2.11). This slow motion regime corresponds to macromolecules, e.g. proteins, which can have correlation times in the range of μs , in aqueous solutions.

Different pools of protons in macromolecules, which have a high proton density and a correlation time in the order of μs , are coupled via intramolecular dipolar couplings with exchange rates of a few Hz. This coupling, which depends on the distance r between two protons according to $\sigma \sim \frac{1}{r^6}$, allows the transfer of magnetization in small regions spanning 3.5–4.5 Å within a macromolecule [Wüthrich (1986)]. Intermolecular dipolar couplings between bound molecules and macromolecules are also possible. However, intermolecular dipolar couplings between free water molecules and macromolecules are strongly suppressed due to the high tumbling rate of free water molecules.

Exchanged-relayed Nuclear Overhauser Effect

In CEST, magnetization transfer processes by exchange-relayed NOE (rNOE) originate mainly from mobile proteins and peptides [Y. Zhou et al. (2020)]. These rNOE signals depend on the protein concentration [Jin et al. (2013) and Goerke et al. (2018)] and the protein folding state [Zaiss et al. (2017), Goerke et al. (2015) and Goerke et al. (2017)]. Hence, these signals have a great potential as a non-invasive diagnostic tool for diseases, like cancer and neurodegenerative diseases. However, the detectability of denaturation processes in living cells by the rNOE CEST signal remains to be verified experimentally, which was one objective of this thesis.

In mobile macromolecules, e.g. proteins and peptides, magnetization transfer between non-exchanging, covalently bound protons and water protons is possible via a two-step

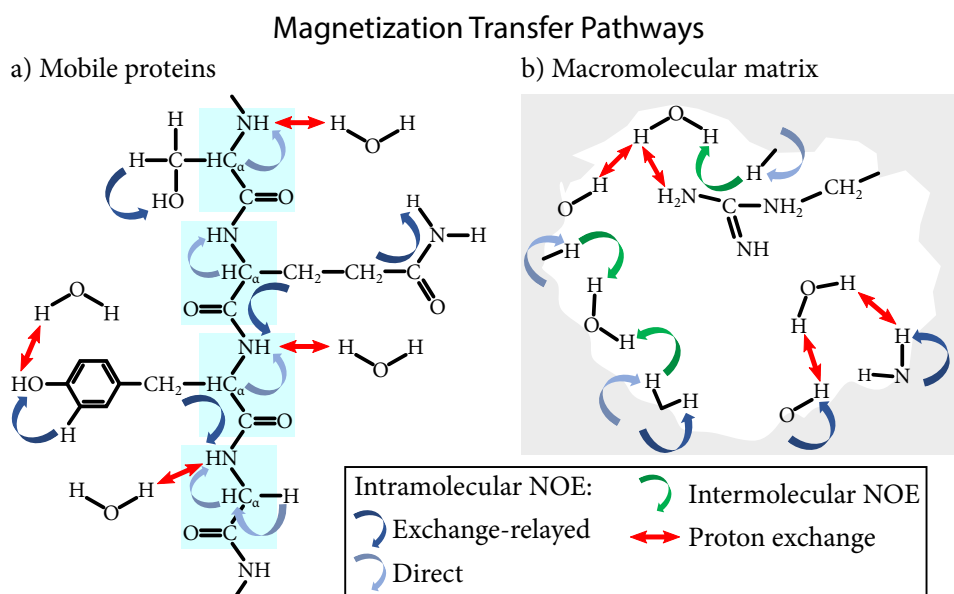


Figure 2.12: Magnetization transfer pathways between protons in mobile proteins or in the macromolecular matrix and water protons. a) In mobile proteins, the magnetization transfer to free water protons occurs via intramolecular dipolar couplings between bound protons and exchangeable protons (dark and light blue arrows) followed by chemical exchange (red arrows). b) Magnetization transfer from protons in the macromolecular matrix (gray background), e.g. cell membrane and cytoskeleton, to free water protons results from the same pathways as in mobile proteins. Furthermore, intermolecular dipolar couplings between protons on the surface of the macromolecular matrix and bound water protons (green arrows) also represent an efficient magnetization transfer pathway. Subsequent molecular exchange yields a transition from bound to free water molecules caused by diffusion. Adapted from P. C. M. van Zijl et al. (2011).

process using dipolar coupling followed by chemical exchange (Figure 2.12a) [P. C. M. van Zijl et al. (2011), J. Xu et al. (2014) and P. C. M. van Zijl et al. (2003)]. At first, intramolecular dipolar couplings between non-exchanging and exchanging protons transfer the magnetization to exchangeable protons. These exchangeable protons then transfer the magnetization to the water protons by chemical exchange. Hence, this magnetization transfer pathway is also called the exchange-relayed NOE (rNOE). The two-step process is the dominant magnetization transfer pathway between non-exchanging protons in mobile macromolecules and water protons. In theory, magnetization transfer via intermolecular dipolar couplings to water protons can also take place. However, the fast tumbling rate of free water molecules makes this process negligible. The limiting rates of this two-step magnetization transfer are the slow dipolar couplings. Aliphatic and aromatic protons are in the spectral range of -5.0 to -1.0 ppm and 1.0 to 5.0 ppm, respectively; they have exchange rates of 2 – 5 Hz [J. Xu et al. (2014), Friedman et al. (2015) and Goerke (2015)]. These

limiting dipolar exchange rates are also the reason why the rNOE signal is insensitive to pH [Y. Zhou et al. (2020), Zaiss et al. (2017), Jin et al. (2013) and Goerke et al. (2015)].

Semi-solid Magnetization Transfer

The Magnetization transfer process between protons in solid-like structures and water protons is called the semi-solid Magnetization Transfer (ssMT). This ssMT signal has a very broad lineshape, which allows the detection of a tissue contrast, also called magnetization transfer contrast, even at large frequency offsets relative to the water frequency [Henkelman et al. (2001) and Wolff et al. (1989)]. In CEST, the ssMT signal overlaps with the CE and rNOE signals of metabolites and proteins. Thus, methods to remove the ssMT signal are necessary, which are described at the end of this section.

In vivo solid-like structures, e.g. cell membrane, surface proteins and cytoskeleton, yield a transverse relaxation time of protons within these solid-like structures in the range of μs [Stanisz et al. (2005)]. Hence, the non-specific resonance peak of protons in the macromolecular matrix covers several kHz in the NMR spectrum (Subsection 2.1.5). Water molecules can bind to the surface of these solid-like structures, also called the macromolecular matrix, which prolongs their rotational correlation time. Consequently, intermolecular dipolar couplings between bound water protons and protons on the surface of the macromolecular matrix also represent an efficient magnetization transfer pathway (Figure 2.12b). The subsequent transition of bound water molecules to free water molecules caused by diffusion results in the final magnetization transfer to the water pool. Besides the magnetization transfer via intermolecular dipolar couplings, intramolecular dipolar couplings and chemical exchange can also contribute to the magnetization transfer to free water protons, as in the case of rNOE. The effective exchange rate of the ssMT signal is in the range of 20–70 Hz [Stanisz et al. (2005)].

2.3.2 Chemical Exchange Saturation Transfer

CEST enhances the signal of low concentrated organic compounds by utilizing magnetization transfer processes between protons from low concentrated organic compounds and water protons. A saturation RF pulse saturates the solute protons and magnetization transfer processes transfer this saturation several times to the large water proton pool ($c \approx 55.5 \text{ M}$) during the saturation RF pulse (Figure 2.13). Consequently, the signal from low concentrated organic compounds is amplified, which can be expressed by the proton transfer ratio (PTR) [P. C. M. van Zijl et al. (2011)]:

$$PTR \approx k_{sw} \cdot T_{1w}, \quad (2.91)$$

where k_{sw} is the exchange rate of the magnetization transfer process and T_{1w} is the longitudinal relaxation time of water.

In CEST, a saturation RF pulse with a pulse length t_{sat} , an RF amplitude B_1^+ and an offset frequency $\Delta\omega = \omega_{\text{RF}} - \omega_w$ is applied prior to the acquisition of the water signal by

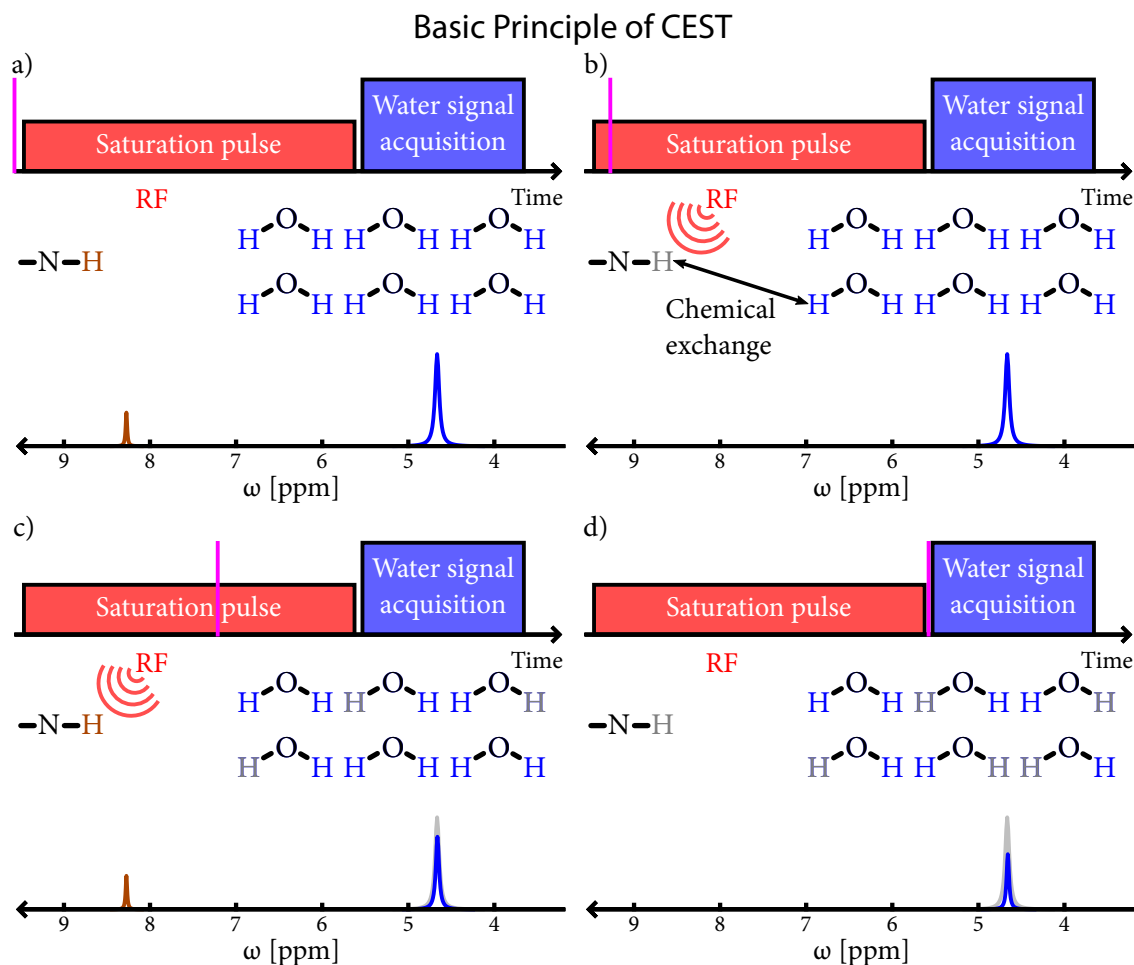


Figure 2.13: Graphical illustration of the basic principle of CEST using a single exchanging pool of amide protons (N–H). The purple line in the sketch of the pulse sequence indicates the current time point. The frequency of the saturation RF pulse is set to the amide proton frequency. a) At thermal equilibrium, both the water and amide pools have a longitudinal magnetization. b) The saturation RF pulse selectively saturates the amide protons, which results in no remaining longitudinal magnetization. Then, this saturation will be transferred via chemical exchange between amide and water protons to the water pool. c) The process of selective saturation of the amide protons followed by chemical exchange with water protons occurs several times during the RF saturation pulse. This saturation transfer causes a reduction in the longitudinal magnetization of the water pool. The repetition of the saturation transfer yields an amplification of the signal of the low concentrated amide protons. d) After the RF saturation pulse is switched off, the reduced longitudinal water magnetization will be measured by a conventional spectroscopic or imaging pulse sequence.

either a spectroscopic or imaging pulse sequence (Figure 2.14a). The frequency-selective saturation RF pulse equilibrates the populations of the energy levels $|\uparrow\rangle$ and $|\downarrow\rangle$ of pool s . Hence, pool s has no remaining longitudinal magnetization (Figure 2.13). The magnetization transfer pathways, described in Subsection 2.3.1, transfer the saturation of pool s to the water pool during the saturation RF pulse. An unsaturated water proton will replace the saturated solute proton, which will also be saturated by the saturation RF pulse. This process of saturation and exchange repeats itself several times during the saturation RF pulse, which amplifies the signal of protons in low concentrated organic compounds (Figure 2.13). The transfer of saturation to the water pool yields a reduction in the population difference of the water pool and consequently results in a reduced water signal $M_{z,w}(\Delta\omega)$. The repetition of the saturation RF pulse at different offset frequencies $\Delta\omega$ and subsequent acquisition of the water signal yields a Z-spectrum (Figure 2.14b):

$$Z(\Delta\omega) = \frac{M_{z,w}(\Delta\omega)}{M_{z,0}}, \quad (2.92)$$

where $M_{z,0}$ is the equilibrium magnetization of water.

The Z-spectrum consists of a variety of different effects with broad and overlapping resonances (Figure 2.14b):

- **Direct water saturation (DS):**
The saturation RF pulse applied at offset frequencies between ± 1 ppm directly saturates the water proton pool. This is the most prominent effect in the Z-spectrum, as it causes a dip in the Z-spectrum due to $Z(\Delta\omega = 0) \approx 0$ (Figure 2.14b).
- **Semi-solid Magnetization Transfer (ssMT):**
The effect of ssMT from protons in solid-like structures can be found in the spectral range of ± 30 ppm. Consequently, at large frequency offsets only the effect of ssMT contributes to Z-values smaller than one neglecting partial saturation $t_{\text{sat}} < 5T_1$ (Figure 2.14b). The maximum of the ssMT is in the negative frequencies offsets around -2.0 to -3.5 ppm.
- **Chemical exchange (CE):**
Chemical exchanging signals of proteins and metabolites are in the range of $+0.5$ to $+5.0$ ppm. Amide (NH) and amine (NH₂) protons, for example, resonate at $+3.5$ and $+2.2$ to $+2.9$ ppm, respectively.
- **Exchange-relayed NOE (rNOE):**
Aliphatic and aromatic protons of mobile proteins and peptides in the spectral range of -5.0 to -1.0 ppm and $+1.0$ to $+5.0$ ppm yield an rNOE signal, respectively. Figure 2.18 and Table 2.3 provide an assignment of chemical shifts to chemical groups of amino acids. These chemical groups can contribute to the rNOE CEST signal of proteins and peptides.

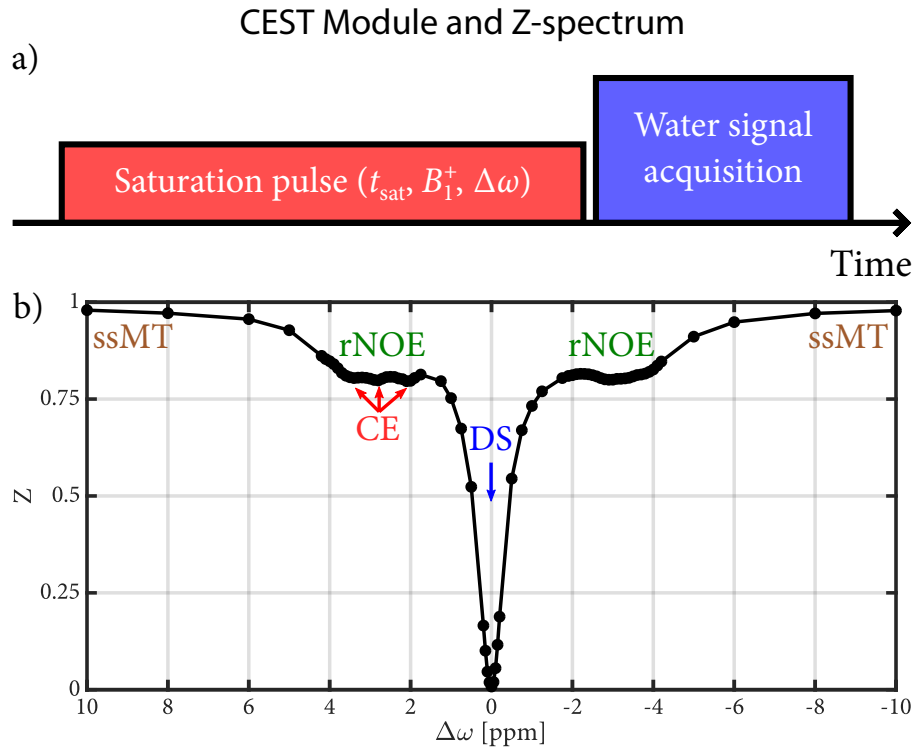


Figure 2.14: a) The CEST pulse sequence consists of a saturation RF pulse (red) and a water signal acquisition (blue). The parameters of the saturation RF pulse are the pulse length t_{sat} , the RF amplitude B_1^+ and the offset frequency $\Delta\omega = \omega_{\text{RF}} - \omega_w$. The repetition of this CEST module at multiple offset frequencies and normalization to the water equilibrium magnetization yields a Z-spectrum as shown in b). b) Z-spectrum of egg white with different CEST pools indicated ($B_0 = 9.4$ T, $B_1^+ = 0.8$ μT and $t_{\text{sat}} = 10$ s).

Analytical Solution of the Bloch-McConnell Equations

McConnell (1958) expanded the Bloch equations (Subsection 2.1.3) to describe the temporal evolution of the magnetization with magnetization transfer between a solute pool s and a water pool w during a saturation RF pulse with offset frequency $\Delta\omega$ and amplitude $\omega_1 = \gamma B_1^+$. The frequency offset of each pool is $\Delta\omega_i = \Delta\omega - \delta\omega_i$ with $i = s, w$ and $\delta\omega_i$ refers to the chemical shift offset of pool i relative to water. The longitudinal and transverse relaxation rates of each pool are R_{1i} and R_{2i} , respectively. The exchange rates k_{sw} and k_{ws} characterize the forward ($s \rightarrow w$) and backward ($w \rightarrow s$) exchange between pool s and w (Figure 2.10), respectively. The equilibrium condition of this exchange is:

$$k_{sw}M_{0s} = k_{ws}M_{0w} \quad (2.93)$$

with the equilibrium magnetization M_{0w} and M_{0s} of pool w and s , respectively. With the use of the proton fraction $f_s = \frac{M_{0s}}{M_{0w}}$, Equation 2.93 simplifies to: $k_{ws} = f_s k_{sw}$. The Bloch

McConnell equations for magnetization transfer between two pools are:

$$\frac{dM_{xw}}{dt} = -\Delta\omega_w M_{yw} - R_{2w} M_{xw} + k_{sw} M_{xs} - k_{ws} M_{xw}, \quad (2.94)$$

$$\frac{dM_{yw}}{dt} = +\Delta\omega_w M_{xw} - R_{2w} M_{yw} - \omega_1 M_{zw} + k_{sw} M_{ys} - k_{ws} M_{yw}, \quad (2.95)$$

$$\frac{dM_{zw}}{dt} = +\omega_1 M_{yw} - R_{1w} (M_{zw} - M_{0w}) + k_{sw} M_{zs} - k_{ws} M_{zw}, \quad (2.96)$$

$$\frac{dM_{xs}}{dt} = -\Delta\omega_s M_{ys} - R_{2s} M_{xs} - k_{sw} M_{xs} + k_{ws} M_{xw}, \quad (2.97)$$

$$\frac{dM_{ys}}{dt} = +\Delta\omega_s M_{xs} - R_{2s} M_{ys} - \omega_1 M_{zs} - k_{sw} M_{ys} + k_{ws} M_{yw}, \quad (2.98)$$

$$\frac{dM_{zs}}{dt} = +\omega_1 M_{ys} - R_{1s} (M_{zs} - M_{0s}) - k_{sw} M_{zs} + k_{ws} M_{zw}. \quad (2.99)$$

This set of equations can be expanded to incorporate several solute pools, which exchange magnetization with the water pool.

The Bloch McConnell equations are a set of first-order linear differential equations, which can be analytically solved by an eigenspace approach [Zaiss et al. (2013a), Zaiss et al. (2013b) and Trott et al. (2002)]:

$$\vec{M}(t) = \begin{pmatrix} M_{xw} \\ M_{yw} \\ M_{zw} \\ M_{xs} \\ M_{ys} \\ M_{zs} \end{pmatrix} = \sum_{n=1}^6 e^{\lambda_n t} \vec{v}_n + \vec{M}^{ss}, \quad (2.100)$$

where λ_n and \vec{v}_n are the n th eigenvalue and eigenvector of the two pool magnetization vector $\vec{M}(t)$, respectively. \vec{M}^{ss} is the steady-state solution. In the case of a long saturation pulse $t_{\text{sat}} \gg T_{2w}$, the only remaining eigenvalue is $\lambda_1 = -R_{1\rho}$. $R_{1\rho}$ is the longitudinal relaxation rate in the rotating frame [Trott et al. (2002)]. The eigenvector \vec{v}_1 corresponding to the eigenvalue λ_1 is co-linear with the effective magnetic field $\vec{B}_{eff} = (B_1, 0, B_0 - \frac{\omega_{RF}}{\gamma})$. For a two pool system, $R_{1\rho}$ is the sum of the water relaxation rate R_{eff} and the exchange dependent relaxation rate R_{ex} :

$$R_{1\rho}(\Delta\omega) = R_{eff}(\Delta\omega) + R_{ex}(\Delta\omega). \quad (2.101)$$

Trott et al. (2002) provided an approximation of R_{eff} by:

$$R_{eff}(\Delta\omega) = R_{1w} \cos^2 \theta + R_{2w} \sin^2 \theta = R_{1w} + (R_{2w} - R_{1w}) \frac{\omega_1^2}{\omega_1^2 + \Delta\omega^2}. \quad (2.102)$$

$\theta = \arctan\left(\frac{\omega_1}{\Delta\omega}\right)$ is the angle between \vec{B}_{eff} and \vec{B}_0 . In summary, the water magnetization decays along the effective magnetic field in the rotating frame, while magnetization transfer pathways, e.g. chemical exchange or dipolar coupling, represent additional relaxation pathways for the water magnetization.

The analytical solution of the Z-spectrum after a continuous wave (cw) RF saturation pulse with t_{sat} and $\Delta\omega$ is:

$$Z(\Delta\omega, t_{sat}) = (Z_i \cos^2 \theta - Z^{ss})e^{-R_{1\rho} t_{sat}} + Z^{ss} \quad (2.103)$$

with the steady-state Z-magnetization

$$Z^{ss}(\Delta\omega) = \frac{R_{1w} \cos^2 \theta}{R_{1\rho}}. \quad (2.104)$$

Consequently, the initial Z-magnetization Z_i decays mono-exponentially with rate $R_{1\rho}$ to the steady state Z-magnetization Z^{ss} . Without an additional pool, the steady state solution of direct water saturation (DS) is given by:

$$Z_{DS}^{ss}(\Delta\omega) = \frac{R_{1w} \cos^2 \theta}{R_{eff}} = 1 - \frac{\Gamma_w^2/4}{\Gamma_w^2/4 + \Delta\omega^2}. \quad (2.105)$$

The FWHM of the Lorentzian-shaped function is $\Gamma_w = 2\omega_1 \sqrt{\frac{R_{2w}}{R_{1w}}}$. The exchange dependent relaxation rate R_{ex} can also be transformed into a Lorentzian-shaped function. For small solute pools $M_{0w} \gg M_{0s}$ the backward exchange rate k_{ws} is negligible. By assuming that $R_{1s} \ll R_{2s}$ and $R_{1s} \ll k_{sw}$, R_{ex} is given by a Lorentzian-shaped function in the large shift limit (LS) ($|\Delta\omega_s| \gg \omega_1$) [Zaiss et al. (2013a)]:

$$R_{ex}(\Delta\omega) = R_{ex}^{max} \frac{\Gamma_s^2/4}{\Gamma_s^2/4 + \Delta\omega_s^2} \quad (2.106)$$

with the FWHM

$$\Gamma_s = 2\sqrt{\frac{k_{sw} + R_{2s}}{k_{sw}} \omega_1^2 + (k_{sw} + R_{2s})^2}. \quad (2.107)$$

The maximum value of R_{ex} at $\Delta\omega = \delta\omega_s$ is:

$$R_{ex}^{max} = f_s k_{sw} \frac{\omega_1^2}{\omega_1^2 + k_{sw}(k_{sw} + R_{2s})} = f_s k_{sw} \alpha, \quad (2.108)$$

where α is the labeling efficiency. The labeling efficiency α , which is a measure for the saturation efficiency, assumes values between zero and one. In this thesis, the LS is valid, due to the high magnetic field of 9.4 T and the interest in the rNOE signal at -3.5 ppm.

Several pools exchange magnetization with the water pool *in vivo* via different magnetization transfer pathways (Figure 2.14b). To incorporate this into the analytical solution,

the two pool model can be expanded by assuming only small solute pool sizes and negligible magnetization exchange between the different solute pools, i.e. $k_{ij} = 0$ for $i, j \neq w$. Then, the longitudinal relaxation rate in the rotating frame is simply a sum of the different relaxation contributions:

$$R_{1\rho} = R_{eff} + \sum_i R_{ex,i}, \quad (2.109)$$

where $R_{ex,i}$ represents either ssMT, rNOE or CE. Consequently, the different magnetization transfer pathways add up inversely to the steady state Z-magnetization:

$$Z^{ss}(\Delta\omega) = \frac{R_{1w} \cos^2 \theta}{R_{eff} + \sum_i R_{ex,i}}. \quad (2.110)$$

A Taylor expansion of Equation 2.110 based on the assumption of small contributions of the different pools to the Z-spectrum yields:

$$Z^{ss}(\Delta\omega) \approx \frac{R_{1w} \cos^2 \theta}{R_{eff}} - \frac{\sum_i R_{ex,i}}{R_{1w}} \approx 1 - \mathcal{L}_w - \sum_i \mathcal{L}_i. \quad (2.111)$$

The last step of Equation 2.111 uses the approximation of R_{ex} by a Lorentzian-shaped function \mathcal{L} (Equation 2.106). A special case represents the ssMT contribution, as it was shown that depending on the tissue type also a Gaussian-shaped or super-Lorentzian function can describe ssMT [Henkelman et al. (2001)].

Z-spectrum Analysis

Figure 2.14b shows an exemplary Z-spectrum of egg white at 9.4 T with signal contributions from CE, rNOE, ssMT and DS. From this Z-spectrum, it is evident that the different signal contributions have a broad lineshape compared to NMR spectroscopy and partially overlap with each other. Therefore, for a quantitative Z-spectrum analysis, an isolation of CE and rNOE signals $R_{ex,i}$ from the contribution of DS R_{eff} and ssMT R_{ssMT} is necessary. The steady state Z-magnetization contains the different relaxation contributions in the denominator:

$$Z_{lab}^{ss}(\Delta\omega) = \frac{R_{1w} \cos^2 \theta}{R_{eff} + R_{ssMT} + \sum_i R_{ex,i}}. \quad (2.112)$$

With the use of a reference Z-spectrum Z_{ref}^{ss} , which contains only the contribution of DS and ssMT, an isolation of CE and rNOE signals is possible:

$$Z_{ref}^{ss}(\Delta\omega) = \frac{R_{1w} \cos^2 \theta}{R_{eff} + R_{ssMT}}. \quad (2.113)$$

Subsection 3.2.5 describes a method to obtain a reference Z-spectrum using Lorentzian fitting of DS and ssMT [Jones et al. (2013)]. The different relaxation contributions to the steady state Z-spectrum appear in the denominator of Equation 2.112. Consequently, an

inverse calculation of the magnetization transfer rate (MTR) yields an isolation of CE and rNOE signals [Zaiss et al. (2013b)]:

$$\text{MTR}_{\text{Rex}}(\Delta\omega) = \frac{1}{Z_{\text{lab}}^{ss}} - \frac{1}{Z_{\text{ref}}^{ss}} = \frac{\sum_i R_{ex,i}}{R_{1w} \cos^2 \theta}. \quad (2.114)$$

Multiplication of Equation 2.114 by R_{1w} , which removes the remaining weighting by R_{1w} , yields the apparent exchange-dependent relaxation (AREX) [Zaiss et al. (2014)]:

$$\text{AREX}(\Delta\omega) = R_{1w} \cdot \text{MTR}_{\text{Rex}} = \frac{\sum_i R_{ex,i}}{\cos^2 \theta}. \quad (2.115)$$

Besides the dependence on $\cos^2 \theta$, AREX completely isolates the contribution of CE and rNOE signals and therefore represents a quantitative parameter. The longitudinal relaxation time of water has to be determined in a separate NMR measurement using for example a saturation recovery pulse sequence (Subsection 3.2.3). The AREX metric was used in this thesis to calculate the rNOE CEST signal.

2.4 Proteins and Sodium in Biology

Not only the physical but also the biological properties of the sodium nucleus are attractive for a variety of biomedical NMR applications. Transient interactions of sodium ions with proteins results in bi-exponential relaxation and consequently a TQ signal. Proteins are the most abundant macromolecules in cells and perform a variety of different biological functions, e.g. transporting molecules and providing structure to organisms. In addition, cells also maintain a sodium concentration gradient across the cell membrane, which is crucial for the cell viability, as cells use this electrochemical energy for many transport processes.

The second method, used in this thesis, to investigate proteins by NMR utilizes magnetization transfer processes between non-exchanging aliphatic protons of proteins and water protons. This rNOE CEST signal is closely linked to the protein conformational state [Zaiss et al. (2013c), Goerke et al. (2015) and Goerke et al. (2017)]. Consequently, this rNOE signal can be a valuable diagnostic tool for non-invasive imaging of diseases associated with pathological changes in the protein expression, such as cancer and neurodegenerative diseases.

The first part of this section reviews briefly the structure of proteins and the influence of the biochemical environment on the protein structure. The second part outlines the sodium concentration gradient across the cell membrane and the physiological importance of sodium ions with a focus on the Na/K-ATPase. This section supports the understanding of the following experiments and is based on the books by Alberts et al. (2017), Heinrich et al. (2014) and Pape et al. (2019).

2.4.1 Proteins

Proteins occupy up to 35% of the cell volume [Brown (1991)] and are responsible for a variety of different biological functions. The building blocks of proteins are amino acids linked by peptide bonds and therefore proteins are also referred to as polypeptides. The sequence of amino acids represents the primary structure of proteins, while their full three-dimensional structure also involves covalent and non-covalent forces [Kumar et al. (2002)]. The native structure of proteins, which is crucial for their biological function, is only marginally stable. Changes in temperature or of the solvents can cause the denaturation of proteins, i.e. loss of their native structure. Unfolded proteins tend to form aggregates due to exposed hydrophobic regions. Furthermore, the protein concentration of a substantial number of proteins *in vivo* is higher than their solubility, which makes them prone to aggregation upon stress [Baldwin et al. (2011), Ciryam et al. (2015), Ciryam et al. (2013) and Kundra et al. (2017)]. Cells combat the toxic effects of denatured proteins by preventing, repairing and degrading denatured proteins [Richter et al. (2010) and Mogk et al. (2018)]. These control mechanisms become less reliable with age and consequently denatured proteins can cause diseases in different body regions. The most prominent diseases are neurodegenerative diseases, such as Alzheimer's disease.

Amino Acids with a Dissociable Side Chain Group

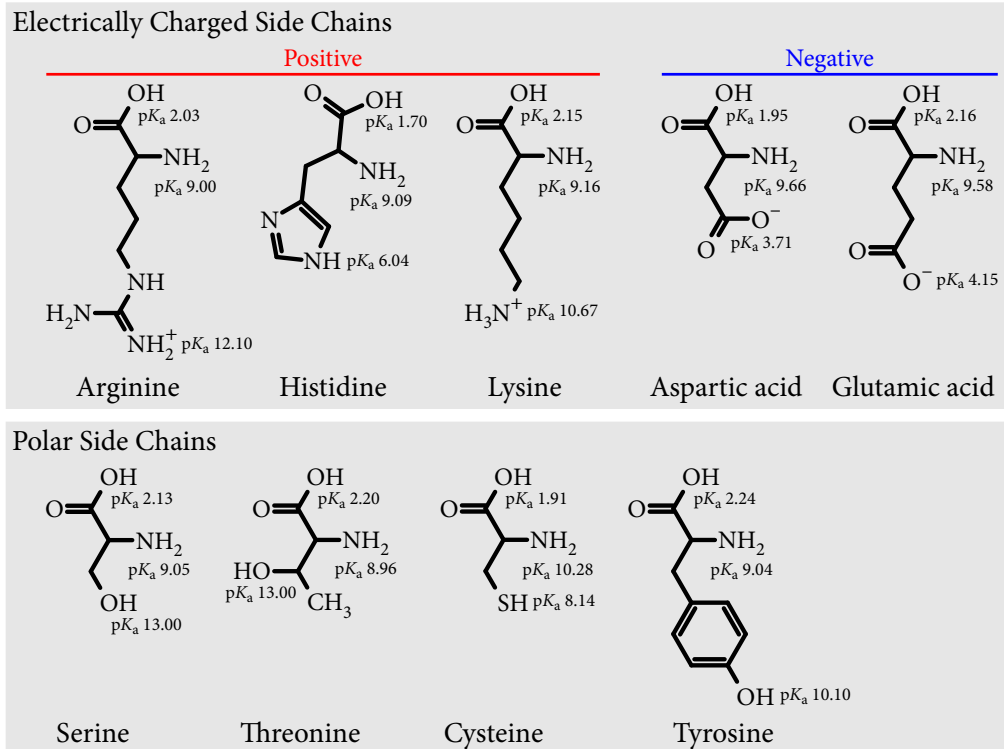


Figure 2.15: Amino acids with a dissociable side chain group and corresponding pK_a values at 25°C. This representation considers only the charge of the side chain groups, which are responsible for the charge of a protein, at a physiological pH of 7.4. It does not take into account the charge of the carboxyl and amine groups at the α -carbon atom. Only the carboxyl and amine groups at the ends of the polypeptide chain, i.e. N-terminus and C-terminus, contribute to the protein charge (Figure 2.17a). The pK_a values are from Haynes (2014).

Amino Acids

Twenty-two proteinogenic amino acids make up the building blocks of proteins. An amino acid consists of an amine group (NH_2), a carboxyl group (COOH) and a side chain group (R group) attached to an α -carbon atom. The α -carbon atom refers to the first carbon atom attached to the carboxyl group. The side chain group determines the physicochemical properties of the amino acids and of proteins, for example charge and hydrophobicity. The charged side chains in proteins are of particular interest as the interaction of sodium ions with these charged side chains contribute to the sodium TQ signal (Figure 2.15). The amino acids in proteins are connected by covalent bonds between the amine and carboxyl groups. Therefore, only the amine and carboxyl groups at the ends of the polypeptide chain carry a charge and contribute to the sodium TQ signal (Figure 2.17a). The charge of a dissociable group of an amino acid depends on its acid dissociation constant pK_a and the pH value. This acid dissociation constant represents the equilibrium constant for the acid-base reaction between an acid and its conjugate base,

for example COOH and COO^- , respectively. The concentration of the acid and the conjugate base depend on the pH value. If $\text{pH} = \text{p}K_a$ the concentration of the acid and its conjugate base are the same. The following paragraphs describe the pH value and the acid dissociation constant in more detail.

Water has a slight tendency to dissociate into hydroxide ions (OH^-) and hydronium ions (H_3O^+), for instance $2\text{H}_2\text{O} \rightleftharpoons \text{OH}^- + \text{H}_3\text{O}^+$. The thermodynamic equilibrium constant for this autodissociation of water equals

$$K_W = K \cdot [\text{H}_2\text{O}]^2 = [\text{H}^+] \cdot [\text{OH}^-]. \quad (2.116)$$

K_W is the ionic product of water, squared brackets indicate concentrations in $\frac{\text{mol}}{\text{L}}$ and H^+ refers to the hydronium ions. The concentration of hydroxide and hydronium ions in pure water at 25°C equals $10^{-7} \frac{\text{mol}}{\text{L}}$. To characterize such low concentrations, S. P. L. Sørensen (1909) introduced the pH value, which is the negative base 10 logarithm of the hydronium concentration, i.e. $\text{pH} = -\log[\text{H}^+]$. Consequently, a higher hydronium concentration results in a lower pH value and vice versa. For pure water, the pH value corresponds to 7. It is important to note that a pH reduction by one increases the hydronium concentration tenfold. Molecules, which are acids or bases, alter the pH value. Acids donate protons, while bases accept protons. The acid-base reaction between an acid HA and a base H_2O is $\text{HA} + \text{H}_2\text{O} \rightleftharpoons \text{A}^- + \text{H}^+$ with the conjugate base A^- . Similar to the ionic product of water, a dissociation constant for this reaction can be defined

$$\text{p}K_a = -\log\left(\frac{[\text{H}^+] \cdot [\text{A}^-]}{[\text{HA}]}\right). \quad (2.117)$$

The temperature-dependent dissociation constant is a scale for the strength of an acid, i.e. the smaller the $\text{p}K_a$ value the stronger the acid. Hence, bases are weak acids which have a large $\text{p}K_a$ value (Figure 2.15). For example, HCl is a strong acid with a $\text{p}K_a = -6.3$, while the carboxyl and amine groups of amino acids are weak acids, see Figure 2.15 for a range of $\text{p}K_a$ values. For a weak acid, the Henderson-Hasselbalch equation links the concentration of an acid HA and the conjugate base A^- to the pH value according to

$$\text{pH} = \text{p}K_a + \log\left(\frac{[\text{A}^-]}{[\text{HA}]}\right). \quad (2.118)$$

The concentrations of both compounds are the same if $\text{pH} = \text{p}K_a$. The fraction of positive charge Q^+ or negative charge Q^- of a dissociable group can be derived from the Henderson-Hasselbalch equation [Moore (1985)]:

$$Q^\pm = \frac{1}{1 + 10^{\pm(\text{pH} - \text{p}K_a)}}. \quad (2.119)$$

The net charge of an amino acid or peptide is then simply the sum of all fractions of positively and negatively charged groups (Figure 2.16). The $\text{p}K_a$ values shown in Figure 2.15 are only valid for free amino acids. In proteins, the $\text{p}K_a$ values of dissociable groups depend on the protein structure, such as the location of an amino acid within the protein,

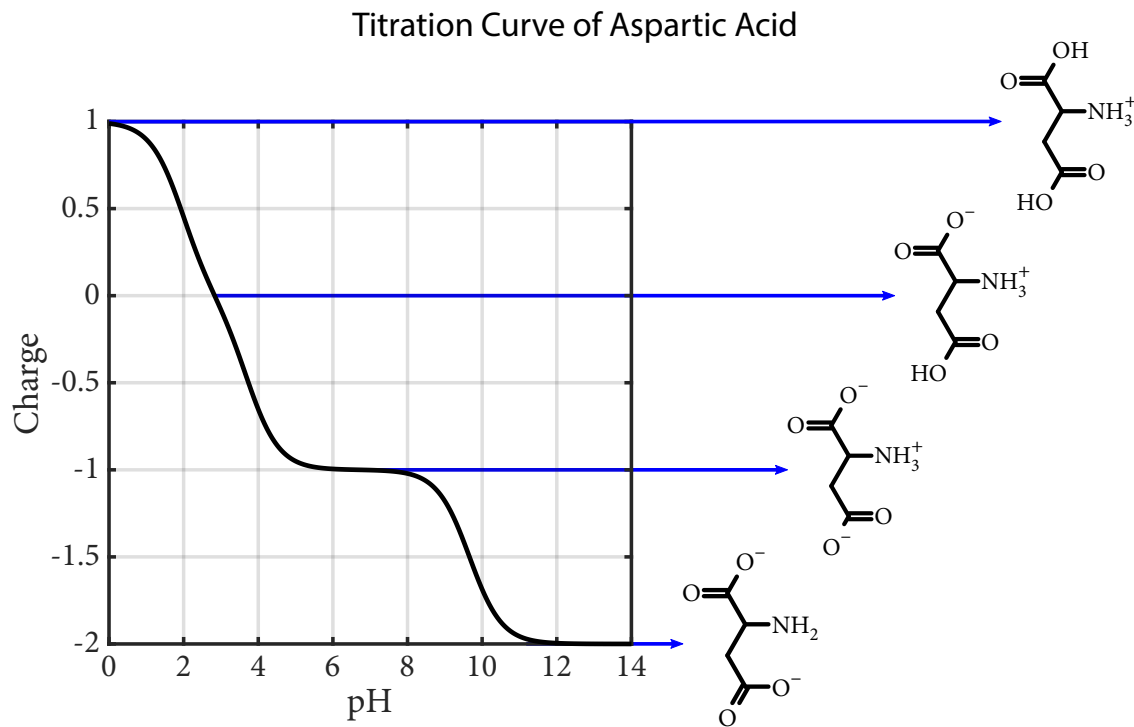


Figure 2.16: The net charge of aspartic acid for the pH range of 0.0 to 14.0 according to Moore (1985). The pK_a of the dissociable groups are: $pK_a(\text{COOH}) = 1.95$, $pK_a(\text{R} - \text{COOH}) = 3.71$ and $pK_a(\text{NH}_3^+) = 9.66$. A titration curve represents the change in the net charge of a molecule against the pH value. At physiological pH, aspartic and glutamic acid are responsible for the negative charge of proteins (Figure 2.15).

and the surrounding charged groups [Kauzmann (1959) and Grimsley et al. (2009)]. At physiological pH, proteins are negatively charged due to the side chains of aspartic and glutamic acid (Figure 2.15). The charge of amino acid side chain groups, which determine the net charge of a protein, depends on pH. Consequently, the sodium TQ signal may also depend on pH, as interactions of sodium ions with negatively charged groups of proteins contribute to the TQ signal. The investigation of the TQ signal dependence on pH was part of this thesis.

Structure of Proteins

Proteins are macromolecules, which are essential constituents in every process of an organism. Consequently, the function of proteins covers a wide range. Proteins with mechanical or structural functions, like actin and myosin, provide a scaffold for the cytoskeleton and enable cells to migrate. Enzymes, another type of protein, act as catalysts, which means that they accelerate chemical reactions. Yet, other proteins within the cell membrane are responsible to transport solutes across the membrane and to receive chemical signals from the extracellular space. The specific biological function of a protein is linked to their native three-dimensional structure, which the following paragraphs describe.

A protein consists of a chain of covalently bonded amino acids. Hence, proteins are polypeptides and the repeating sequence of atoms along the polypeptide chain excluding the amino acid side chains represents the polypeptide backbone. The sequence of amino acids and the corresponding three-dimensional protein structure determine the biological function of a protein. Mainly responsible for the protein structure are four types of weak non-covalent bonds: hydrogen bonds, electrostatic interactions, van der Waals interactions and hydrophobic effects. Many of these weak bonds contribute to the marginally stable native protein structure, which corresponds to the lowest free energy. This native conformation is only a few hydrogen bonds lower in energy compared to other conformational states. The protein structure can be classified according to (Figure 2.17):

- **Primary structure** is the sequence of amino acids. A peptide bond connects the carboxyl group of the α -carbon atom of an amino acid with the amide group of the α -carbon atom of the neighboring amino acid. Therefore, the polypeptide backbone sequence corresponds to $\text{H}_3\text{N}^+ - \text{C}_\alpha\text{HR} - \text{CO} - [\text{NH} - \text{C}_\alpha\text{HR}_i - \text{CO}]_n - \text{O}^-$. The amino acid sequence determines the physicochemical properties of the protein and contains all the information needed for specifying the three-dimensional structure. The synthesis of proteins consumes up to 2% of the ATP produced in the rat brain [Engl et al. (2015)].
- **Secondary structure** constitutes hydrogen bonds between NH and CO groups of the polypeptide backbone. The most common secondary structure elements are α helices and β sheets (Figure 2.17b). In the α helix pattern, elements of the polypeptide chain twist around itself to form a rigid cylinder. β sheets are neighboring segments of the polypeptide chain, which run either in the same or in the opposite direction.
- **Tertiary structure** is the folding of the secondary structure elements to a compact three-dimensional conformation (Figure 2.17c). The main contribution to the compact tertiary protein structure is the hydrophobic effect. The hydrophobic effect results in the burial of hydrophobic side chains, which minimizes the exposure to water, into the protein core. In addition, non-covalent bonds such as electrostatic interactions, hydrogen bonds and van der Waals interactions further stabilize the three-dimensional protein structure. Also covalent bonds, disulfide bonds, contribute to the stability of the three-dimensional protein structure.
- **Quaternary structure** is the assembly of several polypeptide chains to build one functional unit, which are also called oligomeric proteins (Figure 2.17d). The same non-covalent and covalent interactions as in the tertiary structure stabilize these oligomeric proteins. An example of an oligomeric protein is hemoglobin.

Additional to these four structures, proteins can also consist of different domains. A protein domain is a part of the polypeptide chain that can fold independently from the rest of the polypeptide chain into a compact and stable structure. To secure the proper folding of proteins in the crowded intracellular environment, cells contain special proteins,

molecular chaperones [Richter et al. (2010)]. These chaperones assist partly folded proteins to obtain their native structure and therefore to prevent the formation of protein aggregates. These quality control mechanisms degrade with age, which occasionally permits the formation of protein aggregates. This can cause diseases in different tissues, such as neurodegenerative diseases.

Denaturation of Proteins

Except for intrinsically disordered proteins [Wright et al. (2015)], the three-dimensional structural integrity of proteins is crucial for their characteristic biological function. Protein denaturation means the loss of the native protein structure and therefore the loss of the biological function. Protein denaturation can be classified into two different processes:

- **Unfolding** of proteins refers to the disruption of the secondary, tertiary and quaternary structure. This includes the disruption of all non-covalent and covalent bonds responsible for these three types of structures. In addition, the hydrophobic protein core becomes exposed to the aqueous phase.
- **Aggregation** of proteins describes the accumulation and clumping of unfolded proteins. Unfolded proteins expose the hydrophobic protein core to the aqueous phase, which results in the attraction to hydrophobic parts of other unfolded proteins. This hydrophobic force then causes the clumping of proteins to form larger macromolecular structures, i.e. oligomer.

Neither of the two processes changes the primary structure of proteins. The denaturation of proteins can result from the exposure to e.g. heat, detergents and extreme pH values. The stability of the native protein structure and the contribution of the different bonds to the native protein structure influence the sensitivity to protein denaturation by heat or pH.

There are a variety of different diseases associated with misfolded and aggregated proteins [Dobson (2002)]. The most prominent diseases are neurodegenerative diseases, like Alzheimer's disease and Parkinson's disease. Nevertheless, there are also non-neurological diseases, for example type 2 diabetes and inherited cataract. The rNOE CEST signal, which depends on the protein folding state, could be a promising non-invasive diagnostic tool for such diseases. However, the detectability of protein denaturation processes on a physiological relevant scale remains to be verified, which was part of this thesis.

Molecular Chaperones

Heat represents a major stressor for cells, as proteins are evolutionary optimized to be only marginally stable at the respective growth temperature [Richter et al. (2010) and Mogk et al. (2018)]. Furthermore, a substantial number of proteins *in vivo* is prone to aggregation upon stress, as their concentration is higher than their solubility [Baldwin et al. (2011), Ciryam et al. (2015), Ciryam et al. (2013) and Kundra et al. (2017)]. Consequently, a small

increase in temperature can cause protein unfolding and subsequent aggregation. To prevent the formation of protein aggregates and combat the toxic effects thereof, cells can transiently overexpress molecular chaperones. Under normal conditions, these molecular chaperones, which are themselves proteins, bind to hydrophobic regions of other partly folded proteins. By doing so, molecular chaperones assist the partly folded proteins in obtaining their native protein structure. Furthermore, it prevents the formation of intermolecular protein aggregates caused by hydrophobic effects. During stressful conditions, molecular chaperones keep unfolded proteins soluble, actively refold them or dissolve protein aggregate deposits to allow their refolding [Balchin et al. (2016)]. In principle, cells can also degrade misfolded and aggregated proteins. Notably, cells even refold severely aggregated proteins instead of degrading them, as the synthesis of new proteins is an energy consuming process and refolding proteins will save cellular resources [Wallace et al. (2015) and Mogk et al. (2018)].

CEST Signals of Proteins

To study proteins by CEST, it is important to know the underlying chemical groups contributing to the CEST signals. Proteins consist of covalently bonded amino acids. Hence, assignment of ^1H chemical shifts to chemical groups of amino acids provides a qualitative understanding of chemical groups contributing to the CEST signals. Figure 2.18 visualizes chemical shifts of amino acids, which are assigned to chemical groups of amino acids in Table 2.3. These chemical shifts are valid for amino acids and random coil regions of proteins. In general, the ^1H chemical shifts depend on the chemical environment, e.g. polarity and charge of the amino acid, and environmental factors, like pH. In proteins, neighboring amino acids also influence the chemical shifts of identical chemical groups, which causes a dispersion of signals in the NMR spectrum.

In principle, all chemical groups listed in Table 2.3 can contribute to the CEST signals. Protons attached to nitrogen transfer magnetization by chemical exchange, while protons attached to carbon yield rNOE signals (Subsection 2.3.1). Of particular interest are the amid signal at $\Delta\omega = 3.5$ ppm of nitrogen-bonded protons in the polypeptide backbone, $\text{NH}(\text{bb})^*$, and the rNOE signal at $\Delta\omega = -3.5$ ppm of aliphatic protons. Both signals depend on the protein folding state [Goerke et al. (2015) and Goerke et al. (2017)] and have been shown to provide valuable information for various neuro-oncological questions, like treatment response assessment [Meissner et al. (2019)] and differentiation of histologic and genetic subtypes of glioma [Paech et al. (2019)].

2.4.2 Physiological Role of Sodium

The lipid bilayer cell membrane prevents the diffusion of charged molecules and ions between the intra- and extracellular space. While hydrophobic molecules and dissolved gases pass through the cell membrane with their usual diffusion speed, uncharged polar molecules are slowed down by the hydrophobic part of the cell membrane. Specialized membrane transport proteins transport ions and uncharged polar molecules across the

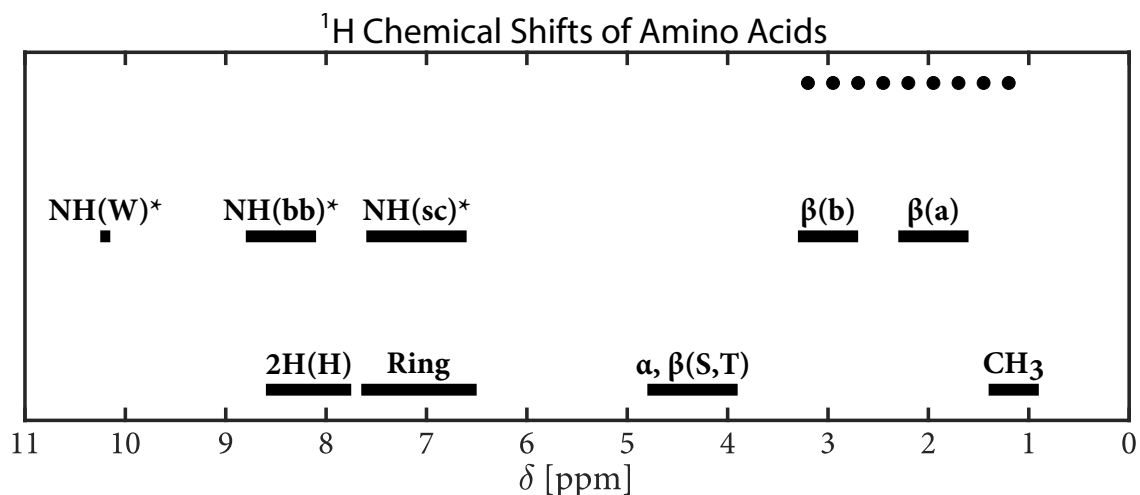


Figure 2.18: Visualization of ^1H chemical shifts of amino acids listed in Table 2.3. The water resonance frequency equals 4.7 ppm, which is set to 0 ppm in CEST experiments. These chemical shifts are valid for amino acids and random coil regions of proteins. Adapted from Wüthrich (1986).

Table 2.3: ^1H chemical shifts of amino acids.

Code	Chemical group	δ [ppm]	Amino acids
CH_3	CH_3	0.9–1.4	A, V, T, L, I, M
$\beta(\text{a})$	C^βH	1.6–2.3	V, I, L, E, Q, M, P, R, K
$\beta(\text{b})$	C^βH	2.7–3.3	C, D, N, F, Y, H, W
•••	other aliphatic CH	1.2–3.3	...
$\alpha, \beta(\text{S, T})$	$\text{C}^\alpha\text{H}, \text{C}^\beta\text{H}$	3.9–4.8	S, T
Ring	aromatic CH	6.5–7.7	F, Y, W, C^4H of H
2H(H)	aromatic CH	7.7–8.6	C^2H of H
$\text{NH}(\text{sc})^*$	side chain NH_x	6.6–7.6	N, Q, K, R
$\text{NH}(\text{bb})^*$	NH	8.1–8.8	backbone
$\text{NH}(\text{W})^*$	indole NH	10.2	W

A visualization of these chemical shifts is provided by Figure 2.18. The asterisk * indicates chemical exchanging protons. Amino acids are abbreviated by their one letter code. The values are from Wüthrich (1986).

cell membrane. These transport proteins are thereby selective to only a specific molecular species or a class of molecules, like ions. The two major classes of membrane transport proteins are transporters and channels. Transporters bind the solutes and transport

them during conformational changes across the membrane. In contrast to transporters, channels are gated, continuous pores across the membrane. The passing through channels is passive, which means that the concentration gradient and the electric potential difference across the membrane drive the transport. Cells are also able to pump solutes against their electrochemical gradient, which requires a source of energy. Such transporters are ATP-driven pumps and coupled transporters.

The most well-known ATP-driven pump is the Na/K-ATPase. This pump uses the energy of the hydrolysis of one ATP molecule to drive three sodium ions out of the cell and two potassium ions into the cell against their electrochemical gradient. The continuous pumping establishes a sodium and potassium concentration gradient across the cell membrane. The intra- and extracellular sodium concentrations correspond to 5–15 mM and 135–145 mM, respectively. On the other hand, the intra- and extracellular potassium concentrations are equal to 140 mM and 5 mM, respectively. This pumping process also contributes 5–10 mV to the negative electric membrane potential. However, the largest contribution to the electric potential is due to passive ion movements. Inside the cell, the abundant potassium ions balance the fixed negative charged inorganic anions. Through potassium leak channels, potassium ions can move freely and come close to their equilibrium potential of -89 mV. Consequently, the resting membrane potential of an animal cell varies between -20 mV and -120 mV, which is close to the equilibrium potential of potassium [Alberts et al. (2017)].

Coupled transporters harness the electrochemical energy of one solute to transport another solute against their electrochemical gradient. In many animal cells, this energy originates from the sodium electrochemical gradient established by the Na/K-ATPase. Cells use these coupled transporters to transport, e.g. ions and nutrients, across their membrane. For example, the sodium glucose transporter builds up a high intracellular glucose concentration despite a low extracellular concentration. Further coupled transporters transport amino acids and neurotransmitters into the cell, while other transporters remove protons and calcium ions from the cell. In general, the active transport of solutes is a rather slow process, for example the Na/K-ATPase has a turnover rate of a few hundreds per second [Gadsby (2009)]. However, a single cell expresses a few million Na/K-ATPases, which consume between one third and two thirds of the produced cellular energy [Clausen et al. (2017)]

In contrast to these transporters, the diffusion through ion channels is due to the electrochemical gradient of a specific ion. Consequently, these ion channels have a high turnover rate of 10^6 – 10^8 ions per second. However, they are only in an open state for a few milliseconds up to seconds [Alberts et al. (2017)]. For instance, sodium channels are crucial for the excitability of muscle cells and for the electric signaling in the nervous system. In general, the expression of ion channels depends on the transported ion and the cell, for instance mammalian heart cells express more than 100 000 sodium channels [Marban et al. (1998)].

A breakdown of the energy supply causes a failure of the Na/K-ATPase. This leads to an influx of sodium ions and an efflux of potassium ions. The influx of sodium ions results in a depolarization of the cell and shifts the membrane potential to positive values. The latter causes an influx of chloride ions. This further increases the intracellular osmolarity, which results in an influx of water and consequently in cell swelling. A failure of the Na/K-ATPase can also be induced by drugs, such as cardiac glycosides, which are used in the treatment of heart diseases [Clausen et al. (2017)].

In summary, the sodium concentration gradient is crucial for the transport of nutrients and ions across the cell membrane and therefore tightly connected with e.g. the cytosolic pH and the cell volume. Both an energy deficit and an increased membrane permeability result in an influx of sodium ions and therefore a reduced cell viability. Consequently, the cell viability is linked to the sodium concentration gradient and alterations thereof reflect the early onset of pathophysiological changes.

3 Materials and Methods

This chapter has four sections. Section 3.1 introduces the experimental setup including the NMR scanner with the RF coils, the model systems and the MR-compatible bioreactor system. Section 3.2 describes the MR pulse sequences, such as the TQ and CEST pulse sequences, and the corresponding methods for data analysis. Section 3.3 outlines the fluorescence measurements for the verification of urea-induced unfolding of BSA. Section 3.4 explains the utilized methods for the quantification of fluorescence and MR signals. Parts in this chapter have been published in Kleimaier et al. (2020c)¹ by John Wiley & Sons, Kleimaier et al. (2020f)² by MDPI, and Kleimaier et al. (2020e)² by Springer Nature and the description of the corresponding materials and methods is replicated here.

3.1 Experimental Setup

This section describes the NMR scanner (Subsection 3.1.1) with the RF coils (Subsection 3.1.2) followed by the model systems (Subsection 3.1.3) and the MR-compatible bioreactor system (Subsection 3.1.4).

3.1.1 Preclinical NMR Scanner

All experiments were performed at a 9.4 T preclinical NMR system (Bruker BioSpec 94/20, Ettlingen, Germany), see Figure 3.1a. At this magnetic field strength, the Larmor frequency of ¹H and ²³Na correspond to $\omega_0 = 400.31$ MHz and $\omega_0 = 105.89$ MHz, respectively. The NMR system is actively shielded and has a bore size of 116 mm including the gradient coils. These gradient coils provide a maximum gradient strength of $706 \frac{\text{mT}}{\text{m}}$ within the default gradient rise time of 122 μs in all directions. The NMR scanner has an integrated shim set up to 2nd order. For X-nuclei measurements, the NMR system has multiple bandpass filters, which are selective to a range of Larmor frequencies. The ²³Na bandpass filter has a frequency range of 70–125 MHz. The animal bed can be heated by an external water bath.

3.1.2 RF Coils

RF coils can be characterized according to volume and surface coils. Volume coils have the advantage that they provide a homogeneous transmit and receive field. However, the large distance between the volume coil and the measurement object results in a reduced

¹©2020 The Authors. NMR in Biomedicine published by John Wiley & Sons Ltd

²Creative Commons Attribution 4.0 International License:

<https://creativecommons.org/licenses/by/4.0/>

9.4 T NMR Scanner and RF Coils



Figure 3.1: a) 9.4 T preclinical NMR system with the used ^{23}Na and ^1H RF coils in b)–h). b) ^1H Bruker 4-channel rat receiver surface array; c) ^1H Bruker quadrature birdcage coil; d) ^{23}Na in-house built surface coil; e) $^1\text{H}/^{23}\text{Na}/^{39}\text{K}$ Bruker volume coil; e) linear polarized $^1\text{H}/^{23}\text{Na}$ Bruker volume coil; f) $^1\text{H}/^{23}\text{Na}$ Rapid quadrature birdcage coil; h) ^{23}Na Rapid receive-only surface coil.

signal sensitivity and consequently a loss in SNR. On the other hand, surface coils have an inhomogeneous transmit and receive field, but have a higher signal sensitivity due to the short distance between the surface coil and the measurement object. To obtain a high signal sensitivity in combination with a homogeneous transmit field, a volume coil can be combined with a receiver surface array.

These differences in the coil setups influence the measured MR signal. Deviations in the transmit field B_1^+ result in a loss of the TQ signal due to the strong dependence on the flip angle (Subsection 2.2.7). In addition, the low sodium SNR requires a high signal sensitivity of a surface coil. To maximize signal sensitivity and minimize B_1^+ inhomogeneity, a volume coil combined with a surface coil is necessary. Such an RF coil setup for ^{23}Na was only available at a later stage of the doctorate studies. Hence, the experiments with model solutions were performed only with a ^{23}Na volume coil to minimize B_1^+ inhomogeneity. For the experiments with the MR-compatible bioreactor system, a ^{23}Na surface coil was used to maximize the signal sensitivity. In CEST experiments, B_1^+ deviations cause different levels of saturation, which affects the SNR of CEST signals and the CEST-image contrast [Windschuh et al. (2015)]. The ^1H CEST measurements were performed using a volume coil combined with a surface coil. The following paragraphs describe in detail the used RF coils.

In all experiments with the model solutions BSA and 5% w/w agarose (Subsection 3.1.3), the linear polarized $^1\text{H}/^{23}\text{Na}$ Bruker volume coil was used (Figure 3.1f). This RF coil has an inner diameter of 72 mm and the length of the ^{23}Na coil is 100 mm. The length of the ^{23}Na 90° RF pulse was in the range of 125–135 μs for an RF power of 690 W. Figure A.1 shows two exemplary ^{23}Na B_1^+ maps for the two sample sizes of 8 and 10 ml. For these samples, the B_1^+ deviation was less than 7.2%.

For the comparison of both TQTPPI pulse sequences (Subsection 3.2.4), the $^1\text{H}/^{23}\text{Na}/^{39}\text{K}$ Bruker volume coil was used (Figure 3.1e). The ^{23}Na birdcage coil has an inner diameter of 40 mm and a length of 43 mm. For the samples with an agarose concentration of 2–6% w/v, the length of the ^{23}Na 90° RF pulse was in the range of 42.0–44.0 μs for an RF power of 690 W.

The RF coil setup of the $^1\text{H}/^{23}\text{Na}$ Rapid (Rapid Biomedical GmbH, Rimpfing, Germany) quadrature birdcage volume coil (Figure 3.1f) combined with the ^{23}Na Rapid receive-only surface coil (Figure 3.1h) was employed for the sodium TQ measurements of amino acids (Subsection 3.1.3). Only the ^{23}Na volume coil is actively decoupled. This volume coil has an inner diameter of 72 mm and the length of the ^{23}Na coil is 103 mm. The ^{23}Na receive-only surface coil has a single loop with a diameter of 30 mm. The length of the ^{23}Na 90° RF pulse was in the range of 130–140 μs for an RF power of 690 W. This RF coil setup is optimized for sodium TQ measurements with the MR-compatible bioreactor system and will replace the ^{23}Na transmit and receive in-house built surface RF coil in future bioreactor experiments (Figure 3.1d). The ^{23}Na in-house built surface coil was used for all sodium TQ measurements with the MR-compatible bioreactor system (Subsection 3.1.4). This single

loop RF coil has a diameter of 35 mm. The length of the ^{23}Na 90° RF pulse was in the range of 56–61 μs for an RF power of 80 W.

In the CEST experiments with the MR-compatible bioreactor system (Subsection 3.1.4), a ^1H Bruker quadrature birdcage volume coil was combined with a ^1H Bruker 4-channel rat receiver surface array. The volume coil has an inner diameter of 72 mm. The length of the ^1H 90° RF pulse was in the range of 48–52 μs for an RF power of 600 W. In the MR-compatible bioreactor system, the B_1^+ deviation was less than 2% across the entire cell culture (Figure A.2).

3.1.3 Model Systems

This section describes the used model systems in respect to their purpose and formulation. The main purpose of these model systems was to obtain a deeper understanding of the sodium TQ signal origin and its capability to serve as a potential biomarker.

Agarose

Agarose is a polysaccharide, which forms a self-supporting gel after heating and subsequent cooling. Low agarose concentrations are already sufficient to cause bi-exponential transverse relaxation for sodium. The validity of this model system is based on the fact that agarose samples can resemble *in vivo* relaxation times of sodium [Andrasko (1974), Nagel et al. (2016) and Schepkin et al. (2017)]. In addition, interactions of sodium ions with negatively charged hydroxyl groups of agarose result in a large sodium TQ signal, which is larger, but still comparable to the *in vivo* sodium TQ signal [Schepkin et al. (2017)]. Consequently, agarose represents a suitable tissue model system for the *in vivo* sodium TQ signal. The following paragraphs describe the formulation of the agarose samples for the respective experimental series.

A small 10 ml phantom (diameter = 28 mm and length = 30 mm) of 5% w/w agarose and 154 mM NaCl was used to investigate the influence of B_0 inhomogeneity on the sodium TQ signal despite a 180° refocusing RF pulse. This small sample size minimizes flip angle deviations as it covers only the homogeneous transmit field of the $^1\text{H}/^{23}\text{Na}$ Bruker volume coil. The agarose sample was prepared in a previous thesis [Kropp (2019)].

For the comparison of the standard TQTPPI pulse sequence with the fixed TQTPPI pulse sequence (Subsection 3.2.4), three 35 ml samples (diameter = 28 mm and length = 75 mm) with [2, 4, 6]% w/v agarose in 134.75 mM NaCl were used. These agarose samples were also prepared in a previous thesis [Hu (2019)]. In these experiments, the $^1\text{H}/^{23}\text{Na}/^{39}\text{K}$ Bruker volume coil was used.

Amino Acids

Proteins, which are the most abundant components of cells [Brown (1991)], consist of covalently bonded amino acids and provide the most important interaction sites leading to a sodium TQ signal. As outlined in Subsection 2.4.1, changes in pH alter the availability of negatively charged groups of amino acids (Figure 2.16). Consequently, the sodium TQ signal, which arises in the interaction of sodium ions with negatively charged groups of macromolecules, can also depend on pH. The investigation of the pH dependence of the sodium TQ signal was part of this thesis. The model system composed of different amino acids was used to investigate if the presence of negatively charged groups of amino acids is already sufficient to yield a sodium TQ signal. If amino acids yield a sodium TQ signal, a possible change in the sodium TQ signal with pH can be correlated with the change in the availability of negatively charged groups (Figure 2.16). A change in the sodium TQ signal of a protein with pH cannot be correlated with the availability of negatively charged groups, as the pK_a values of negatively charged groups depend on the location within the protein and the surrounding charged groups [Kauzmann (1959) and Grimsley et al. (2009)].

The phantoms consisted of one of three different amino acids up to their highest concentration dissolvable in water: L-glutamic acid, L-arginine or L-lysine hydrochloride. To yield a high pH value, which maximizes the availability of negatively charged groups, all

Table 3.1: Composition of the phantoms containing amino acids.

Amino acid	$c_{\text{amino acid}}$ [M]	c_{NaOH} [mM]	pH
Glutamic acid	0.05	154	12.50
	0.25		12.72
Arginine	0.50	154	12.68
	0.75		12.62
	0.90		12.64
	1.00		8.43
Lysine	1.50	154	8.14
	2.00		7.96
	2.50	616	8.74
		154	7.85
	2926	616	8.65
		2926	10.01

phantoms unless specified otherwise were prepared in 154 mM NaOH. Some phantoms composed of lysine contained a higher concentration of NaOH to further increase the pH value. Table 3.1 lists the composition of all phantoms containing amino acids. All phantoms had a size of 15 ml with a diameter of 14 mm and a length of 115 mm. For these measurements, the $^1\text{H}/^{23}\text{Na}$ Rapid quadrature birdcage coil combined with the ^{23}Na Rapid receive-only surface coil was used.

Bovine Serum Albumin

Bovine serum albumin (BSA) is a serum albumin protein extracted from cow blood. Albumin proteins bind to several organic compounds including fatty acids, ions and hormones. The main biological function of an albumin protein is the regulation of colloidal osmotic blood pressure. BSA is often used as a biological concentration standard. BSA represents a suitable model system, as it has been widely studied and is available in high purity. In addition, BSA has a well-known protein structure with a relatively large amino acid chain length of 583. To be a suitable model system for sodium TQ experiments, the correlation time, electric quadrupole coupling constant and the number of negatively charged groups is of importance. The number of negatively charged carboxyl groups is 100, due to 59 glutamic acid side chains, 40 aspartic acid side chains and one carboxyl-terminus. In addition, the 35 cysteine and 20 tyrosine side chains can also carry a negative charge at high pH values (Figure 2.15). Interactions of sodium ions with negatively charged groups of BSA result in a strong sodium TQ signal despite a weak affinity of BSA for sodium ions [Carr (1956), Torres et al. (2005) and Chung et al. (1990)]. Furthermore, Rooney et al. (1991b) showed that the correlation time and the electric quadrupole coupling constant are very similar to the yeast protoplasm.

In summary, BSA is a suitable model system for sodium TQ experiments to investigate a possible sodium TQ signal dependence on the pH value and the protein folding state. For all measurements, the $^1\text{H}/^{23}\text{Na}$ Bruker volume coil was used. The sample sizes were 8 ml (diameter = 16 mm and length = 40 mm) for all experiments except for the unfolding experiments, which had a sample size of 10 ml (diameter = 16 mm and length = 50mm). The following paragraphs describe the formulation of the samples containing BSA and provide a motivation for each experimental series.

In rat liver cell microsomes [Sanui et al. (1959)], and in human and dog erythrocyte ghosts [Sanui et al. (1962) and Sanui et al. (1963)], it has been demonstrated that the addition of potassium ions reduces the amount of bound sodium ions relative to the amount of bound sodium ions in the absence of potassium ions. In accordance with these studies, Schepkin et al. (2017) showed a reduction in the sodium TQ signal upon addition of KCl to agarose samples. Consequently, it is expected that the sodium TQ signal of BSA may decrease upon the addition of potassium. To determine a possible competitive binding effect of sodium ions with potassium ions in BSA samples, 8 samples with 10% w/v BSA with [0, 10, 25, 50, 75, 100, 125, 145] mM KCl in 145 mM NaCl were prepared. The pH of these samples was 6.92.

At higher pH values, the availability of negatively charged groups of macromolecules increases, while at lower pH values it decreases (Subsection 2.4.1). The alteration of negatively charged groups by pH results in a changed affinity of proteins for cations [Carr (1956), Pfister et al. (1964) and Saroff (1957)]. In accordance with these studies, Hutchison et al. (1990) observed a change in sodium DQ signal from BSA in solution with a pH range of 5 to 8. It is expected that not only DQ signal but a sodium TQ signal originating during electric-quadrupole interactions between proteins and sodium ions can also depend on pH. To investigate a possible pH dependence of the sodium TQ signal, 24 samples contained 10% w/v BSA and 154 mM Na⁺. These samples had non-equidistantly distributed pH values in the range of 0.70 to 13.05. To increase the pH value of the sample, a portion of the solution containing 154 mM NaCl in distilled water was replaced by an alkaline solution containing 154 mM NaOH. To decrease the pH value of the sample, a portion of the saline solution was replaced by an acidic solution containing 100 mM HCl and 154 mM NaCl.

The 3D structural integrity of proteins is a fundamental part of their biological function. Unfolding of proteins results in the disruption of the tertiary and secondary protein structure and in the exposure of the hydrophobic protein core to the aqueous phase (Subsection 2.4.1). This can increase the availability of negatively charged groups and consequently affect the sodium TQ signal. Unfolding of BSA was induced by urea, which does not induce the formation of immobile solid-like structures [Zaiss et al. (2013c)]. To investigate a possible sodium TQ signal dependence on the protein folding state, two sets of samples with 154 mM NaCl were prepared:

- Three control samples served to determine if the presence of urea itself might create a sodium TQ signal. For this purpose, samples with urea concentration of [0, 5.5, 8] M were used. All three phantoms contained no BSA.
- Ten BSA unfolding samples contained 5% w/v BSA with a urea concentration of [0, 1, 2, 3, 4, 5, 5.5, 6, 7, 8] M. The pH values were [7.02, 7.03, 7.05, 7.05, 7.03, 7.00, 6.98, 6.99, 7.04, 7.05] in phantoms with a urea concentration of [0, 1, 2, 3, 4, 5, 5.5, 6, 7, 8] M, respectively. The low content of BSA was chosen to prevent gelation of BSA that occurred at high urea concentrations [Katsuta et al. (1997)]. No gelation of BSA was observed during an observation period of three months following our experiments, during which the phantoms were stored at room temperature.

3.1.4 MR-compatible Microcavity Array-based Bioreactor System

An MR-compatible bioreactor system bridges the gap between phantom and *in vivo* measurements, as it enables the non-invasive measurement of cellular responses in living cells in a precisely controlled environment by NMR. Gottwald et al. (2013) recently proposed an MR-compatible bioreactor system (Figure 3.2) containing a 3D cell culture, which resembles tissue more closely. This bioreactor system allows a large flexibility with cellular interventions and the cultivation of different mammalian cell lines. Consequently, this

bioreactor system is a promising research tool to investigate in detail the origin of MR signals to yield potential biomarkers.

This bioreactor contains an organotypic 3D cell culture on a MCA which consists of 634 cavities on an area of $1 \times 1 \text{ cm}^2$. Each cavity has a depth and a diameter of $300 \mu\text{m}$. The MCA, manufactured from polycarbonate, was surface modified by physisorption of collagen I from rat tail [Gottwald et al. (2019)]. For this, after a hydrophilization step with an isopropanol series, a collagen I-solution ($0.24 \frac{\text{mg}}{\text{ml}}$) was pipetted onto the MCA and incubated at 37°C for 1 hour. Collagen is the most abundant protein of the extracellular matrix and plays a vital role in cell attachment and cell migration. In addition, collagen provides tensile strength to the extracellular matrix. In the bioreactor system, collagen on the MCAs provides an extracellular matrix for the attachment of the cells. After the collagenization of the MCA, a drop of $150 \mu\text{l}$ medium containing $6-9 \cdot 10^6$ hepatoblastoma carcinoma cells of line HepG2 (ATCC HB-8065, Manassas, USA) was placed on

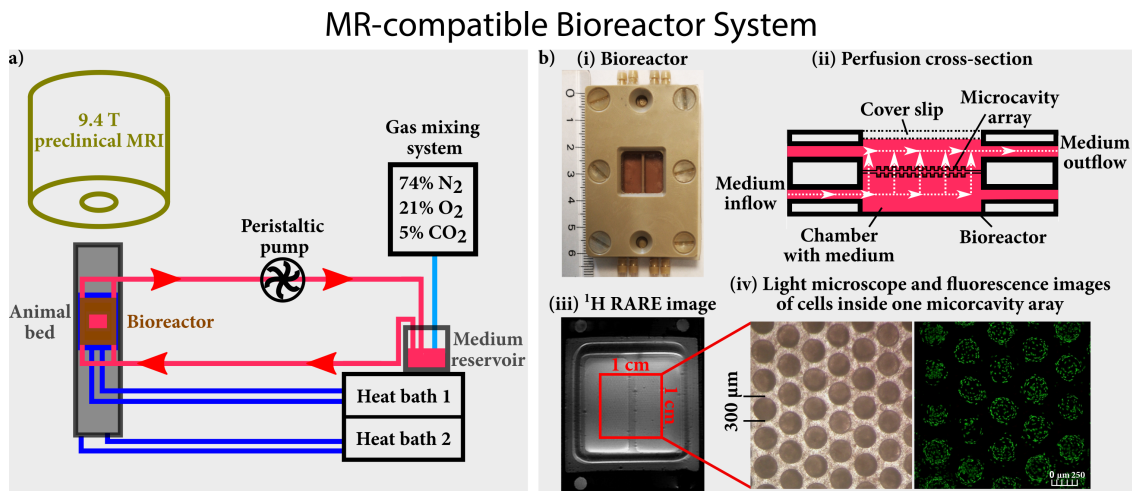


Figure 3.2: a) Graphical sketch of the bioreactor setup. A peristaltic pump supplied cells at $400 \frac{\mu\text{l}}{\text{min}}$ with fresh medium, which was aerated by a gas mixing system. A temperature of 37°C inside the bioreactor was achieved by heating the animal bed and the tubes prior to the bioreactor by the first heat bath. For the heat shock experiments, a second heat bath was added to the bioreactor setup to achieve a heat shock temperature of 42°C (Figure 3.4). b) (i) Dimension of bioreactor, (ii) bioreactor cross-section with perfusion of the medium, (iii) ^1H RARE image of the bioreactor loaded with two MCAs and (iv) light microscope and fluorescence images of cells inside one MCA are shown. Fresh medium entered the bioreactor at the bottom, which was then perfused through the pores of the MCAs and subsequently left the bioreactor on top. The size of the cavity area is $1 \times 1 \text{ cm}^2$, while each cavity has a depth and a diameter of $300 \mu\text{m}$. The fluorescence image shows the cytoplasm of the cells inside one MCA using the fluorescence dye CellTracker Green. Adapted with permission from Kleimaier et al. (2020e) published by Springer Nature.

the collagen-coated MCA. The HepG2 cell line is a robust and fast dividing cell line of human origin. Preparation of HepG2 cells was performed according to previous reports [Gottwald et al. (2013), Gottwald et al. (2007) and Altmann et al. (2008)]. The MCA with cells was placed inside an incubator for initial cultivation before transferring the MCA into the bioreactor. Two MCAs with the upper array placed upside down were used (Figure 3.2b).

A peristaltic pump provided an active perfusion of the cells inside the bioreactor with $400 \frac{\mu\text{l}}{\text{min}}$ medium through the pores within the MCA (Figure 3.2). The medium consisted of minimum essential medium (MEM) with 10% fetal bovine serum, 1% glutamax, 1% non-essential amino acids, 1% sodium pyruvate, 1% penicillin-streptomycin and 0.1% phenol red. This medium formulation contains $3\text{--}4 \frac{\text{mg}}{\text{ml}}$ proteins, while $12\text{--}18 \cdot 10^6$ HepG2 cells contribute to an additional protein concentration of $12\text{--}18 \frac{\text{mg}}{\text{ml}}$. The medium was aerated with 74% N₂, 21% O₂ and 5% CO₂ provided by a gas mixing system (Figure 3.2a). The bioreactor was placed on a heated animal bed and maintained at a temperature of 37°C, which was controlled with an infrared thermometer (Votcraft IR-SCAN-350RH, Hirschau, Germany). For all measurements, the bioreactor was actively perfused under normoxic conditions at 37°C except for the heat shock experiments, where the temperature was increased to 42–43°C for 20 min.

The MR-compatible bioreactor system was used to investigate the cellular response to Na/K-ATPase inhibition and heat shock using the sodium TQ and the rNOE signals, respectively. Both experiments are described in detail in the following paragraphs.

Inhibition of the Na/K-ATPase

Interactions of sodium ions with negatively charged groups of macromolecules result in a sodium TQ signal. Hence, this intrinsic selectivity of the sodium TQ signal yields a large contribution of the intracellular sodium concentration of approximately 30–70% to the total sodium TQ signal [Schepkin et al. (1998) and Eykyn et al. (2015)]. In perfused mouse and rat heart systems, it has been demonstrated that Na/K-ATPase inhibition, which results in an influx of sodium ions into the cell, increases the sodium TQ signal [Schepkin et al. (1998), Tauskela et al. (1997) and Eykyn et al. (2015)]. In contrast, an initial investigation of the cellular response of HepG2 cells to an inhibition of the Na/K-ATPase by ouabain and simultaneous stop of perfusion in this bioreactor system yielded a reduction in the sodium TQ signal [Neubauer et al. (2017)]. Recent studies [Hoesl et al. (2019a) and Hoesl et al. (2019b)] showed a decrease in the sodium TQ signal during a stop of the perfusion using the same bioreactor system. This reduction in the sodium TQ signal due to the perfusion stop potentially interferes with the increase in the sodium TQ signal due to the Na/K-ATPase inhibition. Therefore, the aim of the Na/K-ATPase inhibition experiments in this thesis was to investigate the feasibility of monitoring intracellular sodium changes caused solely by an inhibition of the Na/K-ATPase of living cells in this bioreactor system using the sodium TQ signal.

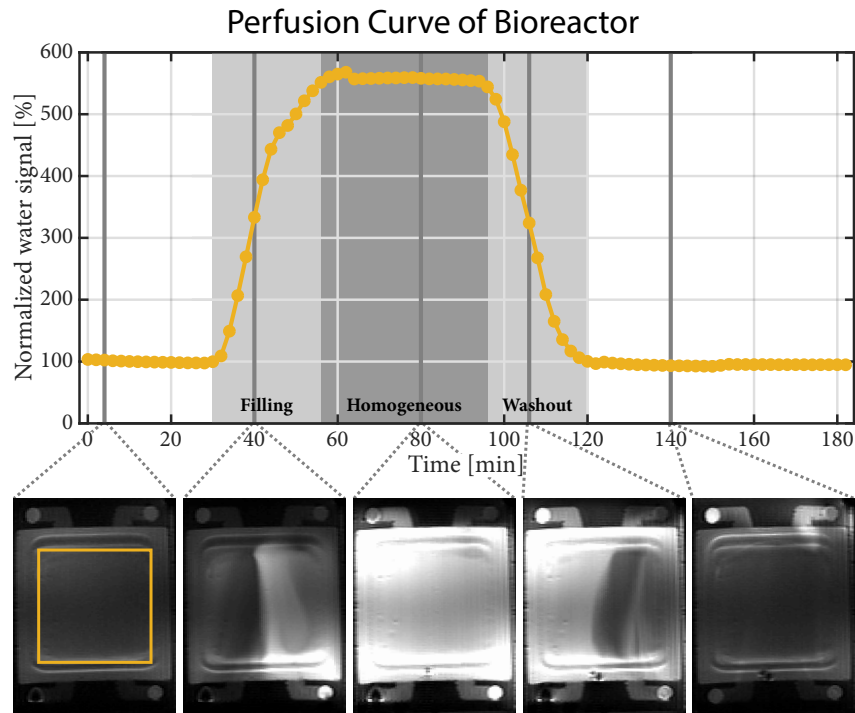


Figure 3.3: Perfusion curve of the MR-compatible bioreactor system without MCAs determined by administration of a bolus containing 2 mM Dotarem for 60 min combined with a T_1 -weighted RARE sequence. The two light gray shaded backgrounds indicate the filling and the washout of the bolus in the bioreactor, while the dark gray shaded background indicates the homogeneous distribution of the bolus in the bioreactor. The signal time course represents the mean signal intensity of a ROI, which included both compartments. The imaging slice was in the place, which would contain the cell culture in the presence of MCAs. The bolus with 2 mM Dotarem started after 2 min. The following time points are relative to the bolus start. After 28 min, the Dotarem bolus arrived in the bioreactor. From approximately 54 min until 90 min, the bolus was homogeneously distributed in the bioreactor. After 118 min, the bolus was completely removed from the bioreactor. Reprinted with permission from Kleimaier et al. (2020f) published by MDPI.

The MR scanner safety rules require the placement of the peristaltic pump outside the RF shielded scanner room. This results in a long tube length of approximately 2.5 m between the bioreactor and the medium reservoir. To determine the delay between the switching of the three-way cock and the arrival of a new medium inside the bioreactor, the MR contrast agent Dotarem (Guebert, France) with a concentration of 2 mM combined with a T_1 -weighted rapid acquisition with relaxation enhancement (RARE) ^1H imaging pulse sequence was used (Figure 3.3). The RARE pulse sequence parameters were: $T_R = 1\text{ s}$, $T_E = 4.6\text{ ms}$, RARE factor 4, 5 averages, 92 repetitions, imaging matrix = 256×128 , slice thickness 1 mm, field of view (FoV) = $50 \times 35\text{ cm}^2$, 8 slices and a scan duration of 2 min.

Figure 3.3 shows the perfusion curve of the bioreactor without MCAs. The signal time course represents the mean signal intensity in a region of interest (ROI) containing both compartments. The imaging slice was chosen such that it would contain the cell culture in the presence of MCAs. The bolus start was around 2 min. The 2 mM Dotarem medium was perfused into the circulation system for 60 min followed by a reperfusion with normal medium for 120 min. The Dotarem medium reached the bioreactor 28 min after the bolus start. From approximately 54 min until 90 min after the bolus start, the Dotarem medium was homogeneously distributed in the bioreactor. The bolus was completely removed from the bioreactor 118 min after the bolus start. This confirmed the excellent filling and washout characteristics determined by Gottwald et al. (2013).

During the Na/K-ATPase inhibition experiments, the sodium TQ signal was acquired with a fixed TQTPPI pulse sequence (Subsection 3.2.4). In a first step, the optimal evolution time and the contribution of cells and medium to the total sodium TQ signal was determined. In a second step, the Na/K-ATPase was blocked in six independent cell cultures with either 1 mM ouabain ($n = 3$) or K^+ -free medium ($n = 3$) for 60 min. The cell cultures were reperfused back with normal medium for 250 min after the 60 min perfusion with 1 mM ouabain or K^+ -free medium. According to Nguyen et al. (2007) and Haas et al. (2002), 1 mM ouabain results in the inhibition of the Na/K-ATPase by approximately 100% compared to control cells. The K^+ -free medium consisted of 1.8 mM $CaCl_2$, 0.8 mM $MgSO_4$, 26.2 mM $NaHCO_3$, 117.2 mM $NaCl$, 1.0 mM $NaH_2PO_4 \cdot H_2O$ and 5.6 mM glucose. This formulation of the K^+ -free medium is based on the formulation of MEM, except that it contained no amino acids, vitamins and 5.3 mM KCl . After the Na/K-ATPase inhibition, the optimal evolution time was determined to compare it with before the Na/K-ATPase inhibition. The Na/K-ATPase inhibition causes an influx of sodium ions into the cells [Deitmer et al. (1978), Ellis (1977) and Pike et al. (1985)], which may affect the optimal evolution time and thus the sodium TQ signal. The time after the Na/K-ATPase inhibition corresponded to approximately 6 h after the dynamic measurements of the Na/K-ATPase inhibition.

The Cellular Heat Shock Response

The rNOE CEST signal depends on the protein content [Jin et al. (2013) and Goerke et al. (2018)] and the protein folding state [Zaiss et al. (2013c), Goerke et al. (2015) and Goerke et al. (2017)]. The dependence on the protein folding state has so far only been demonstrated in experiments with protein solutions and cell lysates. Therefore, the detectability of denaturation processes on a physiologically relevant scale remained to be verified experimentally.

To demonstrate the detectability of protein denaturation processes and the subsequent cellular heat shock response using CEST MRI, a mild non-lethal heat shock was applied to living cells in this thesis. As outlined in Subsection 2.4.1, a slight elevation in temperature above the optimal growth temperature causes the denaturation of certain proteins, which are highly prone to aggregation. To mitigate the toxic effects of misfolded proteins, cells

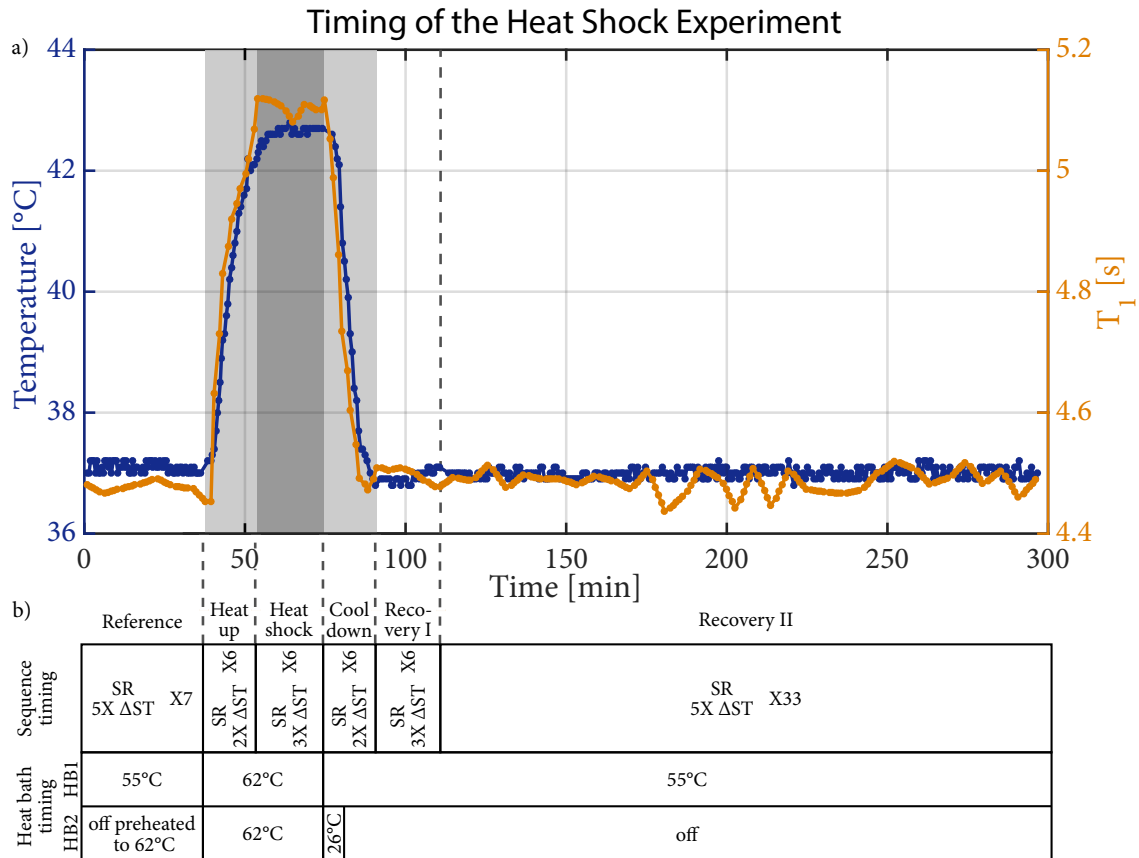


Figure 3.4: a) Temperature and T_1 time course during heat shock of 42°C. Temperature was assessed by an infrared thermometer. The time course of the temperature was measured by placing the bioreactor with collagenized MCAs in medium on the animal bed in front of the MRI scanner. The T_1 time course is from the heat shock experiment of cell culture 1. The heating up to 42°C and the cooling down to 37°C took approximately 15 min, while cells were exposed to a heat shock of 42°C for 20 min. The change in T_1 correlates well with the observed temperature change. After the 15 min cool down, the T_1 value was constant. b) Pulse sequence and heat bath timing of the heat shock protocol. The two offset CEST measurement is abbreviated by Δ ST (Subsection 3.2.5), while saturation recovery (SR) is a fast T_1 measurement technique (Subsection 3.2.3). Sampling of T_1 was finer around the expected time during the heat shock, which occurred at 42°C. Preheating the second water bath to 62°C yielded a fast heat up to 42°C, while addition of ice-cold water to both heat baths resulted in a rapid cooling to 37°C. Adapted with permission from Kleimaier et al. (2020e) published by Springer Nature.

transiently overexpress molecular chaperones. They prevent protein aggregation during heat shock as well as dissolve and refold protein aggregates upon return to native temperatures [Mogk et al. (2018) and Sottile et al. (2018)]. Consequently, an application of a

mild, non-lethal heat shock, which causes the accumulation of misfolded proteins, and the subsequent chaperone-induced refolding of misfolded proteins are expected to affect the protein-based rNOE signal.

To achieve a mild, non-lethal heat shock of 42°C for a duration of 20 min, the bioreactor setup was extended by a second water bath. Prior to the MRI measurements, the parameters and switching times for both water baths were determined by the infrared thermometer (Figure 3.4). A heat shock experiment with the bioreactor containing two collagenized MCAs placed on the animal bed in front of the MRI was performed. After the heat shock, the addition of ice-cold water to both water baths resulted in a rapid cooling to 37°C. The time to heat up to 42°C and to cool down to 37°C was in both cases 15 min (Figure 3.4a).

To attribute rNOE signal changes to the cellular heat shock response, the origin of the rNOE CEST signal in the bioreactor system was determined in a first step. There are three possible contributors to the Z-spectrum of the bioreactor: (i) The medium which contains amino acids, metabolites and proteins; (ii) The collagen on the MCAs, which provides an extracellular matrix for the attachment of the cells, and (iii) a 3D cell culture located on the MCAs. To determine each contribution to the Z-spectrum, full Z-spectra of the medium, two collagenized MCAs in medium and a cell culture on the collagenized MCAs in medium were acquired.

In a second step, the detectability of the cellular heat shock response by the rNOE CEST signal was verified by dynamic CEST measurements. Thus, two 3D cell cultures were exposed to a heat shock of 42°C for 20 min separately. Dynamic CEST measurements are fast CEST measurements interleaved with T_1 measurements (Subsection 3.2.5). To exclude confounding changes in the rNOE signal during dynamic measurements caused by a protein denaturation of medium and collagenized MCAs or due to temporal signal fluctuations, two additional dynamic control experiments were performed.

3.2 MR Methods and Pulse Sequences

This section describes the used MR pulse sequences and methods to analyze the data. Subsection 3.2.1 and Subsection 3.2.2 outline the methods to set up the B_0 shim and the calibration of the RF flip angle, respectively. Subsection 3.2.3 explains the inversion and saturation recovery measurements used to determine T_1 . Subsection 3.2.3 and Subsection 3.2.4 describe the TQTPPI and CEST pulse sequences, respectively. Data analysis was conducted in Matlab (The MathWorks, Natick MA, USA).

3.2.1 B_0 Shim Setup

B_0 inhomogeneity causes reductions in the sodium TQ signal and frequency shifts of the saturation effect in CEST. Consequently, setting up a good B_0 homogeneity prior to measurements is a crucial step in addition to B_0 inhomogeneity correction methods in post-processing. For ^1H experiments, the acquisition of a B_0 map with subsequent localized B_0 shimming provides a good B_0 homogeneity. This ^1H map shim was used for localized B_0 shimming to the location of the cell culture in the CEST measurements. The Bruker system does not allow for a X-nucleus based map shim. There are three different B_0 shim methods for ^{23}Na experiments:

1. ^{23}Na global first and second order Bruker shim routine
2. ^1H global first and second order Bruker shim routine
3. ^1H map shim

To determine the optimal shim routine for ^{23}Na experiments, which aims at yielding a minimal and reproducible B_0 inhomogeneity, each shim routine was repeated 15 times without changing the sample position. The B_0 inhomogeneity was assessed by a single pulse acquisition of the sodium SQ signal and calculation of the sodium SQ FWHM. In the same experiment, the influence of the B_0 inhomogeneity on the sodium TQ signal despite the use of a refocusing RF pulse was also determined. To minimize the influence of flip angle deviations, a small sized sample of 5% w/w agarose was used (Subsection 3.1.3).

3.2.2 Flip Angle Calibration

According to Equation 2.19, the flip angle of an RF pulse depends on the gyromagnetic ratio γ , the pulse duration τ and the RF amplitude B_1^+ . The coil load affects the RF amplitude due to differences in sample conductivity. Hence, the RF flip angle needs to be calibrated for each sample. For ^1H measurements, Bruker provides a slice-selective RF flip angle calibration. This method was used to adjust the RF flip angle at the location of the cell culture in the CEST measurements. In the case of X-nuclei measurements, the signal was too weak and therefore this method failed to calibrate the RF flip angle. To calibrate the RF flip angle for X-nucleus measurements, Neubauer (2015) modified a single

pulse sequence, which varied the RF pulse duration at maximum RF power with subsequent FID readout. To obtain the pulse duration of the 90° RF pulse, the maxima of the phase-corrected FT of the FIDs were fitted by:

$$S(\tau) = |a \sin(2\pi b\tau + c)| + d \quad (3.1)$$

with the fit parameters a , b , c and d . The maximum of the fit function yielded the 90° RF pulse length.

3.2.3 T_1 Measurement

For the ^{23}Na measurements, a non-localized inversion recovery pulse sequence was used. An initial 180° RF pulse inverted the magnetization and after a waiting time, i.e. inversion time T_{inv} , a 90° RF pulse was applied followed by a FID readout. The measurement was repeated using different inversion times and the T_1 value was determined by a fit of the maxima of the phase-corrected spectra according to:

$$S(T_{\text{inv}}) = \left| a \left(1 - b e^{-\frac{T_{\text{inv}}}{T_1}} \right) + c \right| \quad (3.2)$$

with the fit parameters a , b , T_1 and c . In all experiments, 125 inversion times, whereby 80% of them were in the range of 0.3 ms to $2T_{1,\text{est}}$, were used. The remaining 20% of inversion times ranged between $2T_{1,\text{est}}$ and $5T_{1,\text{est}}$. $T_{1,\text{est}}$ represents the estimated T_1 value of the sample determined by a prior T_1 measurement. This higher sampling of inversion times up to $2T_{1,\text{est}}$ yielded an improved determination of T_1 . For each inversion time increment, the magnetization corresponded to the thermal equilibrium magnetization by setting the repetition time to $T_R > 5T_1$. The other parameters were 8 averages and a sampling rate of 50 μs with 1024–2048 complex points.

The ^1H measurements were performed using a saturation recovery pulse sequence combined with a RARE image readout. The saturation recovery method provides a faster determination of T_1 compared to the inversion recovery method. Three adiabatic hyperbolic secant RF pulses resulted in a saturation of the water signal. These RF pulses were interleaved with crusher gradients, which dephased any transverse magnetization. After a variable recovery time T_{rec} , the water signal was acquired by the RARE image readout. The measurement was repeated for different recovery times. A fit of the change in the water signal yielded the T_1 value:

$$S(T_{\text{rec}}) = \left| (a - b) e^{-\frac{T_{\text{rec}}}{T_1}} + c \right| \quad (3.3)$$

with the fit parameters a , b , T_1 and c . The sequence parameters for the saturation recovery measurements with a linear ordered RARE image readout were: 30 non-equidistant spaced recovery times in the range of 4.8 ms to 25 s; $T_E = 45.76$ ms; RARE factor 32; imaging matrix = 70x50; slice thickness 2 mm and FoV = 35x35 cm². During the heat shock experiments, the parameters for the saturation recovery measurement were the same except that only six recovery times [0.0048, 0.1, 3.0, 5.0, 10.0, 17.5] s were sampled.

3.2.4 Triple-quantum Spectroscopy

This subsection has two parts and builds up on the concepts of MQ measurements introduced in Subsection 2.2.7. The first part describes the standard TQTPPI pulse sequence [Schepkin et al. (2017) and Jaccard et al. (1986)], which allows the equal optimal detection of TQ signals with different ion interaction strength. In addition, this pulse sequence separates different coherence orders in frequency, which allows the simultaneous measurement of different coherence orders, for instance the SQ and the TQ signals. The second part introduces a fixed TQTPPI pulse sequence with improved TQ signal sensitivity, which was developed in this thesis. This fixed TQTPPI pulse sequence achieves several times gain in the TQ signal at a fixed ion interaction strength, while preserving the simultaneous measurement of the SQ and the TQ signals at distinct frequencies.

TQTPPI with Evolution Time Increment

Figure 3.5a shows the standard TQTPPI pulse sequence. This pulse sequence is a pseudo 2D sequence, as the signal depends on two frequency domains. The first frequency domain corresponds to the regular FID, which is sampled during the acquisition interval (Figure 3.5a). The standard TQTPPI pulse sequence simultaneously increments the evolution time and the RF pulse phase, which influences the signal of the regular FID. The spectral peak amplitudes of the FT of the regular FID constitute the amplitudes of the evolution time FID (standard TQTPPI FID) in the second frequency domain (Figure 3.5b). A FT of this standard TQTPPI FID yields the standard TQTPPI spectrum, where different coherence orders are separated in frequency (Figure 3.5c).

The standard TQTPPI pulse sequence consisted primarily of three 90° RF pulses. One additional 180° RF pulse was set in the middle between the first two 90° RF pulses, to compensate for B_0 inhomogeneity (Figure 3.5a). The mixing time was set to the minimal value, which corresponds to the 90° RF pulse duration. In the standard TQTPPI pulse sequence, the RF phase α and the evolution time τ_{evo} were simultaneously incremented by 45° and $\Delta\tau_{\text{evo}}$, respectively. Hence, a cycle of eight phase steps, $n_{\text{ps}} = 8$, covered a full rotation of 360° . The incrementation of the RF phase led to a separation of different coherence orders by frequency in a second dimension [Marion et al. (1983)]. The incrementation of the evolution time resulted in a sampling of the evolution time FID, which allowed the equal optimal detection of the sodium TQ signals with different ion interaction strengths. The starting RF phase was $\alpha = 90^\circ$ and the starting evolution time was $\tau_{\text{evo}} = \tau_{\text{min,evo}}$. The minimal evolution time corresponded to the sum of the 90° and 180° RF pulse durations. To cancel out DQ signals, the RF phase of the second 90° RF pulse was alternated between $\pm 90^\circ$, while τ_{evo} was unchanged. The signals of these two RF phase alternations were added. This suppressed the DQ signals, while the SQ and the TQ signals added up constructively. The suppression of the DQ signal was not necessary. However, in the standard TQTPPI spectrum the DQ signal is 90° phase shifted, which can result in an overlap with the real part of the SQ and the TQ signals. After every DQ suppression step, the evolution time was incremented by $\Delta\tau_{\text{evo}}$ alongside an increment of α by 45° .

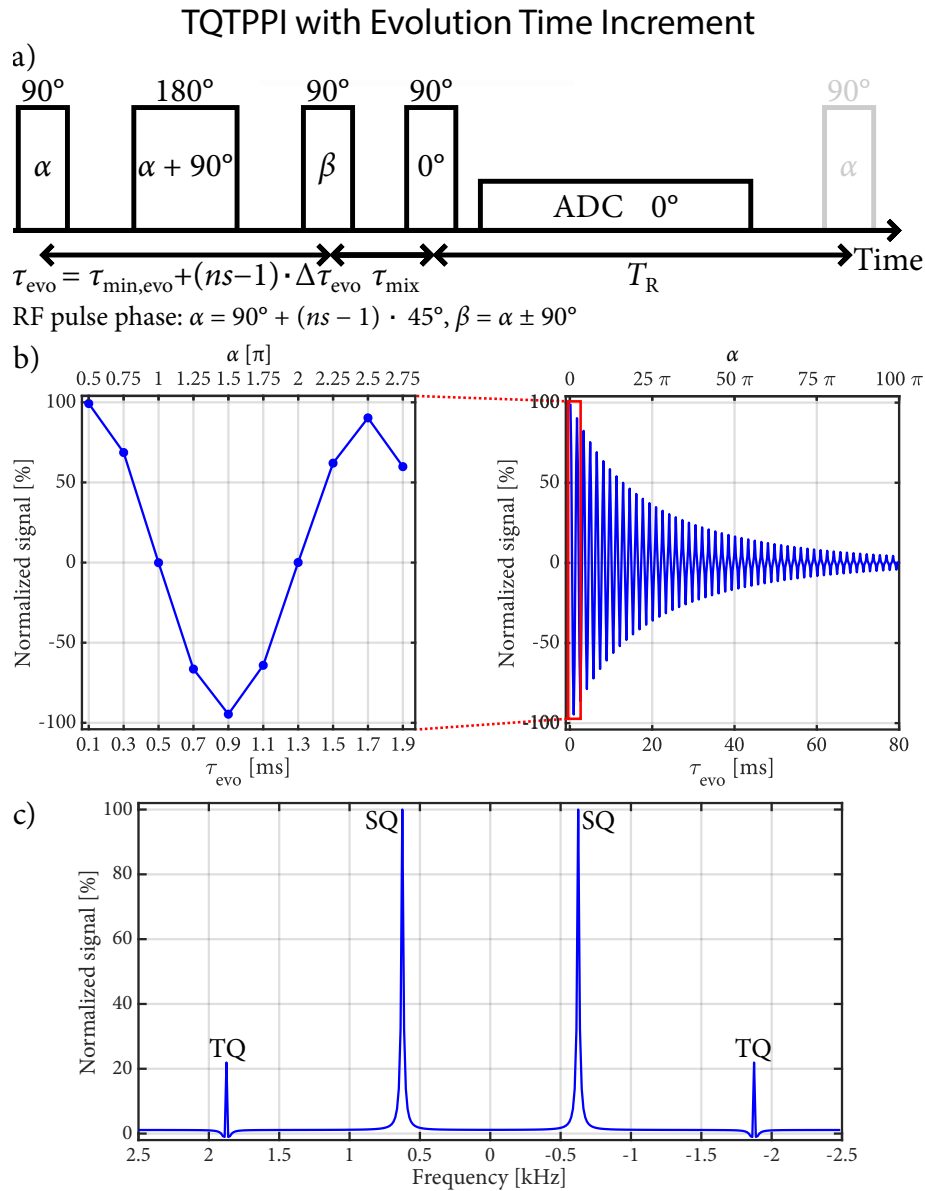


Figure 3.5: a) The TQTPPI pulse sequence with evolution time increment. In this pulse sequence, the RF pulse phase $\alpha = 90^\circ + (ns - 1) \cdot 45^\circ$ and the evolution time $\tau_{\text{evo}} = \tau_{\text{min,evo}} + (ns - 1) \cdot \Delta\tau_{\text{evo}}$ were simultaneously incremented. The τ_{evo} incrementation allowed an equal optimal detection of TQ signals with different ion interaction strengths. b) Standard TQTPPI FID of the pulse sequence in a). The amplitudes of the sodium spectral peak in the first dimension constituted the amplitudes of the standard TQTPPI FID in the second dimension. A FT of the standard TQTPPI FID yielded the standard TQTPPI spectrum shown in c). The RF phase incrementation resulted in a frequency separation of different coherence orders in the standard TQTPPI spectrum.

The total number of increments, ns , is given by $ns = n_{ps} \cdot n_{pc}$, where n_{pc} is the number of phase cycles. This number describes how often these eight phase steps are repeated. Thus, the maximum evolution time is $\tau_{evo} = \tau_{min,evo} + (ns - 1) \cdot \Delta\tau_{evo}$.

For the reconstruction of the standard TQTPPI FID, the first regular FID was Fourier-transformed and phase-corrected by an automatic phasing in frequency domain, which maximizes the real part of the signal amplitude. Then the found phase correction was applied to all other regular FIDs in the first dimension. Subsequently, all spectra were stacked along the evolution time axis. The amplitudes of the sodium spectral peak constituted the amplitudes of the standard TQTPPI FID in a second dimension. A FT of this standard TQTPPI FID yielded the standard TQTPPI spectrum showing an SQ and a TQ peak at distinct frequencies (Figure 3.5c).

The standard TQTPPI FID consists of signal contributions from different coherence orders. The transfer functions $f_{11}^{(1)}(\tau_{evo})$ and $f_{13}^{(1)}(\tau_{evo})$, see Subsection 2.2.6, describe the temporal evolution of the SQ and the TQ signals in the standard TQTPPI FID. By taking into account the standard TQTPPI FID signal modulation due to the RF phase incrementation, a fit function for the standard TQTPPI FID can be derived [Schepkin et al. (2017)]:

$$S(\tau_{evo}) = A_{SQS} \sin(\omega\tau_{evo} + \phi_1) e^{-\frac{\tau_{evo}}{T_{2S}}} + A_{SQF} \sin(\omega\tau_{evo} + \phi_1) e^{-\frac{\tau_{evo}}{T_{2F}}} + A_{TQ} \sin(3\omega\tau_{evo} + \phi_2) \left(e^{-\frac{\tau_{evo}}{T_{2F}}} - e^{-\frac{\tau_{evo}}{T_{2S}}} \right) + DC. \quad (3.4)$$

The parameters A_{SQS} and A_{SQF} are the amplitudes of the slow and the fast SQ relaxation components, respectively. Similarly, T_{2S} and T_{2F} are the respective slow and fast transverse relaxation times. A_{TQ} is the amplitude of the TQ signal. The frequency ω in the second dimension is defined by $\omega = 2\pi\Delta\alpha/(360^\circ\Delta\tau_{evo})$, where $\Delta\alpha = 45^\circ$. Possible phase shifts are compensated by ϕ_1 and ϕ_2 . DC represents a base line shift. The standard TQTPPI FID fit did not include a DQ signal contribution, as in all experiments the DQ signal was suppressed through a combination of phase manipulation and the usage of long repetition times $T_R > 5T_1$. For the standard TQTPPI FID fit function of Equation 3.4, the TQ amplitude is reported as A_{TQ}/A_{SQ} , that is, normalized to the total SQ amplitude $A_{SQ} = A_{SQS} + A_{SQF}$. Additionally, the fraction of the slow component A_{SQS}/A_{SQ} , and both transverse relaxation times, T_{2S} and T_{2F} , are reported.

In the case of a TQ SNR < 3 , the standard TQTPPI FID fit was modified. The TQ SNR was calculated via $SNR = (\text{peak height})/\sigma_{noise}$, where σ_{noise} is the standard deviation of the data points in the standard TQTPPI spectrum containing only noise signal. The modified standard TQTPPI FID fit function omitted the TQ signal fitting:

$$S(\tau_{evo}) = A_{SQ} \sin(\omega\tau_{evo} + \phi_1) e^{-\frac{\tau_{evo}}{T_2}}. \quad (3.5)$$

For a TQ SNR < 3 , the measurement data still contained the large SQ signal. With this modified standard TQTPPI FID fit function at least the mono-exponential transverse relaxation time T_2 could be extracted from the measurement data.

The standard TQTPPI pulse sequence with simultaneous RF pulse phase and evolution time increment was used for all sodium TQ measurements of the model systems (Subsection 3.1.3). The length of the 90° RF pulse depended on the used RF coil setup and therefore τ_{mix} . For all measurements, τ_{mix} was set to the minimal value. The regular FIDs had 1024–2048 complex points and a sampling rate of $50 \mu\text{s}$ per complex point. The number of phase cycles, $n_{\text{pc}} = 50\text{--}100$, was selected to sample the entire standard TQTPPI FID decay in a second dimension. The evolution time increment was $\Delta\tau_{\text{evo}} = 200 \mu\text{s}$ and the range of the evolution time was $\tau_{\text{evo}} = 0.4\text{--}160.4 \text{ ms}$. The T_1 value of each phantom was measured in advance, enabling a repetition time of $T_R > 5T_1$ (or $T_R = 125\text{--}300 \text{ ms}$) to be set for the standard TQTPPI measurements. The total scan duration for one standard TQTPPI measurement was in the range of 2.2–10.1 min. Each phantom measurement was repeated 4–7 times with three averages. Each standard TQTPPI measurement was fitted separately to determine the mean and the standard deviation of all fitting parameters. In the case of a TQ SNR < 3 for each standard TQTPPI measurement, all standard TQTPPI measurements were averaged to yield one standard TQTPPI FID.

TQTPPI with Fixed Evolution Time

To combine the simultaneous measurement of different coherence orders at distinct frequencies with an improved TQ signal sensitivity, a fixed TQTPPI pulse sequence was developed in this thesis (Figure 3.6a). Compared to the standard TQTPPI pulse sequence of Figure 3.5a, the fixed TQTPPI pulse sequence has a fixed evolution time. At the same time, it preserves the RF phase increment, which allows the simultaneous measurement of the SQ and the TQ signals at distinct frequencies.

The transfer function $f_{13}^{(1)}(\tau_{\text{evo}})$ of the TQ signal is the difference between an exponential function with the time constant T_{2F} and an exponential function with the time constant T_{2S} . Thus, the TQ signal is not maximal at minimal τ_{evo} (Figure 3.6b), as it is the case for the SQ signal. The optimal evolution time τ_{opt} for maximum TQ signal depends on both transverse relaxation times according to:

$$\tau_{\text{opt}} = \frac{\ln\left(\frac{T_{2S}}{T_{2F}}\right)}{\frac{1}{T_{2F}} - \frac{1}{T_{2S}}}. \quad (3.6)$$

The evolution time increment therefore represents an elegant way to remove the TQ signal dependence on the transverse relaxation times. This is particularly useful for experimental series where a change in transverse relaxation times is expected or when the relaxation times are unknown. However, incrementation of the evolution time yields a mean TQ amplitude for all evolution times which is lower compared to the maximum TQ signal at optimal evolution time (Figure 3.6b). Thus, a fixed evolution time, which is set to the optimal evolution time, yields several times gain in TQ signal sensitivity.

The fixed TQTPPI pulse sequence also consisted of three 90° RF pulses and one 180° refocusing RF pulse. The starting RF phase was $\alpha = 90^\circ$ and the mixing time was set to the

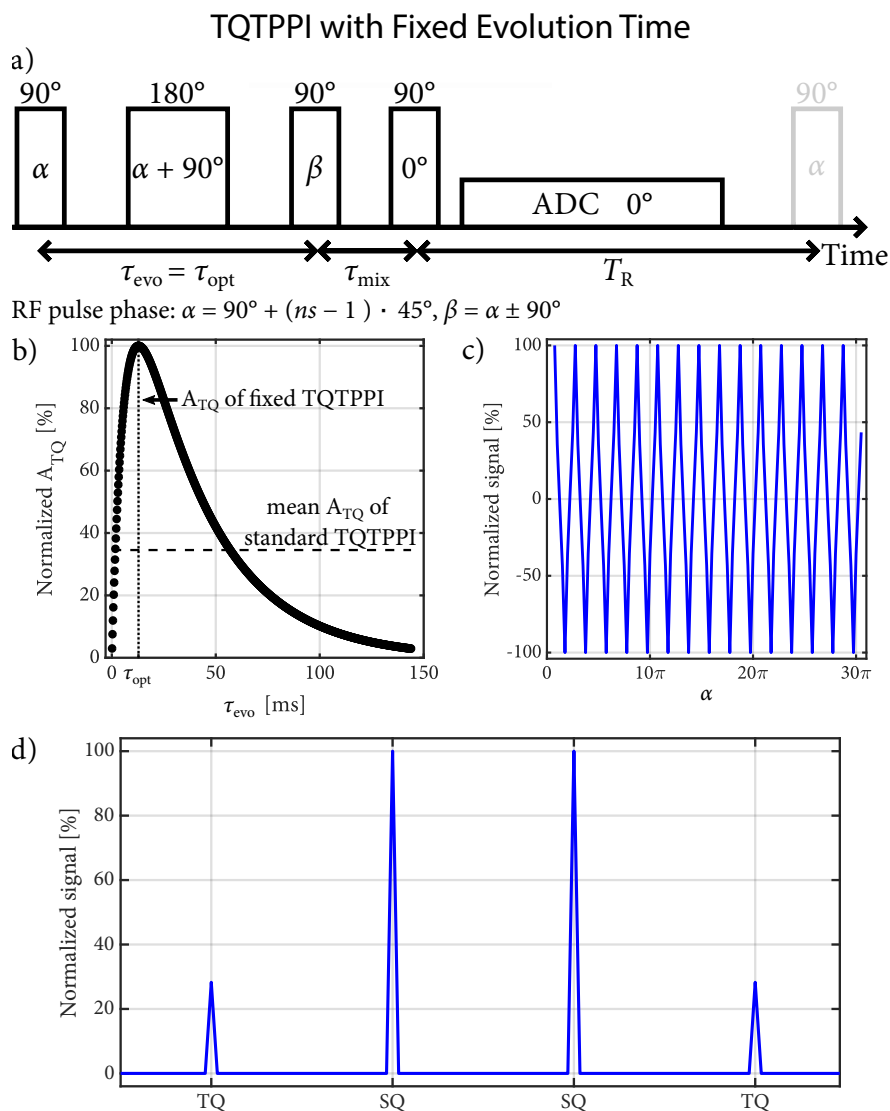


Figure 3.6: a) The TQTPPI pulse sequence with fixed evolution time. In the fixed TQTPPI pulse sequence, only the RF pulse phase $\alpha = 90^\circ + (ns - 1) \cdot 45^\circ$ is incremented. This modification leads to several times gain in the TQ signal if $\tau_{\text{evo}} = \tau_{\text{opt}}$ as shown in b), while preserving the simultaneous measurement of the SQ and the TQ signals at distinct frequencies. b) TQ signal build up for $T_{2S} = 35$ ms and $T_{2F} = 6$ ms. The mean TQ amplitude for all τ_{evo} of the standard TQTPPI pulse sequence is lower compared to maximum TQ signal at τ_{opt} of the fixed TQTPPI pulse sequence. c) Fixed TQTPPI FID of the pulse sequence in a). The signal of the fixed TQTPPI FID does not include relaxation effects and only oscillates between the maximum and minimum signal, due to the RF phase incrementation. A FT of the fixed TQTPPI FID yields the fixed TQTPPI spectrum shown in d). d) In the fixed TQTPPI spectrum, the lineshape of the different coherence orders are close to delta functions.

minimal value. In the fixed TQTPPI pulse sequence, only the RF phase was incremented by 45° , which resulted in eight phase steps, $n_{ps} = 8$, to cover a full rotation of 360° . Before the RF phase increment of α , the phase β was alternated between $\pm 90^\circ$ and the signal of these two RF phase alternations were added to suppress DQ signals. Then the RF phase α was incremented by 45° . Repetition of these eight phase steps without averaging yielded an improved separation of different coherence orders in the fixed TQTPPI spectrum and a gain in the SQ and the TQ SNR (Figure 3.6d). The total number of increments, ns , is given by $ns = n_{ps} \cdot n_{pc}$, where n_{pc} is the number of phase cycles. The reconstruction of the fixed TQTPPI FID (Figure 3.6c) is the same as for the standard TQTPPI FID.

The fixed TQTPPI FID does not contain any relaxation effects. The RF phase increment results in an oscillation of the SQ and the TQ signals. Consequently, a modification of the standard TQTPPI FID function (Equation 3.4) allows extraction of the SQ and the TQ amplitudes from the fixed TQTPPI FID:

$$S(\alpha) = A_{SQ} \sin(\alpha + \phi_1) + A_{TQ} \sin(3\alpha + \phi_2) + DC. \quad (3.7)$$

A_{SQ} and A_{TQ} are the SQ and the TQ amplitudes, respectively. ϕ_i are phase offsets and DC is a baseline offset.

To evaluate the TQ SNR gain for the fixed TQTPPI pulse sequence compared to the standard TQTPPI pulse sequence, three samples with [2, 4, 6]% w/v agarose in 134.75 mM NaCl were used. The standard TQTPPI FID was fitted by Equation 3.4, which allowed the calculation of the optimal evolution time for each phantom. To compare the SQ and the TQ amplitudes between the standard and the fixed TQTPPI pulse sequences, the sodium SQ and TQ amplitudes of the standard TQTPPI FID were corrected to the optimal evolution time, which was set for the fixed TQTPPI measurements, according to Equation 3.4. The TQ SNR gain was calculated by dividing the TQ amplitude by the standard deviation. To further compare the fixed TQTPPI pulse sequence with the standard TQTPPI pulse sequence, the evolution time was varied for the fixed TQTPPI pulse sequence. This allowed extracting the transverse relaxation times by fitting the sodium SQ and TQ amplitudes for different evolution times by the transfer functions $f_{11}^{(1)}(\tau_{evo})$ and $f_{13}^{(1)}(\tau_{evo})$, respectively:

$$A_{SQ}(\tau_{evo}) = A_{SQS} e^{-\frac{\tau_{evo}}{T_{2S}}} + A_{SQF} e^{-\frac{\tau_{evo}}{T_{2F}}}, \quad (3.8)$$

$$A_{TQ}(\tau_{evo}) = A_{TQ} \left(e^{-\frac{\tau_{evo}}{T_{2S}}} - e^{-\frac{\tau_{evo}}{T_{2F}}} \right). \quad (3.9)$$

Both equations were simultaneously fitted to the measured SQ and TQ signals using non-linear data fitting. This allowed the comparison of the transverse relaxation times between the standard and the fixed TQTPPI pulse sequences. The sequence parameters for the fixed TQTPPI pulse sequence were: $T_R = 300$ ms, 1 average, 3 repetitions, 2048 complex points, $50 \mu\text{s}$ sampling rate, $n_{pc} = 90$ and a scan duration of 7.2 min. For the calculation of the TQ SNR gain, the evolution time was set to [18.6, 12.8, 10.2] ms for [2, 4, 6]% agarose, respectively. To compare the transverse relaxation times, 43–46 non-equidistant evolution times covered a range of 0.1 to 120.0 ms. The pulse sequence parameters for the

standard TQTPPI pulse sequence were the same as for the fixed TQTPPI pulse sequence except that the evolution time was incremented by $\Delta\tau_{\text{evo}} = 0.2$ ms to cover an evolution time range of 0.1 to 144.1 ms.

In the cell experiments, the fixed TQTPPI pulse sequence was used due to the higher TQ signal sensitivity. The pulse sequence parameters were: $T_R = 250$ ms, 1 average, 2048 complex points, 50 μs sampling rate, $\tau_{\text{evo}} = 10$ ms, $n_{\text{pc}} = 60$ and a scan duration of 4.2 min. For the evaluation of the optimal evolution time, the evolution time was varied in a range of 5 to 20 ms with a step of 5 ms and 5 averages. This optimization was performed for three and two cell cultures before and after the Na/K-ATPase inhibition, respectively. The optimization of the sodium TQ signal after the Na/K-ATPase inhibition corresponded to approximately 6 h after the dynamic measurements.

The sodium TQ signal during the Na/K-ATPase inhibition by 1 mM ouabain ($n = 3$) or K^+ -free medium ($n = 3$) was dynamically monitored 20 min before the bolus start until 250 min after the bolus stop. The $A_{\text{TQ}}/A_{\text{SQ}}$ was normalized to the first 37 min. Then the background sodium TQ signal of medium and 0 mM K^+ medium was subtracted from the $A_{\text{TQ}}/A_{\text{SQ}}$ time course. Each $A_{\text{TQ}}/A_{\text{SQ}}$ time course was denoised using a Bayes-based wavelet denoising [Johnstone et al. (2004)]. Finally, the three denoised $A_{\text{TQ}}/A_{\text{SQ}}$ time courses of each Na/K-ATPase inhibition were averaged to yield one $A_{\text{TQ}}/A_{\text{SQ}}$ time course for each Na/K-ATPase inhibition. An additional dynamic measurement was performed to evaluate the baseline of the temporal signal fluctuations in a control experiment containing a cell culture but without intervention.

A second perfusion curve of the bioreactor was obtained using the sodium SQ signal during the Na/K-ATPase inhibition experiments with 0 mM K^+ medium. In contrast to the perfusion curve of Figure 3.3, in these experiments the bioreactor did contain a cell culture. The sodium SQ signal was normalized to the first 37 min and the average of three Na/K-ATPase inhibitions reported here and of three further experiments was calculated. Then a smoothing spline was used to smooth this averaged A_{SQ} time course [Reinsch (1967)].

3.2.5 CEST Imaging

This subsection has two parts and builds up on the concept of CEST introduced in Subsection 2.3.2. The first part describes the cw CEST pulse sequence for the acquisition of a full Z-spectrum. The second part outlines a reliable and fast high-resolution CEST pulse sequence for the dynamic CEST measurements of the rNOE signal during the heat shock experiments.

Spectroscopic CEST Imaging

The CEST pulse sequence consists of a saturation RF pulse followed by a water signal acquisition, as shown in Figure 2.14a. The use of a preclinical NMR scanner allows employing

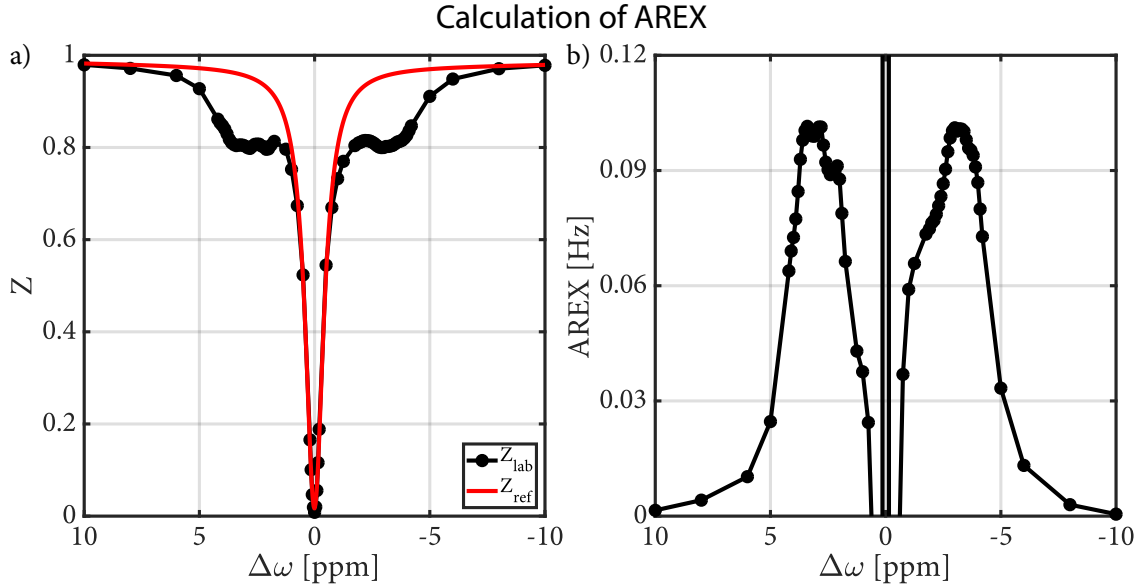


Figure 3.7: a) Z-spectrum of egg white at 9.4 T ($B_1^+ = 0.8 \mu\text{T}$ and $t_{\text{sat}} = 10$ s). Z_{lab} represents the measurement data, while Z_{ref} is the contribution of DS and ssMT to the Z-spectrum approximated by a fit of a sum of two Lorentzian functions (Equation 3.10). For the calculation of Z_{ref} , data points in the Z-spectrum containing CE or rNOE signals were excluded. b) AREX spectrum of the Z-spectrum of egg white shown in a).

a cw RF block pulse of length t_{sat} , offset frequency $\Delta\omega$ and amplitude B_1^+ for the saturation RF pulse. The cw RF pulse in contrast to a pulse train of RF pulses has the advantages that it has a well-defined B_1^+ amplitude, a small bandwidth and achieves an efficient saturation. Crusher gradients dephased any transverse magnetization after the cw RF block pulse. This saturation scheme was added to a RARE pulse sequence, which was provided by Bruker. The RARE pulse sequence provides a fast image readout of the water signal and reduces susceptibility-induced signal losses. The reduction of magnetic susceptibility artifacts was especially beneficial for the generation of MR images of the MR-compatible bioreactor system due to strong susceptibility differences between water and plastic as well as between water and air.

Repetition of the saturation RF pulse with subsequent image readout for n different offset frequencies $\Delta\omega$ yields a Z-spectrum (Equation 2.92). In a Z-spectrum, the saturated water signals $M_{\text{sat}}(\Delta\omega)$ are normalized to the water signal $M_0(\Delta\omega)$, which represents the equilibrium water signal saturated at a frequency offset of $\Delta\omega = -200$ ppm. Acquisition of an equilibrium magnetization $M_0(\Delta\omega)$ before and after acquisition of $M_{\text{sat}}(\Delta\omega)$ minimized signal fluctuations, which can occur during the acquisition of $M_{\text{sat}}(\Delta\omega)$. Linear interpolation of $M_0(\Delta\omega)$ yielded an individual $M_0(\Delta\omega)$ for each saturation frequency. B_0 correction was performed on a pixel-by-pixel basis using the intrinsic minimum of the spline interpolated Z-spectrum. The minimum of the Z-spectrum yields the resonance

frequency shift relative to $\Delta\omega = 0$ ppm. Next, the acquired Z-spectra were interpolated to a frequency resolution of 0.01 ppm. The individual Z-spectra were then shifted by ΔB_0 determined by the intrinsic minimum of the Z-spectrum. The missing Z-values at the edge of the Z-spectrum were linearly extrapolated. This step can be critical for Z-spectra which are only sampled around the water frequency. However, the acquired Z-spectra in this thesis also contained frequency offsets larger than $\Delta\omega \geq 50$ ppm. In the last step, the Z-spectra were transformed back to their original frequency resolution. The use of a quadrature ^1H volume coil caused a negligible B_1^+ deviation across the cell culture (Figure A.2). Consequently, a B_1^+ correction was not performed.

The Z-spectrum contains not only the contribution of CE and rNOE but also that of DS and ssMT (Figure 2.14a). In addition, the effects are also scaled by T_1 of water. The calculation of AREX (Equation 2.115), which represents a quantitative parameter of isolated CE and rNOE signals, removes the contribution of DS, ssMT and T_1 to the Z-spectrum [Zaiss et al. (2014)]. AREX requires a reference Z-spectrum Z_{ref} , which contains only the contribution of DS and ssMT. One possibility to obtain a reference Z-spectrum is to fit a part of the acquired Z-spectrum, which only contains the contribution of DS and ssMT [Jones et al. (2013)]. Hence, only data points in the frequency range of $\Delta\omega \leq \pm 0.75$ ppm and $\Delta\omega \geq \pm 8$ ppm were included for the fit of DS and ssMT. According to Equation 2.111, the Z-spectrum of DS and ssMT can be approximated by the sum of two Lorentzian functions (Figure 3.7a):

$$Z_{\text{ref}}(\Delta\omega) = Z_{\text{max}} - \mathcal{L}_{\text{DS}}(\Delta\omega) - \mathcal{L}_{\text{ssMT}}(\Delta\omega), \quad (3.10)$$

where Z_{max} compensates for incomplete water relaxation, which yields a Z-value of less than one at large frequency offsets. $\mathcal{L}_{\text{DS}}(\Delta\omega)$ and $\mathcal{L}_{\text{ssMT}}(\Delta\omega)$ are Lorentzian-shaped functions for DS and ssMT, respectively. An additional measurement of the water T_1 relaxation time allows the calculation of isolated CE and rNOE signals by AREX. In the Z-spectra of medium and those of collagenized MCAs in medium, ssMT was not apparent. Thus, in those samples $Z_{\text{ref}}(\Delta\omega)$ consisted of only one Lorentzian-shaped function for DS.

A full Z-spectrum was sampled to determine the contribution of medium, collagenized MCAs and cells to the total Z-spectrum from the bioreactor system. A full Z-spectrum was additionally acquired before and after the heat shock experiments. Such a Z-spectrum consisted of 93 non-equidistant frequency offsets between $\Delta\omega = \pm 200$ ppm. The cw RF block pulse had a length of $t_{\text{sat}} = 10$ s and an amplitude of $B_1^+ = 0.8 \mu\text{T}$. The RARE readout was centric reordered with following parameters: $T_E = 2.86$ ms, RARE factor 32, imaging matrix = 70x50, slice thickness 2 mm, FoV = 35x35 cm² and a scan time of 16 min.

Dynamic CEST Imaging

The acquisition of a full Z-spectrum, which consists of several measurements at different offset frequencies $\Delta\omega$, is a time consuming process. To achieve a high temporal resolution and still suppress the contribution of DS and ssMT, Chen et al. (2019) recently proposed

a 2-point contrast metric. This 2-point contrast metric requires only an offset measurement at 8 and -3.5 ppm for the measurement of the aliphatic rNOE signal. Consequently, this method can achieve a temporal resolution of less than 1 min, which was needed for the measurement of the rNOE signal during the heat shock experiments. The proposed 2-point contrast metric by Chen et al. (2019) was adapted to the AREX metric:

$$\text{AREX}_{\Delta\text{ST}}(-3.5 \text{ ppm}) = \frac{1}{T_1} \left(\frac{1}{Z(-3.5 \text{ ppm})} - \frac{1}{Z(8 \text{ ppm})} \right). \quad (3.11)$$

The quantity $\text{AREX}_{\Delta\text{ST}}(-3.5 \text{ ppm})$ describes the approximated rNOE signal at -3.5 ppm from which the contribution of DS and ssMT was removed by the offset measurement at 8 ppm. The applicability of $\text{AREX}_{\Delta\text{ST}}$ to the bioreactor system was verified by comparison of $\text{AREX}_{\Delta\text{ST}}(-3.5 \text{ ppm})$ with $\text{AREX}(-3.5 \text{ ppm})$ for the Z-spectra of medium, two collagenized MCAs in medium and a cell culture on the collagenized MCAs in medium. Residual contributions from DS and ssMT to $\text{AREX}_{\Delta\text{ST}}(-3.5 \text{ ppm})$ were calculated from the estimated Lorentzian fit of DS and ssMT for $Z_{\text{ref}}(\Delta\omega)$ (Figure 3.7a).

The calculation of $\text{AREX}_{\Delta\text{ST}}(-3.5 \text{ ppm})$ requires a measurement of the water T_1 relaxation time. Therefore, dynamic CEST measurements were interleaved with saturation recovery measurements from 37 min before the heat shock until 200 min after the heat shock. The T_1 sampling was adapted for a finer sampling around the heat shock and a sparser sampling before and after the heat shock (Figure 3.4b). T_1 values were linearly interpolated to obtain one T_1 value for each of the two offset CEST measurements. Prior to each CEST or saturation recovery measurement, the water frequency was set to correct for frequency drifts over time. The $\text{AREX}_{\Delta\text{ST}}(-3.5 \text{ ppm})$ time course was normalized pixel-wise to the first 37 min prior to the heat shock application. Then the ROI averaged $\text{AREX}_{\Delta\text{ST}}(-3.5 \text{ ppm})$ was calculated and the time course was convolved with a block pulse of width four. The pulse sequence parameters for the dynamic CEST measurements were the same as for the acquisition of a full Z-spectrum, while the pulse sequence parameters for the saturation recovery measurements are described in Subsection 3.2.3.

3.3 Fluorescence Measurements

Fluorescence measurements represent an established and widely used method to characterize protein conformational changes [Ghisaidoobe et al. (2014) and Cohen et al. (2005)]. The intrinsic fluorescence signal of the tryptophan amino acid, which is the dominant fluorescent signal of proteins, is highly sensitive to its local environment. In the native protein conformation, tryptophan is located in the hydrophobic protein core. Exposure of tryptophan to an aqueous environment, which occurs during protein unfolding, results in a reduced emission intensity and in a red shift of the emission wavelength.

Fluorescence measurements were used as a gold standard to monitor the protein folding state during urea-induced unfolding of BSA. The urea-induced unfolding of BSA was used to investigate a possible dependence of the sodium TQ signal on the protein folding state. For the fluorescence measurements, a second set of phantoms was produced, identical to the ones used in the MR experiments (Subsection 3.1.3). Fluorescence spectra were acquired by a Tecan Infinite 200 PRO plate reader (Tecan Group, Männedorf, Switzerland) using three 200 μ l volumes per phantom. The two tryptophan residues of BSA were excited at $\lambda = 295$ nm with a subsequent detection of response between $\lambda = 320$ nm and $\lambda = 400$ nm with a resolution of $\Delta\lambda = 2$ nm. The detected fluorescence spectra were integrated, and the relative changes compared to the control phantom without urea were plotted as a function of urea concentration to obtain a denaturation curve.

3.4 Quantitative Analysis

This section has two parts. The first part describes the methods to quantify the observed signal changes from the investigation of pH and the urea-induced unfolding of BSA. The second part introduces the rNOE signal quantification of the cellular heat shock response.

3.4.1 Quantification of Protein Conformational Changes

The relative change of the sodium TQ signal and the integrated fluorescence signal during urea-induced unfolding of BSA was calculated by using the measurements at $c_{\text{urea}} = 0 \text{ M}$ as a reference. Measurement data from the investigation of pH and the protein folding state $Y(x)$ were fitted by a sigmoid function, which is commonly used for investigation of a dependence on pH [Wenzel et al. (2013)] and the protein folding state [Pace (1986) and Zaiss et al. (2013c)]:

$$Y(x) = A + \frac{B - A}{1 + e^{(V_{50} - x)C}}. \quad (3.12)$$

For the pH experiment, A and B are the minimum and maximum values of the sodium TQ signal, respectively, and x represents the pH value. For the urea experiment, A and B are the minimum and maximum values, respectively, of the relative change of either the sodium TQ or the fluorescence signal. In this case, x is the urea concentration. V_{50} is the transition midpoint and C is the growth rate of the sigmoid function. For the fitting of the data from the urea-induced unfolding of BSA, the minimum value A was set to zero. The reported standard deviation of all fit parameters is the 95% confidence interval of the Levenberg-Marquardt fit.

In addition to the sigmoid function fit, the Pearson correlation coefficient (PCC) was used to correlate the relative change in the fluorescence signal with the relative change in the sodium TQ signal during urea-induced unfolding of BSA. The PCC is a statistical measure for the linear correlation between two variables. The range of the PCC value is between ± 1 . A total positive linear correlation results in a PCC of 1, while a total negative linear correlation has a PCC value of -1 . A PCC of 0 means no linear correlation. The PCC result is statistical significant if the p value is smaller than 0.01.

3.4.2 Quantification of Heat Shock Recovery

To the best of our knowledge a quantification of the cellular heat shock recovery has not been performed so far. The cellular heat shock response resulted in a continuous increase in the rNOE signal comparable to an exponential function. To quantify the heat shock response, the time course from 100 min, which corresponded to the time immediately after the temperature has returned to 37°C , until the end was fitted by:

$$Y(t) = (Y_{\text{start}} - Y_{\text{end}}) e^{-\frac{t}{T_{\text{rec}}}} + Y_{\text{end}}, \quad (3.13)$$

where $Y(t)$ is the normalized $\text{AREX}_{\Delta\text{ST}}(-3.5 \text{ ppm})$; Y_{start} is the minimum value; Y_{end} is the maximum value and T_{rec} is the recovery time. The standard deviation of all fit parameters corresponded to the 95% confidence interval of the Levenberg-Marquardt fit.

4 Results

The sodium TQ experiments aim to provide insights giving a deeper understanding of the origin of the sodium TQ signal and its capability to serve as a potential biomarker for cell viability. The investigation of the cellular heat shock response by the rNOE signal aims to experimentally verify the detectability of denaturation processes on a physiologically relevant scale in living cells by CEST NMR. This chapter starts with the results of the influence of B_0 inhomogeneity (Section 4.1) and amino acids (Section 4.2) on the sodium TQ signal. The following section (Section 4.3) describes the results of the investigation of the sodium TQ signal dependence on pH and the protein folding state. Section 4.4 compares the standard and the fixed TQTPPI pulse sequences. Section 4.5 presents the results of the capability of the sodium TQ signal to monitor intracellular sodium changes during the Na/K-ATPase inhibition of living cells using the improved TQ signal sensitivity of the fixed TQTPPI pulse sequence. The last section (Section 4.6) outlines the results of the heat shock experiments of living cells dynamically monitored by the rNOE CEST signal. Parts of the results have been published in Kleimaier et al. (2020c)¹ by John Wiley & Sons, Kleimaier et al. (2020f)² by MDPI, and Kleimaier et al. (2020e)² by Springer Nature and the corresponding descriptions and figures are adapted thereof.

4.1 Influence of B_0 Inhomogeneity on TQ Signal

To investigate the robustness of the TQ signal against B_0 inhomogeneity despite the use of a 180° refocusing RF pulse, the shim process of three different shim routines, which lead to a different B_0 inhomogeneity, were repeated 15 times. Figure 4.1a shows three exemplary standard TQTPPI spectra, where a 180° refocusing RF pulse compensated for B_0 inhomogeneity, for three different sodium SQ FWHM. For a larger B_0 inhomogeneity,

Table 4.1: Mean standard TQTPPI fit parameters for the three different shim routines.

Shim routine	A_{TQ}/A_{SQ} [%]	A_{SQS}/A_{SQ} [%]	T_{2S} [ms]	T_{2F} [ms]
²³ Na global shim	12.55 ± 2.59	40.19 ± 0.50	34.7 ± 0.4	4.43 ± 0.10
¹ H global shim	14.37 ± 8.72	40.52 ± 1.14	34.1 ± 0.6	4.29 ± 0.12
¹ H map shim	30.90 ± 0.06	41.40 ± 0.13	34.1 ± 0.2	4.32 ± 0.02

¹©2020 The Authors. NMR in Biomedicine published by John Wiley & Sons Ltd

²Creative Commons Attribution 4.0 International License:

<https://creativecommons.org/licenses/by/4.0/>

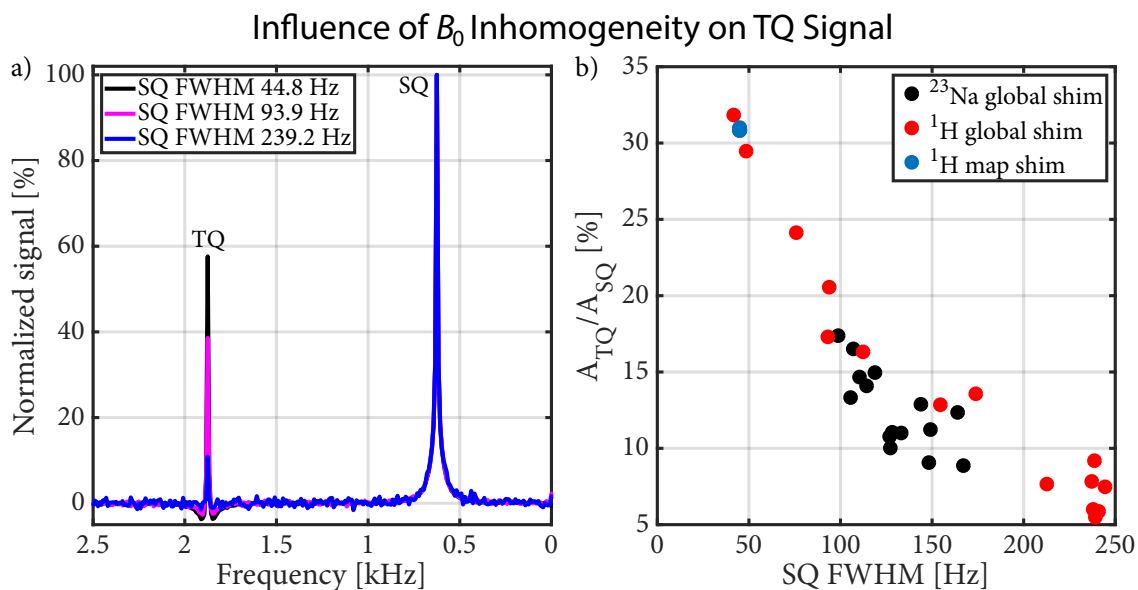


Figure 4.1: a) Standard TQTPPI spectrum of 5% w/v agarose in 154 mM NaCl for three different sodium SQ FWHM. The sodium TQ signal decreased for a larger sodium SQ FWHM, meaning a larger B_0 inhomogeneity, while the noise in the standard TQTPPI spectrum also increased. b) The A_{TQ}/A_{SQ} ratio for different SQ FWHM created by the three different shim routines. Only the ^1H map shim resulted in a reproducible B_0 inhomogeneity, which yielded a reproducible and maximum TQ signal. In contrast to the TQ signal using the ^1H map shim routine, the TQ signal showed large variations, which were larger than the 95% confidence interval of the fit, using the ^{23}Na or ^1H global shim routine. Table 4.1 lists the mean standard TQTPPI fit parameters for the three different shim routines.

i.e. larger sodium SQ FWHM, the noise in the standard TQTPPI spectrum increased and the sodium TQ signal substantially decreased. Figure 4.1b shows the A_{TQ}/A_{SQ} ratio for different sodium SQ FWHM created by the three shim routines. In general, a smaller B_0 inhomogeneity resulted in a larger value of A_{TQ}/A_{SQ} . Only the ^1H map shim yielded a reproducible and minimal B_0 inhomogeneity, which resulted in a reproducible and maximum sodium TQ signal. The largest variations in the A_{TQ}/A_{SQ} ratio and the sodium SQ FWHM were observed for the ^1H global shim routine. Table 4.1 lists the mean standard TQTPPI fit parameters for the three different shim routines. Both mean transversal relaxation times agreed within the standard deviation for all three shim routines, while the mean A_{TQ}/A_{SQ} using the ^1H map shim routine was more than a factor of two larger than the mean A_{TQ}/A_{SQ} using the ^{23}Na or ^1H global shim routine. Consequently, a good and reproducible B_0 homogeneity is crucial to obtain a reproducible and maximum TQ signal despite the use of a 180° refocusing RF pulse.

4.2 Sodium TQ Signal of Amino Acids

This section presents the results for the sodium TQ measurements of the samples containing amino acids. Amino acids are the constituents of proteins and a sodium TQ signal in the presence of amino acids would allow to correlate a possible sodium TQ signal dependence on pH to the number of available negatively charged groups.

Table 4.2 summarizes the relaxation times and the sodium TQ SNR for the amino acid samples consisting of either glutamic acid, arginine or lysine. Despite a large pH value, which results in a maximum number of available negatively charged groups, the sodium TQ SNR was below three in all standard TQTPPI measurements. It is important to note that all standard TQTPPI measurements for each sample were averaged to yield one standard TQTPPI FID, which was fitted by a mono-exponential decay for the sodium SQ signal, while the TQ terms were omitted (Equation 3.5). No sodium TQ signal was detected despite the fact that interactions of sodium ions with the amino acid lysine can shorten the sodium relaxation times T_1 and T_2 to 8.8 ± 0.1 ms and 8.9 ± 0.1 ms, respectively. In general, the sodium relaxation times T_1 and T_2 were close in value and decreased for increasing amino acid concentration.

Table 4.2: Standard TQTPPI fitting results of the amino acid samples using the fit function of Equation 3.5.

Amino acid	Concentration [M]	pH	T_1 [ms]	T_2 [ms]	TQ SNR
Glutamic acid	0.05	12.50	47.5 ± 0.1	48.1 ± 0.1	0.7 ± 0.1
	0.25	12.72	43.8 ± 0.1	45.1 ± 0.1	1.2 ± 0.1
Arginine	0.50	12.68	38.7 ± 0.1	38.7 ± 0.1	1.7 ± 0.1
	0.75	12.62	33.7 ± 0.1	34.2 ± 0.1	-1.4 ± 0.1
	0.90	12.64	30.1 ± 0.1	31.4 ± 0.1	-0.2 ± 0.1
	1.00	8.43	33.9 ± 0.1	35.3 ± 0.1	1.6 ± 0.1
Lysine	1.50	8.14	26.1 ± 0.1	26.9 ± 0.1	0.1 ± 0.1
	2.00	7.96	19.2 ± 0.1	19.5 ± 0.1	0.5 ± 0.1
		8.74	18.3 ± 0.1	18.1 ± 0.1	2.0 ± 0.1
	2.50	7.85	12.7 ± 0.1	13.4 ± 0.1	0.5 ± 0.1
		8.65	12.2 ± 0.1	12.5 ± 0.1	0.8 ± 0.1
		10.01	8.8 ± 0.1	8.9 ± 0.1	0.4 ± 0.1

The samples of 2.0 M lysine with pH 8.74 and 2.5 M lysine with pH 8.65 had a NaOH concentration of 0.6 M, while 2.5 M lysine with pH 10.01 had a NaOH concentration of 2.9 M. All other samples had a NaOH concentration of 154 mM.

4.3 Bovine Serum Albumin

This section shows the results of the standard TQTPPI measurements using the model system BSA. Subsection 4.3.1 presents the results of a competitive binding of potassium ions with sodium ions for the interactions sites yielding a sodium TQ signal. Subsection 4.3.2 and Subsection 4.3.3 show the result of a possible sodium TQ signal dependence on pH and the protein folding state, respectively.

4.3.1 Competitive Binding of Sodium Ions with Potassium Ions

Figure 4.2 presents the results of the standard TQTPPI measurements upon addition of up to 145 mM KCl in the 10% w/v BSA samples with 145 mM NaCl. The addition of up to 50 mM KCl did not change the A_{TQ}/A_{SQ} ratio within its standard deviation (Figure 4.2b). Higher concentrations of KCl yielded a substantial decrease in the A_{TQ}/A_{SQ} ratio. Addition of 145 mM KCl reduced the A_{TQ}/A_{SQ} ratio by $20.9 \pm 3.0\%$ compared to the A_{TQ}/A_{SQ} ratio of the sample with 0 mM KCl. These reductions in the sodium TQ signal correlate with an increase in both transverse relaxation times (Figure 4.2a). T_{2S} increased from 36.0 ± 0.1 ms to 37.2 ± 0.3 ms in the presence of potassium, while T_{2F} increased from 28.0 ± 0.1 ms to 29.4 ± 0.5 ms. This increase in the transverse relaxation times changed the optimal evolution time for maximum sodium TQ signal from 31.7 ± 0.1 ms to 33.0 ± 0.3 ms. The values of the fraction of the slow component A_{SQS}/A_{SQ} showed no clear trend upon addition of KCl (Figure 4.2a). The sodium SQ FWHM was in the range of 24–34 Hz for all samples.

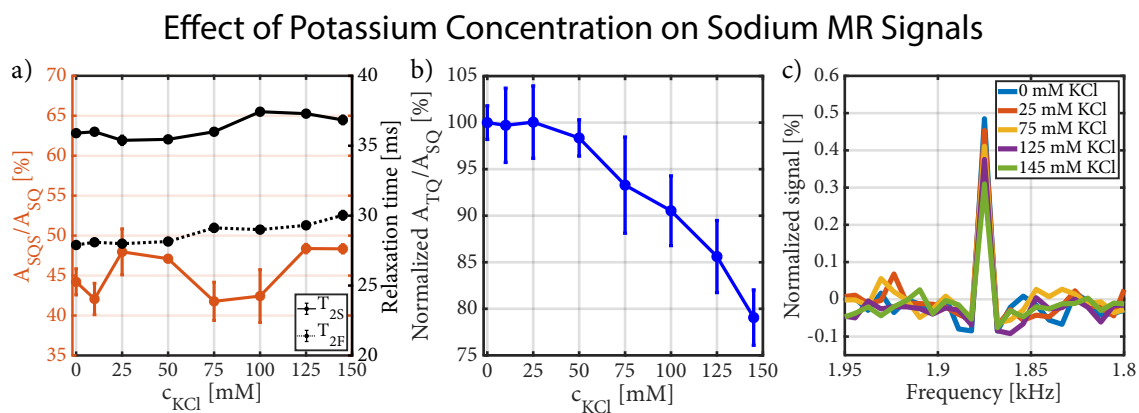


Figure 4.2: a) Dependence of sodium transverse relaxation times and the fraction of the slow component on the potassium concentration in the 10% w/v BSA samples. An increase in the potassium concentration up to 145 mM resulted in a slight increase in both transverse relaxation times. b) Dependence of the sodium TQ signal on the potassium concentration in the BSA samples. An increase in the potassium concentration of up to 50 mM did not change the ratio of A_{TQ}/A_{SQ} within its standard deviation. Addition of 145 mM KCl reduced the value of A_{TQ}/A_{SQ} by $20.9 \pm 3.0\%$. c) Zoomed TQTPPI spectra for different potassium concentrations.

4.3.2 Variation of the pH Value

To investigate a possible pH dependence of the sodium TQ signal, the pH in 10% w/v BSA samples with 154 mM Na⁺ was varied over a wide range of 0.70 to 13.05. Figure 4.3 presents the results of the standard TQTPPI measurements upon variation of pH. The ratio of A_{TQ}/A_{SQ} at the extremely low pH of 0.70 to 2.09 was constant at an average value of $1.27 \pm 0.07\%$. This was a reduction by $20 \pm 7\%$ compared with the average A_{TQ}/A_{SQ} ratio of $1.59 \pm 0.12\%$ at a pH of 3.55 to 6.50. An increase in the pH value from 6.50 to 8.84 yielded an almost linear increase in the ratio of A_{TQ}/A_{SQ} with pH (Figure 4.3b). In the samples with a pH of 8.84 to 9.64, the A_{TQ}/A_{SQ} ratio reached a constant value of $5.16 \pm 0.09\%$. This is an increase of the A_{TQ}/A_{SQ} ratio by $224.5 \pm 25.1\%$ relative to the average A_{TQ}/A_{SQ} value in the pH range of 3.55 to 6.50. An extremely high pH value of 13.05 resulted in a A_{TQ}/A_{SQ} ratio of $5.22 \pm 0.13\%$, which was within the standard deviation of the A_{TQ}/A_{SQ} ratio for a pH of 8.84 to 9.64. Consequently, the maximum sodium TQ signal was already reached at a pH value of 8.84. The fitting analysis of the sodium TQ measurement during pH variation by a sigmoid function (Equation 3.12) yielded a transition midpoint at a pH of 7.60 ± 0.11 and a growth rate of $2.05 \pm 0.401/\text{pH}$ (Table 4.3).

In addition to the increase in the sodium TQ signal, both transverse relaxation times decreased for increasing pH, while T_{2F} decreased at a higher rate than T_{2S} (Figure 4.3a). At the low pH values of 0.70 to 3.55, T_{2S} and T_{2F} were 44.5 ± 0.7 ms and 34.2 ± 0.4 ms,

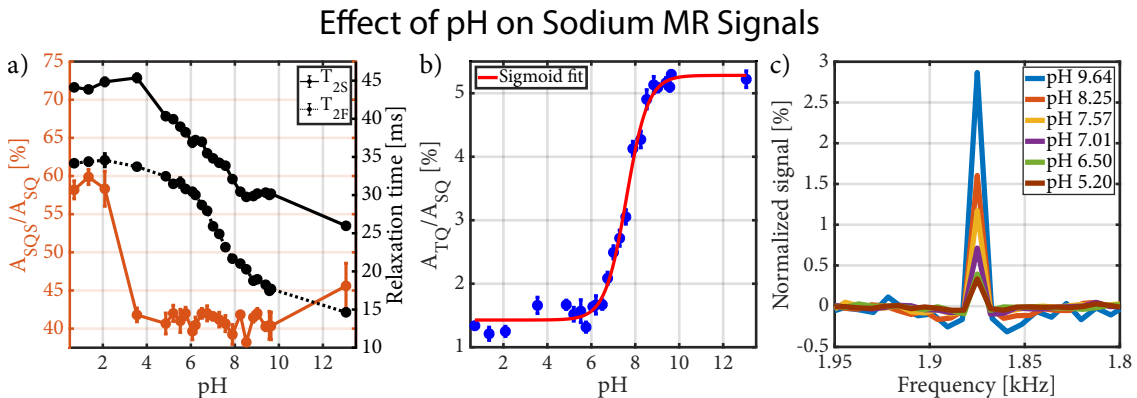


Figure 4.3: a) Dependence of sodium transverse relaxation times and the fraction of the slow component A_{SQS}/A_{SQ} on pH in the 10% w/v BSA samples. T_{2F} showed a much faster decrease at the high pH values compared to T_{2S} . b) Dependence of the sodium TQ signal on pH in the BSA samples. The A_{TQ}/A_{SQ} ratio remained relatively unchanged up to pH 6.50. Between pH 6.50 and 8.84, the ratio of A_{TQ}/A_{SQ} increased with pH, which correlates with the fact that at higher pH values the availability of negatively charged groups is increasing (Figure 2.16). Table 4.3 shows the results of the sigmoid fit. c) Zoomed standard TQTPPI spectra for different pH values. Reprinted with permission from Kleimaier et al. (2020c) published by John Wiley & Sons.

respectively. For the pH range of 8.84 to 9.64, T_{2S} and T_{2F} decreased to 30.1 ± 0.2 ms and 18.2 ± 0.6 ms, respectively. A further reduction of T_{2S} and T_{2F} to 25.9 ± 0.1 ms and 14.6 ± 0.2 ms was observed for the extremely high pH value of 13.05, respectively. The longitudinal relaxation times were close in value to T_{2S} for all samples.

The change in the fraction of the slow component is shown in Figure 4.3a. The ratio of A_{SQS}/A_{SQ} was $58.8 \pm 0.9\%$ for the pH values of 0.70 to 2.09. In the pH range of 3.55 to 9.64, the ratios of A_{SQS}/A_{SQ} were unchanged at an average value of $41.2 \pm 0.9\%$. The ratio of A_{SQS}/A_{SQ} increased to $45.6 \pm 2.9\%$ for pH 13.05. The sodium SQ FWHM was in the range of 25–30 Hz for all samples.

4.3.3 Urea-induced Unfolding of BSA

To investigate a possible dependence of the sodium TQ signal on the protein folding state, urea was added to samples containing 5% w/v BSA and 154 mM NaCl. Figure 4.4 presents the change in the sodium MR and fluorescence signals during BSA unfolding by urea. In the control experiments of samples containing urea without BSA, no significant sodium TQ signal was found. The sodium TQ SNR was -2.4 , -0.1 and $1.0 (\pm 0.1)$ for 0, 5.5 and 8 M urea, respectively. Figure 4.4d shows the standard TQTPPI spectrum of the sample containing 8 M urea and 154 mM NaCl without BSA. In contrast to the control experiments, a significant sodium TQ SNR of at least 24.3 ± 0.1 was measured in samples containing BSA during the unfolding experiments. Hence, the presence of urea did not produce any background sodium TQ signal in our unfolding experiments. The addition of urea substantially reduced the sodium MR relaxation times. The T_2 relaxation times were 50.6, 34.7 and 25.2 (± 0.1) ms for the samples with 0, 5.5 and 8 M urea, respectively. In the unfolding experiments, a similar reduction in the sodium relaxation times was observed (Figure 4.4a). In the control and unfolding experiments, the longitudinal relaxation times were close to the corresponding T_2 or T_{2S} values.

Table 4.3: Sigmoid function fit of the results for sodium TQ MR signal and fluorescent response.

Fit parameter	A_{TQ}/A_{SQ} vs pH	A_{TQ}/A_{SQ} vs c_{urea}	Fluorescence signal vs c_{urea}
A	$1.43 \pm 0.12\%$	0%	0%
B	$5.28 \pm 0.18\%$	$43.22 \pm 11.64\%$	$46.04 \pm 7.94\%$
V_{50}	7.60 ± 0.11 pH	5.73 ± 0.60 M	5.92 ± 0.35 M
C	2.05 ± 0.40 1/pH	1.48 ± 1.14 1/M	1.89 ± 1.06 1/M

Sigmoid function is presented by Equation 3.12. A is the minimum value, B is the maximum value, V_{50} is the transition midpoint of the sigmoid function and C is the growth rate.

Figure 4.4b shows the relative change in the sodium TQ and the fluorescence signals in the unfolding experiments. Addition of up to 4 M urea did not change the sodium TQ signal within its standard deviation relative to the 0 M urea sample. For higher urea concentrations, the sodium TQ signal increased and reached a constant value above 7 M urea. The sodium TQ signal increased by $40.7 \pm 2.3\%$ for 7–8 M urea relative to the sample with 0 M urea. In addition to the increase in the sodium TQ signal, the fraction of the slow component A_{SQS}/A_{SQ} changed from $49.5 \pm 4.2\%$ to $59.6 \pm 4.6\%$ for 0 and 1–2 M urea, respectively. The ratio of A_{SQS}/A_{SQ} reached a plateau of $52.1 \pm 1.9\%$ for 3–5.5 M urea. For 6–8 M urea, the value of A_{SQS}/A_{SQ} decreased to $42.2 \pm 1.1\%$. The sodium SQ FWHM was in the range of 25–30 Hz for all samples.

The above observed sodium TQ signal changes were compared with the results of fluorescence measurements, which represent an established method to detect protein unfolding. For the fluorescence measurements, the signals from two intrinsic tryptophan residues of BSA were used. Figure 4.4b and Figure 4.4c present the changes of the fluorescence spectra reflecting the protein denaturation. It is important to note that the A_{TQ}/A_{SQ} y-axis in Figure 4.4b was reverted to overlay the results of the sodium TQ experiments with the data from the fluorescence experiments. Both experiments revealed a similar sigmoidal shape during BSA unfolding by urea. Correlation analysis resulted in a negative linear correlation of the A_{TQ}/A_{SQ} ratio with the fluorescence signal (PCC = -0.99 , $p < 0.01$). This indicated a high correlation of the sodium TQ signal with the protein folding state. A sigmoid fit of both denaturation curves also revealed a similar transition midpoint at ~ 5.7 – 5.9 M urea (Table 4.3). Complete unfolding of BSA by urea was reached above 7 M urea in both experiments.

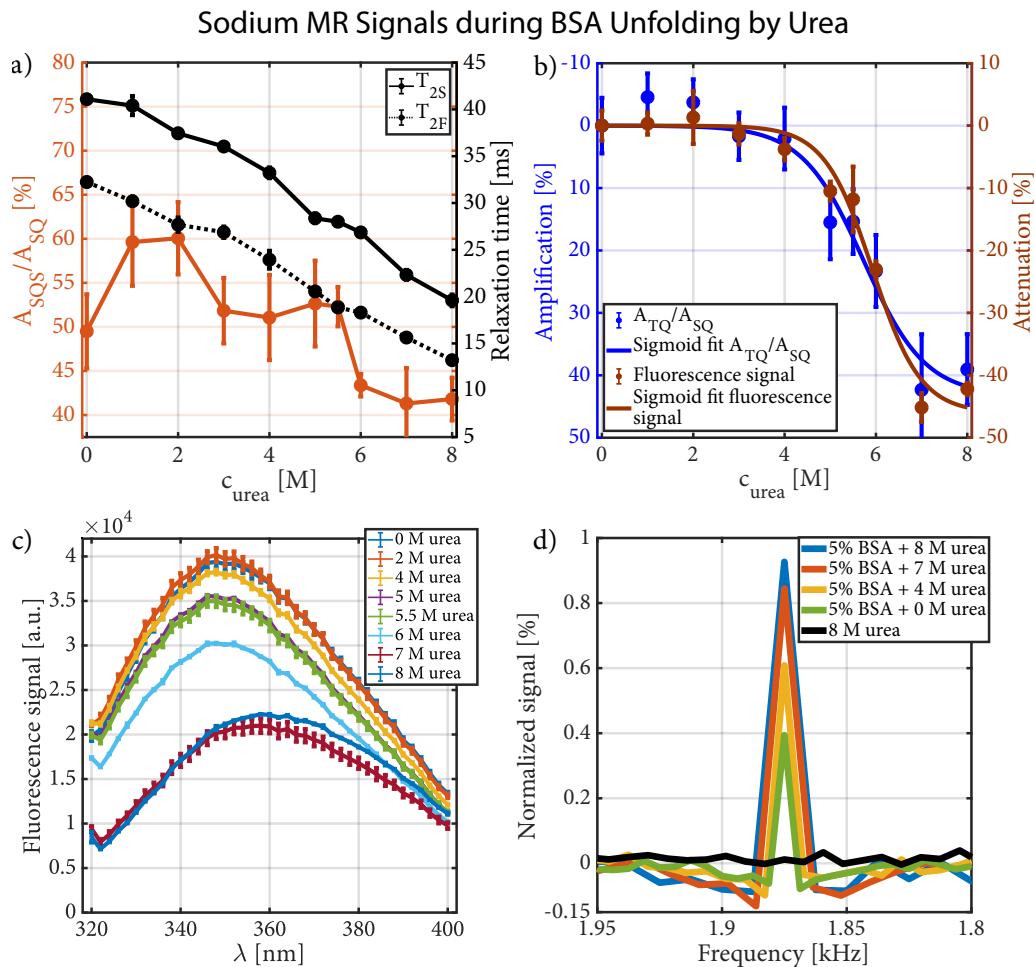


Figure 4.4: a) Dependence of sodium transverse relaxation times and the fraction of the slow component on the urea concentration in the samples during the BSA unfolding experiments. The addition of urea caused a reduction in both sodium transverse relaxation times and in the percentage of A_{SQS}/A_{SQ} . b) Comparison of the A_{TQ}/A_{SQ} ratio and the fluorescence signal at different urea concentrations in the samples during the BSA unfolding experiments. The A_{TQ}/A_{SQ} y-axis was inverted for a better comparison of the shapes of the TQ signal with denaturation curve detected by fluorescence signal. For calculation of the relative changes in both curves, the measurement with 0 M urea was used as a 100% reference. Both denaturation curves show a similar sigmoidal shape (Table 4.3) and the correlation analysis revealed a negative linear correlation of the A_{TQ}/A_{SQ} ratio to the fluorescence signal (PCC = -0.99). c) Fluorescence spectra of 5% w/v BSA at different urea concentrations. Protein unfolding reduced the fluorescence signal. d) Zoomed standard TQTPPI spectra of 5% w/v BSA at different urea concentrations as well as for 8 M urea without BSA are shown. Urea alone, without BSA, even at a concentration of 8 M urea did not create any sodium TQ signal. Reprinted with permission from Kleimaier et al. (2020c) published by John Wiley & Sons.

4.4 Comparison of the Standard and the Fixed TQTPPI Pulse Sequences

This section presents the results of the comparison of the sodium TQ SNR and transverse relaxation times between the standard and the fixed TQTPPI pulse sequences using agarose samples. The fixed TQTPPI pulse sequence (Section 3.2.4), which results in a higher TQ signal sensitivity, was developed in this thesis. Figure 4.5 shows an exemplary FID and spectrum for the standard and the fixed TQTPPI pulse sequences using 4% agarose in 134.75 mM NaCl. In contrast to the standard TQTPPI FID, the fixed TQTPPI FID does not contain any relaxation effects as the evolution time is optimized and fixed throughout the pulse sequence. The remaining oscillations in the fixed TQTPPI FID are caused by the RF phase increment, which results in SQ and TQ signals at distinct frequencies after Fourier transformation (Figure 4.5d).

Table 4.4 lists the sodium TQ SNR comparison of the FID fit results of the standard and the fixed TQTPPI pulse sequences using agarose samples. It is important to note that the amplitudes of the sodium SQ and TQ signals of the standard TQTPPI FID were corrected to the optimal evolution time, which was used for the fixed TQTPPI pulse sequence, by using Equation 3.4. For all agarose samples, the values of A_{SQ} , A_{TQ} and A_{TQ}/A_{SQ} agreed within the 95% confidence interval determined by the nonlinear FID fit. The expected theoretical sodium TQ SNR gain for the fixed TQTPPI pulse sequence with the optimized and fixed evolution time was in the range of 2.4 to 3.2 for the agarose samples compared to the standard TQTPPI pulse sequence with the evolution time increment. Based on the sodium TQ amplitude and its standard deviation, the measured sodium TQ SNR gain was in the range of 3.2 to 3.8. Fewer fitting parameters for the fixed TQTPPI FID fit compared

Table 4.4: Comparison of the SQ and the TQ amplitudes of agarose samples for the standard and the fixed TQTPPI pulse sequences.

Agarose [%]	TQTPPI sequence	A_{SQ} [10^6 a.u.]	A_{TQ} [10^6 a.u.]	A_{TQ}/A_{SQ} [%]	TQ SNR gain theoretical	TQ SNR gain measured
2	standard	28.92 ± 0.39	7.84 ± 0.12	27.1 ± 1.6		
	fixed	28.64 ± 0.03	7.67 ± 0.03	26.8 ± 0.1	2.4 ± 0.1	3.2 ± 0.4
4	standard	20.00 ± 0.03	9.01 ± 0.08	45.1 ± 1.9		
	fixed	20.18 ± 0.01	8.95 ± 0.02	44.3 ± 0.1	2.9 ± 0.1	3.6 ± 0.1
6	standard	22.38 ± 0.27	11.66 ± 0.12	52.1 ± 1.4		
	fixed	22.58 ± 0.03	11.71 ± 0.03	51.9 ± 0.2	3.2 ± 0.1	3.8 ± 0.2

A_{SQ} and A_{TQ} of the standard TQTPPI pulse sequence were corrected to τ_{opt} , which corresponded to the used evolution time of the fixed TQTPPI pulse sequence, by using Equation 3.4.

Table 4.5: Comparison of the transverse relaxation times between the standard and the fixed TQTPPI pulse sequences using agarose samples.

Agarose [%]	TQTPPI sequence	T_{2S} [ms]	T_{2F} [ms]	τ_{opt} [ms]
2	standard	41.1 ± 1.7	10.3 ± 0.1	19.0 ± 0.3
	fixed	43.2 ± 1.1	9.9 ± 0.2	18.8 ± 0.3
4	standard	34.2 ± 0.8	5.8 ± 0.1	12.4 ± 0.1
	fixed	33.9 ± 0.7	5.8 ± 0.1	12.3 ± 0.2
6	standard	30.0 ± 0.4	4.4 ± 0.1	9.8 ± 0.1
	fixed	32.2 ± 1.5	4.2 ± 0.2	9.9 ± 0.3

A simultaneous fit of the SQ and the TQ amplitudes for different evolution times by Equation 3.8 and Equation 3.9 yielded the transverse relaxation times of the fixed TQTPPI pulse sequence, respectively. The optimal evolution time was calculated according to Equation 3.6.

to the standard TQTPPI FID fit (cf. Equation 3.7 and Equation 3.4) could explain the higher measured sodium TQ SNR gain.

Table 4.5 lists the transverse relaxation times determined by both TQTPPI pulse sequences using agarose samples. To obtain the transverse relaxation times from the fixed TQTPPI pulse sequence, the evolution time was varied and the amplitudes of A_{SQ} and A_{TQ} were simultaneously fitted to their transfer functions using Equation 3.8 and Equation 3.9, respectively. Both TQTPPI pulse sequences resulted in the same values for T_{2S} , T_{2F} and τ_{opt} within the 95% confidence interval.

In summary, the fixed TQTPPI pulse sequence yielded the same values for A_{SQ} , A_{TQ} and the transverse relaxation times compared to the standard TQTPPI pulse sequence. But the fixed TQTPPI pulse sequence with the optimized and fixed evolution time resulted in an improved sodium TQ signal sensitivity (Table 4.4).

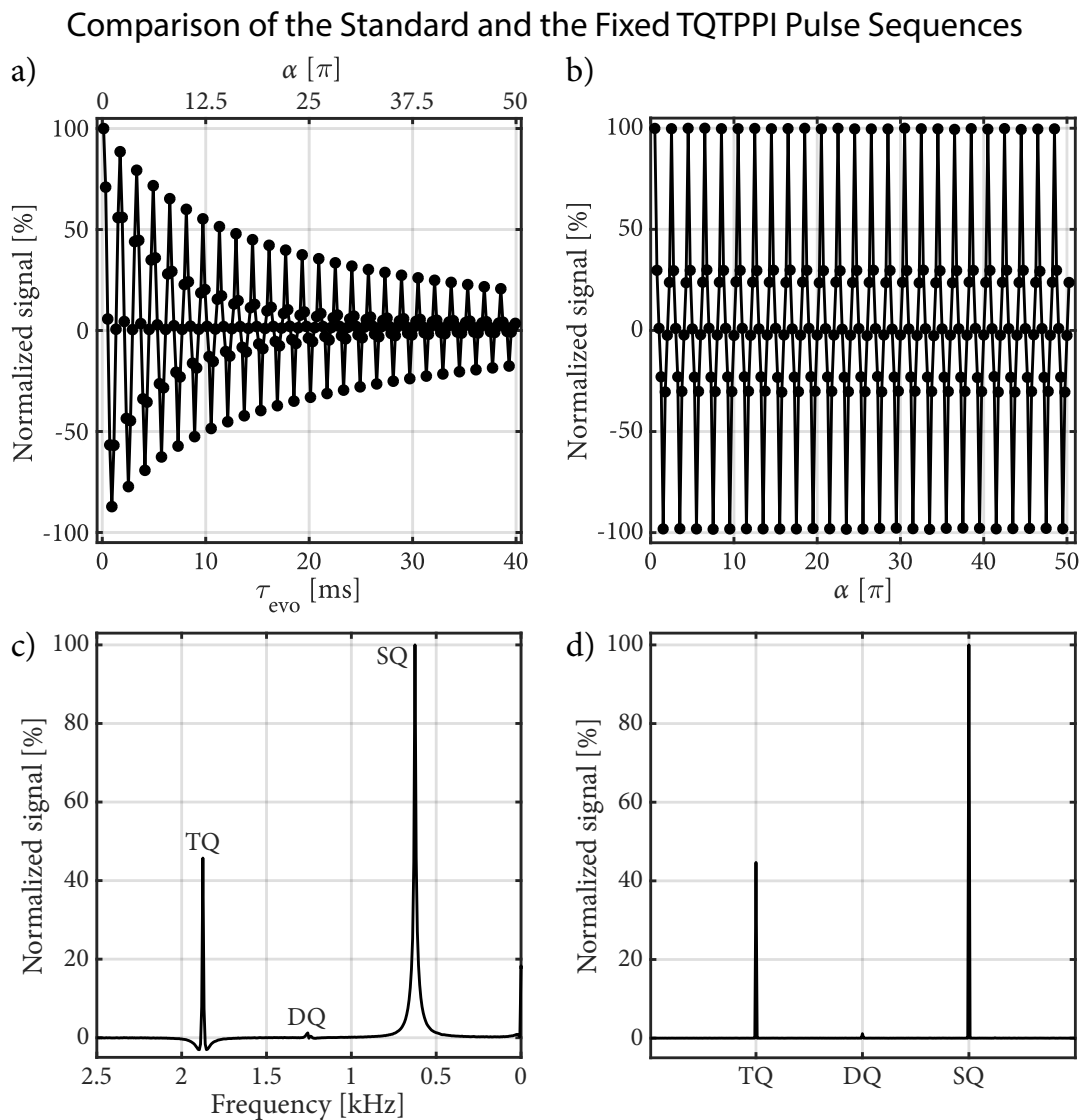


Figure 4.5: a) Standard TQTPPI FID of 4% agarose in 134.75 mM NaCl. The standard TQTPPI pulse sequence has an equal optimal detection of TQ signals for a wide range of ion interaction strengths due to the evolution time increment. However, this does not result in a maximum TQ signal sensitivity. b) Fixed TQTPPI FID of 4% agarose in 134.75 mM NaCl. The fixed TQTPPI pulse sequence uses an optimized and fixed evolution time throughout the pulse sequence, while it preserves the RF phase increment to yield SQ and TQ signals at distinct frequencies after Fourier transformation. c) Standard TQTPPI spectrum of a). The lineshape of the different coherences are Lorentzian functions. d) Fixed TQTPPI spectrum of b). The different coherences are close to delta functions. Reprinted with permission from Kleimaier et al. (2020f) published by MDPI.

4.5 Sodium TQ Spectroscopy of the MR-compatible Bioreactor System

This section presents the results of the capability of monitoring intracellular sodium alterations by an inhibition of the Na/K-ATPase of HepG2 cells for 60 min using the sodium TQ signal. Subsection 4.5.1 shows the contributions to the sodium TQ signal from the bioreactor using an optimized and fixed evolution time for maximum sodium TQ signal. Subsection 4.5.2 presents the results of the Na/K-ATPase inhibition by 1 mM ouabain or by 0 mM K⁺ medium for 60 min using sodium TQ signal.

4.5.1 Contributions to the Sodium TQ Signal

Figure 4.6 illustrates the contributions to the sodium TQ signal from the bioreactor and the optimal evolution time for maximum sodium TQ signal before and after the inhibition

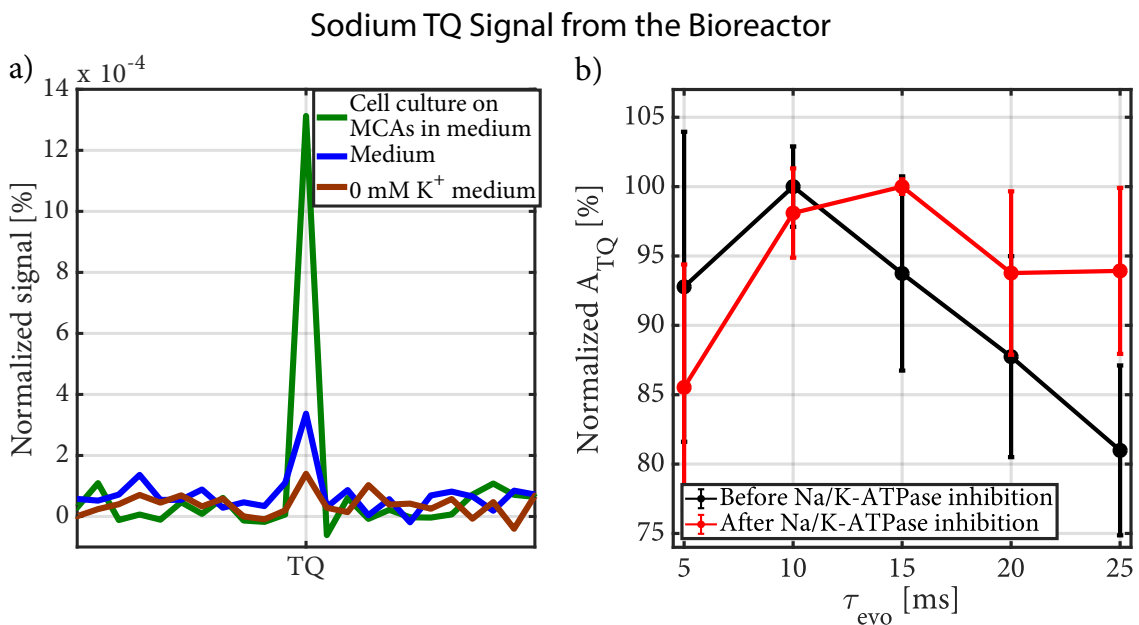


Figure 4.6: a) Sodium TQ signal of 0 mM K⁺ medium, normal medium and a 3D cell culture on collagenized MCAs in medium from the MR-compatible bioreactor system. The sodium TQ signal in 0 mM K⁺ medium was $A_{TQ}/A_{SQ} = 0.02 \pm 0.01\%$, which could be caused by incomplete relaxation. Proteins in normal medium resulted in a sodium TQ signal of $A_{TQ}/A_{SQ} = 0.04 \pm 0.01\%$, while the sodium TQ signal substantially increased in the presence of a 3D cell culture to $A_{TQ}/A_{SQ} = 0.13 \pm 0.04\%$. b) Optimization of the evolution time for maximum sodium TQ signal before and after the Na/K-ATPase inhibition. The optimal evolution time for maximum sodium TQ signal was between 10 and 15 ms in both cases. Reprinted with permission from Kleimaier et al. (2020f) published by MDPI.

of the Na/K-ATPase. The 0 mM K⁺ medium, which consisted of inorganic salts and glucose, resulted in a sodium TQ signal of $A_{TQ}/A_{SQ} = 0.02 \pm 0.01\%$. This tiny sodium TQ signal could be caused by incomplete relaxation as $T_R \approx 3.6T_1$. The background sodium TQ signal of proteins in normal medium was $A_{TQ}/A_{SQ} = 0.04 \pm 0.01\%$. The sodium TQ signal substantially increased by more than a factor of three to $A_{TQ}/A_{SQ} = 0.13 \pm 0.04\%$ in the presence of $12\text{--}14 \cdot 10^6$ HepG2 cells. Hence, the main contributor to the sodium TQ signal from the bioreactor was the 3D cell culture, while proteins in medium resulted in a small background sodium TQ signal.

The optimization of the evolution time for maximum sodium TQ signal was performed in the presence of a 3D cell culture (Figure 4.6b). The maximum sodium TQ signal was obtained for an evolution time of approximately 10 ms before the Na/K-ATPase inhibition. After the dynamic measurements of the Na/K-ATPase inhibition, additional optimization experiments for maximum sodium TQ signal were performed. In these optimization experiments, which corresponded to approximately 6 h after the Na/K-ATPase inhibition, the sodium TQ signal was more than a factor of two larger compared to the optimization experiments before the Na/K-ATPase inhibition. Hence, this sodium TQ signal should reflect less viable and dying cells. The optimal evolution time for maximum sodium TQ signal was between 10 and 15 ms in the optimization experiments after the Na/K-ATPase inhibition. Consequently, the optimal evolution time for maximum sodium TQ signal did not substantially change between both optimization experiments.

4.5.2 Inhibition of the Na/K-ATPase

Figure 4.7a visualizes the dynamic measurements of the sodium TQ signal during the Na/K-ATPase inhibition for 60 min using 1 mM ouabain ($n = 3$) or 0 mM K⁺ medium ($n = 3$). The start of the 1 mM ouabain medium or the 0 mM K⁺ medium was after 20 min. Arrival of the bolus in the bioreactor and the washout of the bolus from the bioreactor is indicated by the two gray shaded backgrounds. These time points for the arrival and washout of the bolus were determined using the ¹H MR contrast agent experiment (Figure 3.3). From 46–75 min the sodium TQ signal increased with an initial growth rate of $\sim 1.09\%/min$. Then the sodium TQ signal growth rate decreased to $\sim 0.05\%/min$ from 75–142 min and the sodium TQ signal reached an intermediate plateau of $138.9 \pm 4.1\%$. Reperfusion by normal medium increased the sodium TQ signal growth rate to $\sim 0.20\%/min$ and the sodium TQ signal reached a maximum of $169.2 \pm 5.3\%$ at the end of the dynamic measurement.

The Na/K-ATPase inhibition by 0 mM K⁺ medium resulted in a similar initial growth rate of the sodium TQ signal of $\sim 1.11\%/min$ from 46–120 min (Figure 4.7a). The time period of sodium TQ signal increase with the initial and maximum growth rate was much longer compared to the ouabain experiment. After 120–160 min the sodium TQ signal reached a plateau of $183.4 \pm 8.9\%$. Reperfusion by normal medium caused a partial recovery of the sodium TQ signal to $128.5 \pm 6.8\%$ within 20 min. The sodium TQ signal showed only fluctuations around this mean value until the end of the dynamic measurement (Figure 4.7a).

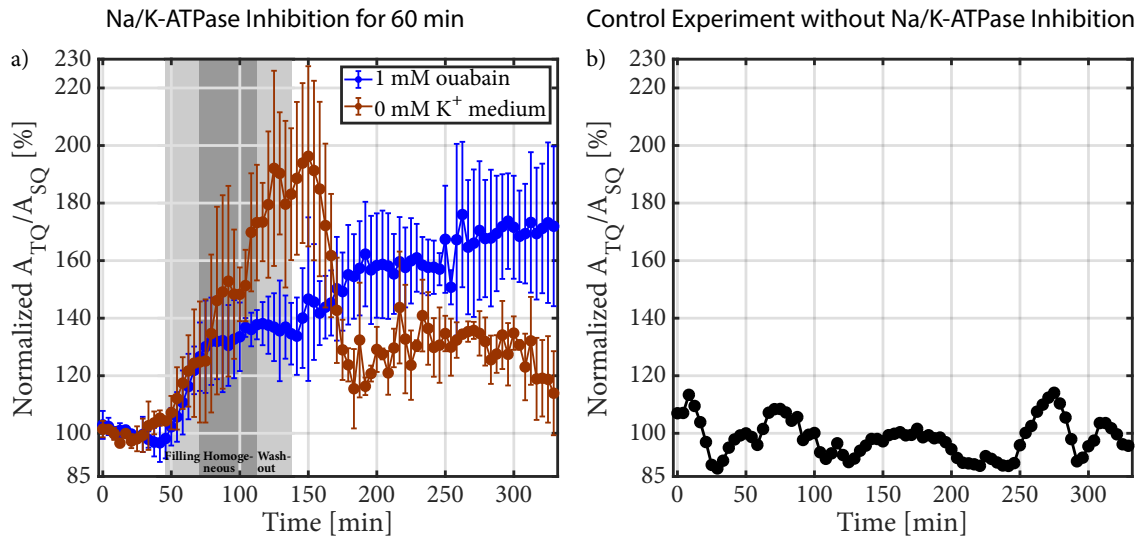


Figure 4.7: a) Sodium TQ signal time course during the Na/K-ATPase inhibition for 60 min using 1 mM ouabain ($n = 3$) or 0 mM K⁺ medium ($n = 3$). The dark gray shaded background indicates the homogeneous distribution of the bolus in the bioreactor, while the two light gray shaded backgrounds indicate the filling and washout of the bolus in the bioreactor. The bolus start was after 20 min. Both Na/K-ATPase inhibitions caused a similar initial increase in the sodium TQ signal. In the ouabain experiment, the sodium TQ signal reached an intermediate plateau of $138.9 \pm 4.1\%$ from 75–142 min. Reperfusion by normal medium led to a further increase in the sodium TQ signal to $169.2 \pm 5.3\%$, which indicated irreversible cell damage during ouabain perfusion. In the 0 mM K⁺ medium experiment, the sodium TQ signal reached a plateau of $183.4 \pm 8.9\%$ from 120–160 min, while reperfusion by normal medium resulted in a decrease of the sodium TQ signal to $128.5 \pm 6.8\%$. This indicated that the cells remained viable and partially restored the Na/K-ATPase pump activity. b) Dynamic measurement of the sodium TQ signal in the presence of a 3D cell culture but without Na/K-ATPase inhibition. The fluctuations of the sodium TQ signal around the mean value were smaller than the observed changes of the sodium TQ signal during the Na/K-ATPase inhibitions. Reprinted with permission from Kleimaier et al. (2020f) published by MDPI.

Temporal signal fluctuations potentially could alter the sodium TQ signal, which would confound the interpretation of sodium TQ signal changes during the Na/K-ATPase inhibition experiments. Figure 4.7b shows the temporal fluctuations of the sodium TQ signal in the presence of a 3D cell culture but without Na/K-ATPase inhibition. The changes in the sodium TQ signal during the Na/K-ATPase inhibition using 1 mM ouabain or 0 mM K⁺ medium were larger compared to the sodium TQ signal fluctuations around its mean value during the control measurement (cf. Figure 4.7a and Figure 4.7b).

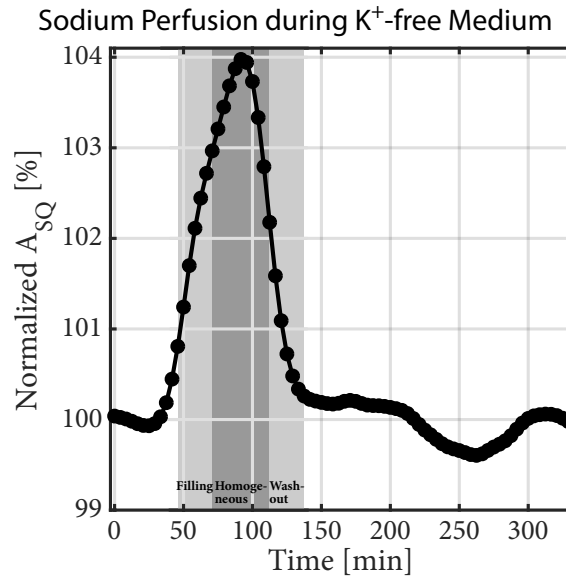


Figure 4.8: Changes in the sodium SQ signal during the 0 mM K^+ experiments ($n = 6$). The dark gray shaded background indicates the homogeneous distribution of the bolus in the bioreactor, while the two light gray shaded backgrounds indicate the filling and washout of the bolus in the bioreactor. The perfusion experiment with the MR contrast agent (Figure 3.3) was used to determine these time points. The sodium SQ signal increase was caused by a slight change in the sodium relaxation times and the sodium concentration for 0 mM K^+ medium compared to normal medium. The change in the sodium SQ signal agrees with the change in the water signal using an MR contrast agent (Figure 3.3). Reprinted with permission from Kleimaier et al. (2020f) published by MDPI.

Figure 4.8 shows the changes in the sodium SQ signal during the 0 mM K^+ experiments. The increase during the filling of the bioreactor with the 0 mM K^+ medium was caused by a minor difference in the sodium concentration and the sodium transverse relaxation times between normal medium and 0 mM K^+ medium. This minor difference allowed monitoring the sodium perfusion during the intervention in the presence of a 3D cell culture on MCAs. The perfusion curve using 1H MR contrast agent (Figure 3.3) showed a slightly later increase in the water signal compared to the increase in the sodium SQ signal during the 0 mM K^+ experiment (Figure 4.8). The use of a non-localized pulse sequence for the sodium measurements could explain this difference, as in the perfusion mode of the bioreactor the medium enters at the bottom and leaves the bioreactor on top (Figure 3.2). In the experiment with an MR contrast agent (Figure 3.3), the change in the water signal was determined in a slice, in the place which would contain the cell culture in the presence of MCAs. Despite this minor difference, the sodium perfusion curve agreed well with the perfusion curve using 1H MR contrast agent. The maximum sodium SQ signal increase during the 0 mM K^+ experiments was $103.9 \pm 0.1\%$ around 87.5–95.8 min. The sodium MR relaxation times $T_1 = 72.2 \pm 0.6$ ms and $T_2 = 67.8 \pm 0.6$ ms of the 0 mM K^+ medium

were slightly higher relative to the sodium MR relaxation times $T_1 = 69.9 \pm 0.6$ ms and $T_2 = 63.2 \pm 0.4$ ms of the normal medium. The 0 mM K^+ medium did not contain proteins or amino acids, which caused this slight increase in the sodium MR relaxation times of the 0 mM K^+ medium compared to the normal medium. Based on a mono-exponential T_2 decay, this increase in the sodium transverse relaxation time for the 0 mM K^+ medium relative to the normal medium resulted in a sodium SQ signal increase of $1.1 \pm 0.2\%$. A slightly increased sodium content in the 0 mM K^+ medium relative to the normal medium could explain the remaining increase in the sodium SQ signal.

4.6 CEST Spectroscopic Imaging of the MR-compatible Bioreactor System

This section presents the results of the dynamic measurement of the cellular heat shock response of living cells in the MR-compatible bioreactor system using the aliphatic rNOE CEST signal. Subsection 4.6.1 shows the contributors to the Z-spectrum from the bioreactor and the applicability of the 2-point contrast metric for reliable and fast high-resolution CEST imaging during the heat shock experiments. Subsection 4.6.2 presents the results of the control experiments, while Subsection 4.6.3 shows the results of the heat shock experiments of two independent 3D cell cultures.

4.6.1 Contributions to the Z-spectrum from the Bioreactor

There are three possible contributors to the Z-spectrum of the bioreactor: (i) The medium containing amino acids, metabolites and proteins; (ii) The MCAs which were collagenized to provide an extracellular matrix for the attachment of the cells and (iii) a 3D cell culture located on the MCAs. Figure 4.9a shows the contributions of medium, two collagenized MCAs in medium and a 3D cell culture on the collagenized MCAs in medium to the Z-spectrum. Only a small contribution of medium and collagenized MCAs to the Z-spectrum was observed, while the presence of a 3D cell culture led to distinctive CEST signals of amide, amine and guanidinium protons resonating around 3.5, 2.7 and 2.0 ppm. The aliphatic rNOE signal using the AREX metric was also more than three times larger compared to the rNOE signal from collagenized MCAs in medium (Table 4.6). Consequently, the CEST signals originated mainly from the 3D cell culture, while medium and collagenized MCAs contributed only to a small background rNOE signal. This is also visible in the -3.5 ppm AREX images of the three contributors shown in Figure 4.9b.

Table 4.6: Comparison of $\text{AREX}_{\Delta\text{ST}}$ and AREX for bioreactor.

	$\text{AREX}_{\Delta\text{ST}}$ [10^{-3} Hz]	$\text{AREX}(-3.5 \text{ ppm})$ [10^{-3} Hz]	Contribution of DS to $\text{AREX}_{\Delta\text{ST}}$ [10^{-3} Hz]	Contribution of ssMT to $\text{AREX}_{\Delta\text{ST}}$ [10^{-3} Hz]
Medium	2.8 ± 0.2	2.5 ± 0.1	0.2 ± 0.1	–
MCAs in medium	3.8 ± 0.4	3.5 ± 0.3	0.3 ± 0.1	–
Cell culture on MCAs in medium	13.9 ± 0.8	11.8 ± 0.4	1.4 ± 0.1	0.9 ± 0.2

Contribution of DS and ssMT to $\text{AREX}_{\Delta\text{ST}}$ were calculated using the Lorentzian fit result from the calculation of AREX. In Z-spectra of medium and MCAs in medium, no ssMT was apparent. Thus, for these samples the Lorentzian fit constituted only of DS.

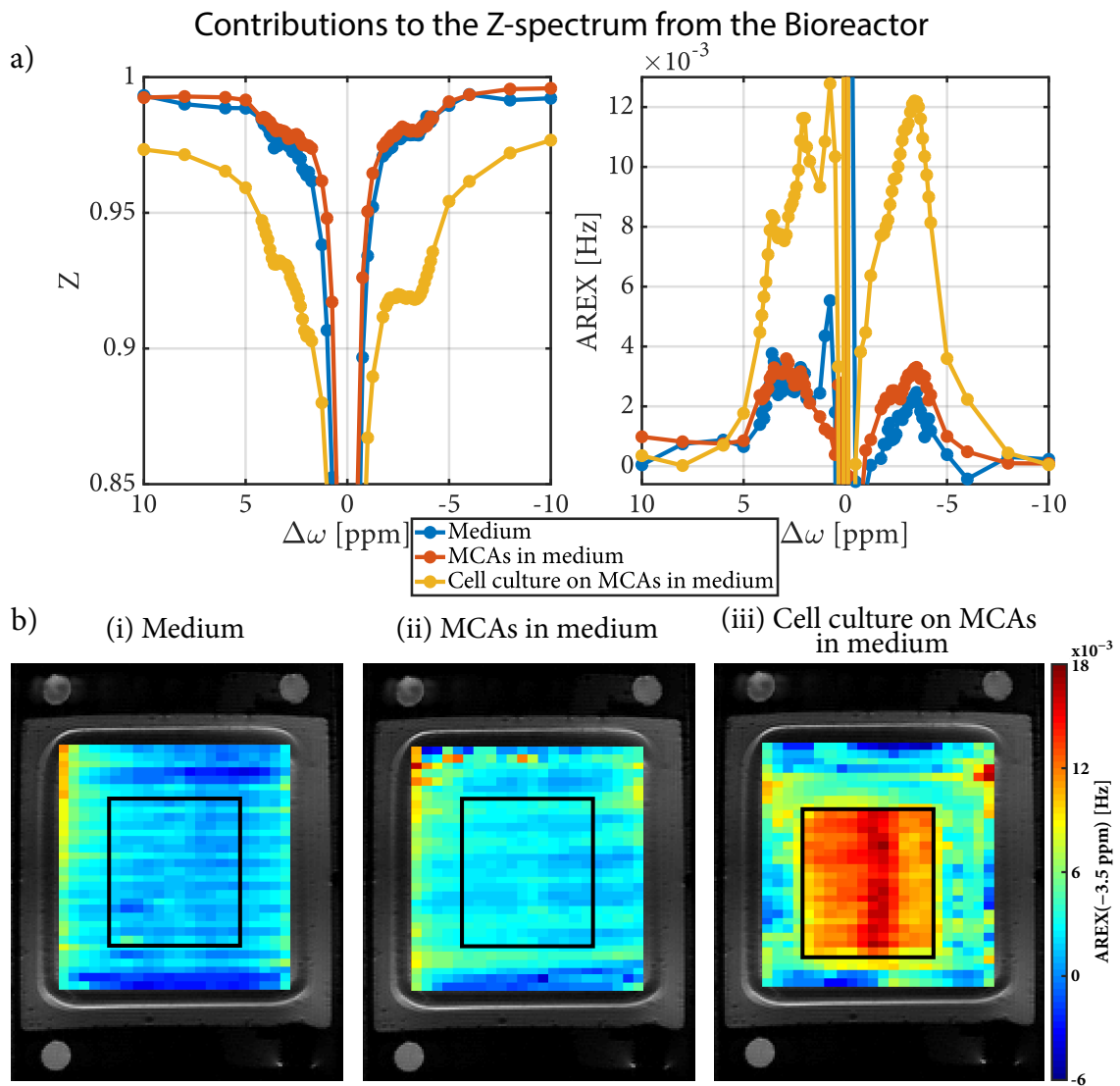


Figure 4.9: a) Contributions of CEST signals from medium, collagenized MCAs and cells to the total Z-spectrum and AREX spectrum ($B_0 = 9.4 \text{ T}$ and $B_1^+ = 0.8 \mu\text{T}$). The CEST signals originated mainly from the 3D cell culture of $16\text{--}18 \cdot 10^6$ HepG2 cells, while proteins in medium and collagenized MCAs contributed only to a small background rNOE signal (Table 4.6). b) rNOE AREX images of different contributions to the -3.5 ppm rNOE signal overlaid on a ^1H RARE image. In the two images without cells, a small rNOE signal across the bioreactor was observed, while the presence of cells led to distinct rNOE signals in the expected size and location of the cavity structure on the MCAs. Reprinted with permission from Kleimaier et al. (2020e) published by Springer Nature.

To monitor the cellular heat shock response by the rNOE CEST signal, a reliable and fast dynamic CEST technique was implemented. Chen et al. (2019) recently proposed a fast 2-point contrast metric $\text{AREX}_{\Delta\text{ST}}$ (Equation 3.11), which required only an offset

measurement at 8 ppm and -3.5 ppm. To investigate the applicability of this 2-point contrast metric to the bioreactor system, the Z-spectra shown in Figure 4.9a were analyzed by comparing the rNOE signal calculated by AREX and the above-mentioned 2-point contrast metric $\text{AREX}_{\Delta\text{ST}}$ (Equation 3.11). The AREX signal served as a reference, as it represents a quantitative parameter of isolated CE and rNOE signals. For all three samples, $\text{AREX}_{\Delta\text{ST}}$ resulted in an only slightly higher rNOE signal compared to the AREX reference signal (Table 4.6). The calculation of AREX required a Lorentzian fit of DS and ssMT. Based on the fit result, the residual contribution of DS and ssMT to $\text{AREX}_{\Delta\text{ST}}$ was estimated (Table 4.6). The residual contribution of DS and ssMT to $\text{AREX}_{\Delta\text{ST}}$ was approximately 10% and 6%, respectively. Without these residual contributions, AREX and $\text{AREX}_{\Delta\text{ST}}$ were the same within the standard deviation. Thus, the 2-point contrast metric suppressed the contribution of DS and ssMT to a high degree verifying the assignment of $\text{AREX}_{\Delta\text{ST}}$ to the rNOE signal. This allowed us to monitor the cellular heat shock response by fast dynamic measurements of the rNOE signal with a temporal resolution of 1 min.

4.6.2 Control Experiments

The rNOE signal potentially could also be altered by the effect of the heat shock on the background rNOE signals from medium and collagenized MCAs or by temporal signal fluctuations, which would confound the interpretation of rNOE signal changes during the heat shock experiments with cells. Figure 4.10a shows the effect of a 42°C heat shock for 20 min on the rNOE background signal from the collagenized MCAs in medium. The application of the heat shock had no significant impact on the background rNOE signal. Only during the heat shock an initial increase in the rNOE signal and thereafter a strong reduction was observed. This could be explained by a mismatch between the T_1 and CEST measurements or a prolonged T_1 at 42°C , which leads to reduced levels of saturation. As the temperature cooled down to 37°C , the rNOE signal was the same as before the heat shock and no further rNOE signal changes were observed. This was also confirmed by nearly identical AREX spectra before and after the dynamic measurements (Figure 4.10b). In all heat shock experiments, the full AREX spectra labelled as before and after the dynamic measurement were acquired at time 0 and 295 min of the rNOE signal time course, respectively. Figure 4.10c presents the temporal stability of the rNOE signal of a cell culture during dynamic measurements but without heat shock application. Again, the normalized rNOE signal showed only fluctuations around the mean value, while these fluctuations were smaller than in the dynamic measurement without a cell culture (cf. Figure 4.10a and Figure 4.10c, please note the different y-axis ranges). Almost equal AREX spectra confirmed that the rNOE signal was constant during the heat shock protocol (Figure 4.10d). Thus, the rNOE signal was stable over time and there was no detectable change of the background rNOE signal after the heat shock that would have originated from medium or collagenized MCAs.

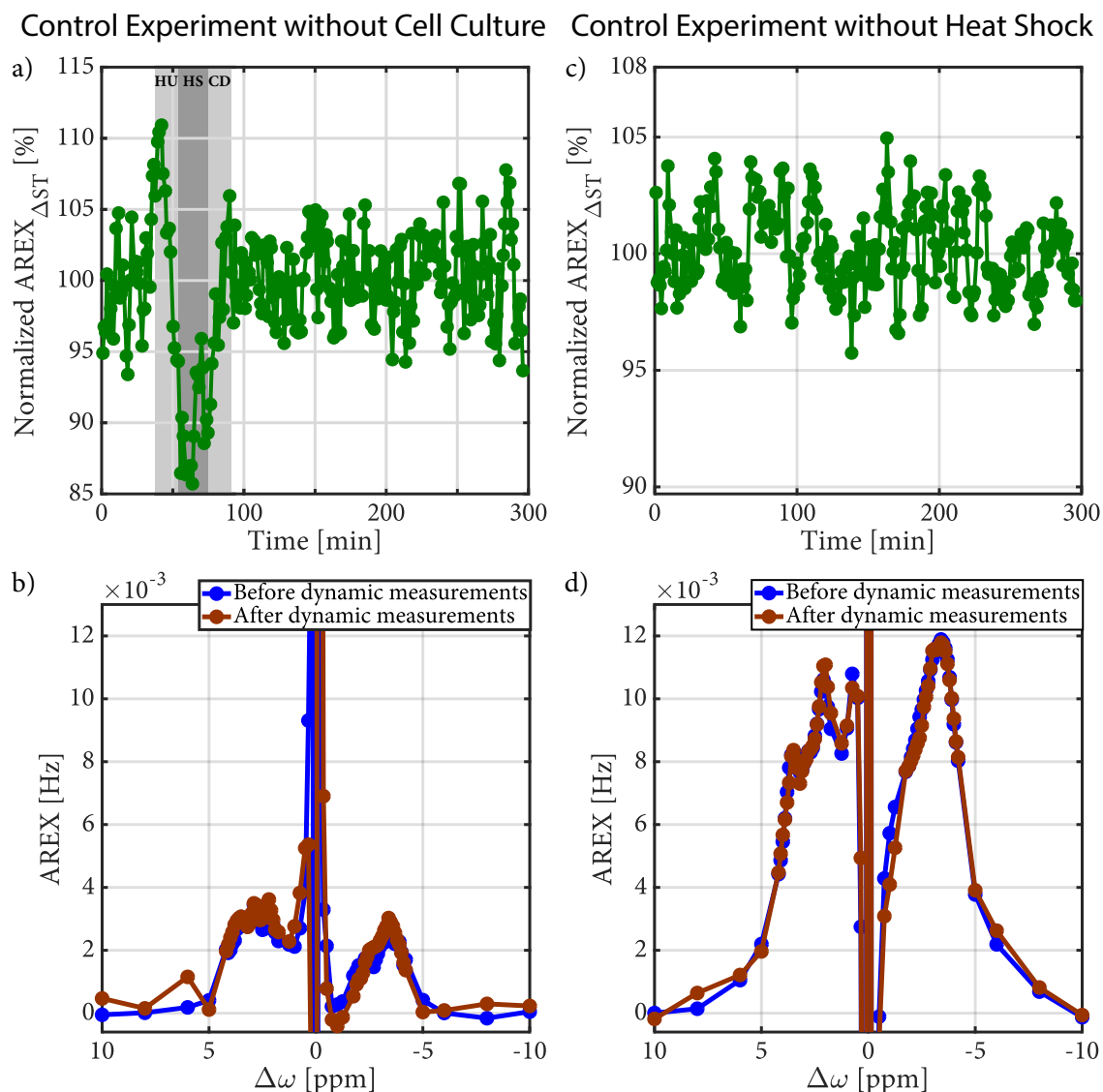


Figure 4.10: a) rNOE time course of the effect of the heat shock on collagenized MCAs in medium. The dark grey shaded background indicates the heat shock (HS) of 42°C, while the two light gray shaded backgrounds indicate the heat up (HU) to 42°C and the cool down (CD) to 37°C. c) Temporal stability of the rNOE signal from a cell culture during dynamic measurements but without heat shock application. The rNOE signal was constant over time, which was also confirmed by similar AREX spectra before and after dynamic measurements acquired at time 0 and 295 min respectively, as shown in b) and d). Reprinted with permission from Kleimaier et al. (2020e) published by Springer Nature.

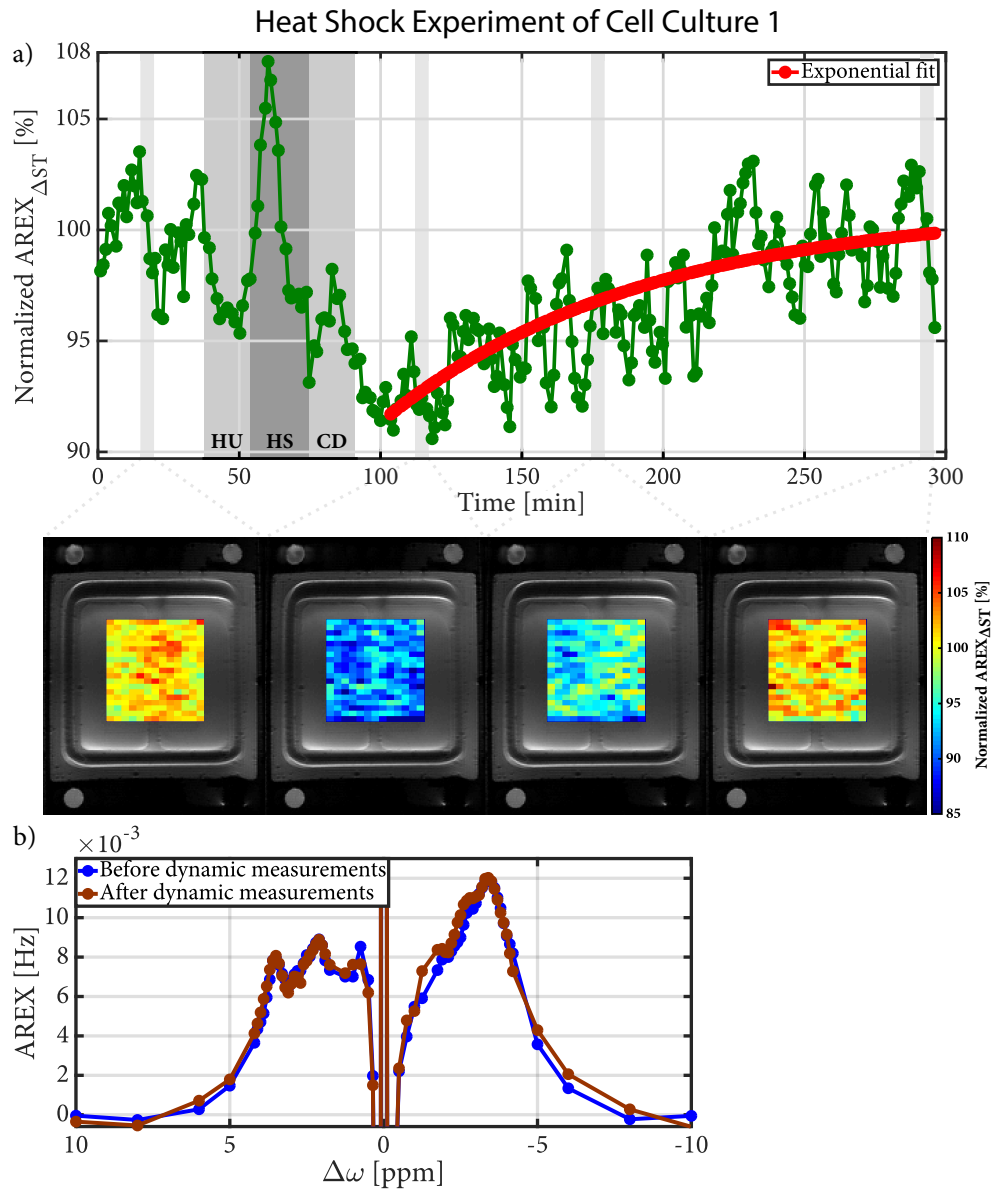


Figure 4.11: a) Time course of the rNOE signal from cell culture 1 during dynamic measurements. The heat shock (HS) of 42°C is indicated by the dark gray shaded background, while the two light gray shaded backgrounds close by indicate the heat up (HU) to 42°C and the cool down (CD) to 37°C. Below the time course, normalized $AREX_{\Delta ST}$ images of the cell area overlaid on a 1H RARE image are shown. After the heat shock, a substantial rNOE signal reduction of $8.3 \pm 1.1\%$ followed by an exponential recovery with a recovery time of 100.0 ± 52.5 min was observed. An rNOE signal recovery to the initial value was also confirmed by the AREX spectra before and after dynamic measurements acquired at time 0 and 295 min, respectively, which are shown in b). Reprinted with permission from Kleimaier et al. (2020e) published by Springer Nature.

4.6.3 Heat Shock Experiments

In two independent experiments, the cellular heat shock response to a mild, non-lethal heat shock was monitored by dynamic measurements of the rNOE CEST signal to verify the detectability of denaturation processes on a physiologically relevant scale. Figure 4.11 shows the change in the rNOE signal of cell culture 1 during dynamic measurements. Before the heat shock, the rNOE signal showed a small signal oscillation similarly to a previous study with the same bioreactor [Neubauer et al. (2017)]. After the cooling down to 37°C, the rNOE signal substantially decreased followed by a continuous rNOE signal increase. An exponential fit of the rNOE signal using Equation 3.13 revealed an rNOE signal reduction of $8.3 \pm 1.1\%$ ($Y_{\text{start}} = 91.7 \pm 1.1\%$) compared to the rNOE signal before heat shock application. The recovery time determined by the exponential fit was $T_{\text{rec}} = 100.0 \pm 52.5$ min. At the end of the dynamic measurements, the rNOE signal was $Y_{\text{end}} = 101.4 \pm 3.9\%$. Consequently, the rNOE signal was within its error the same value as before heat shock application as the rNOE signal was normalized to the first 37 min prior to the heat shock application. This was also confirmed by nearly identical AREX spectra before and after dynamic measurements (Figure 4.11b). A very similar rNOE signal response was observed with cell culture 2 during dynamic measurements (Figure 4.12a). After the temperature had reached 37°C again, a substantial reduction in the rNOE signal of $7.7 \pm 0.8\%$ ($Y_{\text{start}} = 92.3 \pm 0.8\%$) was measured, followed by an exponential-like recovery. The recovery time of $T_{\text{rec}} = 98.1 \pm 42.4$ min was comparable to cell culture 1. The rNOE signal at the end of the dynamic measurements was $Y_{\text{end}} = 101.0 \pm 2.0\%$, which within its error nicely corresponded to the initial rNOE signal. The nearly identical rNOE signal was further confirmed by both AREX spectra before and after dynamic measurements (Figure 4.12b). Additionally to the time courses, the CEST technique also allows the visualization of these rNOE signal changes in high-resolution images, see the rNOE maps below each time course in Figure 4.11a and Figure 4.12a. The inhomogeneity of the rNOE maps in Figure 4.11a originates from inherent signal fluctuations as the noise suppression was only applied on the ROI averaged time courses.

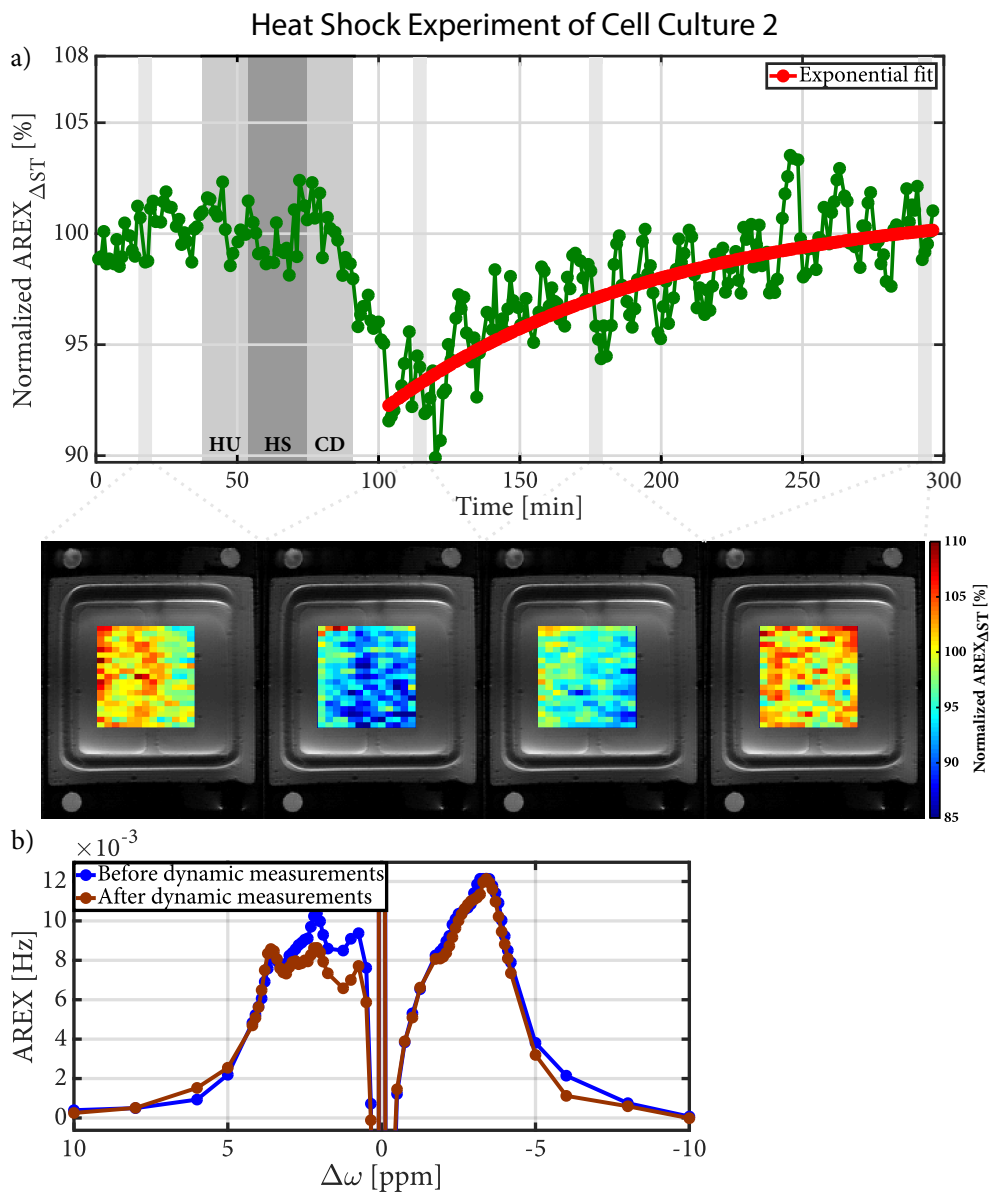


Figure 4.12: a) Time course of the rNOE signal from cell culture 2 during dynamic measurements. The dark gray shaded background indicates the heat shock (HS) of 42°C and the two light gray shaded backgrounds close by indicate the heat up (HU) to 42°C and the cool down (CD) to 37°C. Below the time course, normalized $AREX_{\Delta ST}$ images of the cell area overlaid on a 1H RARE image are shown. Similarly to the dynamic measurements of cell culture 1 (Figure 4.11), the rNOE signal substantially reduced by $7.7 \pm 0.8\%$ followed by an exponential recovery with a recovery time of 98.1 ± 42.4 min. A recovery of the rNOE signal to the initial value was also confirmed by the nearly identical AREX spectra before and after dynamic measurements acquired at time 0 and 295 min, respectively, which are shown in b). Reprinted with permission from Kleimaier et al. (2020e) published by Springer Nature.

5 Discussion

The main aim of this dissertation was the non-invasive investigation of proteins by NMR. Two different NMR signals were utilized for that: The sodium TQ signal and the rNOE CEST signal.

Electric quadrupole interactions of positively charged sodium ions with surrounding electric field gradients created by negatively charged groups within macromolecules, e.g. proteins, yield a sodium TQ signal. Consequently, the sodium TQ signal has an intrinsic selectivity and the intracellular sodium concentration contributes approximately 30–70% to the total sodium TQ signal. Experiments with a perfused rat heart system [Dizon et al. (1996), Schepkin et al. (1996), Schepkin et al. (1998), Schepkin et al. (1999), Choy et al. (1997) and Tauskela et al. (1997)], brain ischemia [LaVerde et al. (2007)] and tumors [Babsky et al. (2007) and Winter et al. (2001b)] demonstrated a correlation of sodium TQ signal increase with the loss of cell viability. However, recent investigations of living cells in an MR-compatible bioreactor system by our group indicated a reduction in the sodium TQ signal during ischemia [Hoesl et al. (2019a) and Hoesl et al. (2019b)] or Na/K-ATPase inhibition with simultaneous stop of perfusion [Neubauer et al. (2017)]. Hence, a deeper understanding of the origin of the sodium TQ signal is required to determine its capability to serve as a potential biomarker for cell viability.

On the other hand, the rNOE CEST signal, which can be mainly associated with mobile proteins and peptides [Yan et al. (2015)], has great potential for the non-invasive investigation of diseases associated with pathological changes in protein expression and proteome structure. The rNOE signal depends on the protein content [Jin et al. (2013) and Goerke et al. (2018)] and the protein folding state [Goerke et al. (2017), Goerke et al. (2015) and Zaiss et al. (2013c)], whereas the dependence on the protein folding state was yet only experimentally demonstrated in protein solutions and cell lysates. Therefore, the detectability of denaturation processes on a physiologically relevant scale in living organisms remained to be verified experimentally to obtain a deeper understanding of rNOE signal alterations *in vivo* and its capability to serve as a potential biomarker in diseases with aberrant protein folding states.

This chapter has three sections. In the first section, the results of the sodium TQ measurements using model solutions of agarose and BSA are discussed. For the first time, to the best of the author's knowledge, a dependence of the sodium TQ signal on pH and the protein folding state was demonstrated using the protein BSA. The second section discusses the results of the sodium TQ measurements of living cells using the MR-compatible bioreactor system. For the cell experiments, a fixed TQTPPI pulse sequence was developed,

which yields several times gain in TQ SNR, while it preserves the simultaneous measurement of the SQ and the TQ signals at distinct frequencies. The fixed TQTPPI pulse sequence enabled the detection of the signal of only $12\text{--}14 \cdot 10^6$ cells. Furthermore, the improved TQ signal sensitivity allowed the monitoring of the cellular response to a Na/K-ATPase inhibition by 1 mM ouabain or by 0 mM K^+ medium for 60 min in living cells using sodium TQ signal. The third section discusses the results of the dynamic monitoring of the cellular heat shock response to a mild, non-lethal heat shock using reliable and fast high-resolution CEST imaging of the rNOE signal. Parts of the discussion have been published in Kleimaier et al. (2020c)¹ by John Wiley & Sons, Kleimaier et al. (2020f)² by MDPI, and Kleimaier et al. (2020e)² by Springer Nature and the corresponding descriptions are replicated thereof.

5.1 Sodium TQ Spectroscopy of Model Solutions

Influence of B_0 Inhomogeneity on TQ Signal

It is well known that the TQ signal is sensitive to B_0 inhomogeneity [Tanase et al. (2005), Matthies et al. (2010), Fleysher et al. (2010), Fiege et al. (2013b), Tsang et al. (2013) and Hoesl et al. (2020)]. Consequently, the conventional TQ pulse sequence includes a 180° refocusing RF pulse between the first two 90° RF pulses to compensate for B_0 inhomogeneity (Figure 3.5). The use of a 180° refocusing RF pulse is not feasible in a clinical setting due to the SAR limitations, as it would lead to a long repetition time. Hence, dedicated RF phase cycles for the three RF pulse sequence have been developed to correct for TQ signal losses due to B_0 inhomogeneity [Tanase et al. (2005), Matthies et al. (2010), Fleysher et al. (2010), Fiege et al. (2013b) and Hoesl et al. (2020)]. For a non-localized pulse sequence, the refocusing RF pulse represents the only method to compensate for B_0 inhomogeneity. However, the performance of the refocusing RF pulse to compensate for B_0 inhomogeneity still remained to be verified.

A strong dependence of the sodium TQ signal on the FWHM of the sodium SQ signal despite the use of a 180° refocusing RF pulse was observed. The ratio of A_{TQ}/A_{SQ} at a SQ FWHM of ~ 240 Hz decreased by more than a factor of four compared to the A_{TQ}/A_{SQ} ratio at a SQ FWHM of ~ 45 Hz. This reduction in the sodium TQ signal for larger B_0 inhomogeneity was caused by a relative phase accumulation of the four TQ signal components, i.e. $\hat{T}_{3,1} \rightarrow \hat{T}_{3,3}$, $\hat{T}_{3,1} \rightarrow \hat{T}_{3,-3}$, $\hat{T}_{3,-1} \rightarrow \hat{T}_{3,3}$ and $\hat{T}_{3,-1} \rightarrow \hat{T}_{3,-3}$, during the evolution time. Thus, the sum of all four TQ signal components leads to a reduction in the TQ signal. To minimize the effects of B_1^+ deviations, which cause an incomplete refocusing of B_0 inhomogeneity during the evolution time, a small sized sample (length = 30 mm and diameter = 28 mm) was placed in the homogeneous part of a $^1\text{H}/^{23}\text{Na}$ Bruker volume coil. The B_1^+ deviation in the agarose sample was not measured, but in a larger sample the

¹©2020 The Authors. NMR in Biomedicine published by John Wiley & Sons Ltd

²Creative Commons Attribution 4.0 International License:
<https://creativecommons.org/licenses/by/4.0/>

B_1^+ deviation was less than 6.6% using this volume coil (Figure A.1a). Additionally, the bandwidth of the refocusing pulse of ~ 1900 Hz for a pulse duration of ~ 270 μ s should be sufficiently wide to yield a refocusing of the possible B_0 offsets.

Further investigations of the capability of the refocusing RF pulse to compensate for B_0 inhomogeneity are required. For example the three and the four RF pulse sequences can be compared for the same B_0 offsets, while a simulation of the four RF pulse sequence can additionally provide valuable insights for the limitations of the refocusing RF pulse. Nevertheless, the refocusing RF pulse is the only method to compensate for B_0 inhomogeneity using a non-localized spectroscopic pulse sequence. To ensure reproducible TQ measurements for an experimental series, the FWHM of the sodium SQ signal must be consistent. Furthermore, the reproducibility of TQ measurements between different sites can be increased by stating the FWHM of the sodium SQ signal.

Competitive Binding of Sodium Ions with Potassium Ions

In this part, a competitive binding of sodium and potassium ions was found for the interaction sites, which yield a sodium TQ signal, using the protein BSA.

The addition of 145 mM KCl to 10% w/v BSA with 145 mM NaCl caused a reduction in the A_{TQ}/A_{SQ} ratio by $20.9 \pm 3.0\%$ compared to the control sample with 0 mM KCl. In accordance with our results, Schepkin et al. (2017) observed a reduction in the sodium A_{TQ}/A_{SQ} ratio by $14.2 \pm 3.4\%$ and $10.8 \pm 3.1\%$ upon the addition of 154 mM KCl to 5% and 7.5% agarose in 154 mM NaCl compared to the control sample with 0 mM KCl, respectively. Similarly, in rat liver cell microsomes [Sanui et al. (1959)] as well as in human and dog erythrocyte ghosts [Sanui et al. (1962) and Sanui et al. (1963)] the addition of potassium ions reduced the amount of bound sodium ions compared to the amount of bound sodium ions in the absence of potassium ions. This reduction in the amount of bound sodium ions upon addition of potassium ions may indicate that the number of sodium ions interacting with negatively charged groups of macromolecules reduces upon addition of potassium ions. This can explain the observed decrease of the sodium TQ signal upon addition of potassium ions. This is also consistent with the observed slight increase in both transverse relaxation times upon addition of potassium ions. Such an increase in sodium relaxation times upon addition of potassium ions was also shown in the agarose samples [Schepkin et al. (2017)], in samples containing phosphatidylserine vesicles [Kurland et al. (1979)] and in micellar solutions [Romsted et al. (1993)]. Hence, potassium ions compete with sodium ions for the interaction sites of macromolecules, which yield a sodium TQ signal.

Influence of Protein Conformational Changes on TQ Signal

In this part, a dependence of the sodium TQ signal on pH using 10% w/v BSA samples over a wide pH range of 0.70 to 13.05 and on the protein folding state during urea-induced unfolding of BSA was observed.

In general, negatively charged groups within proteins are mainly found in the carboxyl-terminus and the amino acids, aspartic acid and glutamic acid (Figure 2.15). The observed increase in the A_{TQ}/A_{SQ} ratio by $224.5 \pm 25.1\%$ for a pH range of 6.50 to 8.84 (Figure 4.3) can be explained by a combination of the following two effects: (i) The protonation level of each carboxyl group depends on the dissociation constant pK_a . At low pH, almost all carboxyl groups are protonated and therefore are almost neutrally charged. With increasing pH, the availability of negatively charged groups increases as more carboxyl groups become deprotonated or more negatively charged. (ii) Oppositely charged groups within close range can interact via electrostatic interactions and form ion pairs. These ion pairs can contribute to the overall stability of the protein tertiary structure [Kumar et al. (2002)], while their numbers and strength of interaction also depend on pH. For increasing pH, the increase in available negatively charged groups and the reduction of available positively charged groups decreases the number of ion pairs, which also increases the availability of the negatively charged groups [Heinrich et al. (2014)]. Both effects lead to an increase in the availability of negatively charged groups and can contribute to the observed increase of the A_{TQ}/A_{SQ} ratio with increasing pH. However, which effect is more dominant has yet to be investigated. But the large increase in the sodium TQ signal during variation of pH underlines the importance of the availability of negatively charged groups for the creation of a sodium TQ signal. Increasing pH also caused a reduction in sodium relaxation times, which was also demonstrated for human erythrocytes over a pH range of 5.2 to 8.5 [Knubovets et al. (1996)]. The reduction in sodium relaxation times and increase of the sodium TQ signal for increasing pH are in accordance with the observed higher affinity of proteins for cations with increasing pH [Carr (1956), Pfister et al. (1964) and Saroff (1957)].

The extreme variation in pH can cause denaturation of BSA. According to Lin et al. (1976), the onset of acidic and alkaline denaturation of BSA is found around pH 5.0 and 9.5–10.0, respectively. For the pH range of 6.50 to 8.84, denaturation of BSA is not expected and therefore the increase in the sodium TQ signal in this pH range was a consequence of the reasons mentioned above. However, denaturation of BSA could have influenced the estimation of the minimum and maximum sodium TQ signals of 10% w/v BSA. For pH 0.70 to 2.09, an average sodium TQ signal of $A_{TQ}/A_{SQ} = 1.27 \pm 0.07\%$ was still found. In particular, at pH 0.70, the effect of negatively charged groups on the sodium TQ signal is minimized, because almost all of the negatively charged groups are protonated and therefore neutrally charged [Grimsley et al. (2009)]. For these very low pH values, the slow relaxing fraction of the sodium signal A_{SQS}/A_{SQ} changed to $58.8 \pm 0.9\%$ compared with $41.2 \pm 0.9\%$ for pH 3.55 to 9.56. The deviation of A_{SQS}/A_{SQ} from the theoretically expected value of 40% at low pH suggest that sodium ions were exposed to multiple environments with different bi-exponential or mono-exponential relaxation properties [Burstein et al. (2019)]. The fact that the sodium TQ signal was unchanged in the pH range of 0.70 to 2.09 can be attributed to protein unfolding and aggregation of BSA. At these low pH values, amine groups are positively charged (Figure 2.16) and, in combination with aggregation of BSA, could cause electric quadrupole interactions which are sufficient for the creation of a sodium TQ signal. Further investigations of different proteins with a minimized influence

of negatively charged groups using the sodium TQ signal are required to confirm this observation.

The observed pH dependence may affect the analysis of the sodium TQ signal in pathologies, such as ischemic stroke [Kobatake et al. (1984), Nedergaard et al. (1991) and Sako et al. (1985)] or tumor [White et al. (2017) and Marathe et al. (2016)]. LaVerde et al. (2007) investigated the sodium TQ signal in focal brain ischemia of a nonhuman primate model. After 0.6 hours the sodium TQ signal increased by $126 \pm 70\%$, and after 3 hours by $175 \pm 91\%$. It was concluded that these changes were only caused by an increased intracellular sodium concentration. However, both extra- and intracellular pH could drop to 6.2–6.9 during ischemia, depending on the duration of ischemia [Kobatake et al. (1984), Nedergaard et al. (1991) and Sako et al. (1985)]. According to estimates from the current study, a decrease in pH from 7.0 to 6.5 could cause a A_{TQ}/A_{SQ} reduction of $33 \pm 4\%$. Thus, the actual increase of the sodium TQ signal due to changes in the intracellular sodium content might have been larger than the values reported by LaVerde et al. (2007), as both the extra- and intracellular sodium TQ signal could have been decreased by a reduced pH. It is important to note that alterations in the sodium TQ signal due to changes in the intracellular sodium content or pH cannot be separated. To exclude the effect of pH changes on the sodium TQ signal, NMR-based methods to assess the pH can be used [Makela et al. (2001), Moon et al. (1973) and Pavuluri et al. (2017)].

Thus, in addition to biological and physical environmental factors, such as sodium [Schepkin et al. (1998) and Dizon et al. (1996)] and protein [Torres et al. (2005)] concentration, the sodium TQ signal depends on the availability of negatively charged groups and therefore on the pH value. This should be considered in the interpretation of sodium TQ signals from pathologies causing a pH change, for example ischemic conditions [Seshan et al. (1997), Schepkin et al. (1996), Neubauer et al. (2017), Hoesl et al. (2019a), Kalyanapuram et al. (1998), Tauskela et al. (1997), Colet et al. (1999) and Bansal et al. (1995)]. This pH dependence, however, cannot be used to directly measure the pH value, as sodium interactions with macromolecules are needed for the sodium TQ signal. Thus, without macromolecules, pH variation may lead to small changes in sodium relaxation times.

Going one step further, a possible correlation between the sodium TQ signal and the protein folding state was investigated. Protein folding states include natively folded proteins, partially folded proteins, unfolded proteins and protein aggregates [Heinrich et al. (2014)]. Only the native protein structure possesses a biological function.

In the control measurements of NaCl with urea, a strong reduction of the sodium relaxation times was observed, which was not accompanied by the formation of a sodium TQ signal. Similarly, in the measurements of the amino acids samples a reduction of the sodium relaxation times up to $T_1 = 8.8 \pm 0.1 \text{ ms}$ and $T_2 = 8.9 \pm 0.1 \text{ ms}$ (Table 4.2) was observed, which was also not accompanied by the formation of a sodium TQ signal. Schepkin et al. (2017) observed a similar effect in solutions of glycerol and saline in equal volumes. They measured a similar substantial reduction of the sodium relaxation times

as in the amino acid samples and did not detect any sodium TQ signal due to the very short tumbling time of the glycerol molecule. The tumbling time of the urea and the even larger amino acid molecules is also too short for the formation of a sodium TQ signal [Rooney et al. (1991a)]. Consequently, amino acid samples could not be used to correlate the change in the sodium TQ signal with the availability of negatively charged groups during pH variation. A correlation of the change in the sodium TQ signal of the protein BSA with the availability of negatively charged groups during pH variation is not possible, as the pK_a values of negatively charged groups depend on the location within the protein and the surrounding charged groups [Kauzmann (1959) and Grimsley et al. (2009)]. In our unfolding experiments, the presence of urea did not contribute to the measured increase of the sodium TQ signal.

The urea-induced unfolding of BSA resulted in an increase of the sodium TQ signal with a sigmoid function profile similar to the fluorescence measurements. Both methods had similar curves as a function of urea concentration with a negative linear correlation of $PCC = -0.99$, indicating a correlation of the sodium TQ signal with the changes in protein structure. The pH value was practically unchanged and it was verified directly after each NMR measurement in each sample to control a possible pH effect on the unfolding experiments.

Urea unfolds proteins, due to the preferential solvation of hydrophobic residues and the preferential binding of urea to the protein backbone [Das et al. (2009) and Matouschek et al. (1989)]. Protein unfolding by urea disrupts the protein tertiary and secondary structure and exposes the protein backbone to the aqueous phase [Heinrich et al. (2014)]. These effects lead to a random coil formation of the protein. The observed increase of the sodium TQ signal in the BSA unfolding experiments can be explained by a combination of two effects: (i) The loss of the tertiary structure disrupts ion pairs, which increases the availability of negatively charged groups compared with the native state. However, it has recently been suggested that in denatured proteins new long range ion pairs are formed to minimize energy [Pace et al. (2000)]. (ii) Protein unfolding exposes the hydrophobic protein core to the aqueous phase. This exposure of the hydrophobic core increases the availability of negatively charged groups, which are exposed to the aqueous phase [Ui (1973)]. In addition, the transformation from a hydrophobic to a hydrophilic environment can affect the sodium TQ signal [Rooney et al. (1991a)]. Our current experiments cannot distinguish between the two effects referenced above, which can potentially cause the observed sodium TQ signal to increase during a rising degree of protein denaturation. It is interesting to note that the effect (ii) correlates with the change in the slow fraction A_{SQS}/A_{SQ} . This ratio is getting close to the theoretical value of 40% for 6–8 M urea due to the change of environment from hydrophobic to hydrophilic. This process results in one or more sites with similar relaxation properties for all sodium ions. In accordance with our results, Uzman (1953) observed that a larger fraction of an organic anion was bound to denatured BSA compared with native BSA.

The observed sodium TQ signal dependence on the protein folding state could be of importance for the analysis of sodium TQ signals in diseases associated with pathological changes in protein expression, such as cancer and neurodegenerative diseases. Recent studies [Fiege et al. (2013a), Schepkin et al. (2003), Choi et al. (2018) and Choi et al. (2020)] showed a reduced sodium TQ signal in cancer, whereas in recurrent cancer an increased sodium TQ signal was demonstrated [Boada et al. (2004)]. In cancer, a reduction in the sodium TQ signal could be caused by reduced extracellular pH [White et al. (2017)] and decreased protein content in the tumor core [Ray et al. (2019)] due to edema and necrosis. On the other hand, the intracellular sodium content [Cameron et al. (1980)], intracellular pH [White et al. (2017)] and the protein content in the tumor rim [Ray et al. (2019)] are increased, which could lead to an increase in the sodium TQ signal. The contribution of each environmental change to the altered sodium TQ signal in cancer has yet to be investigated to obtain a deeper understanding of the sodium TQ signal origin in different pathologies. In addition, the influence of protein denaturation processes on the *in vivo* sodium TQ signal, where many confounding factors are present, remains to be verified. Misfolded proteins also tend to form aggregates, which could also affect the sodium TQ signal.

In all measurements of the protein BSA, the influence of B_0 and B_1^+ inhomogeneity on the sodium TQ signal was minimized in order to prevent a reduction in the sodium TQ signal [Hancu et al. (1999), Matthies et al. (2010) and Tanase et al. (2005)]. The use of a 20-step shim routine including the first and second order shims resulted in a comparable FWHM of the sodium SQ signal for all samples in each experimental series. Furthermore, the standard TQTPPI pulse sequence included a 180° RF pulse to compensate for B_0 inhomogeneity (Figure 3.5a). With respect to B_1^+ , the use of a volume coil and the placement of all phantoms in the homogeneous part of the volume coil minimized the effect of B_1^+ inhomogeneity in our experiments. Accurate repositioning of all samples provided similar minimum B_1^+ deviation for all samples. Exemplary B_1^+ maps for both sample sizes showed a minimal B_1^+ deviation of less than 7.2% (Figure A.1). Based on calculations of Wigner matrix elements [Mueller et al. (1987)] and transfer functions [Maarel (2003a)], the B_1^+ deviation of 7.2% resulted in a negligible sodium TQ signal contribution, which was created by an imperfect refocusing RF pulse [Reddy et al. (1994) and Hancu et al. (1999)], of 1.8% to the total sodium TQ signal. Any sodium DQ signals created by an imperfect refocusing RF pulse were cancelled by the phase alteration of the third RF pulse.

5.2 Sodium TQ Spectroscopy of the MR-compatible Bioreactor System

In this part, the feasibility of monitoring intracellular sodium changes caused solely by an inhibition of the Na/K-ATPase of living cells in the MR-compatible bioreactor system using sodium TQ signal was investigated. Changes in the intracellular sodium concentration were non-invasively detected without contrast agents using the sodium TQ signal. The MR-compatible bioreactor system allows a large flexibility with cellular interventions and combined with the non-invasive capability of MR is a promising research tool for a variety of applications, for example anti-cancer drug development.

Perfusion of cells with 1 mM ouabain or 0 mM K⁺ medium is well known to cause an inhibition of the Na/K-ATPase [Eykyn et al. (2015), Schepkin et al. (1998), Deitmer et al. (1978), Ellis (1977) and Pike et al. (1985)]. A Na/K-ATPase inhibition results in an increase of the intracellular sodium concentration, which leads to the growth of the sodium TQ signal (Figure 4.7a). In both experiments, the initial growth rates of the sodium TQ signal were approximately the same, which is similar to the sodium TQ measurements during the Na/K-ATPase inhibitions in a perfused rat heart system [Schepkin et al. (1998)]. In the ouabain experiment, the growth rate of the sodium TQ signal substantially decreased after approximately 30 min and the sodium TQ signal reached an intermediate plateau. A similar response to high concentrations of ouabain has been observed for sheep heart Purkinje fibers [Deitmer et al. (1978) and Ellis (1977)] and in the perfused rat heart system [Schepkin et al. (1998)]. The larger sodium TQ signal increase also confirms that perfusion with 0 mM K⁺ medium can inhibit the Na/K-ATPase stronger than perfusion with ouabain medium observed by others [Eykyn et al. (2015) and Schepkin et al. (1998)].

In the ouabain experiment, reperfusion with normal medium yielded a further increase in the sodium TQ signal. This continued growth of the sodium TQ signal indicates a continuation of sodium influx into the cells caused by irreversible cell damage during ouabain perfusion. The slow dissociation of ouabain from their inhibitory binding sites [Deitmer et al. (1978) and Ellis (1977)] could explain, why the effects of ouabain are almost irreversible. In contrast to the ouabain experiment, reperfusion with normal medium resulted in a partial recovery of the sodium TQ signal in the 0 mM K⁺ experiment. This recovery is in agreement with the results in the perfused rat heart system [Schepkin et al. (1998)]. Despite the high intracellular sodium concentration, cells remained viable and partially restored the Na/K-ATPase pump activity. However, the incomplete recovery of the sodium TQ signal indicates some irreversible cell damage during perfusion with 0 mM K⁺ medium.

In contrast to this study, a recent study by our group [Neubauer et al. (2017)] observed a decrease in the sodium TQ signal during an exposure of HepG2 cells to 20 mM ouabain and simultaneous perfusion stop using the same MR-compatible bioreactor system. This reduction in the sodium TQ signal is also contrary to the results of others [Eykyn et al.

(2015), Schepkin et al. (1998) and Tauskela et al. (1997)], which observed an increase in the sodium TQ signal during perfusion with ouabain. Recently, Hoesl et al. (2019a) and Hoesl et al. (2019b) showed that a perfusion stop, which leads to ischemia, results in a decrease of the sodium TQ signal using the same MR-compatible bioreactor system. Ischemia causes a reduction in intra- and extracellular pH [Nedergaard et al. (1991)] and an influx of sodium ions into the cell. Hence, the reduction in pH, which can decrease the sodium TQ signal [Kleimaier et al. (2020c)], outweighed the increase in the sodium TQ signal due to the increase in the intracellular sodium concentration during ischemia. Consequently, the reduction in the sodium TQ signal observed in the previous study [Neubauer et al. (2017)] could be caused by a decrease in intra- and extracellular pH, which outweighed the increase in the sodium TQ signal due to the influx of sodium ions into the cell caused by the Na/K-ATPase inhibition using ouabain. In this study, we also achieved several times gain in the sodium TQ signal by doubling the cell number in the bioreactor system and by using the fixed TQTPPI pulse sequence compared to the previous study [Neubauer et al. (2017)].

The increases in the sodium TQ signal in the perfused rat heart system [Schepkin et al. (1998)] were $190 \pm 9\%$ and $\sim 265\%$ during perfusion with 1 mM ouabain for 30 min and with 0 mM K^+ medium for 60 min, respectively. In this study, the relative sodium TQ signal increases of $138.9 \pm 4.1\%$ and $183.4 \pm 8.9\%$ during perfusion with 1 mM ouabain and 0 mM K^+ medium for 60 min were substantially lower compared to the perfused rat heart system [Schepkin et al. (1998)], respectively. These differences in the sodium TQ signal increases may be an indirect indication of a higher intracellular sodium content in cancer cells compared to noncancerous cells [Cameron et al. (1980)]. A higher intracellular sodium concentration would reduce the relative growth in the intracellular sodium concentration and subsequently the sodium TQ signal. The effect of changes in sodium transverse relaxation times between before and after Na/K-ATPase inhibition could be excluded as a cause for these lower sodium TQ signal increases. The optimal evolution time for a maximum sodium TQ signal did not substantially change between before and after the Na/K-ATPase inhibition (Figure 4.6b).

There are also other techniques to monitor changes in the intracellular sodium concentration compared to the sodium TQ signal. Several fluorescence dyes are commercially available, which require a fluorescence microscopy or flow cytometry and administration of the fluorescence dyes into the cells [Amorino et al. (1995), Gao et al. (2017) and Yin et al. (2015)]. Dye leakage out of the cells, the shallow fluorescence penetration depth, photobleaching and cellular autofluorescence are some drawbacks of the fluorescence technique [Amorino et al. (1995), Gao et al. (2017), Yin et al. (2015) and Iamshanova et al. (2016)]. In contrast to the fluorescence technique, the MR technique is non-invasive, as it exploits the intrinsic property of the sodium nucleus. The main benefit of using the sodium TQ MR technique is the possibility to transfer it to *in vivo* studies. The sodium TQ signal is also not without its limitations. The sodium TQ signal has contributions from intra- and extracellular sodium [Dizon et al. (1996), Eykyn et al. (2015), Jelicks et al. (1993), Knubovets et al. (1998), Schepkin et al. (1996), Schepkin et al. (1998), Seshan et al. (1997),

and Winter et al. (2001a)]. Similar to fluorescence dyes, a calibration of the sodium TQ signal as proposed by Schepkin et al. (1998) and Schepkin et al. (1999) allows the correlation of the sodium TQ signal to the intracellular sodium concentration in the presence of an unchanged extracellular sodium TQ signal and the exclusion of possible pH changes. With respect to other MR techniques, only the administration of chemical shift reagents yields a separation of the intra- and extracellular sodium MR signals [Winter et al. (2001a), Naritomi et al. (1987) and Navon (1993)]. However, the toxicity of these compounds limits the *in vivo* applications [Simor et al. (1999)]. The major benefit of the proposed technique is that the MR-compatible bioreactor system allows to perform a variety of interventions with a variety of cells and to correlate MR signal changes to cellular processes. Several efforts are already made to image the sodium SQ and TQ signals simultaneously *in vivo*, as both may represent valuable biomarkers for cell viability [Fiege et al. (2013a), Hoesl et al. (2020) and Worthoff et al. (2019)].

The optimized and fixed evolution time in the fixed TQTPPI pulse sequence yielded a measured sodium TQ SNR gain of 3–4 times using the agarose samples compared to the standard TQTPPI pulse sequence with the evolution increment (Table 4.4 and Figure 3.6b). This gain in sodium TQ signal sensitivity allowed us to achieve a cell sensitivity of $12\text{--}14 \cdot 10^6$ (Figure 4.6a). The fixed TQTPPI pulse sequence still preserves the simultaneous measurement of the SQ and the TQ signals at distinct frequencies. This is in contrast to a commonly used TQ filtration pulse sequence [Jaccard et al. (1986)], where the evolution time is also fixed throughout the pulse sequence. The phase cycle of a TQ filtration pulse sequence cancels out SQ and DQ signals and the TQ signals are detected at the same frequency as the SQ and the DQ signals. Hence, an imperfect cancellation of the SQ and the DQ signals can interfere with the measurement of TQ signals, especially in the case of weak TQ signals. In contrast to the filtration procedure, the fixed TQTPPI pulse sequence introduces no extra noise [Schepkin et al. (2017)], which allows a more sensitive detection of TQ signals and their changes. This was crucial in the current experiments. Further, the simultaneous measurement of the SQ signal in the fixed TQTPPI pulse sequence yields an internal reference signal which represents a valuable feature for *in vivo* applications.

The non-invasive capability of the MR technique to obtain a variety of physiological information resulted in a large effort to investigate living cells in bioreactor systems by MR [Gottwald et al. (2013), Hoesl et al. (2019a), Neubauer et al. (2017), Bartusik-Aebischer et al. (2020), Carvalho et al. (2019), Cox et al. (2019), Grivet et al. (2009), Hemminga et al. (2000), Hertig et al. (2020), Keshari et al. (2010), Macdonald et al. (1998), Macdonald et al. (1993), Majors et al. (2008), Mancuso et al. (1990), Narayan et al. (1990), Siegal et al. (2019), Thelwall et al. (1999) and Trouard et al. (2008)]. In general, the low sensitivity of the MR technique requires a high cell density/number, which can be obtained by densely packed 3D cell cultures, to achieve a sufficient SNR within a high temporal resolution. In addition, the bioreactor system has to feature an active perfusion of cells with fresh medium, which supplies the cells with nutrients and oxygen. The active perfusion with fresh medium will maintain the cells under physiological metabolic conditions [Siegal et al. (2019)]. To supply cells with oxygen, the medium in a medium reservoir needs to be

aerated with the desired composition of N_2 , O_2 and CO_2 . For long-term measurements, a pH control system is necessary to compensate for the metabolic activity of the cells [Macdonald et al. (1998) and Giusti et al. (2017)]. A versatile bioreactor system or the possibility to extract the cells from the bioreactor system is beneficial to obtain complementary or additional information using other methods, e.g. fluorescence measurements [Gottwald et al. (2013), Gottwald et al. (2019) and Cox et al. (2019)].

The presented sodium TQ MR signal detection method combined with the MR-compatible bioreactor system could be used to non-invasively monitor the cellular response of a variety of cells upon disease progression or treatment-related changes in an isolated manner using sodium TQ signal. Machine-learning [Madelin et al. (2015), Wang et al. (2016) and Lundervold et al. (2019)] or compressed sensing [Lustig et al. (2007) and Madelin et al. (2012)] approaches could further speed up the sodium TQ measurements, which would greatly assist the study of the involved cellular mechanisms. For these suggested long-term measurements, an electronic control unit to regulate the CO_2 concentration could provide a precise control of the pH of the medium [Biechele et al. (2015) and Giusti et al. (2017)], as the metabolic activity of the cells can change the pH of the medium on a long term. In the current experiments, the influence of the metabolic activity of the cells on the pH of the medium could be excluded, as the medium reservoir contained approximately 80 ml medium and the cells were only placed in the bioreactor system for a maximum of 10 hours.

5.3 CEST Spectroscopic Imaging of the MR-compatible Bioreactor System

In this part, the cellular heat shock response of an organotypic 3D cell culture after a mild, non-lethal heat shock of 42°C using an MR-compatible bioreactor system was monitored by dynamic measurements of the rNOE CEST signal. These results aim to provide a deeper understanding of rNOE signal alterations *in vivo* and its capability to serve as a potential biomarker in diseases with aberrant protein folding states.

Apart from intrinsically disordered proteins [Wright et al. (2015)] the three-dimensional integrity of cellular proteins is crucial for their specific biological function. However, this native structure is often only marginally stable. As a consequence, elevated temperatures cause the protein unfolding, which is usually followed by aggregation due to exposed hydrophobic regions. Furthermore, a substantial number of proteins reside in a metastable state, *in vivo*, meaning that their concentration is higher than their solubility, making them prone to aggregation upon temperature stress [Baldwin et al. (2011), Ciryam et al. (2015), Ciryam et al. (2013) and Kundra et al. (2017)]. To prevent aggregation as well as to dissolve and refold protein aggregate deposits the cellular heat shock response reacts by overexpressing molecular chaperones [DiDomenico et al. (1982) and Richter et al. (2010)]. The latter are proteins which keep unfolded proteins soluble, actively refold them or dissolve aggregated protein deposits to allow their refolding [Balchin et al. (2016)]. Protein unfolding and aggregation caused by temperature stress can explain the observed reduction in the rNOE signal after heat shock application observed in both cell culture experiments (Figure 4.11a and Figure 4.12a). Notably, this rNOE signal reduction is consistent with the observed rNOE signal reduction in protein unfolding [Goerke et al. (2015) and Zaiss et al. (2013c)] and aggregation [Goerke et al. (2017)] experiments of protein solutions and cell lysates. However, a heat shock not only causes unfolding and aggregation of proteins, but also affects the internal organization of the cell, like reorganization of the cytoskeleton and fragmentation of organelles [Richter et al. (2010)]. Therefore, the contribution of other heat shock induced cellular effects to the observed rNOE signal reduction cannot be excluded.

The exposure of cells to elevated temperatures can be lethal depending on the time and temperature of the heat shock due to the accumulation of misfolded proteins [Roti Roti (2008)]. To minimize cell death, a mild, non-lethal heat shock of 42°C for 20 min was applied in this study, as experiments of cells exposed to a similar heat shock showed that the survival rate was close to one [Borrelli et al. (1992), Schröder et al. (1993) and Stege et al. (1994)]. However, in this case the accumulation of misfolded proteins compared to the total proteome is expected to be rather low [Schröder et al. (1993), Stege et al. (1994), Wallace et al. (2015) and Leuenberger et al. (2017)], which was also suggested by the rNOE signal reduction of $8.3 \pm 1.1\%$ and $7.7 \pm 0.8\%$. In contrast, the high survival rate was of importance for the observation of the rNOE recovery, as only viable cells can refold unfolded and aggregated proteins by molecular chaperones [Mogk et al. (2018), Wallen et al.

(1990) and Kampinga et al. (1987)]. This chaperone-induced protein refolding process after heat shock therefore increases the number of correctly folded proteins, which would be reflected in the observed rNOE signal recovery. The time from heat shock to full structural recovery of the proteome can last up to several hours dependent on the severity of the heat shock [Richter et al. (2010)]. Interestingly, in hamster cells exposed to a comparable mild, non-lethal heat shock, a similar time duration to complete protein refolding was found [Michels et al. (1997)]. In principle, misfolded proteins can also be degraded and newly synthesized [Mogk et al. (2018)]. However, a recent study [Wallace et al. (2015)] in budding yeast cells exposed to a mild, non-lethal heat shock showed that even severely aggregated proteins were refolded instead of degraded. The recovery of the rNOE signal to the initial value is consistent with the disaggregation of proteins without degradation and with the expected high survival rate of cells.

For the comparison of the heat shock experiments from both cell cultures, the rNOE signal recovery was fitted by an exponential function (Equation 3.13). Notably, heat shock experiments in eukaryotic cells monitored by luciferase activity [Schröder et al. (1993), Michels et al. (1997), Nollen et al. (1999), Parsell et al. (1994) and Pinto et al. (1991)] or by nuclear protein content [Borrelli et al. (1992), Stege et al. (1994), Wallen et al. (1990), Kampinga et al. (1987) and Kampinga et al. (1989)] showed a similar exponential-like recovery after the exposure to heat. However, to the best of our knowledge a quantification of the heat shock recovery has not been performed so far. Based on literature analysis and the results of the heat shock experiments in this study, quantification of the heat shock recovery by an exponential function seemed to be a good representation of the available data and should facilitate the comparability of heat shock experiments.

To rule out further causes for the observed rNOE signal recovery, the effect of a heat shock on the background rNOE signal from medium and collagenized MCAs and the temporal stability of the rNOE signal without heat shock application was investigated (Figure 4.10). However, rNOE signal changes that occur during the application of the heat shock should be interpreted with care, as T_1 strongly varies as a function of temperature [Bloembergen et al. (1948)] leading to different levels of saturation [Zaiss et al. (2014) and Zaiss et al. (2013a)]. In contrast, explaining the observed rNOE signal recovery simply by T_1 changes (Equation 3.11) could be ruled out, as in all heat shock experiments a constant T_1 value after cooling to 37°C until the end of the experiment was observed (Figure 3.4a). Furthermore, the T_1 value after the heat shock reached the same level as prior to heat shock application. This was also confirmed by the calculation of the rNOE signal by alternative metrics without T_1 correction (i.e. ΔST (Equation A.3) [Chen et al. (2019)] or $MTR_{\text{Rex}\Delta ST}$ (Equation A.4) [Zaiss et al. (2013b)]) which showed a similar recovery of the rNOE signal with a comparable T_{rec} (Table A.1). Thus, the effect of a T_1 recovery as an explanation for the observed rNOE signal recovery could be ruled out.

The applied 2-point contrast metric, proposed by Chen et al. (2019), to achieve fast and reliable CEST imaging, sufficiently suppressed confounding contributions to the Z-spectrum (i.e. from DS and ssMT) to selectively investigate changes in the rNOE signal.

The 2-point contrast metric suppresses DS and ssMT by assuming that these contributions are only marginally different between the two offset frequencies 8 and -3.5 ppm [Chen et al. (2019)]. Although, this method was developed at an ultrahigh magnetic field strength of 11.7 T, we were also able to confirm the applicability of AREX_{ΔST} in the bioreactor system at 9.4 T (Table 4.6). Nonetheless, the aggregation of proteins during the heat shock experiments could have caused an increase in ssMT [Chen et al. (2019) and Goerke et al. (2017)], which would alter the residual ssMT contribution. However, the amount of residual ssMT contribution of approximately 6.5% is not enough to explain the observed average change in rNOE signal upon heat shock of about $8.0 \pm 0.4\%$. With the used setup, also field inhomogeneities across the cell culture do not have a large impact on the rNOE signal calculation by the 2-point metric. Regarding B_0 , the inhomogeneity was smaller than ± 0.2 ppm and changed only marginally by ± 0.02 ppm during dynamic measurements, which is negligible in comparison to the observed spectral widths of the peaks in the acquired Z-spectrum (Figure 4.9). During dynamic measurements, a possible change in the water resonance frequency was prevented by setting the global frequency for each 2-point and saturation recovery measurement. With respect to B_1^+ , inhomogeneities were also negligible using a quadrature ^1H birdcage coil with an average B_1^+ deviation smaller than 2% across the entire cell culture (Figure A.2). In addition, B_1^+ values were set consistently to 0.8 μT between all measurements.

With the presented bioreactor CEST NMR setup at hand, besides heat shock experiments, in the future one could also investigate CEST signal changes upon disease progression or treatment-related contrast changes in an isolated manner to identify potential new biomarkers. In doing so, ultrafast CEST techniques [Dopfert et al. (2014), Swanson (1991) and X. Xu et al. (2013)], which allow the acquisition of the full Z-spectrum with a high temporal resolution during the intervention, would greatly assist the study of the involved mechanisms.

6 Conclusion

The two objectives of this theses were (i) to obtain a deeper understanding of the sodium TQ signal on a cellular level using model solutions and an MR-compatible bioreactor system, and (ii) to experimentally verify the detectability of denaturation processes in living cells using the rNOE CEST signal. These two objectives were achieved in three parts.

The first part of this thesis investigated the influence of the availability of negatively charged groups on the sodium TQ signal by evaluating two major environmental effects, i.e. pH and the protein folding state, using the protein BSA. In accordance with the increase in the availability of negatively charged groups, the pH variation revealed a sigmoidal-shaped increase of the sodium TQ signal with rising pH. At the high pH values, the sodium TQ signal increased by $\sim 225\%$ relative to the low pH values. During selective BSA unfolding by urea, the sodium TQ signal increased by $\sim 40\%$ due to an increase in the availability of negatively charged groups. The protein folding state was independently monitored by fluorescence measurements. The denaturation curve of the sodium TQ signal correlated linearly with the denaturation curve of the fluorescence signal. In summary, the sodium TQ signal depends on the availability of negatively charged groups and thus on pH and the protein folding state. The results demonstrate the sensitivity of the sodium TQ signal to the biochemical environment, while they also provide a first evaluation of the effects of pH changes and protein unfolding during *in vivo* applications of the sodium TQ signal. As the sodium TQ signal can be a valuable biomarker for cell viability, consideration of these additional dependencies of the sodium TQ signal is essential for a proper interpretation of changes in the sodium TQ signal *in vivo*.

In the second part, the capability of the sodium TQ signal to monitor intracellular sodium changes during the Na/K-ATPase inhibition of living cells was verified using an MR-compatible bioreactor system. For this purpose, a fixed TQTPPI pulse sequence with a fixed evolution time was developed. This modification yielded several times gain in the TQ SNR compared to the standard TQTPPI pulse sequence. The fixed TQTPPI pulse sequence preserved the simultaneous measurement of the SQ and the TQ signals at distinct frequencies. The improved TQ signal sensitivity enabled the detection of the signal of only $12\text{--}14 \cdot 10^6$ cells using a bioreactor system. The Na/K-ATPase inhibition by 1 mM ouabain or 0 mM K^+ medium caused an influx of sodium ions into the cells, which was confirmed by the significant increase in the sodium TQ signal. Further influx of sodium ions into the cells during reperfusion with normal medium indicated irreversible cell damage in the ouabain experiment. In contrast, the cells remained viable in the 0 mM K^+ medium experiment, as the Na/K-ATPase pump activity was partially preserved during reperfusion with normal medium. The improved sodium TQ signal detection allowed monitoring

of intracellular sodium changes in living cells using an MR-compatible bioreactor system. Changes in the intracellular sodium concentration correlate with an alteration of the cell viability. Hence, the sodium TQ signal can be a valuable biomarker for cell viability. Additionally, the bioreactor system allows the non-invasive investigation of the cellular response for a variety of cells during treatment-related interventions or disease progression using sodium TQ signal.

The final part demonstrated for the first time the detectability of denaturation processes on a physiologically relevant scale in living cells using the rNOE CEST signal. The cellular heat shock response after a mild, non-lethal heat shock applied to organotypic 3D cell cultures was observed using reliable and fast high-resolution CEST imaging. The cell culture was the main contributor to the CEST signals from the bioreactor, which allowed the correlation of rNOE signal changes to the cellular heat shock response. Heat shock application caused protein unfolding and protein aggregation, which was confirmed by the substantially decreased rNOE signal after heat shock. Chaperone-induced refolding of misfolded proteins after heat shock resulted in the continuous recovery of the rNOE signal. Consequently, the protein folding state is a relevant physiological parameter for the interpretation of rNOE CEST signal alterations *in vivo*. The rNOE signal dependence on the protein folding state can be a valuable, non-invasive diagnostic tool for diseases associated with changes in the protein expression, such as cancer and neurodegenerative diseases.

In conclusion, a sodium TQ and a rNOE CEST signal detection method was established to investigate the correlation of MR signal changes with cellular processes using an MR-compatible bioreactor system. Both MR signals provided information about a dysfunction of proteins and thus a reduction in cell viability. Besides a different physical origin, both MR signals allowed the early detection of physiological alterations prior to changes on a macroscopic level. Therefore, both MR signals can provide a deeper understanding of disease progression and treatment response on a cellular level. Furthermore, the bioreactor system allows the investigation of organotypic 3D cell cultures of human origin. Hence, the bioreactor system can potentially reduce the number of animal experiments, as it can resemble more closely human *in vivo* conditions and allows a large flexibility with cellular interventions. Consequently, the non-invasive capability of the MR technique combined with the bioreactor system is a promising research tool for a variety of biomedical applications, such as drug development and pharmaceutical treatments.

A Appendix

A.1 B_1^+ Maps

This section provides B_1^+ maps for the linear polarized $^1\text{H}/^{23}\text{Na}$ Bruker volume coil, replicated from the supporting information of Kleimaier et al. (2020c), (Figure A.1) and the ^1H Bruker quadrature volume coil (Figure A.2), which are described in Subsection 3.1.2. These B_1^+ maps were acquired with the double flip angle method (DAM) [Insko et al. (1993)]. In this method, two images with different flip angles α_1 and $\alpha_2 = 2\alpha_1$ were acquired. In the case of a gradient echo pulse sequence, the actual flip angle α_{GRE} in a voxel depends on the ratio of the signal intensities according to:

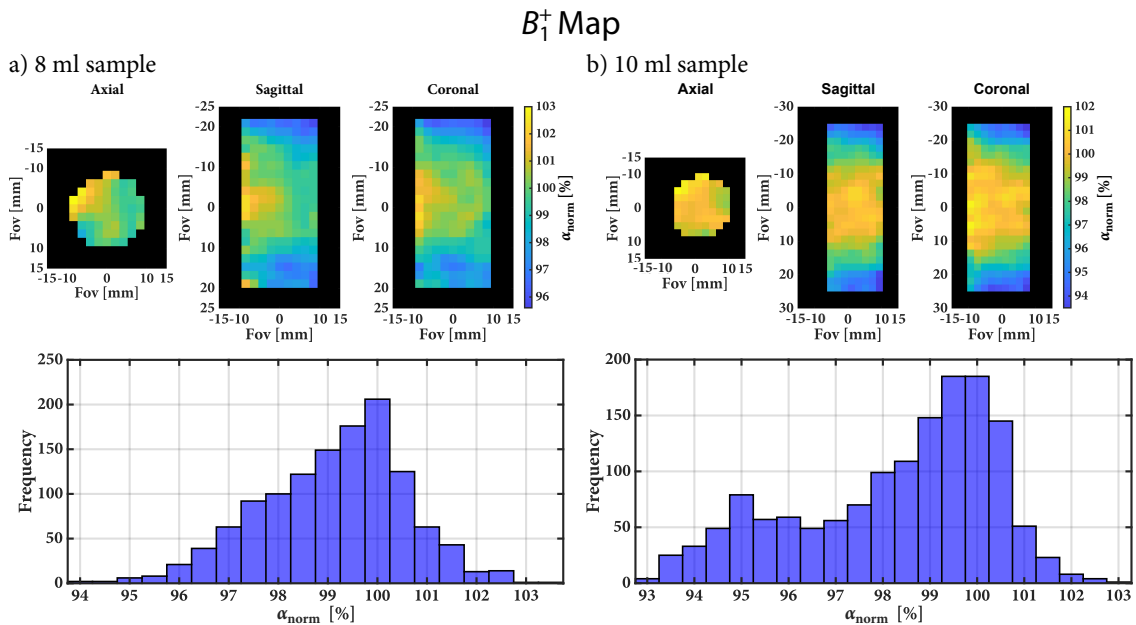


Figure A.1: a) ^{23}Na B_1^+ map of an 8 ml sample with 10% w/v BSA and pH 7.01 using the $^1\text{H}/^{23}\text{Na}$ Bruker volume coil. The histogram below the three B_1^+ images shows the B_1^+ distribution over the whole sample. The B_1^+ deviation was less than 6.6% for the 8 ml sample. b) ^{23}Na B_1^+ map of an 10 ml sample with 5% w/v BSA and pH 7.02 using the $^1\text{H}/^{23}\text{Na}$ Bruker volume coil. The histogram below the three B_1^+ images shows again the B_1^+ distribution over the whole sample. For the 10 ml sample, the B_1^+ deviation was less than 7.2%. In both cases, the B_1^+ map was acquired with DAM using a density adapted radial sequence.

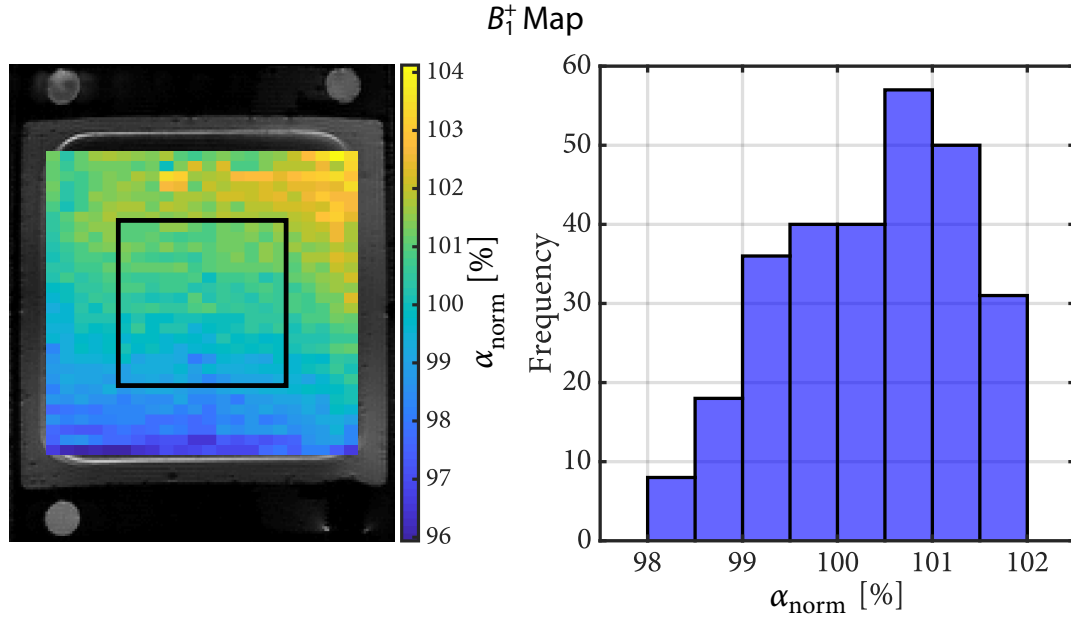


Figure A.2: The left image shows a ^1H B_1^+ map of the MR-compatible bioreactor including a cell culture on two MCAs in medium using the ^1H Bruker quadrature volume coil. The histogram on the right visualizes the B_1^+ distribution across the cell culture, which is indicated by the black box on the B_1^+ map. The B_1^+ deviation was less than 2% across the entire cell culture.

$$\alpha_{\text{GRE}} = \arccos\left(\frac{S_2(2\alpha_1)}{2S_1(\alpha_1)}\right). \quad (\text{A.1})$$

For a spin echo pulse sequence with two images of $\alpha_1 - \frac{T_E}{2} - 2\alpha_1 - \frac{T_E}{2}$ and $2\alpha_1 - \frac{T_E}{2} - 4\alpha_1 - \frac{T_E}{2}$, the actual flip angle α_{SE} in a voxel can be calculated by:

$$\alpha_{\text{SE}} = \arccos\left(\left[\frac{S_2(2\alpha_1)}{8S_1(\alpha_1)}\right]^{\frac{1}{3}}\right). \quad (\text{A.2})$$

The actual flip angle can be rewritten in terms of the RF amplitude B_1^+ by using Equation 2.19.

For the ^{23}Na B_1^+ map, a density adapted radial readout was used [Nagel et al. (2009)]. The pulse sequence parameters for the 8 ml sample were: $T_R = 250$ ms, $T_E = 96$ μs , 6 averages, $\alpha_1 = 60^\circ$, 2100 projections, imaging matrix = $25 \times 25 \times 25$, FoV = $50 \times 50 \times 50$ mm^3 , 8 ms acquisition time and a scan time of 52.5 ms. For the 10 ml sample, the pulse sequence parameters were the same except of: $T_R = 300$ ms, 3100 projections, imaging matrix = $30 \times 30 \times 30$, FoV = $60 \times 60 \times 60$ mm^3 and a scan time of 90 min.

For the ^1H B_1^+ map of the MR-compatible bioreactor system, a RARE pulse sequence with following parameters was used: $T_R = 25$ s, $T_E = 2.4$ ms, RARE factor 1, $\alpha_1 = 60^\circ$, imaging matrix = 70×50 , slice thickness 2 mm, FoV = 35×35 mm^2 and a scan time of 20 min.

A.2 Alternative rNOE CEST Evaluation Metrics

This part was published in the supporting information of Kleimaier et al. (2020e).

To exclude a change in T_1 for the cause of the observed rNOE signal recovery after heat shock, the 2-point offset measurement was additionally evaluated by the saturation transfer difference ΔST [Chen et al. (2019)] and by the spillover corrected magnetization transfer ratio MTR_{Rex} [Zaiss et al. (2013b)]:

$$\Delta ST(-3.5 \text{ ppm}) = Z(8 \text{ ppm}) - Z(-3.5 \text{ ppm}), \quad (\text{A.3})$$

$$MTR_{\text{Rex}\Delta ST}(-3.5 \text{ ppm}) = \frac{1}{Z(-3.5 \text{ ppm})} - \frac{1}{Z(8 \text{ ppm})}. \quad (\text{A.4})$$

The quantities $\Delta ST(-3.5 \text{ ppm})$ and $MTR_{\text{Rex}\Delta ST}(-3.5 \text{ ppm})$ represent the approximated rNOE signal at -3.5 ppm from which the contribution of DS and ssMT was removed by the offset measurement at 8 ppm . Table A.1 lists the results of the quantification of the rNOE signal recovery after the heat shock using the $\text{AREX}_{\Delta ST}$, $MTR_{\text{Rex}\Delta ST}$ and ΔST metrics.

Table A.1: Exponential fit results of the cellular heat shock response.

	Cell culture 1		
	$\text{AREX}_{\Delta ST}$	$MTR_{\text{Rex}\Delta ST}$	ΔST
Y_{start}	$91.7 \pm 1.1\%$	$91.6 \pm 1.1\%$	$91.9 \pm 1.1\%$
Y_{end}	$101.4 \pm 3.9\%$	$101.5 \pm 2.2\%$	$101.6 \pm 2.3\%$
T_{rec}	$100.0 \pm 52.5 \text{ min}$	$100.0 \pm 53.1 \text{ min}$	$100.0 \pm 54.9 \text{ min}$
	Cell culture 2		
	$\text{AREX}_{\Delta ST}$	$MTR_{\text{Rex}\Delta ST}$	ΔST
Y_{start}	$92.3 \pm 0.8\%$	$91.8 \pm 0.8\%$	$92.3 \pm 0.8\%$
Y_{end}	$101.0 \pm 2.0\%$	$101.7 \pm 2.0\%$	$101.5 \pm 1.8\%$
T_{rec}	$98.1 \pm 42.4 \text{ min}$	$100.0 \pm 40.1 \text{ min}$	$100.0 \pm 43.2 \text{ min}$

Equation 3.13 describes the exponential function for the quantification of the rNOE signal recovery after the heat shock (Figure 4.11a and Figure 4.12a). Y_{start} is the minimum value, Y_{end} is the maximum value and T_{rec} is the recovery time.

Bibliography

- Alberts, B., Johnson, A., Lewis, J., Raff, M., Roberts, K., and Walter, P. (2017). *Molecular biology of the cell*. Garland Science.
- Altmann, B., Giselbrecht, S., Weibezahn, K. F., Welle, A., and Gottwald, E. (2008). The three-dimensional cultivation of the carcinoma cell line HepG2 in a perfused chip system leads to a more differentiated phenotype of the cells compared to monolayer culture. *Biomed Mater*, 3(3):034120.
- Amorino, G. P. and Fox, M. H. (1995). Intracellular Na⁺ measurements using sodium green tetraacetate with flow cytometry. *Cytometry*, 21(3):248–256.
- Andrasko, J. (1974). Nonexponential relaxation of ²³Na⁺ in agarose gels. *J Magn Reson*, 16(3):502–504.
- Babsky, A. M., Zhang, H., Hekmatyar, S. K., Hutchins, G. D., and Bansal, N. (2007). Monitoring chemotherapeutic response in RIF-1 tumors by single-quantum and triple-quantum-filtered ²³Na MRI, ¹H diffusion-weighted MRI and PET imaging. *Magn Reson Imaging*, 25(7):1015–1023.
- Bai, Y., Milne, J. S., Mayne, L., and Englander, S. W. (1993). Primary structure effects on peptide group hydrogen exchange. *Proteins*, 17(1):75–86.
- Bain, A. D. (1984). Coherence levels and coherence pathways in NMR. A simple way to design phase cycling procedures. *J Magn Reson*, 56(3):418–427.
- Balchin, D., Hayer-Hartl, M., and Hartl, F. U. (2016). In vivo aspects of protein folding and quality control. *Science*, 353(6294):aac4354.
- Baldwin, A. J., Knowles, T. P., Tartaglia, G. G., Fitzpatrick, A. W., Devlin, G. L., Shammash, S. L., Waudby, C. A., Mossuto, M. F., Meehan, S., Gras, S. L., Christodoulou, J., Anthony-Cahill, S. J., Barker, P. D., Vendruscolo, M., and Dobson, C. M. (2011). Metastability of native proteins and the phenomenon of amyloid formation. *J Am Chem Soc*, 133(36):14160–14163.
- Bansal, N. and Seshan, V. (1995). Three-dimensional triple quantum-filtered ²³Na imaging of rabbit kidney with weighted signal averaging. *J Magn Reson Imaging*, 5(6):761–767.
- Bartusik-Aebischer, D., Aebischer, D., Czml, A., and Mazur, D. (2020). Evaluation of MR relaxation times following trastuzumab treatment of breast cancer cells in a 3D bioreactor. *Acta Pol. Pharm.*, 77(1):35–41.
- Berendsen, H. J. and Edzes, H. T. (1973). The observation and general interpretation of sodium magnetic resonance in biological material. *Ann N Y Acad Sci*, 204:459–485.

- Biechele, P., Busse, C., Solle, D., Scheper, T., and Reardon, K. (2015). Sensor systems for bioprocess monitoring. *Eng. Life Sci.*, 15(5):469–488.
- Bloch, F. (1946). Nuclear induction. *Phys Rev*, 70(7-8):460–474.
- Bloembergen, N., Purcell, E. M., and Pound, R. V. (1948). Relaxation effects in nuclear magnetic resonance absorption. *Phys Rev*, 73(7):679–712.
- Boada, F. E., Davis, D., Walter, K., Torres-Trejo, A., Kondziolka, D., Bartynski, W., and Lieberman, F. (2004). Triple quantum filtered sodium MRI of primary brain tumors. *2nd IEEE International Symposium on Biomedical Imaging: Nano to Macro*, 2:1215–1218.
- Borrelli, M. J., Stafford, D. M., Rausch, C. M., Lepock, J. R., Lee, Y. J., and Corry, P. M. (1992). Reduction of levels of nuclear-associated protein in heated cells by cycloheximide, D₂O, and thermotolerance. *Radiat Res*, 131(2):204.
- Bowden, G. J. and Hutchison, W. D. (1986a). Tensor operator formalism for multiple-quantum NMR. 1. Spin-1 nuclei. *J Magn Reson*, 67(3):403–414.
- Bowden, G. J., Hutchison, W. D., and Khachan, J. (1986b). Tensor operator formalism for multiple-quantum NMR. 2. Spins $\frac{3}{2}$, 2, and $\frac{5}{2}$ and general I. *J Magn Reson*, 67(3):415–437.
- Brown, G. C. (1991). Total cell protein-concentration as an evolutionary constraint on the metabolic control distribution in cells. *J Theor Biol*, 153(2):195–203.
- Burstein, D. and Springer C. S., J. (2019). Sodium MRI revisited. *Magn Reson Med*, 82(2):521–524.
- Cameron, I. L., Smith, N. K., Pool, T. B., and Sparks, R. L. (1980). Intracellular concentration of sodium and other elements as related to mitogenesis and oncogenesis in vivo. *Cancer Res*, 40(5):1493–1500.
- Carr, C. W. (1956). Studies on the binding of small ions in protein solutions with the use of membrane electrodes. VI. The binding of sodium and potassium ions in solutions of various proteins. *Arch Biochem Biophys*, 62(2):476–484.
- Carvalho, J., Alves, S., Castro, M., Galdes, C., Queiroz, J. A., Fonseca, C. P., and Cruz, C. (2019). Development of a bioreactor system for cytotoxic evaluation of pharmacological compounds in living cells using NMR spectroscopy. *J Pharmacol Toxicol Methods*, 95:70–78.
- Chen, L., Wei, Z., Chan, K. W. Y., Cai, S., Liu, G., Lu, H., Wong, P. C., van Zijl, P. C. M., Li, T., and Xu, J. (2019). Protein aggregation linked to Alzheimer’s disease revealed by saturation transfer MRI. *Neuroimage*, 188:380–390.
- Choi, C. H., Stegmayr, C., Shymanskaya, A., Worthoff, W. A., Silva, N. A. da, Felder, J., Langen, K. J., and Shah, N. J. (2020). An in vivo multimodal feasibility study in a rat

- brain tumour model using flexible multinuclear MR and PET systems. *EJNMMI Phys*, 7(1):50.
- Choi, C. H., Stegmayr, C., Shymanskaya, A., Worthoff, W. A., Silva, N. A. d., Felder, J., Langen, K. J., and Shah, N. J. (2018). Feasibility study of multinuclear MR at 9.4 T and PET in a rat brain tumor model. *Proc Int Soc Magn Reson Med.*, 26:3032.
- Choy, I. O., Schepkin, V. D., Budinger, T. F., Obayashi, D. Y., Young, J. N., and DeCampli, W. M. (1997). Effects of specific sodium/hydrogen exchange inhibitor during cardioplegic arrest. *Ann Thorac Surg*, 64(1):94–99.
- Chung, C.-W. and Wimperis, S. (1990). Optimum detection of biexponential relaxation using multiple-quantum filtration techniques. *J Magn Reson*, 88(2):440–447.
- Ciryam, P., Kundra, R., Morimoto, R. I., Dobson, C. M., and Vendruscolo, M. (2015). Supersaturation is a major driving force for protein aggregation in neurodegenerative diseases. *Trends Pharmacol Sci*, 36(2):72–77.
- Ciryam, P., Tartaglia, G. G., Morimoto, R. I., Dobson, C. M., and Vendruscolo, M. (2013). Widespread aggregation and neurodegenerative diseases are associated with supersaturated proteins. *Cell Rep*, 5(3):781–790.
- Clausen, M. V., Hilbers, F., and Poulsen, H. (2017). The structure and function of the Na,K-ATPase isoforms in health and disease. *Front Physiol*, 8:371.
- Cohen, B. E., Pralle, A., Yao, X., Swaminath, G., Gandhi, C. S., Jan, Y. N., Kobilka, B. K., Isacoff, E. Y., and Jan, L. Y. (2005). A fluorescent probe designed for studying protein conformational change. *Proc Natl Acad Sci USA*, 102(4):965–970.
- Colet, J. M., Bansal, N., Malloy, C. R., and Sherry, A. D. (1999). Multiple quantum filtered ^{23}Na NMR spectroscopy of the isolated, perfused rat liver. *Magn Reson Med*, 41(6):1127–1135.
- Cox, B. L., Erickson-Bhatt, S., Szulczewski, J. M., Squirrell, J. M., Ludwig, K. D., Macdonald, E. B., Swader, R., Ponik, S. M., Eliceiri, K. W., and Fain, S. B. (2019). A novel bioreactor for combined magnetic resonance spectroscopy and optical imaging of metabolism in 3D cell cultures. *Magn Reson Med*, 81(5):3379–3391.
- Damadian, R. (1971). Tumor detection by nuclear magnetic resonance. *Science*, 171(3976):1151–1153.
- Das, A. and Mukhopadhyay, C. (2009). Urea-mediated protein denaturation: A consensus view. *J Phys Chem B*, 113(38):12816–12824.
- Deitmer, J. W. and Ellis, D. (1978). The intracellular sodium activity of cardiac Purkinje fibres during inhibition and re-activation of the Na-K pump. *J Physiol*, 284:241–259.
- DiDomenico, B. J., Bugaisky, G. E., and Lindquist, S. (1982). Heat shock and recovery are mediated by different translational mechanisms. *Proc Natl Acad Sci USA*, 79(20):6181–6185.

- Dizon, J. M., Tauskela, J. S., Wise, D., Burkhoff, D., Cannon, P. J., and Katz, J. (1996). Evaluation of triple-quantum-filtered ^{23}Na NMR in monitoring of intracellular Na content in the perfused rat heart: Comparison of intra- and extracellular transverse relaxation and spectral amplitudes. *Magn Reson Med*, 35(3):336–345.
- Dobson, C. M. (2002). Protein-misfolding diseases: Getting out of shape. *Nature*, 418(6899):729–730.
- Dopfert, J., Zaiss, M., Witte, C., and Schroder, L. (2014). Ultrafast CEST imaging. *J Magn Reson*, 243:47–53.
- Eliav, U., Keinan-Adamsky, K., and Navon, G. (2003). A new method for suppressing the central transition in $I = 3/2$ NMR spectra with a demonstration for ^{23}Na in bovine articular cartilage. *J Magn Reson*, 165(2):276–281.
- Ellis, D. (1977). The effects of external cations and ouabain on the intracellular sodium activity of sheep heart Purkinje fibres. *J Physiol*, 273(1):211–240.
- Engl, E. and Attwell, D. (2015). Non-signalling energy use in the brain. *J Physiol*, 593(16):3417–3429.
- Eykyn, T. R., Aksentijevic, D., Aughton, K. L., Southworth, R., Fuller, W., and Shattock, M. J. (2015). Multiple quantum filtered ^{23}Na NMR in the Langendorff perfused mouse heart: Ratio of triple/double quantum filtered signals correlates with $[\text{Na}]_i$. *J Mol Cell Cardiol*, 86:95–101.
- Fiege, D. P., Romanzetti, S., Mirkes, C. C., Brenner, D., and Shah, N. J. (2013a). Simultaneous single-quantum and triple-quantum-filtered MRI of ^{23}Na (SISTINA). *Magn Reson Med*, 69(6):1691–1696.
- Fiege, D. P., Romanzetti, S., Tse, D. H., Brenner, D., Celik, A., Felder, J., and Shah, N. J. (2013b). B_0 insensitive multiple-quantum resolved sodium imaging using a phase-rotation scheme. *J Magn Reson*, 228:32–36.
- Fleysher, L., Oesingmann, N., and Inglese, M. (2010). B_0 inhomogeneity-insensitive triple-quantum-filtered sodium imaging using a 12-step phase-cycling scheme. *NMR Biomed*, 23(10):1191–1198.
- Friedman, J. I., Xia, D., Regatte, R. R., and Jerschow, A. (2015). Transfer rate edited experiment for the selective detection of chemical exchange via saturation transfer (TRE-CEST). *J Magn Reson*, 256:43–51.
- Gadsby, D. C. (2009). Ion channels versus ion pumps: The principal difference, in principle. *Nat Rev Mol Cell Biol*, 10(5):344–352.
- Gao, G., Cao, Y., Liu, W., Li, D., Zhou, W., and Liu, J. (2017). Fluorescent sensors for sodium ions. *Anal. Methods*, 9(38):5570–5579.

- Gast, L. V., Gerhalter, T., Hensel, B., Uder, M., and Nagel, A. M. (2018). Double quantum filtered ^{23}Na MRI with magic angle excitation of human skeletal muscle in the presence of B_0 and B_1 inhomogeneities. *NMR Biomed*, 31(12):e4010.
- Gerlach, W. and Stern, O. (1924). Über die Richtungsquantelung im Magnetfeld. *Ann Phys*, 379(16):673–699.
- Ghisaidoobe, A. B. and Chung, S. J. (2014). Intrinsic tryptophan fluorescence in the detection and analysis of proteins: A focus on Förster resonance energy transfer techniques. *Int J Mol Sci*, 15(12):22518–22538.
- Giusti, S., Mazzei, D., Cacopardo, L., Mattei, G., Domenici, C., and Ahluwalia, A. (2017). Environmental control in flow bioreactors. *Processes*, 5(4):16.
- Goerke, S. (2015). “Effect of unfolding and aggregation on the ^1H -magnetization transfer between proteins and free water”. Thesis.
- Goerke, S., Breitling, J., Zaiss, M., Windschuh, J., Kunz, P., Schuenke, P., Paech, D., Longo, D. L., Klika, K. D., Ladd, M. E., and Bachert, P. (2018). Dual-frequency irradiation CEST-MRI of endogenous bulk mobile proteins. *NMR Biomed*, 31(6):e3920.
- Goerke, S., Milde, K. S., Bukowiecki, R., Kunz, P., Klika, K. D., Wiglenda, T., Mogk, A., Wanker, E. E., Bukau, B., Ladd, M. E., Bachert, P., and Zaiss, M. (2017). Aggregation-induced changes in the chemical exchange saturation transfer (CEST) signals of proteins. *NMR Biomed*, 30(1):e3665.
- Goerke, S., Zaiss, M., Kunz, P., Klika, K. D., Windschuh, J. D., Mogk, A., Bukau, B., Ladd, M. E., and Bachert, P. (2015). Signature of protein unfolding in chemical exchange saturation transfer imaging. *NMR Biomed*, 28(7):906–913.
- Gottwald, E., Giselbrecht, S., Augspurger, C., Lahni, B., Dambrowsky, N., Truckenmuller, R., Piottter, V., Gietzelt, T., Wendt, O., Pfleging, W., Welle, A., Rolletschek, A., Wobus, A. M., and Weibezahn, K. F. (2007). A chip-based platform for the in vitro generation of tissues in three-dimensional organization. *Lab Chip*, 7(6):777–785.
- Gottwald, E., Kleintschek, T., Giselbrecht, S., Truckenmuller, R., Altmann, B., Worgull, M., Dopfert, J., Schad, L., and Heilmann, M. (2013). Characterization of a chip-based bioreactor for three-dimensional cell cultivation via magnetic resonance imaging. *Z Med Phys*, 23(2):102–110.
- Gottwald, E., Nies, C., Wuchter, P., Saffrich, R., Truckenmuller, R., and Giselbrecht, S. (2019). A microcavity array-based 3D model system of the hematopoietic stem cell niche. *Methods Mol Biol*, 2017:85–95.
- Graaf, R. A. de (2019). In vivo NMR spectroscopy. John Wiley & Sons.
- Grimsley, G. R., Scholtz, J. M., and Pace, C. N. (2009). A summary of the measured pK values of the ionizable groups in folded proteins. *Protein Sci*, 18(1):247–251.

- Grivet, J.-P. and Delort, A.-M. (2009). NMR for microbiology: In vivo and in situ applications. *Prog Nucl Magn Reson Spectrosc*, 54(1):1–53.
- Haacke, E. M., Brown, R. W., Thompson, M. R., and Venkatesan, R. (1999). Magnetic resonance imaging: Physical principles and sequence design. John Wiley & Sons.
- Haas, M., Wang, H., Tian, J., and Xie, Z. (2002). Src-mediated inter-receptor cross-talk between the Na⁺/K⁺-ATPase and the epidermal growth factor receptor relays the signal from ouabain to mitogen-activated protein kinases. *J Biol Chem*, 277(21):18694–18702.
- Hancu, I., Boada, F. E., and Shen, G. X. (1999). Three-dimensional triple-quantum-filtered ²³Na imaging of in vivo human brain. *Magn Reson Med*, 42(6):1146–1154.
- Hanson, R. M., Prilusky, J., Renjian, Z., Nakane, T., and Sussman, J. L. (2013). JSmol and the next-generation web-based representation of 3D molecular structure as applied to proteopedia. *Isr J Chem*, 53(3-4):207–216.
- Harris, R. K., Becker, E. D., Cabral de Menezes, S. M., Goodfellow, R., and Granger, P. (2002). NMR nomenclature: Nuclear spin properties and conventions for chemical shifts. IUPAC recommendations 2001. *Solid State Nucl Magn Reson*, 22(4):458–483.
- Haynes, W. M. (2014). Handbook of chemistry and physics. 95th edition. CRC Press.
- Heinrich, P. C., Müller, M., and Graeve, L. (2014). Löffler/Petrides Biochemie und Pathobiochemie. Springer-Verlag Berlin Heidelberg.
- Hemminga, M. A. and Visser, J. (2000). NMR in biotechnology. *J Biotechnol*, 77(1):1–3.
- Henkelman, R. M., Stanisz, G. J., and Graham, S. J. (2001). Magnetization transfer in MRI: A review. *NMR Biomed*, 14(2):57–64.
- Hertig, D., Maddah, S., Memedovski, R., Felser, A., Moreno, A., Pennestri, M., Nuoffer, J.-M., and Vermathen, P. (2020). Life monitoring of cellular metabolism and mitochondrial respiration in 3D cell culture system using NMR spectroscopy. *Proc. Int. Soc. Magn. Reson. Med.*, 28:2994.
- Hoesl, M. A. U., Kleimaier, D., Hu, R., Malzacher, M., Nies, C., Gottwald, E., and Schad, L. R. (2019a). ²³Na triple-quantum signal of in vitro human liver cells, liposomes, and nanoparticles: Cell viability assessment vs. separation of intra- and extracellular signal. *J Magn Reson Imaging*, 50(2):435–444.
- Hoesl, M. A. U., Schad, L. R., and Rapacchi, S. (2020). Efficient ²³Na triple-quantum signal imaging on clinical scanners: Cartesian imaging of single and triple-quantum ²³Na (CRISTINA). *Magn Reson Med*, 84(5):2412–2428.
- Hoesl, M. A. U., Wuestemann, T., Malzacher, M., Nies, C., Gottwald, E., and Schad, L. (2019b). Non-invasive assessment of myocardial cell viability based on ²³Na triple-quantum signal. *Proc. Int. Soc. Magn. Reson. Med.*, 27:4202.

- Hu, R. (2019). “Exploring quadrupolar interactions of ^{23}Na and ^{35}Cl with triple-quantum MRI/MRS”. Thesis.
- Hu, R., Kleimaier, D., Malzacher, M., Hoesl, M. A. U., Paschke, N. K., and Schad, L. R. (2020). X-nuclei imaging: Current state, technical challenges, and future directions. *J Magn Reson Imaging*, 51(2):355–376.
- Hubbard, P. S. (1970). Nonexponential nuclear magnetic relaxation by quadrupole interactions. *J Chem Phys*, 53(3):985–987.
- Hutchison, R. B., Malhotra, D., Hendrick, R. E., Chan, L., and Shapiro, J. I. (1990). Evaluation of the double-quantum filter for the measurement of intracellular sodium concentration. *J Biol Chem*, 265(26):15506–15510.
- Iamshanova, O., Mariot, P., Lehen’kyi, V., and Prevarskaya, N. (2016). Comparison of fluorescence probes for intracellular sodium imaging in prostate cancer cell lines. *Eur Biophys J*, 45(7):765–777.
- Inglese, M., Madelin, G., Oesingmann, N., Babb, J. S., Wu, W., Stoeckel, B., Herbert, J., and Johnson, G. (2010). Brain tissue sodium concentration in multiple sclerosis: A sodium imaging study at 3 tesla. *Brain*, 133(Pt 3):847–857.
- Insko, E. K. and Bolinger, L. (1993). Mapping of the radiofrequency field. *J Magn Reson A*, 103(1):82–85.
- Jaccard, G., Wimperis, S., and Bodenhausen, G. (1986). Multiple-quantum NMR spectroscopy of $S = 3/2$ spins in isotropic phase: A new probe for multiexponential relaxation. *J Chem Phys*, 85(11):6282–6293.
- Jacobs, M. A., Ouwerkerk, R., Wolff, A. C., Gabrielson, E., Warzecha, H., Jeter, S., Bluemke, D. A., Wahl, R., and Stearns, V. (2011). Monitoring of neoadjuvant chemotherapy using multiparametric, ^{23}Na sodium MR, and multimodality (PET/CT/MRI) imaging in locally advanced breast cancer. *Breast Cancer Res Treat*, 128(1):119–126.
- Jelicks, L. A. and Gupta, R. K. (1993). On the extracellular contribution to multiple quantum filtered ^{23}Na NMR of perfused rat heart. *Magn Reson Med*, 29(1):130–133.
- Jin, T., Wang, P., Zong, X., and Kim, S. G. (2013). MR imaging of the amide-proton transfer effect and the pH-insensitive nuclear Overhauser effect at 9.4 T. *Magn Reson Med*, 69(3):760–770.
- Johnstone, I. M. and Silverman, B. W. (2004). Needles and straw in haystacks: Empirical Bayes estimates of possibly sparse sequences. *Ann Stat*, 32(4):1594–1649.
- Jones, C. K., Huang, A., Xu, J., Edden, R. A., Schar, M., Hua, J., Oskolkov, N., Zaca, D., Zhou, J., McMahon, M. T., Pillai, J. J., and van Zijl, P. C. M. (2013). Nuclear Overhauser enhancement (NOE) imaging in the human brain at 7 T. *Neuroimage*, 77:114–124.
- Kalyanapuram, R., Seshan, V., and Bansal, N. (1998). Three-dimensional triple-quantum-filtered ^{23}Na imaging of the dog head in vivo. *J Magn Reson Imaging*, 8(5):1182–1189.

- Kampinga, H. H., Luppens, J. G., and Konings, A. W. (1987). Heat-induced nuclear protein binding and its relation to thermal cytotoxicity. *Int J Hyperthermia*, 3(5):459–465.
- Kampinga, H. H., Turkel-Uygur, N., Roti, J. L. R., and Konings, A. W. T. (1989). The relationship of increased nuclear protein content induced by hyperthermia to killing of HeLa S3 cells. *Radiat Res*, 117(3):511.
- Katsuta, K., Hatakeyama, M., and Hiraki, J. (1997). Isothermal gelation of proteins. 1. Urea-induced gelation of whey proteins and their gelling mechanism. *Food Hydrocolloid*, 11(4):367–372.
- Kauzmann, W. (1959). Some factors in the interpretation of protein denaturation. *Adv Protein Chem*, 14:1–63.
- Kemp-Harper, R., Brown, S. P., Hughes, C. E., Styles, P., and Wimperis, S. (1997). ^{23}Na NMR methods for selective observation of sodium ions in ordered environments. *Prog Nucl Magn Reson Spectrosc*, 30(3-4):157.
- Keshari, K. R., Kurhanewicz, J., Jeffries, R. E., Wilson, D. M., Dewar, B. J., Van Criekinge, M., Zierhut, M., Vigneron, D. B., and Macdonald, J. M. (2010). Hyperpolarized ^{13}C spectroscopy and an NMR-compatible bioreactor system for the investigation of real-time cellular metabolism. *Magn Reson Med*, 63(2):322–329.
- Kleimaier, D., Schepkin, V., Hu, R., and Schad, L. R. (2020c). Protein conformational changes affect the sodium triple-quantum MR signal. *NMR Biomed*, 33(10):e4367.
- Kleimaier, D., Goerke, S., Nies, C., Zaiss, M., Kunz, P., Bachert, P., Ladd, M. E., Gottwald, E., and Schad, L. R. (2020e). The cellular heat shock response monitored by chemical exchange saturation transfer MRI. *Sci Rep*, 10(1):11118.
- Kleimaier, D., Schepkin, V., Nies, C., Gottwald, E., and Schad, L. R. (2020f). Intracellular sodium changes in cancer cells using a microcavity array-based bioreactor system and sodium triple-quantum MR signal. *Processes*, 8(10):1267.
- Knubovets, T., Shinar, H., Eliav, U., and Navon, G. (1996). A ^{23}Na multiple-quantum-filtered NMR study of the effect of the cytoskeleton conformation on the anisotropic motion of sodium ions in red blood cells. *J Magn Reson B*, 110(1):16–25.
- Knubovets, T., Shinar, H., and Navon, G. (1998). Quantification of the contribution of extracellular sodium to ^{23}Na multiple-quantum-filtered NMR spectra of suspensions of human red blood cells. *J Magn Reson*, 131(1):92–96.
- Kobatake, K., Sako, K., Izawa, M., Yamamoto, Y. L., and Hakim, A. M. (1984). Autoradiographic determination of brain pH following middle cerebral artery occlusion in the rat. *Stroke*, 15(3):540–547.
- Kropp, M. (2019). “Effects of B_1^+ -inhomogeneity in sodium triple quantum NMR spectroscopy”. Thesis.

- Kumar, S. and Nussinov, R. (2002). Close-range electrostatic interactions in proteins. *Chembiochem*, 3(7):604–617.
- Kundra, R., Ciryam, P., Morimoto, R. I., Dobson, C. M., and Vendruscolo, M. (2017). Protein homeostasis of a metastable subproteome associated with Alzheimer’s disease. *Proc Natl Acad Sci USA*, 114(28):E5703–E5711.
- Kurland, R., Newton, C., Nir, S., and Papahadjopoulos, D. (1979). Specificity of Na⁺ binding to phosphatidylserine vesicles from a ²³Na NMR relaxation rate study. *Biochim Biophys Acta Biomembr*, 551(1):137–147.
- Ladd, M. E., Bachert, P., Meyerspeer, M., Moser, E., Nagel, A. M., Norris, D. G., Schmitter, S., Speck, O., Straub, S., and Zaiss, M. (2018). Pros and cons of ultra-high-field MRI/MRS for human application. *Prog Nucl Magn Reson Spectrosc*, 109:1–50.
- Lauterbur, P. C. (1973). Image formation by induced local interactions: Examples employing nuclear magnetic resonance. *Nature*, 242(5394):190–191.
- LaVerde, G., Nemoto, E., Jungreis, C. A., Tanase, C., and Boada, F. E. (2007). Serial triple quantum sodium MRI during non-human primate focal brain ischemia. *Magn Reson Med*, 57(1):201–205.
- Leuenberger, P., Ganscha, S., Kahraman, A., Cappelletti, V., Boersema, P. J., Mering, C. von, Claassen, M., and Picotti, P. (2017). Cell-wide analysis of protein thermal unfolding reveals determinants of thermostability. *Science*, 355(6327).
- Levitt, M. H. (2008). Spin dynamics: Basics of nuclear magnetic resonance, 2nd edition. John Wiley & Sons.
- Lin, V. J. and Koenig, J. L. (1976). Raman studies of bovine serum albumin. *Biopolymers*, 15(1):203–218.
- Liu, G., Song, X., Chan, K. W., and McMahon, M. T. (2013). Nuts and bolts of chemical exchange saturation transfer MRI. *NMR Biomed*, 26(7):810–828.
- Lundervold, A. S. and Lundervold, A. (2019). An overview of deep learning in medical imaging focusing on MRI. *Z Med Phys*, 29(2):102–127.
- Lustig, M., Donoho, D., and Pauly, J. M. (2007). Sparse MRI: The application of compressed sensing for rapid MR imaging. *Magn Reson Med*, 58(6):1182–1195.
- Maarel, J. R. C. van der (2003a). Thermal relaxation and coherence dynamics of spin 3/2. I. Static and fluctuating quadrupolar interactions in the multipole basis. *Concepts Magn Reson*, 19A(2):97–116.
- Maarel, J. R. C. van der (2003b). Thermal relaxation and coherence dynamics of spin 3/2. II. Strong radio-frequency field. *Concepts Magn Reson*, 19A(2):117–133.
- Macdonald, J. M., Kurhanewicz, J., Dahiya, R., Espanol, M. T., Chang, L. H., Goldberg, B., James, T. L., and Narayan, P. (1993). Effect of glucose and confluency on phosphorus

- metabolites of perfused human prostatic adenocarcinoma cells as determined by ^{31}P MRS. *Magn Reson Med*, 29(2):244–248.
- Macdonald, J. M., Grillo, M., Schmidlin, O., Tajiri, D. T., and James, T. L. (1998). NMR spectroscopy and MRI investigation of a potential bioartificial liver. *NMR Biomed*, 11(2):55–66.
- Madelin, G., Chang, G., Otazo, R., Jerschow, A., and Regatte, R. R. (2012). Compressed sensing sodium MRI of cartilage at 7 T: Preliminary study. *J Magn Reson*, 214(1):360–365.
- Madelin, G., Lee, J. S., Regatte, R. R., and Jerschow, A. (2014). Sodium MRI: Methods and applications. *Prog Nucl Magn Reson Spectrosc*, 79:14–47.
- Madelin, G., Poidevin, F., Makrymallis, A., and Regatte, R. R. (2015). Classification of sodium MRI data of cartilage using machine learning. *Magn Reson Med*, 74(5):1435–1448.
- Madelin, G. and Regatte, R. R. (2013). Biomedical applications of sodium MRI in vivo. *J Magn Reson Imaging*, 38(3):511–529.
- Majors, P. D., McLean, J. S., and Scholten, J. C. (2008). NMR bioreactor development for live in-situ microbial functional analysis. *J Magn Reson*, 192(1):159–166.
- Makela, H. I., Grohn, O. H., Kettunen, M. I., and Kauppinen, R. A. (2001). Proton exchange as a relaxation mechanism for T_1 in the rotating frame in native and immobilized protein solutions. *Biochem Biophys Res Commun*, 289(4):813–818.
- Mancuso, A., Fernandez, E. J., Blanch, H. W., and Clark, D. S. (1990). A nuclear magnetic resonance technique for determining hybridoma cell concentration in hollow fiber bioreactors. *Biotechnology*, 8(12):1282–1285.
- Mansfield, P. and Grannell, P. K. (1973). NMR 'diffraction' in solids? *J Phys C: Solid State Phys*, 6(22):L422–L426.
- Marathe, K., McVicar, N., Li, A., Bellyou, M., Meakin, S., and Bartha, R. (2016). Topiramate induces acute intracellular acidification in glioblastoma. *J Neurooncol*, 130(3):465–472.
- Marban, E., Yamagishi, T., and Tomaselli, G. F. (1998). Structure and function of voltage-gated sodium channels. *J Physiol*, 508 (Pt 3):647–657.
- Marion, D. and Wüthrich, K. (1983). Application of phase sensitive two-dimensional correlated spectroscopy (COSY) for measurements of ^1H - ^1H spin-spin coupling constants in proteins. *Biochem. Biophys. Res. Commun.*, 113(3):967–974.
- Matouschek, A., Kellis J. T., J., Serrano, L., and Fersht, A. R. (1989). Mapping the transition state and pathway of protein folding by protein engineering. *Nature*, 340(6229):122–126.

- Matthies, C., Nagel, A. M., Schad, L. R., and Bachert, P. (2010). Reduction of B_0 inhomogeneity effects in triple-quantum-filtered sodium imaging. *J Magn Reson*, 202(2):239–244.
- McConnell, H. M. (1958). Reaction rates by nuclear magnetic resonance. *J Chem Phys*, 28(3):430–431.
- Meissner, J. E., Korzowski, A., Regnery, S., Goerke, S., Breitling, J., Floca, R. O., Debus, J., Schlemmer, H. P., Ladd, M. E., Bachert, P., Adeberg, S., and Paech, D. (2019). Early response assessment of glioma patients to definitive chemoradiotherapy using chemical exchange saturation transfer imaging at 7 T. *J Magn Reson Imaging*, 50(4):1268–1277.
- Michels, A. A., Kanon, B., Konings, A. W., Ohtsuka, K., Bensaude, O., and Kampinga, H. H. (1997). Hsp70 and Hsp40 chaperone activities in the cytoplasm and the nucleus of mammalian cells. *J Biol Chem*, 272(52):33283–33289.
- Mogk, A., Bukau, B., and Kampinga, H. H. (2018). Cellular handling of protein aggregates by disaggregation machines. *Mol Cell*, 69(2):214–226.
- Monoi, H. (1985). Nuclear magnetic resonance of ^{23}Na ions interacting with the gramicidin channel. *Biophys J*, 48(4):643–662.
- Moon, R. B. and Richards, J. H. (1973). Determination of intracellular pH by ^{31}P magnetic resonance. *J Biol Chem*, 248(20):7276–7278.
- Moore, D. S. (1985). Amino acid and peptide net charges: A simple calculational procedure. *Biochem Educ*, 13(1):10–11.
- Mueller, N., Bodenhausen, G., and Ernst, R. R. (1987). Relaxation-induced violations of coherence transfer selection rules in nuclear magnetic resonance. *J Magn Reson*, 75(2):297–334.
- Nagel, A. M., Laun, F. B., Weber, M. A., Matthies, C., Semmler, W., and Schad, L. R. (2009). Sodium MRI using a density-adapted 3D radial acquisition technique. *Magn Reson Med*, 62(6):1565–1573.
- Nagel, A. M., Umathum, R., Rosler, M. B., Ladd, M. E., Litvak, I., Gor'kov, P. L., Brey, W. W., and Schepkin, V. D. (2016). ^{39}K and ^{23}Na relaxation times and MRI of rat head at 21.1 T. *NMR Biomed*, 29(6):759–766.
- Narayan, K. S., Moress, E. A., Chatham, J. C., and Barker, P. B. (1990). ^{31}P NMR of mammalian cells encapsulated in alginate gels utilizing a new phosphate-free perfusion medium. *NMR Biomed*, 3(1):23–26.
- Naritomi, H., Kanashiro, M., Sasaki, M., Kuribayashi, Y., and Sawada, T. (1987). In vivo measurements of intra- and extracellular Na^+ and water in the brain and muscle by nuclear magnetic resonance spectroscopy with shift reagent. *Biophys J*, 52(4):611–616.

- Navon, G. (1993). Complete elimination of the extracellular ^{23}Na NMR signal in triple quantum filtered spectra of rat hearts in the presence of shift reagents. *Magn Reson Med*, 30(4):503–506.
- Nedergaard, M., Kraig, R. P., Tanabe, J., and Pulsinelli, W. A. (1991). Dynamics of interstitial and intracellular pH in evolving brain infarct. *Am J Physiol*, 260(3 Pt 2):R581–R588.
- Neubauer, A. (2015). “Modeling and validation of ionic regulatory processes with X-nuclei-MRI”. Thesis.
- Neubauer, A., Nies, C., Schepkin, V. D., Hu, R., Malzacher, M., Chacon-Caldera, J., Thiele, D., Gottwald, E., and Schad, L. R. (2017). Tracking protein function with sodium multi quantum spectroscopy in a 3D-tissue culture based on microcavity arrays. *Sci Rep*, 7(1):3943.
- Neuhaus, D. and Williamson, M. P. (2000). The nuclear Overhauser effect in structural and conformational analysis, 2nd edition. John Wiley & Sons.
- Neumaier-Probst, E., Konstandin, S., Ssozi, J., Groden, C., Hennerici, M., Schad, L. R., and Fatar, M. (2015). A double-tuned $^1\text{H}/^{23}\text{Na}$ resonator allows ^1H -guided ^{23}Na -MRI in ischemic stroke patients in one session. *Int J Stroke*, 10:56–61.
- Nguyen, A. N., Wallace, D. P., and Blanco, G. (2007). Ouabain binds with high affinity to the Na,K-ATPase in human polycystic kidney cells and induces extracellular signal-regulated kinase activation and cell proliferation. *J Am Soc Nephrol*, 18(1):46–57.
- Nollen, E. A., Brunsting, J. F., Roelofsen, H., Weber, L. A., and Kampinga, H. H. (1999). In vivo chaperone activity of heat shock protein 70 and thermotolerance. *Mol Cell Biol*, 19(3):2069–2079.
- Otting, G. and Liepinsh, E. (2002). Protein hydration viewed by high-resolution NMR spectroscopy: Implications for magnetic resonance image contrast. *Acc Chem Res*, 28(4):171–177.
- Pace, C. N. (1986). Determination and analysis of urea and guanidine hydrochloride denaturation curves. *Methods Enzymol*, 131:266–280.
- Pace, C. N. and Shaw, K. L. (2000). Linear extrapolation method of analyzing solvent denaturation curves. *Proteins*, 41(S4):1–7.
- Paech, D., Dreher, C., Regnery, S., Meissner, J. E., Goerke, S., Windschuh, J., Oberhollenzer, J., Schultheiss, M., Deike-Hofmann, K., Bickelhaupt, S., Radbruch, A., Zaiss, M., Unterberg, A., Wick, W., Bendszus, M., Bachert, P., Ladd, M. E., and Schlemmer, H. P. (2019). Relaxation-compensated amide proton transfer (APT) MRI signal intensity is associated with survival and progression in high-grade glioma patients. *Eur Radiol*, 29(9):4957–4967.
- Pape, H.-C., Kurtz, A., and Silbernagl, S. (2019). Physiologie. Thieme.

- Parsell, D. A., Kowal, A. S., Singer, M. A., and Lindquist, S. (1994). Protein disaggregation mediated by heat-shock protein Hsp104. *Nature*, 372(6505):475–478.
- Pavuluri, K. and McMahon, M. T. (2017). pH imaging using chemical exchange saturation transfer (CEST) MRI. *Isr J Chem*, 57(9):862–879.
- Petracca, M., Fleysher, L., Oesingmann, N., and Inglese, M. (2016a). Sodium MRI of multiple sclerosis. *NMR Biomed*, 29(2):153–161.
- Petracca, M., Vancea, R. O., Fleysher, L., Jonkman, L. E., Oesingmann, N., and Inglese, M. (2016b). Brain intra- and extracellular sodium concentration in multiple sclerosis: A 7 T MRI study. *Brain*, 139(3):795–806.
- Pfister, H. and Pauly, H. (1964). Membranpotential und Ionenbindung in Proteinlösungen. *Biophysik*, 1(4):364–369.
- Pike, M. M., Frazer, J. C., Dedrick, D. F., Ingwall, J. S., Allen, P. D., Springer, C. S., and Smith, T. W. (1985). ^{23}Na and ^{39}K nuclear magnetic resonance studies of perfused rat hearts. Discrimination of intra- and extracellular ions using a shift reagent. *Biophys J*, 48(1):159–173.
- Pinto, M., Morange, M., and Bensaude, O. (1991). Denaturation of proteins during heat-shock. In vivo recovery of solubility and activity of reporter enzymes. *J Biol Chem*, 266(21):13941–13946.
- Purcell, E. M., Torrey, H. C., and Pound, R. V. (1946). Resonance absorption by nuclear magnetic moments in a solid. *Phys Rev*, 69(1-2):37–38.
- Rabi, I. I., Zacharias, J. R., Millman, S., and Kusch, P. (1938). A new method of measuring nuclear magnetic moment. *Phys Rev*, 53(4):318–318.
- Ray, K. J., Simard, M. A., Larkin, J. R., Coates, J., Kinches, P., Smart, S. C., Higgins, G. S., Chappell, M. A., and Sibson, N. R. (2019). Tumor pH and protein concentration contribute to the signal of amide proton transfer magnetic resonance imaging. *Cancer Res*, 79(7):1343–1352.
- Reddy, R., Shinnar, M., Wang, Z., and Leigh, J. S. (1994). Multiple-quantum filters of spin- $\frac{3}{2}$ with pulses of arbitrary flip angle. *J Magn Reson B*, 104(2):148–152.
- Reinsch, C. H. (1967). Smoothing by spline functions. *Numer Math*, 10(3):177–183.
- Richter, K., Haslbeck, M., and Buchner, J. (2010). The heat shock response: Life on the verge of death. *Mol Cell*, 40(2):253–266.
- Roesler, M. B., Nagel, A. M., Umathum, R., Bachert, P., and Benkhedah, N. (2016). In vivo observation of quadrupolar splitting in ^{39}K magnetic resonance spectroscopy of human muscle tissue. *NMR Biomed*, 29(4):451–457.
- Romsted, L. S. and Yoon, C. O. (1993). Counterion affinity orders in aqueous micellar solutions of sodium decyl phosphate and sodium dodecyl sulfate determined by changes

- in sodium-23 NMR relaxation rates: A surprising dependence on head group charge. *J Am Chem Soc*, 115(3):989–994.
- Rooney, W. D., Li, X., Sammi, M. K., Bourdette, D. N., Neuwelt, E. A., and Springer C. S., J. (2015). Mapping human brain capillary water lifetime: High-resolution metabolic neuroimaging. *NMR Biomed*, 28(6):607–623.
- Rooney, W. D. and Springer C. S., J. (1991a). A comprehensive approach to the analysis and interpretation of the resonances of spins 3/2 from living systems. *NMR Biomed*, 4(5):209–226.
- Rooney, W. D. and Springer, C. S. (1991b). The molecular environment of intracellular sodium: ^{23}Na NMR relaxation. *NMR Biomed*, 4(5):227–245.
- Rose, M. E. (1957). Elementary theory of angular momentum. John Wiley & Sons.
- Roti Roti, J. L. (2008). Cellular responses to hyperthermia (40–46°C): Cell killing and molecular events. *Int J Hyperthermia*, 24(1):3–15.
- Sako, K., Kobatake, K., Yamamoto, Y. L., and Diksic, M. (1985). Correlation of local cerebral blood flow, glucose utilization, and tissue pH following a middle cerebral artery occlusion in the rat. *Stroke*, 16(5):828–834.
- Sanui, H. and Pace, N. (1959). Sodium and potassium binding by rat liver cell microsomes. *J Gen Physiol*, 42(6):1325–1345.
- Sanui, H. and Pace, N. (1962). Sodium and potassium binding by human erythrocyte ghosts. *J Cell Comp Physiol*, 59:251–257.
- Sanui, H. and Pace, N. (1963). Sodium, potassium and hydrogen ion binding characteristics of dog erythrocyte ghosts. *J Cell Comp Physiol*, 62:95–103.
- Saroff, H. A. (1957). The binding of ions to the muscle proteins. A theory for K^+ and Na^+ binding based on a hydrogen-bonded and chelated model. *Arch Biochem Biophys*, 71(1):194–203.
- Schepkin, V. D., Choy, I. O., and Budinger, T. F. (1996). Sodium alterations in isolated rat heart during cardioplegic arrest. *J Appl Physiol*, 81(6):2696–2702.
- Schepkin, V. D., Choy, I. O., Budinger, T. F., Obayashi, D. Y., Taylor, S. E., DeCampli, W. M., Amartur, S. C., and Young, J. N. (1998). Sodium TQF NMR and intracellular sodium in isolated crystalloid perfused rat heart. *Magn Reson Med*, 39(4):557–563.
- Schepkin, V. D., Choy, I. O., Budinger, T. F., Young, J. N., and DeCampli, W. M. (1999). Multi-dose crystalloid cardioplegia preserves intracellular sodium homeostasis in myocardium. *J Mol Cell Cardiol*, 31(9):1643–1651.
- Schepkin, V. D., Gawlick, U., Ross, B. D., and Chenevert, T. L. (2003). Detection of triple quantum Na NMR in normal and tumored mouse brain. *Proc Int Soc Magn Reson Med.*, 11:39.

- Schepkin, V. D., Neubauer, A., Nagel, A. M., and Budinger, T. F. (2017). Comparison of potassium and sodium binding in vivo and in agarose samples using TQTPPI pulse sequence. *J Magn Reson*, 277:162–168.
- Schepkin, V. D., Ross, B. D., Chenevert, T. L., Rehemtulla, A., Sharma, S., Kumar, M., and Stojanovska, J. (2005). Sodium magnetic resonance imaging of chemotherapeutic response in a rat glioma. *Magn Reson Med*, 53(1):85–92.
- Schröder, H., Langer, T., Hartl, F. U., and Bukau, B. (1993). DnaK, DnaJ and GrpE form a cellular chaperone machinery capable of repairing heat-induced protein damage. *EMBO Journal*, 12(11):4137–4144.
- Seshan, V., Sherry, A. D., and Bansal, N. (1997). Evaluation of triple quantum-filtered ^{23}Na NMR spectroscopy in the in situ rat liver. *Magn Reson Med*, 38(5):821–827.
- Siegal, G. and Selenko, P. (2019). Cells, drugs and NMR. *J Magn Reson*, 306:202–212.
- Simor, T., Lóránd, T., Szöllösy, Á., Gaszner, B., Digerness, S. B., and Elgavish, G. A. (1999). ^{23}Na NMR shift reagents enhance cardiac staircase effect in isolated perfused rat hearts. *NMR Biomed*, 12(5):267–274.
- Slichter, C. P. (1990). Principles of magnetic resonance. Springer Series in Solid-State Sciences. Springer-Verlag Berlin Heidelberg.
- Solomon, I. (1955). Relaxation processes in a system of two spins. *Phys Rev*, 99(2):559–565.
- Sørensen, O. W., Eich, G. W., Levitt, M. H., Bodenhausen, G., and Ernst, R. R. (1984). Product operator formalism for the description of NMR pulse experiments. *Prog Nucl Magn Reson Spectrosc*, 16:163–192.
- Sørensen, S. P. L. (1909). Über die Messung und die Bedeutung der Wasserstoffionenkonzentration bei enzymatischen Prozessen. *Biochem. Zeitschr.*, 21:131–304.
- Sottile, M. L. and Nadin, S. B. (2018). Heat shock proteins and DNA repair mechanisms: An updated overview. *Cell Stress Chaperones*, 23(3):303–315.
- Stanisz, G. J., Odobina, E. E., Pun, J., Escaravage, M., Graham, S. J., Bronskill, M. J., and Henkelman, R. M. (2005). T_1 , T_2 relaxation and magnetization transfer in tissue at 3T. *Magn Reson Med*, 54(3):507–512.
- Stege, G. J., Li, G. C., Li, L., Kampinga, H. H., and Konings, A. W. (1994). On the role of hsp72 in heat-induced intranuclear protein aggregation. *Int J Hyperthermia*, 10(5):659–674.
- Stobbe, R. W. and Beaulieu, C. (2016). Residual quadrupole interaction in brain and its effect on quantitative sodium imaging. *NMR Biomed*, 29(2):119–128.
- Swanson, S. D. (1991). Broadband excitation and detection of cross-relaxation NMR spectra. *J Magn Reson*, 95(3):615–618.

- Tanase, C. and Boada, F. E. (2005). Triple-quantum-filtered imaging of sodium in presence of B_0 inhomogeneities. *J Magn Reson*, 174(2):270–278.
- Tauskela, J. S., Dizon, J. M., Whang, J., and Katz, J. (1997). Evaluation of multiple-quantum-filtered ^{23}Na NMR in monitoring intracellular Na content in the isolated perfused rat heart in the absence of a chemical-shift reagent. *J Magn Reson*, 127(1):115–127.
- Thelwall, P. E. and Brindle, K. M. (1999). Analysis of CHO-K1 cell growth in a fixed bed bioreactor using magnetic resonance spectroscopy and imaging. *Cytotechnology*, 30(1-3):121–132.
- Thulborn, K. R. (2018). Quantitative sodium MR imaging: A review of its evolving role in medicine. *Neuroimage*, 168:250–268.
- Thulborn, K. R., Davis, D., Snyder, J., Yonas, H., and Kassam, A. (2005). Sodium MR imaging of acute and subacute stroke for assessment of tissue viability. *Neuroimaging Clin N Am*, 15(3):639–653.
- Torres, A. M., Philp, D. J., Kemp-Harper, R., Garvey, C., and Kuchel, P. W. (2005). Determination of Na^+ binding parameters by relaxation analysis of selected ^{23}Na NMR coherences: RNA, BSA and SDS. *Magn Reson Chem*, 43(3):217–224.
- Trott, O. and Palmer A. G., 3. (2002). $R_{1\rho}$ relaxation outside of the fast-exchange limit. *J Magn Reson*, 154(1):157–160.
- Trouard, T. P., Harkins, K. D., Divijak, J. L., Gillies, R. J., and Galons, J. P. (2008). Ischemia-induced changes of intracellular water diffusion in rat glioma cell cultures. *Magn Reson Med*, 60(2):258–264.
- Tsang, A., Stobbe, R. W., and Beaulieu, C. (2013). Evaluation of B_0 -inhomogeneity correction for triple-quantum-filtered sodium MRI of the human brain at 4.7 T. *J Magn Reson*, 230:134–144.
- Tsang, A., Stobbe, R. W., and Beaulieu, C. (2015). In vivo double quantum filtered sodium magnetic resonance imaging of human brain. *Magn Reson Med*, 73(2):497–504.
- Ui, N. (1973). Conformational studies on proteins by isoelectric focusing. *Ann N Y Acad Sci*, 209:198–209.
- Uzman, L. L. (1953). Organic anion binding by denatured bovine serum albumin. *Nature*, 171(4354):653–654.
- Wallace, E. W., Kear-Scott, J. L., Pilipenko, E. V., Schwartz, M. H., Laskowski, P. R., Rojek, A. E., Katanski, C. D., Riback, J. A., Dion, M. F., Franks, A. M., Airoidi, E. M., Pan, T., Budnik, B. A., and Drummond, D. A. (2015). Reversible, specific, active aggregates of endogenous proteins assemble upon heat stress. *Cell*, 162(6):1286–1298.
- Wallen, C. A. and Landis, M. (1990). Removal of excess nuclear protein from cells heated in different physiological states. *Int J Hyperthermia*, 6(1):87–95.

- Wang, S., Su, Z., Ying, L., Peng, X., Zhu, S., Liang, F., Feng, D., and Liang, D. (2016). Accelerating magnetic resonance imaging via deep learning. *IEEE*, 16:514–517.
- Wenzel, T. J., Skoog, D. A., West, D. M., Holler, J. F., and Crouch, S. R. (2013). Fundamentals of analytical chemistry. *Cengage Learning*.
- White, K. A., Grillo-Hill, B. K., and Barber, D. L. (2017). Cancer cell behaviors mediated by dysregulated pH dynamics at a glance. *J Cell Sci*, 130(4):663–669.
- Wilson, M., Andronesi, O., Barker, P. B., Bartha, R., Bizzi, A., Bolan, P. J., Brindle, K. M., Choi, I. Y., Cudalbu, C., Dydak, U., Emir, U. E., Gonzalez, R. G., Gruber, S., Gruetter, R., Gupta, R. K., Heerschap, A., Henning, A., Hetherington, H. P., Huppi, P. S., Hurd, R. E., Kantarci, K., Kauppinen, R. A., Klomp, D. W. J., Kreis, R., Kruiskamp, M. J., Leach, M. O., Lin, A. P., Luijten, P. R., Marjanska, M., Maudsley, A. A., Meyerhoff, D. J., Mountford, C. E., Mullins, P. G., Murdoch, J. B., Nelson, S. J., Noeske, R., Oz, G., Pan, J. W., Peet, A. C., Poptani, H., Posse, S., Ratai, E. M., Salibi, N., Scheenen, T. W. J., Smith, I. C. P., Soher, B. J., Tkac, I., Vigneron, D. B., and Howe, F. A. (2019). Methodological consensus on clinical proton MRS of the brain: Review and recommendations. *Magn Reson Med*, 82(2):527–550.
- Windschuh, J., Zaiss, M., Meissner, J. E., Paech, D., Radbruch, A., Ladd, M. E., and Bachert, P. (2015). Correction of B_1 -inhomogeneities for relaxation-compensated CEST imaging at 7 T. *NMR Biomed*, 28(5):529–537.
- Winter, P. M. and Bansal, N. (2001a). Triple-quantum-filtered ^{23}Na NMR spectroscopy of subcutaneously implanted 9L gliosarcoma in the rat in the presence of TmDOTP^{5-1} . *J Magn Reson*, 152(1):70–78.
- Winter, P. M., Poptani, H., and Bansal, N. (2001b). Effects of chemotherapy by 1,3-bis(2-chloroethyl)-1-nitrosourea on single-quantum- and triple-quantum-filtered ^{23}Na and ^{31}P nuclear magnetic resonance of the subcutaneously implanted 9L glioma. *Cancer Res*, 61(5):2002–2007.
- Woessner, D. E. (2001). NMR relaxation of spin- $\frac{3}{2}$ nuclei: Effects of structure, order, and dynamics in aqueous heterogeneous systems. *Concepts Magn Reson*, 13(5):294–325.
- Wolff, S. D. and Balaban, R. S. (1989). Magnetization transfer contrast (MTC) and tissue water proton relaxation in vivo. *Magn Reson Med*, 10(1):135–144.
- Wolff, S. D. and Balaban, R. S. (1990). NMR imaging of labile proton exchange. *J Magn Reson*, 86(1):164–169.
- Worthoff, W. A., Shymanskaya, A., and Shah, N. J. (2019). Relaxometry and quantification in simultaneously acquired single and triple quantum filtered sodium MRI. *Magn Reson Med*, 81(1):303–315.
- Wright, P. E. and Dyson, H. J. (2015). Intrinsically disordered proteins in cellular signalling and regulation. *Nat Rev Mol Cell Biol*, 16(1):18–29.
- Wüthrich, K. (1986). NMR of proteins and nucleic acids. John Wiley & Sons.

- Xu, J., Yadav, N. N., Bar-Shir, A., Jones, C. K., Chan, K. W., Zhang, J., Walczak, P., McMahon, M. T., and van Zijl, P. C. M. (2014). Variable delay multi-pulse train for fast chemical exchange saturation transfer and relayed-nuclear Overhauser enhancement MRI. *Magn Reson Med*, 71(5):1798–1812.
- Xu, X., Lee, J.-S., and Jerschow, A. (2013). Ultrafast scanning of exchangeable sites by NMR spectroscopy. *Angew Chem Int Ed. Engl*, 52(32):8281–8284.
- Yan, K., Fu, Z., Yang, C., Zhang, K., Jiang, S., Lee, D. H., Heo, H. Y., Zhang, Y., Cole, R. N., Van Eyk, J. E., and Zhou, J. (2015). Assessing amide proton transfer (APT) MRI contrast origins in 9L gliosarcoma in the rat brain using proteomic analysis. *Mol Imaging Biol*, 17(4):479–487.
- Yin, J., Hu, Y., and Yoon, J. (2015). Fluorescent probes and bioimaging: Alkali metals, alkaline earth metals and pH. *Chem Soc Rev*, 44(14):4619–4644.
- Zaaraoui, W., Konstandin, S., Audoin, B., Nagel, A. M., Rico, A., Malikova, I., Soulier, E., Viout, P., Confort-Gouny, S., Cozzone, P. J., Pelletier, J., Schad, L. R., and Ranjeva, J. P. (2012). Distribution of brain sodium accumulation correlates with disability in multiple sclerosis: A cross-sectional ^{23}Na MR imaging study. *Radiology*, 264(3):859–867.
- Zaiss, M. and Bachert, P. (2013a). Chemical exchange saturation transfer (CEST) and MR Z-spectroscopy in vivo: A review of theoretical approaches and methods. *Phys Med Biol*, 58(22):R221–R269.
- Zaiss, M. and Bachert, P. (2013b). Exchange-dependent relaxation in the rotating frame for slow and intermediate exchange – Modeling off-resonant spin-lock and chemical exchange saturation transfer. *NMR Biomed*, 26(5):507–518.
- Zaiss, M., Kunz, P., Goerke, S., Radbruch, A., and Bachert, P. (2013c). MR imaging of protein folding in vitro employing nuclear-Overhauser-mediated saturation transfer. *NMR Biomed*, 26(12):1815–1822.
- Zaiss, M., Windschuh, J., Goerke, S., Paech, D., Meissner, J. E., Burth, S., Kickingreder, P., Wick, W., Bendszus, M., Schlemmer, H. P., Ladd, M. E., Bachert, P., and Radbruch, A. (2017). Downfield-NOE-suppressed amide-CEST-MRI at 7 Tesla provides a unique contrast in human glioblastoma. *Magn Reson Med*, 77(1):196–208.
- Zaiss, M., Windschuh, J., Paech, D., Meissner, J. E., Burth, S., Schmitt, B., Kickingreder, P., Wiestler, B., Wick, W., Bendszus, M., Schlemmer, H. P., Ladd, M. E., Bachert, P., and Radbruch, A. (2015). Relaxation-compensated CEST-MRI of the human brain at 7 T: Unbiased insight into NOE and amide signal changes in human glioblastoma. *Neuroimage*, 112:180–188.
- Zaiss, M., Xu, J., Goerke, S., Khan, I. S., Singer, R. J., Gore, J. C., Gochberg, D. F., and Bachert, P. (2014). Inverse Z-spectrum analysis for spillover-, MT-, and T_1 -corrected steady-state pulsed CEST-MRI-application to pH-weighted MRI of acute stroke. *NMR Biomed*, 27(3):240–252.

- Zaric, O., Pinker, K., Zbyn, S., Strasser, B., Robinson, S., Minarikova, L., Gruber, S., Farr, A., Singer, C., Helbich, T. H., Trattnig, S., and Bogner, W. (2016). Quantitative sodium MR imaging at 7 T: Initial results and comparison with diffusion-weighted imaging in patients with breast tumors. *Radiology*, 280(1):39–48.
- Zhou, J. and van Zijl, P. C. M. (2006). Chemical exchange saturation transfer imaging and spectroscopy. *Prog Nucl Magn Reson Spectrosc*, 48(2-3):109–136.
- Zhou, Y., van Zijl, P. C. M., Xu, J., and Yadav, N. N. (2020). Mechanism and quantitative assessment of saturation transfer for water-based detection of the aliphatic protons in carbohydrate polymers. *Magn Reson Med*.
- van Zijl, P. C. M. and Yadav, N. N. (2011). Chemical exchange saturation transfer (CEST): What is in a name and what isn't? *Magn Reson Med*, 65(4):927–948.
- van Zijl, P. C. M., Zhou, J., Mori, N., Payen, J. F., Wilson, D., and Mori, S. (2003). Mechanism of magnetization transfer during on-resonance water saturation. A new approach to detect mobile proteins, peptides, and lipids. *Magn Reson Med*, 49(3):440–449.
- van Zijl, P. C. M., Lam, W. W., Xu, J., Knutsson, L., and Stanisz, G. J. (2018). Magnetization transfer contrast and chemical exchange saturation transfer MRI. Features and analysis of the field-dependent saturation spectrum. *Neuroimage*, 168:222–241.

List of Publications

Peer-Reviewed Journal Articles

- D. Kleimaier, V. Schepkin, R. Hu, and L. R. Schad (2020c). Protein conformational changes affect the sodium triple-quantum MR signal. *NMR Biomed*, 33(10):e4367
- D. Kleimaier, V. Schepkin, C. Nies, E. Gottwald, and L. R. Schad (2020f). Intracellular sodium changes in cancer cells using a microcavity array-based bioreactor system and sodium triple-quantum MR signal. *Processes*, 8(10):1267
- D. Kleimaier, S. Goerke, C. Nies, M. Zaiss, P. Kunz, P. Bachert, M. E. Ladd, E. Gottwald, and L. R. Schad (2020e). The cellular heat shock response monitored by chemical exchange saturation transfer MRI. *Sci Rep*, 10(1):11118
- R. Hu, D. Kleimaier, M. Malzacher, M. A. U. Hoesl, N. K. Paschke, and L. R. Schad (2020). X-nuclei imaging: Current state, technical challenges, and future directions. *J Magn Reson Imaging*, 51(2):355–376
- M. A. U. Hoesl, D. Kleimaier, R. Hu, M. Malzacher, C. Nies, E. Gottwald, and L. R. Schad (2019a). ^{23}Na triple-quantum signal of in vitro human liver cells, liposomes, and nanoparticles: Cell viability assessment vs. separation of intra- and extracellular signal. *J Magn Reson Imaging*, 50(2):435–444

Conference Contributions

- D. Kleimaier, V. D. Schepkin, C. Nies, E. Gottwald, and L. R. Schad (2020d). Intracellular sodium changes of cancer cells in a microcavity array-based bioreactor system by sodium triple-quantum signal. *Proc. Int. Soc. Magn. Reson. Med.*, 28:2979
- D. Kleimaier, S. Goerke, C. Nies, M. Zaiss, P. Kunz, E. Gottwald, and L. R. Schad (2020a). The cellular heat shock response monitored by chemical exchange saturation transfer MRI. *Proc. Int. Soc. Magn. Reson. Med.*, 28:3131
- D. Kleimaier and L. R. Schad (2020b). Sodium TQ signal cancelation due to B_0 inhomogeneities despite using a refocusing pulse. *Proc. Int. Soc. Magn. Reson. Med.*, 28:2978
- D. Kleimaier, R. Hu, and L. R. Schad (2019c). Solution pH affects the sodium triple-quantum signal of bovine serum albumin. *Proc. ESMRMB Congress*, 36:281
- D. Kleimaier, R. Hu, and L. R. Schad (2019b). Protein unfolding affects the sodium triple-quantum signal. *Proc. ESMRMB Congress*, 36:43

- D. Kleimaier and L. R. Schad (2019d). Feasibility of single voxel CEST measurements with a transceiver surface coil. *Proc. ESMRMB Congress*, 36:408
- D. Kleimaier, S. Goerke, C. Nies, E. Gottwald, and L. R. Schad (2019a). Initial CEST study in a microcavity array based 3D cell culture system. *Proc. Int. Soc. Magn. Reson. Med.*, 27:4000
- D. Kleimaier, S. Goerke, C. Nies, E. Gottwald, and L. R. Schad (2018a). Translation of biomarkers to in vivo: Initial CEST study in a microcavity array based 3D cell culture system. *Translational Biomedical Imaging (TraBI) - From Molecule to Man*
- D. Kleimaier, A. Neubauer, M. A. U. Hoesl, C. Nies, E. Gottwald, and L. R. Schad (2018d). Investigation of ethanol stimulation on HepG2 cells in a high density cell culture on chip by correlation spectroscopy. *Proc. Int. Soc. Magn. Reson. Med.*, 26:3895
- D. Kleimaier, M. A. U. Hoesl, A. Neubauer, M. Malzacher, C. Nies, E. Gottwald, and L. R. Schad (2018c). Measurement of oxygen consumption in a high density 3D cell culture on chip by ^{19}F spectroscopy. *Proc. Int. Soc. Magn. Reson. Med.*, 26:3885
- D. Kleimaier, M. A. U. Hoesl, M. Malzacher, C. Nies, E. Gottwald, and L. R. Schad (2018b). Feasibility study of localized oxygen consumption measurements in a microcavity array based 3D cell culture system by ^{19}F MRI. *MR Imaging of ^nX -Nuclei (^{23}Na and Friends): From Controversies to Potential Clinical Applications*
- M. A. U. Hoesl, D. Kleimaier, R. Hu, M. Malzacher, E. Gottwald, C. Nies, and L. R. Schad (2018b). Can sodium triple-quantum signal separate extra- and intracellular signals? – Investigation on HEP G2 liver cells, liposomes and nanoparticles. *Proc. Int. Soc. Magn. Reson. Med.*, 26:3875
- M. A. U. Hoesl, D. Kleimaier, M. Malzacher, R. Hu, and L. R. Schad (2018c). Voxel localization for sodium NMR triple-quantum signal; sequence design and test in agarose phantoms and in-vivo rat. *Proc. Int. Soc. Magn. Reson. Med.*, 2018:3874
- R. Hu, M. Malzacher, M. A. U. Hoesl, D. Kleimaier, and L. R. Schad (2018b). Simultaneously acquired single- and triple-quantum spectroscopic imaging with density-adapted projection reconstruction and time proportional phase increment. *Proc. Int. Soc. Magn. Reson. Med.*, 26:3866
- M. A. U. Hoesl, D. Kleimaier, R. Hu, M. Malzacher, E. Gottwald, C. Nies, and L. R. Schad (2018a). ^{23}Na triple-quantum signal: A clinical biomarker for the functionality of the Na/K pump? *MR Imaging of ^nX -Nuclei (^{23}Na and Friends): From Controversies to Potential Clinical Applications*
- R. Hu, M. Malzacher, M. A. U. Hoesl, D. Kleimaier, and L. R. Schad (2018a). Simultaneously acquired ^{23}Na single- and triple-quantum imaging in rat in vivo at 9.4 T. *MR Imaging of ^nX -Nuclei (^{23}Na and Friends): From Controversies to Potential Clinical Applications*

List of Figures

2.1	Zeeman splitting for ^1H and ^{23}Na	8
2.2	Longitudinal and transverse relaxation	12
2.3	NMR spectrum	15
2.4	Nuclear charge distribution	16
2.5	Density matrix	18
2.6	Spin $\frac{3}{2}$ NMR spectra	24
2.7	Sodium electric-quadrupole interactions in an isotropic environment	26
2.8	Coupling of irreducible tensor operators	29
2.9	Multi-quantum pulse sequence	33
2.10	2-pool model	35
2.11	Homonuclear two-spin system	37
2.12	Magnetization transfer pathways	39
2.13	Basic principle of CEST	41
2.14	CEST pulse sequence and Z-spectrum	43
2.15	Amino acids with a dissociable side chain group	49
2.16	Titration curve of aspartic acid	51
2.17	Protein structure	52
2.18	^1H chemical shifts of amino acids	56
3.1	9.4 T preclinical NMR system and RF coils	60
3.2	MR-compatible bioreactor system	66
3.3	Perfusion curve of the MR-compatible bioreactor system	68
3.4	Timing of the heat shock experiment	70
3.5	TQTPPI pulse sequence with evolution time increment	75
3.6	TQTPPI pulse sequence with fixed evolution time	78
3.7	Calculation of AREX	81
4.1	Influence of B_0 inhomogeneity on TQ signal	88
4.2	Effect of potassium concentration on sodium MR signals	90
4.3	Effect of pH on sodium MR signals	91
4.4	Sodium MR signals during BSA unfolding by urea	94
4.5	Comparison of the standard and the fixed TQTPPI pulse sequences	97
4.6	Sodium TQ signal from the bioreactor	98
4.7	Na/K-ATPase inhibition and control experiments	100
4.8	Sodium perfusion curve during K^+ -free medium	101
4.9	Contributions to the Z-spectrum from the bioreactor	104
4.10	Control experiments	106

4.11	Heat shock experiment of cell culture 1	107
4.12	Heat shock experiment of cell culture 2	109
A.1	^{23}Na B_1^+ map of an 8 and 10 ml sample using the $^1\text{H}/^{23}\text{Na}$ Bruker volume coil	126
A.2	^1H B_1^+ map of the MR-compatible bioreactor using the ^1H Bruker quadrature volume coil	127

List of Tables

2.1	Properties of some commonly used NMR nuclei	14
2.2	Irreducible spherical tensor operators for spin $I = \frac{3}{2}$	19
2.3	^1H chemical shifts of amino acids	56
3.1	Composition of the phantoms containing amino acids	63
4.1	Mean standard TQTPPI fit parameters for the three different shim routines	87
4.2	Standard TQTPPI fitting results of the amino acid samples using the fit function of Equation 3.5	89
4.3	Sigmoid function fit of the results for sodium TQ MR signal and fluorescent response	92
4.4	Comparison of the SQ and the TQ amplitudes of agarose samples for the standard and the fixed TQTPPI pulse sequences	95
4.5	Comparison of the transverse relaxation times between the standard and the fixed TQTPPI pulse sequences using agarose samples	96
4.6	Comparison of $\text{AREX}_{\Delta\text{ST}}$ and AREX for bioreactor	103
A.1	Exponential fit results of the cellular heat shock response	128

Declaration

This thesis is the result of my independent investigation under supervision. Where my work is indebted to the work or ideas of others, for example from the literature or the internet, I have acknowledged this within the thesis.

I declare that this study has not already been accepted for any degree, nor is it currently being submitted in candidature for any other degree.

I am aware that a false declaration could have legal implications.

Erklärung:

Ich versichere, dass ich diese Arbeit selbstständig verfasst habe und keine anderen als die angegebenen Quellen und Hilfsmittel benutzt habe.

Mannheim, November 23rd 2020

Dennis Kleimaier